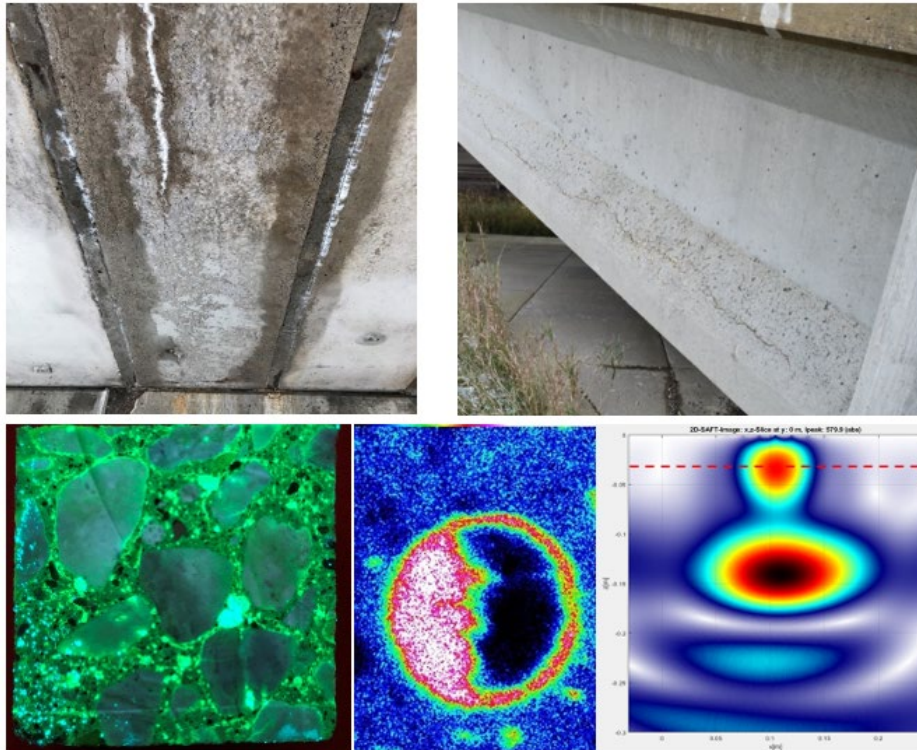




Concrete Deterioration of Prestressed Bridge Beams

FINAL REPORT – SEPTEMBER 2022



Department of Civil & Construction Engineering
College of Engineering and Applied Sciences

Western Michigan University

Intentionally left blank

1. Report No. SPR-1703	2. Government Accession No. N/A	3. Recipient's Catalog No. N/A.	
4. Title and Subtitle Concrete Deterioration of Prestressed Bridge Beams		5. Report Date 07/31/2022	
		6. Performing Organization Code N/A	
7. Author(s) Upul Attanayake, Ph.D., P.E. Neil Berke, Ph.D. Harsha Amunugama, M.Sc. Kanchani Basnayake, M.Sc.		8. Performing Org. Report No. N/A	
		10. Work Unit No. N/A	
9. Performing Organization Name and Address Western Michigan University College of Engineering and Applied Sciences 1903 West Michigan Avenue Kalamazoo, Michigan 49008-5316		11. Contract or Grant No. Contract 2016-0069 Z9	
		13. Type of Report & Period Covered Final Report 03/01/2019 – 07/31/2022	
12. Sponsoring Agency Name and Address Michigan Department of Transportation Research Administration 8885 Ricks Road P.O. Box 30049 Lansing, Michigan 48909		14. Sponsoring Agency Code N/A	
		15. Supplementary Notes Conducted in cooperation with the U.S. Department of Transportation, Federal Highway Administration. MDOT research reports are available at www.michigan.gov/mdotresearch .	
16. Abstract The mild to significant concrete deterioration observed on many prestressed concrete (PSC) beam bridges constructed in the 1970's and 1980's was suspected to be due to alkali-aggregate reactivity (AAR) and other material compatibility issues. The inventory analysis and field inspections identified a total of 136 I-beam bridges (~12% of the I-beam bridge population) with material related distress in the beams. An agency developed element (ADE) is recommended to document fascia beam conditions since the concrete deterioration was limited to the bottom flange of the fascia beams. Also, a collection of photographs is provided in the report; these can be included in inspection manuals to provide better clarifications on the types of cracks observed on PSC beams. Moreover, two staining techniques were evaluated to select a suitable method to detect alkali-silica reaction (ASR) in concrete. Only uranyl acetate is capable of providing reliable results to effectively identify ASR. For load rating of beams with concrete deterioration, one of the major challenges is to identify the ineffective strands in a section. For I-beams, it is recommended to use 2.5 in. crack depth for longitudinal cracks at the bottom flange when the crack width is less than 0.016 in. to identify the ineffective strands. Guidelines are provided to identify the ineffective strands in box beams. A Mathcad calculation sheet was developed to calculate input data for AASHTOWare BrR for flexural load rating of distressed box beams. The same Mathcad can be used as a stand-alone tool for load rating of box beams. Breathable penetrating sealants and surface coatings were identified through an experimental program to protect concrete beams. Protectosil® BH-N, SIL-ACT® ATS-200, and Si-Rex 03 with Si-Primer performed better than the other products evaluated during this study. .			
17. Key Words Alkali-Aggregate Reactivity, Alkali-Silica Reactivity, Concrete, Coatings, Beams, Delayed Ettringite Formation, Distress, Freeze-thaw, Prestressed, Rating, Sealants		18. Distribution Statement No restrictions. This document is available to the public through the Michigan Department of Transportation.	
19. Security Classif. (of this report) Unclassified	20. Security Classif. (of this page) Unclassified	21. No. of Pages 362	22. Price N/A

Intentionally left blank

Concrete Deterioration of Prestressed Bridge Beams

**Final Report
(2019 - 2022)**

Project Manager: Rick Liptak, P.E.

Submitted to:



Submitted by:

Upul Attanayake, Ph.D., P.E.
Presidential Innovation Professor and Director
Center of Excellence for Structural Durability
(269) 276 – 3217
upul.attanayake@wmich.edu

Harsha Amunugama, M.Sc.
Graduate Research Assistant
Center of Excellence for Structural Durability
(269) 276 – 3210
a.amunugama@wmich.edu

Neal Berke, Ph.D.
Vice President Research
Tourney Consulting Group, LLC
(269) 384 – 9980
nberke@tourneyconsulting.com

Kanchani Basnayake, M.Sc.
Graduate Research Assistant
Center of Excellence for Structural Durability
(269) 276 – 3210
k.basnayakemudiyanselage@wmich.edu

Western Michigan University
Department of Civil & Construction Engineering
College of Engineering and Applied Sciences
Kalamazoo, MI 49008-5316
Fax: (269) 276 – 3211



DISCLAIMER

“This publication is disseminated in the interest of information exchange. The Michigan Department of Transportation (hereinafter referred to as MDOT) expressly disclaims any liability, of any kind, or for any reason, that might otherwise arise out of any use of this publication or the information or data provided in the publication. MDOT further disclaims any responsibility for typographical errors or accuracy of the information provided or contained within this information. MDOT makes no warranties or representations whatsoever regarding the quality, content, completeness, suitability, adequacy, sequence, accuracy or timeliness of the information and data provided, or that the contents represent standards, specifications, or regulations.”

“This material is based upon work supported by the Federal Highway Administration under SPR OR19-017. Any opinions, findings and conclusions or recommendations expressed in this publication are those of the author(s) and do not necessarily reflect the views of the Federal Highway Administration.”

ACKNOWLEDGEMENTS

This project is funded by the Michigan Department of Transportation (MDOT). The authors would like to acknowledge the support and effort of Mr. Jonathan Bruinsma for initiating this research and managing it during his tenure at MDOT until March 2022. The authors greatly appreciate the support and effort of Mr. Rick Liptak for coordinating and managing this project to have a successful conclusion. The authors also wish to acknowledge the continuing assistance of the Research Advisory Panel (RAP) members in contributing to the advancement of this study. The authors appreciate the contribution of graduate students (Abul Mazumder, Sanjoy Bhowmik, Shresta Wosti, and Srikanth Vemula) along with undergraduate students (Kavya Kurupparachchi and Uresh Wijesinghe) for the successful completion of the experimental activities. Special thanks are due to Dr. Kaczmarek and Ashley Scott of WMU and Larry Wachowski and Joe Duke of Tourney Consulting Group (TCG) for their contribution to the project. Thanks are also due to TCG staff Mike Wachowski, Dave Agopian, and several others for their help during specimen fabrication. The authors offer their gratitude to John Cernius of WMU for his help during the project. Troy Place's and Pavitra Attanayake's untiring efforts in editing the report are greatly appreciated. Last but not least, the authors thank Professor Haluk Aktan for his support and guidance during the project.

Intentionally left blank

EXECUTIVE SUMMARY

INTRODUCTION

The mild to significant concrete deterioration observed on many prestressed concrete (PSC) beam bridges constructed in the 1970's and 1980's was suspected to be due to alkali-aggregate reactivity (AAR) and other material compatibility issues. This project was initiated to determine the status of the Michigan Department of Transportation (MDOT) bridge inventory with regards to the concrete deterioration of PSC beams, develop inspection guidelines, evaluate screening test methods for detecting alkali-silica reaction (ASR) in concrete for field applications, create capacity calculation and load rating guidelines of PSC beams with varying stages of concrete deterioration, and offer rehabilitation options.

BRIDGES WITH CONCRETE DETERIORATION OF I-BEAMS

As an initial attempt to identify the bridges with concrete deterioration in beams, MDOT region bridge engineers were surveyed. The survey responses included a total of 202 I-beam bridges, 36 spread box-beam bridges, and 96 side-by-side box-beam bridges with longitudinal and map cracking. Out of all the regions in Michigan, the University Region indicated having 127 I-beam bridges, 36 spread box-beam bridges, and 96 side-by-side box-beam bridges with such cracking. The analysis of I-beam bridge condition data from the University Region indicated that many of these bridges were located on specific corridors, which was a significant constraint to conduct a meaningful statistical analysis of a subset for all three bridge superstructure types. Therefore, it was decided to limit this study to PSC I-beam bridges. After conducting a comprehensive review of the inspection records of 1136 bridges since 1994, field inspections of a subset to confirm the distresses documented in the inspection reports, and ASR screening tests on a selected number of bridges, *a total of 136 I-beam bridges (~12% of the I-beam bridge population) were identified to have material related distress in the beams.* Chapter 3 describes the data analysis process and presents the number of I-beam bridges in each region with concrete deterioration. Concrete deterioration was predominantly observed at the bottom flange exterior surfaces of the fascia beams. A minor level of fine aggregate ASR and longitudinal cracking were recorded. Subsequently, an ArcGIS file showing the geographic locations of the bridges was developed.

INSPECTION GUIDELINES

The activities conducted to identify the I-beam bridges with concrete deterioration in the beams indicated that the deteriorations were limited to beam ends and the bottom flange of the fascia beams. The current MDOT inspection and documentation process includes an element to document beam end conditions. However, the longitudinal and/or map cracking along the fascia bottom flange was not consistently recorded. Even if the longitudinal cracking is recorded, its significance on the condition state is not properly reflected since the crack length is considered as a fraction of the total beam length. Hence, an agency developed element (ADE) is proposed to document fascia beam conditions. The other limitations were the inconsistent documentation of the type of cracks and the abbreviations used in the inspector comments. The use of inconsistent abbreviations and terms in inspector comments limited the use of advanced natural language processing tools to extract information for further analysis. To eliminate these deficiencies, one approach would be to provide a list of crack types as a drop-down list or as a list with checkboxes. When an inspector selects the crack type(s), a unique code can be recorded through the software used by the inspector. Until such an improvement to the current inspection data recording is implemented, a set of photographs illustrating each crack type, along with the name of the crack type, can be provided as a guidance to the inspectors. Chapter 4 includes necessary photographs and suggested changes to the current inspection guidelines.

ASR SCREENING TEST METHODS FOR FIELD APPLICATION

So far, three staining techniques have been developed and evaluated to identify the presence of ASR in concrete. These stains include cuprammonium sulfate, uranyl acetate, and a sodium cobaltinitrite/rhodamine B combination. However, only uranyl acetate and the combination of sodium cobaltinitrite/rhodamine B have shown the ability to highlight ASR gel in distinct colors. The application of uranyl acetate to identify ASR gel is well documented and had an ASTM (the American Society for Testing and Materials) standard, which was later withdrawn due to undocumented reasons. The dual staining technique (sodium cobaltinitrite/rhodamine B) is capable of identifying ASR gels with K^+ and Ca^{2+} . This technique is not suitable for detecting Na^+ rich ASR gels since sodium cobaltinitrite is a well-known product used in analytical chemistry to determine the K^+ content of a solution. The strengths and challenges of implementing these

staining techniques were evaluated and documented in Chapter 5. The findings indicate that uranyl acetate is the only method available so far to be implemented with confidence in the field.

LOAD RATING GUIDELINES

Guidelines for incorporating PSC box- and I-beam deteriorations and distresses during flexural rating of beams were developed using the information collected through a comprehensive review of literature, inspection of a selected number of I-beam bridges, the measurement of crack depths on two fascia beams, and the past experience of the research team. Since the depth of concrete degradation was limited to the near surface area of the I-beam bottom flange, the major concern for flexural load rating of I-beams is the number of ineffective prestressing strands. The impact of longitudinal cracks on strand durability and bond integrity depends on the locations of the cracks and strand layout. As a rule of thumb, it is recommended to assume a 2.5 in. depth for cracks that are narrower than 0.016 in. To develop more rational guidelines, a crack width vs. depth relationship needs to be developed for the typical bridge beams. For flexural capacity calculation and load rating of box-beams, a Mathcad calculation sheet was developed and delivered with the report. Detailed guidelines are provided in the report to help decide the number of prestressing strands to be excluded from a section for flexural load rating. A user manual for the Mathcad sheet is provided in Appendix E.

CONCRETE PROTECTIVE SYSTEMS

Concrete deterioration of I-beams is limited to the outside surface of the fascia beams. Past research shows a significant deterioration at beam ends, too. One of the primary factors that contributes to concrete deterioration is the moisture. Hence, the protective systems for PSC beams should allow breathability of concrete while preventing moisture intrusion. Consequently, four types of protective systems were considered by evaluating the degree of concrete deterioration, the functional requirements of concrete protective systems, and the products in the MDOT approved list. These protective systems included (i) penetrating sealants, (ii) coatings, (iii) a penetrating sealant and a coating, and (iv) lithium nitrate and a coating. Even though breathable sealants and coatings were used, these materials might not be 100% breathable. When the outside concrete surface of fascia beams heats up with solar exposure, moisture is drawn towards the heated surface. This will allow moisture accumulation beneath the sealants and coatings. Hence, lithium nitrate was used as a primer for coatings to control possible development of ASR underneath the coating.

Breathability is the performance parameter, whereas the internal relative humidity (IRH) is the measurand. The following observations were documented from the experimental results:

1. The Protectosil[®] BH-N had slightly better breathability than the SIL-ACT[®] ATS-200.
2. The Si-Rex 03 with Si-Primer performed better than the Ultra Spec[®] Masonry Elastomeric Waterproofing Coating Flat 0359 with the recommended primer. However, Si-Rex 03 is more sensitive to coating thickness, and special attention is required during the application to prevent cracking. It is recommended to adhere to the manufacturer guidelines and evaluate the use of a sprayer to control the coating thickness.
3. The application of SIL-ACT[®] ATS-200 as the primer for Ultra Spec[®] Masonry Elastomeric Waterproofing Coating Flat 0359 enhanced the concrete drying rate, and the performance was similar to the Si-Rex 03 with Si-Primer. Since SIL-ACT[®] ATS-200 and Si-Primer are silanes, using them as the primer provides an added protection to concrete.
4. Applying 30% LiNO₃ as a pretreatment for Ultra Spec[®] Masonry Elastomeric Waterproofing Coating Flat 0359 lowers the water vapor permeance compared to the other multi-layer concrete protective systems.

RECOMMENDATIONS

The following recommendations are provided for the implementation consideration:

1. About 12% of the MDOT I-beam bridge inventory has map and/or longitudinal cracking on fascia beams, which is an indication of concrete deterioration. The location of these bridges is provided in the ArcGIS file submitted with this report. The fascia beams need to be inspected to identify the type of maintenance and repair actions needed to extend the service life.
2. The inspection guidelines presented in this report can be seamlessly integrated into the current practice. An implementation example demonstrating the updated procedures is provided in the report. It is recommended to upgrade the current procedures using an image-based inspection template to collect consistent and quality data that can be used for the causal evaluation of deteriorations and distresses of bridge elements to develop appropriate maintenance and repair strategies.
3. Uranyl acetate is the most reliable method available to screen for ASR under field conditions. A major challenge of implementing this method in the field is the interference from the

ambient light while observing the unique fluorescence signatures using ultraviolet (UV) light. It is recommended to develop a remote-controlled digital imaging system to alleviate the field implementation challenges.

4. It is necessary to identify the effective number of prestressing strands in deteriorated PSC I-beam sections for flexural load rating. It is recommended to follow the procedure demonstrated in this report to develop crack depth vs. crack width relationships to identify the possibly damaged strands in a beam cross-section. Until then, it is recommended to assume a 2.5 in. depth for longitudinal cracks that are narrower than 0.016 in.
5. It is recommended to use the Mathcad calculation sheet provided with this report to calculate necessary input parameters for AASHTOWare BrR for load rating of box-beams. The sheet can also be used as a stand-alone load rating tool for box-beams. The report provides the necessary guidelines to identify the ineffective strands in a distressed box-beam section.
6. A suitable concrete protection method needs to be selected based on the degree of concrete deterioration, life-cycle performance, and the cost. Considering the available guidelines, 100% silane sealants can be applied to protect components with surface crack widths less than 0.002 in. However, when a surface is exposed directly to a source of moisture, such as the outside and bottom surfaces of a fascia beam, it is recommended to use a concrete protective system consisting of a breathable coating and a penetrating sealant as the primer. Based on the crack bridging ability of the breathable coatings evaluated in this study, concrete surfaces with cracks as wide as 0.004 in. can be protected.
7. The MDOT product qualification process requires evaluating penetrating sealant performance using a Grade D structural concrete mix with a 0.45 water-cementitious material ratio (w/c). The product evaluation methods listed in the current MDOT specifications need to be revised to reflect the concrete mixes used in PSC bridge beams, curing methods, and the concrete age at the time of sealant application. It is recommended to review and evaluate the Alberta Transportation specifications for Type 1c sealers, which are recommended for precast concrete, to develop MDOT specifications for the selection of sealers for PSC bridge beams.
8. Considering the cost and breathability performance, Si-Rex 03 with Si-Primer is recommended over the Ultra Spec[®] Masonry Elastomeric Waterproofing Coating Flat 0359 with SIL-ACT[®] ATS-200 as the primer. It will improve protection to the surface as long as there are no active cracks that are wider than the crack bridging limits specified in the

manufacturer technical data sheets. As of 09/2021, Si-Rex 03 with Si-Primer costs \$542 per 1000 ft², whereas the Ultra Spec[®] Masonry Elastomeric Waterproofing Coating Flat 0359 with SIL-ACT[®] ATS-200 costs \$1058 to cover the same area.

9. It is recommended to use the above-stated coating systems at the fabrication yard on new fascia beams to protect all the surfaces, except the top. Available guidelines support the application of coatings at the 4th day from fabrication. For the fascia beams on in-service bridges, all the exposed surfaces are recommended to be protected using any of the above coating systems since the moisture is drawn towards the outside surface as it warms up when exposed to sunlight, while the moisture enters through other surfaces.
10. It is recommended to evaluate the crack bridging ability and long-term performance of Si-Rex 03 with Si-Primer and the Ultra Spec[®] Masonry Elastomeric Waterproofing Coating Flat 0359 with SIL-ACT[®] ATS-200 as the primer to define the service life of such systems/products.
11. It is recommended to adopt the sealant and coating evaluation method implemented in this study to evaluate the system performance since it considers the substrate, substrate preparation, application, curing, and the type of sealants and coatings as system parameters.

TABLE OF CONTENTS

DISCLAIMER	vi
ACKNOWLEDGEMENTS	vii
EXECUTIVE SUMMARY	ix
TABLE OF CONTENTS	xv
LIST OF TABLES	xix
LIST OF FIGURES	xxi
1 Introduction.....	1
1.1 Overview.....	1
1.2 Objectives and Tasks	3
1.3 Report Organization.....	3
2 State-of-the-Art and Practice Literature Review	5
2.1 Overview.....	5
2.2 PSC Box- and I-Beam Distresses.....	5
2.3 Deterioration of Prestressed/Reinforced Concrete Components.....	7
2.3.1 Alkali-Aggregate Reaction (AAR).....	7
2.3.2 Delayed Ettringite Formation (DEF)	10
2.3.3 Cracking Due to ASR	11
2.4 PSC Box- and I-Beam Inspection.....	13
2.4.1 National and Agency Specific Guidelines	14
2.5 Staining Techniques for Detecting ASR.....	22
2.5.1 Detection of ASR in Concrete.....	22
2.5.2 Uranyl Acetate Test	24
2.5.3 Sodium Cobaltinitrite/Rhodamine B Test.....	28
2.5.4 Summary	30
2.6 Load Rating of PSC Beams/Bridges.....	31
2.6.1 LFR Method	31
2.6.2 LRFR Method.....	32
2.6.3 Load Rating Parameters Impacted by Distresses	33
2.6.4 AASHTOWare BrR for Load Rating of Distressed PSC Beams	34
2.7 Concrete Degradation in PSC Beams	46
2.7.1 Compressive Strength.....	47
2.7.2 Modulus of Elasticity.....	50

2.7.3	Tensile Strength.....	52
2.7.4	Ultrasonic Pulse Velocity (UPV)	53
2.7.5	Impact of Concrete Deterioration (Other than ASR) on Mechanical Properties.....	54
2.7.6	Effective Section Properties	54
2.8	Prestressing Strands	56
2.8.1	Material Properties.....	56
2.8.2	Number of Effective Prestressing Strands	57
2.8.3	Redevelopment of Severed Prestressing Strands.....	59
2.9	Distress Quantification.....	60
2.9.1	Crack Density	61
2.9.2	Damage Rating Index (DRI)	61
2.9.3	Crack Index	64
2.9.4	Depth of Degradation.....	65
2.10	Crack Depth Evaluation Using Non-destructive Techniques	70
2.10.1	Two-Transducer Method.....	71
2.10.2	Application of Multi-Array Transducers.....	79
2.11	Uniaxial vs. Biaxial Section Analysis for Distressed Beam(s).....	82
2.12	Live Load Distribution in the Presence of Distressed PSC Beams	83
2.13	Finite Element (FE) Analysis of Damaged PSC Beams.....	86
2.14	Concrete Surface Coatings.....	87
2.14.1	Impact of Surface Coatings on Concrete Durability.....	88
2.14.2	Guidelines for Crack Sealing and Repair.....	89
2.14.3	Performance-Based Selection.....	91
2.15	Penetrating Sealants.....	96
3	Concrete Deterioration in PSC Bridge Beams	100
3.1	Overview.....	100
3.2	Data Analysis	101
3.2.1	Data and Information from Inspection Reports.....	101
3.2.2	Distress Charts.....	102
3.2.3	Scatter Plots.....	105
3.2.4	Geospatial Distribution of Bridge Clusters	107
3.3	Data Analysis Challenges, Assumptions, and Lessons Learned.....	108
3.3.1	Challenges During Data Compilation.....	108
3.4	Bridges with Concrete Deterioration in PSC Beams.....	111

3.4.1	Bridges with Map and/or Longitudinal Cracking in Beams	111
3.4.2	Field Inspection - Summary of Observations.....	111
3.4.3	Concrete Deterioration in the Kalamazoo River Bridge Beams	118
3.4.4	Concrete Deterioration in the Brady Street Bridge Beams	118
3.5	Depth of Cracks in PSC I-Beams	119
3.5.1	Device Description	120
3.5.2	Crack Depth Evaluation Using Laboratory Specimens	122
3.5.3	Crack Depth Evaluation in PSC I-Beams	137
3.5.4	Summary of Findings and Recommendations.....	146
4	Recommended Inspection Guidelines for PSC Box- and I-Beams	148
4.1	Overview.....	148
4.2	Agency-Developed Element (ADE).....	148
4.3	Defect Types in PSC Beams	150
4.3.1	Modifications to CS Table 2 of MiBEIM.....	150
4.4	Implementation Example	156
5	Evaluation of Staining Techniques	159
5.1	Uranyl Acetate Testing	159
5.1.1	Performance Evaluation Using Reactive Aggregate	159
5.1.2	Performance Evaluation Using Mortar Bars	162
5.1.3	Performance Evaluation Using Concrete Prisms.....	164
5.2	Sodium Cobaltinitrite/ Rhodamine B Testing.....	166
5.2.1	Performance Evaluation Using Reactive Aggregates	166
5.2.2	Performance Evaluation Using Mortar Bars	168
5.3	Summary	169
6	Guidelines for Load Rating of Distressed PSC Box- and I-Beams	171
6.1	Overview.....	171
6.2	Recommended Guidelines	171
6.2.1	Concrete Material Properties.....	171
6.2.2	Effective Concrete Section Properties	172
6.2.3	Prestressing Steel Material Properties	173
6.2.4	Effective Number of Prestressing Strands	173
6.3	Implementation of the Recommended Guidelines in AASHTOWare BrR.....	186
6.3.1	Defining Concrete Material Properties in AASHTOWare BrR.....	186
6.3.2	Defining Beam Cross-Section Properties in AASHTOWare BrR	186

6.3.3	Defining Prestressing Strand Layout in AASHTOWare BrR.....	187
7	Performance Evaluation of Concrete Protective Systems.....	189
7.1	Overview.....	189
7.2	Impact of Mix Design and Exposure on Mortar and Concrete Expansion.....	189
7.2.1	Accelerated Mortar Bar Test.....	189
7.2.2	Expansion of Concrete Prisms and Slabs.....	193
7.3	PERFORMANCE of Concrete Protective Systems	199
7.3.1	Reactivity Level of Aggregates	200
7.3.2	Influence of Curing Conditions	201
7.3.3	Evaluation of Protective Systems	201
7.3.4	Results and Discussion.....	204
7.4	Cost Estimation	211
7.5	Summary	212
8	Summary, Conclusions, and Recommendations	215
8.1	Summary.....	215
8.2	Conclusions and Recommendations	215
8.2.1	Concrete Deterioration in PSC Beams.....	215
8.2.2	Inspection Guidelines.....	216
8.2.3	Staining Techniques for Detecting ASR Under Field Conditions.....	216
8.2.4	Load Rating Guidelines	217
8.2.5	Concrete Protective Systems	217
8.3	Recommendations for Further Research.....	219
9	References.....	221

Appendix A: Guidelines for estimating prestressing strand loss

Appendix B: Survey of regional bridge engineers and fabricators

Appendix C: Causal evaluation of concrete deterioration in the Kalamazoo River bridge beams

Appendix D: Causal evaluation of concrete deterioration in the Brady Street bridge beams

Appendix E: Load rating of PSC box beams – User manual

LIST OF TABLES

Table 2-1. Mineralogy, Atomic Structure, and Reactivity Level of SiO ₂ Arrangements	9
Table 2-2. Uranyl Acetate Solution Preparation, Treatment, and Observation Methods	25
Table 2-3. Load Rating Parameters Impacted by Beam Distress	34
Table 2-4. Fitting Coefficients and Standard Deviations (Esposito et al. 2016).....	50
Table 2-5. Strength of Corroded Strands (Naito et al. 2011)	56
Table 2-6. The Impact of Cracks on Strand Condition and Strength (Naito et al. 2011).....	56
Table 2-7. DRI-Based Classification System for ASR Damaged Structures (Shrimer 2015)	61
Table 2-8. Correlation of Field Observations to DRI (Shrimer 2019).....	62
Table 2-9. Damage Classification of ASR Affected Concrete (Sanchez et al. 2017).....	64
Table 2-10. Cracking Index Based Damage Classification (Godart et al. 1992).....	65
Table 2-11. Propagation of Cracks with Expansion (Fan and Hanson 1998)	66
Table 2-12. Member Distress and the Average Expansion (Bérubé et al. 2005)	68
Table 2-13. Live Load Distribution with Damaged Beams (Wipf et al. 2004).....	85
Table 2-14. Water Absorption and Chloride Diffusivity of Surface Treated Concrete and Adhesion and Crack Bridging Ability of Coatings.....	89
Table 2-15. Performance Parameters and Limits for the MDOT Approved Coatings	93
Table 2-16. Approved Products in Other Highway Agency Lists.....	94
Table 2-17. MDOT Approved Penetrating Sealants.....	97
Table 2-18. Penetrating Sealant Performance Parameters and Limits.....	98
Table 3-1. Bridges in Each Region and the Numbers Identified from the Survey	101
Table 3-2. Distress or Condition Rating, Priority Level, and Color Code.....	103
Table 3-3. Abbreviated Terms in the Inspection Reports	109
Table 3-4. Number of Bridges with Map and/or Longitudinal Crack in PSC I-Beams.....	111
Table 3-5. Bridges Selected for Inspection	112
Table 3-6. Number of Bridges Showing Concrete Deterioration in PSC I-Beams	117
Table 3-7. Technical Specifications of the Pundit 250 Array (Proceq 2017).....	122
Table 3-8. Transducer Groups Selected for the Reconstruction of B-Scans.....	127
Table 3-9. Estimated Crack Depth in Slabs.....	136
Table 3-10. The Depth of Longitudinal Cracking in a Fascia Beam (S.N. 424).....	138
Table 3-11. The Depth of Longitudinal Cracking in a Fascia Beam (S.N. 2618).....	142

Table 4-1. Element Description for the PSC Fascia/Exterior Beam Element.....	149
Table 4-2. List of Girder Elements Updated with the New ADE XXX.....	149
Table 4-3. Updated Condition State Descriptions for the Cracking in PSC	150
Table 4-4. Updated CS Table 2	153
Table 5-1. Exposure Conditions and Duration for Coarse Aggregate (Spratt)	159
Table 5-2. Exposure Conditions and Duration for Fine Aggregate (Arcosa Sand).....	159
Table 5-3. Observation of Coarse Aggregate (Spratt) Exposed to Various Conditions	160
Table 5-4. Observation of UA Treated Coarse Aggregate (Spratt) Against Drying Time	161
Table 6-1. Reduction in Concrete Modulus of Elasticity and Tensile Strength Due to ASR	172
Table 6-2. Guidelines for Excluding Ineffective Strands Due to Cracking in Box-Beams	174
Table 6-3. Guidelines for Excluding Ineffective Strands from Distressed Box-Beams	178
Table 7-1. The Design of Mortar Mixes for Three Specimens - Phase 1 Testing.....	190
Table 7-2. Exposure Conditions and Labels for Mortar Bars.....	190
Table 7-3. Concrete Mix for Slabs and Prisms (per yd ³)	194
Table 7-4. Experimental Program for Concrete Specimens Investigated During Phase 1.....	195
Table 7-5. Fresh and Hardened Concrete Properties - Phase 1	196
Table 7-6. Concrete Mix Design for Protective System Performance Evaluation (per yd ³).....	200
Table 7-7. Exposure Conditions and Specimens for Expansion Evaluation.....	201
Table 7-8. Evaluation of Exposure Conditions on Concrete Prism Expansion.....	201
Table 7-9. Concrete Protective Systems.....	203
Table 7-10. Concrete Protective System Performance at the End of 73-Day Exposure to 120° F at 25% RH	208
Table 7-11. Coating Conditions Recorded Through Visual Inspection.....	210
Table 7-12. Cost of Penetrating Sealants	211
Table 7-13. Cost of Surface Coatings	212
Table 7-14. Cost of Multi-Layer Coating Systems.....	212

LIST OF FIGURES

Figure 1-1. Longitudinal and map cracking in PSC I-beams	2
Figure 1-2. PSC box-beam cracking	2
Figure 2-1. PSC box- and I-beam distresses.....	6
Figure 2-2. Typical causes of prestressed/reinforced concrete deterioration.....	7
Figure 2-3. Stages of ASR and formation of swelling and non-swelling products	10
Figure 2-4. Early ettringite formation (EEF) and delayed ettringite formation (DEF).....	11
Figure 2-5. Factors contributing to DEF and concrete degradation.....	11
Figure 2-6. The role of drying shrinkage and ASR in developing surface cracking in concrete members (Helmuth 1993).....	12
Figure 2-7. The time of appearance of material related distress in concrete (Van Dam et al. 2002)	13
Figure 2-8. A bridge safety inspection report showing the CSs of PSC I-beams.....	17
Figure 2-9. CS Table 2 for PSC elements with supplemental information for inspectors (MiBEIM 2017)	18
Figure 2-10. A bridge safety inspection report showing the CSs of PSC I-beams and ADEs.....	19
Figure 2-11. CS Table 9 with beam end condition state definitions (MiBEIM 2017)	20
Figure 2-12. Element inspection record format showing the contribution of specific defect(s) to a condition state: PSC I-beam bridge inspection summary (AASHTO MBEI 2019)	21
Figure 2-13. Structure of silica gel (Ahrland et al. 1960a).....	23
Figure 2-14. Fluorescent micrography observations (a) microcracks - one crack is running from the aggregate into the paste (red arrows) while another one travels along the interface between aggregate and paste before running into the paste (white arrow), (b) a crack running from one large aggregate to another by cutting through a small aggregate in between (Leemann and Griffa 2013), and (c) air voids filled with ettringite showing similar fluorescence (Peterson 1999)	26
Figure 2-15. Impact of specimen exposure duration to uranyl acetate on detectable ASR gel fluorescence (Igarashi et al. 2016).....	27
Figure 2-16. Impact of drying time (in brackets) on ASR gel fluorescence intensity (Igarashi et al. 2016).....	28
Figure 2-17. Impact of storage duration to exudation of ASR gel onto the specimen surface in the presence of high relative humidity (Igarashi et al. 2016).....	28

Figure 2-18. Cores treated with sodium cobaltinitrite (b and e) and rhodamine B (c and f) reagents; core 2 shows a higher probability of having non-expansive ASR gels (Frybort et al. 2020)	30
Figure 2-19. Concrete material property data input window	36
Figure 2-20. Prestressing steel material property data input window.....	36
Figure 2-21. Concrete stress limits data input window.....	37
Figure 2-22. <i>Dimensions</i> tab in the PSC I-beam section property data input window	38
Figure 2-23. <i>Properties</i> tab in the PSC I-beam section property data input window.....	38
Figure 2-24. <i>Strand Grid</i> tab in the PSC I-beam section property data input window.....	39
Figure 2-25. Strand layout data input window with <i>P and CGS</i> option	40
Figure 2-26. Strand layout data input window with <i>Strands in rows</i> option.....	40
Figure 2-27. Dialog box to define live load distribution factors for the LFD (<i>Standard</i>) method when the superstructure is modeled as a Girder System Superstructure.....	41
Figure 2-28. Dialog box to define live load distribution factors for the <i>LRFD</i> method when the superstructure is modeled as a Girder System Superstructure	42
Figure 2-29. Dialog box to assign a beam condition factor	43
Figure 2-30. Control options selection window.....	44
Figure 2-31. Dialog box to assign user-defined points of interest.....	44
Figure 2-32. Stress limit override option in AASHTOWare BrR	45
Figure 2-33. Positive flexural capacity override option in AASHTOWare BrR.....	46
Figure 2-34. Variation of normalized concrete compressive strength with % expansion due to ASR (Abd-Elssamad et al. 2020 and ISE 1992).....	48
Figure 2-35. Variation of normalized concrete elasticity modulus with ASR expansion (Abd-Elssamad et al. 2020 and ISE 1992)	51
Figure 2-36. Residual elasticity modulus variation with concrete expansion due to ASR (Nguyen et al. 2019).....	51
Figure 2-37. Reduction in normalized splitting tensile strength due to ASR (Sanchez 2014 and ISE 1992).....	52
Figure 2-38. Variation of normalized splitting tensile strength, modulus of rupture (MOR), and direct tensile strength with ASR expansion (Esposito et al. 2016).....	53

Figure 2-39. Modeling of beams with spalled concrete and severed strands (Tabatabai and Nabizadeh 2019)	55
Figure 2-40. Saw cut surface of a box-beam showing strand conditions (Harries 2006)	57
Figure 2-41. Deteriorated strands in an I-beam (Williams and Choudhuri 2010).....	59
Figure 2-42. Concept of the redevelopment of a severed strand (Kasan and Harries 2011).....	60
Figure 2-43. DRI vs. ASR expansion for concrete cylinders (Smaoui et al. 2004a and 2004b)..	63
Figure 2-44. Crack patterns at different depths from the surface (Miki et al. 2013) (1 mm = 0.0394 in).....	69
Figure 2-45. Crack depth vs. width variation in reinforced concrete members (CSA 2000) (1 mm = 0.0394 in.).....	69
Figure 2-46. The two transducer TOF measurement system to measure crack depth.....	71
Figure 2-47. Transducer arrangements to measure surface crack depth.....	72
Figure 2-48. Estimated and actual crack depths for four transducer arrangements (Pinto et al. 2010)	76
Figure 2-49. Crack depth calculation using Proceq Pundit PL-200 data (Proceq 2014)	77
Figure 2-50. Check for slope direction of an oblique crack (BSI 1997).....	78
Figure 2-51. MIRA A1040 - Commercially available linear array system (ACS 2021).....	79
Figure 2-52. Evaluation of surface cracks using a linear array device (Helmerich et al. 2015) ..	80
Figure 2-53. Evaluation of surface cracks using a linear array device (Helmerich et al. 2015) ..	80
Figure 2-54. Positions of MIRA A1040 w.r.t the surface crack (Popovics et al. 2017).....	81
Figure 2-55. B-scans recorded with the unit placed above the crack (Popovics et al. 2017).....	82
Figure 2-56. B-scans recorded with the unit offset from the crack (Popovics et al. 2017).....	82
Figure 2-57. Rotation of the NA of a 33 × 36 in. box-beam-section due to an asymmetric loss of strands (Harries 2006).....	83
Figure 2-58. Detail of the distressed exterior beam in the Main Street Bridge in Winnipeg, Canada (Kim 2008) (Note: Dimensions are in mm).....	84
Figure 2-59. Practices of state highway and other agencies.....	90
Figure 2-60. Concrete surface coating performance chart	95
Figure 2-61. Performance of concrete treated with penetrating sealants	99
Figure 3-1. MiBRIDGE database showing bridge information and inspection reports.....	102
Figure 3-2. Spreadsheet with the data extracted from inspection reports	102

Figure 3-3. Example of a distress chart organized with respect to <i>structure number</i>	104
Figure 3-4. Beam condition and distress variation with respect to <i>year built</i>	105
Figure 3-5. Beam condition and distress variation with respect to <i>Age (year built)</i> arranged in the ascending order)	105
Figure 3-6. A data set showing the age at which a distress was first observed on beams	106
Figure 3-7. Scatter plot showing the age at which a distress was first observed on beams	107
Figure 3-8. Location of bridges with concrete deterioration in PSC I-beams (an example).....	108
Figure 3-9. Map and longitudinal cracks in PSC I-beams	112
Figure 3-10. Structure 2273 fascia beam: Surface condition and fine aggregate ASR.....	113
Figure 3-11. Structure 12775 fascia beam: Surface condition and fine aggregate ASR.....	114
Figure 3-12. Concrete surface coating damage and lack of crack bridging ability	114
Figure 3-13. Orientation and exposure of the bridge carrying M-57 over Flint River	115
Figure 3-14. Orientation and exposure of the bridge carrying Lincoln Road over I-75	116
Figure 3-15. Geospatial distribution of bridges with potential material distress in I-beams	117
Figure 3-16. Proceq Pundit 250 array unit (Proceq 2017)	121
Figure 3-17. Concrete slab with a simulated crack.....	123
Figure 3-18. <i>Arrangement-1</i> : Excitation direction parallel to the crack and the unit placed symmetrically over the crack.....	124
Figure 3-19. <i>Arrangement-2</i> : Excitation direction parallel to the crack and the unit placed offset from the crack	124
Figure 3-20. <i>Arrangement-3</i> : Excitation direction perpendicular to the crack and the unit placed symmetrically over the crack.....	125
Figure 3-21. The options available in <i>InterSAFT</i> to select transducer combinations.....	126
Figure 3-22. The impact of crack depth and transducer arrangement on surface wave propagation	129
Figure 3-23. Processed B-scans using <i>Arrangement-1</i> data with two transmitter-receiver combinations for the slab with a 1.25 in. deep crack.....	130
Figure 3-24. B-scans of slabs reconstructed using <i>Arrangement-1</i> data with T ₁ to T ₄ as transmitters and T ₅ to T ₈ as receivers.....	132
Figure 3-25. B-scans of slabs reconstructed using <i>Arrangement-1</i> data with T ₃ to T ₄ as transmitters and T ₅ to T ₆ as receivers.....	133

Figure 3-26. B-scans of slabs reconstructed using <i>Arrangement-2</i> data.....	134
Figure 3-27. B-scans of slabs reconstructed using <i>Arrangement-3</i> data.....	135
Figure 3-28. Measurement grid, crack location, and the array position on the fascia beam (S.N. 424)	137
Figure 3-29. B-scans of the PSC I-beam of the S.N. 424 bridge reconstructed using transducer <i>Arrangement-1</i> data at lines $x = 4, 8,$ and 16	139
Figure 3-30. B-scans of the PSC I-beam of S.N. 424 reconstructed using transducer <i>Arrangement-1</i> data at lines $x = 12$ and 20	140
Figure 3-31. Measurement grid and array position on the fascia beam (S.N. 2618).....	141
Figure 3-32. B-scans of the PSC I-beam of the S.N. 2618 bridge reconstructed using transducer <i>Arrangement-1</i> data at lines $x = 0, 14$ and 16	143
Figure 3-33. B-scans of the PSC I-beam of the S.N. 2618 bridge reconstructed using transducer <i>Arrangement-1</i> data at $x = 2, 4,$ and 6	144
Figure 3-34. B-scans of the PSC I-beam of the S.N. 2618 bridge reconstructed using transducer <i>Arrangement-1</i> data at $x = 8, 10,$ and 12	145
Figure 4-1. PSC box-beam defect types and condition states	154
Figure 4-2. PSC I-beam defect types and condition states.....	155
Figure 4-3. Different crack types observed in PSC beams.....	155
Figure 4-4. A template for documenting crack types under defect 1110.....	156
Figure 4-5. An implementation of the updated MI safety inspection report format.....	158
Figure 5-1. Observation of Arcosa sand exposed to 1N NaOH at 176° F for 63 days (a) under daylight, (b) prescreening, and (c) under UV light immediately after uranyl acetate treatment.	161
Figure 5-2. Observation of Arcosa sand exposed to 1N NaOH at 73° F for 63 days	162
Figure 5-3. Observation of Arcosa sand exposed to 3% NaCl at 176° F for 56 days.....	162
Figure 5-4. Observation of mortar bars with Arcosa sand exposed to 1N NaOH at 176° F (a) under daylight - cracks in an aggregate are highlighted in red and a void in the surface is circled, (b) prescreening (c) immediately after uranyl acetate treatment – red arrows show reaction rims and white arrows show the fluorescence in the cracks, (d) 15-minute observation, (e) 30-minute observation, and (f) 60-minute observation after the uranyl acetate treatment.	163
Figure 5-5. Yellowish-green fluorescence observed on mortar bars exposed to 3% NaCl and elevated temperatures for 238 days.....	164

Figure 5-6. Observation of 3 × 3 × 11.25 in. concrete prisms with Arcosa sand and Spratt coarse aggregate exposed to 1N NaOH at 176° F (a) under daylight, (b) prescreening, (c) immediately after uranyl acetate treatment – red arrows show the fluorescence in reaction rims and white arrows show the fluorescence in aggregate cracks, (d) 15-minute observation, (e) 30-minute observation, and (f) 60-minute observation after uranyl acetate treatment.....	165
Figure 5-7. Observation of coarse aggregate (Spratt) stored under various exposure conditions and treated with ASR Detect®	167
Figure 5-8. Observation of fine aggregate (Arcosa Sand) stored under various exposure conditions and treated with uranyl acetate and ASR Detect®	168
Figure 5-9. Observation of mortar bars prepared with chert aggregate, stored under various exposure conditions, and treated with uranyl acetate and ASR Detect®.....	169
Figure 6-1. Measurements to define bottom flange edge spalls	173
Figure 6-2. Guidelines for excluding ineffective strands in the presence of longitudinal, map, and random cracks in box-beams (Case #3 is not shown)	177
Figure 6-3. Guidelines for determining the deteriorated concrete area and prestressing strands in box-beams.....	182
Figure 6-4. Estimating the loss of strands in a distressed PSC I-beam of S.N. 424 bridge	184
Figure 6-5. Estimating the loss of strands in a distressed PSC I-beam of S.N. 2618 bridge	185
Figure 6-6. AASHTOWare BrR dialog box for defining material properties.....	186
Figure 6-7. AASHTOWare BrR dialog box for defining section properties	187
Figure 6-8. AASHTOWare BrR dialog box for defining strands in rows	187
Figure 6-9. AASHTOWare BrR dialog box for defining prestressing force and the center of gravity.....	188
Figure 7-1. Expansion of mortar bars with 0.35 w/c in 1N NaOH at 176° F (MB-0.35/0.51-1N NaOH-176)	191
Figure 7-2. Expansion of mortar bars with 0.35 w/c under different exposure conditions.....	192
Figure 7-3. Expansion of mortar bars with 0.47 and 0.35 w/c under different exposure conditions	193
Figure 7-4. Instrumented slab for the evaluation of concrete expansion	194
Figure 7-5. Expansion of concrete prisms with 0.35 w/c exposed to 1N NaOH at 176° F (P1-CP-0.96-1N NaOH-176)	196

Figure 7-6. Cracking observed on a concrete prism with 0.35 w/c after exposing it to 1N NaOH at 176° F (P1-CP-0.96-1N NaOH-176).....	197
Figure 7-7. Expansion of concrete slabs with 0.35 w/c exposed to 1N and 0.1N NaOH solutions	198
Figure 7-8. Temperature and strain variation against the exposure duration.....	199
Figure 7-9. Instrumentation for concrete protective system performance evaluation	200
Figure 7-10. Insulated treated slab before exposure to 120° F at 25% RH.....	204
Figure 7-11. Expansion of concrete prisms with Na ₂ O _{eq} of 0.96% in 1N NaOH at 176° F.....	205
Figure 7-12. Expansion of concrete slabs with Na ₂ O _{eq} of 0.96% in 1N NaOH at 176° F (P2-CS-0.96-1N NaOH-176-07)	205
Figure 7-13. Expansion of slabs with 0.35 w/c exposed to 1N NaOH at 176° F	206
Figure 7-14. Top surface of a slab before and after sandblasting.....	206
Figure 7-15. Variation of slab temperature and IRH against the exposure duration.....	207
Figure 7-16. Variation of IRH in the sealant applied slabs against drying time	207
Figure 7-17. Variation of IRH in the coated slabs against drying time	208
Figure 7-18. Variation of IRH in the slabs with multi-coating systems against drying time.....	209
Figure 7-19. Cracking in Si-Rex 03 coating.....	209

Intentionally left blank

1 INTRODUCTION

1.1 OVERVIEW

The Michigan Department of Transportation (MDOT) conducts routine National Bridge Inventory (NBI) and Michigan Bridge Element (MBE) inspections. MDOT suspected that the mild to significant concrete deterioration observed on many prestressed concrete (PSC) beam bridges constructed in the 1970's and 1980's was due to alkali-aggregate reactivity (AAR) and other material compatibility issues. Map and longitudinal cracking are reported on PSC beams due to chemical reactions and/or physical mechanisms that result in volume expansion of concrete components. Concrete volume expansion and cracking are reported in beams with delayed ettringite formation (DEF) and AAR when subjected to moisture. In Michigan, the deterioration is further aggravated due to freeze-thaw exposure. Thus, the location of beams, the location of cracks, and exposure to environmental elements control the initiation and rate of deterioration. To clarify, Figure 1-1 shows the longitudinal and map cracking documented on PSC I-beams. Figure 1-2 shows PSC box-beam end cracking, typical bottom flange longitudinal cracking, map cracking on the exterior web, and random cracking on a highly deteriorated bottom flange. The cracking shown in Figure 1-1 and Figure 1-2c and d are considered 'atypical' when compared with the other deteriorations documented during routine and scoping inspections.

According to the Michigan Bridge Element Inspection Manual (MiBEIM 2017), condition states are assigned based on the amount of deterioration. Element numbers 109 and 823 are assigned to the PSC beams commonly used in Michigan bridges. Element number 826 represents beam end deterioration. Condition State (CS) Tables 2 and 9 present defect descriptions, defect severity, and guidelines for defining the condition states. Since there are no smart flags to identify beams with 'atypical' deteriorations from other types, it is currently unknown how widespread this problem is, and if it extends to PSC beam bridges constructed in the 1990's and beyond.



(a) Bottom flange longitudinal cracking



(b) Bottom flange map and longitudinal cracking

Figure 1-1. Longitudinal and map cracking in PSC I-beams



(a) End cracking



(b) Bottom flange longitudinal cracking



(c) Map cracking on exterior girder web



(d) Bottom flange random cracking

Figure 1-2. PSC box-beam cracking

1.2 OBJECTIVES AND TASKS

The objectives are to determine the status of MDOT bridge inventory with regards to atypical concrete deterioration of PSC beams, develop inspection guidelines, evaluate ASR screening test methods for field application, produce capacity calculations and load rating guidelines for PSC beams with varying stages of concrete deterioration, and offer rehabilitation options.

The following tasks were completed to accomplish the above stated objectives:

1. Assess the extent of AAR and other similar deterioration mechanisms of in-service MDOT PSC bridge beams.
2. Provide guidelines for Bridge Inspectors for both NBI component ratings and AASHTO National Bridge Element ratings in alignment with the Michigan Structure Inspection Manual and Michigan Bridge Element Inspection Manual.
3. Assess/develop/recommend the best methods for ASR detection, with an emphasis on field testing.
4. Evaluate the effect of concrete deterioration on beam capacity to develop load rating guidelines in alignment with the Michigan Bridge Analysis Guide.
5. Study and determine the best rehabilitation options and make recommendations based on severity and type of deterioration.
6. Produce a final report and other deliverables.

1.3 REPORT ORGANIZATION

This report is organized into 9 chapters.

Chapter 1 includes the introduction and research project objectives and tasks.

Chapter 2 documents the state-of-the-art and practice review on concrete deterioration mechanisms, PSC beam inspection procedures and limitations, staining techniques for detecting ASR, load rating procedures, ASR affected concrete and corroded steel properties, procedures to determine effective prestressing strands in a section, surface crack depth evaluation methods, live load distribution with distressed beams, and concrete protective systems.

Chapter 3 describes the process implemented to identify bridges with longitudinal and map cracking on fascia beams, causal evaluation of fascia beam deterioration and results, and the geographical distribution of PSC I-beam bridges with fascia beam deterioration.

Chapter 4 presents guidelines for inspecting and documenting concrete deterioration in PSC beams.

Chapter 5 describes the evaluation of staining techniques for detecting ASR affected concrete.

Chapter 6 describes flexural capacity assessment and load rating guidelines for PSC beams with deteriorated concrete.

Chapter 7 describes the evaluation of silane penetrating sealants, concrete surface coatings, and multi-layer protective systems.

Chapter 8 includes a summary, conclusions, and recommendations.

Chapter 9 presents the cited references.

2 STATE-OF-THE-ART AND PRACTICE LITERATURE REVIEW

2.1 OVERVIEW

The concrete deterioration in prestressed beams leads to cracking, steel corrosion, delamination, and spalling. Moisture intrusion through the damaged area further deteriorates concrete due to mechanisms such as freeze-thaw. As a result, the load bearing capacity of beams is reduced. The reduction in the capacity depends on the concrete deterioration mechanism and the extent of deterioration. Depending on the concrete deterioration mechanism and the existing capacity, bridge management decisions are taken to either replace or implement a mix of fixes to assure safety and extend the service-life of the structure. This chapter describes prestressed concrete deterioration mechanisms, inspection procedures and limitations to document vital information for causal evaluation of concrete deterioration and beam distress, staining techniques for detecting ASR in concrete, load rating procedures, impact of ASR on concrete properties, corroded prestressing strand properties, quantification of concrete damages, surface crack depth evaluation methods, live load distribution with distressed beams, and concrete protective methods.

2.2 PSC BOX- AND I-BEAM DISTRESSES

Other than the damages due to high-load-hits, bottom flange longitudinal cracking, concrete spalling, staining, concrete delamination, map cracks (with or without staining), exposed or/and broken prestressing strands, corroded prestressing strands, and exposed stirrups are commonly documented as beam distresses. Figure 2-1a through Figure 2-1e show a few typical box-beam distresses (Frosch et al. 2020a; 2020b). Figure 2-1f shows longitudinal cracking observed in I-beams.

In adjacent box-beam bridges, deteriorations are frequently observed along the beam bottom flange edges. The primary reason for box-beam deterioration is the chloride-laden moisture that seeps through reflective deck cracking and the interface between the beams and shear keys (Attanayake and Aktan 2015, Aktan et al. 2005). The threshold levels of chloride initiate prestressing strand and reinforcement corrosion. The continuation of corrosion leads to cracking, delamination, spalls, and broken strands. In several adjacent box-beam bridges, longitudinal cracking along the beam soffit is documented. These cracks were commonly observed in beams with open stirrups. In certain instances, prestressing strands at or near these cracks were in good condition (Attanayake and Aktan 2011). Even though several reasons are listed in the literature as

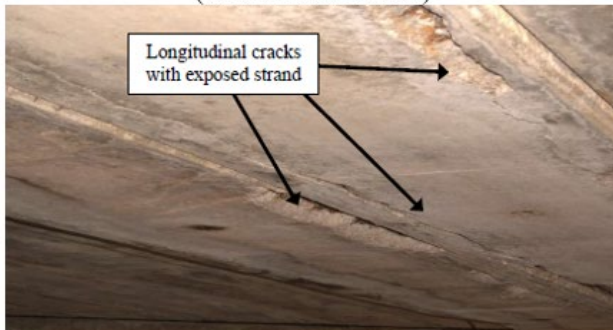
the causes of such cracking (Frosch et al. 2020b), investigations thus far failed to identify reasonably accepted evidence to support such speculations. All the distresses presented in Figure 2-1a through Figure 2-1d are typical for box-beams, except the random cracks or the so called ‘spider web cracks’ presented in Figure 2-1e. Longitudinal cracking parallel to prestressing strands in PSC I-beams, as shown in Figure 2-1f, could impact the integrity of prestressing strands depending on the crack depth and strand layout. Moreover, structures with distressed beams need to be load rated since the distresses compromise concrete section properties, prestressing steel area, and concrete mechanical properties.



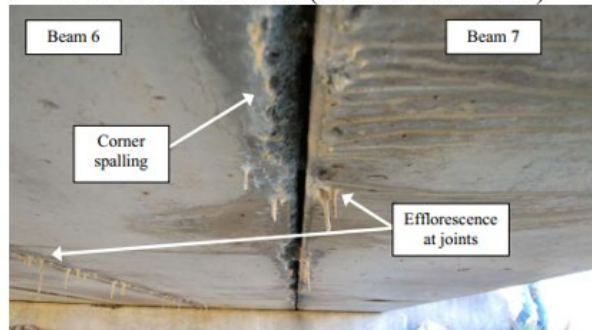
(a) Longitudinal cracks in box-beam bottom flange (Frosch et al. 2020a)



(b) Spalling, corrosion, and broken prestressing strands in box-beams (Frosch et al. 2020a)



(c) Longitudinal box-beam cracking with exposed strands (Frosch et al. 2020b)



(d) Spalling and efflorescence along box-beam edges (Frosch et al. 2020b)



(e) Spider web cracks in box-beam bottom flange (Frosch et al. 2020b)



(f) Longitudinal cracks in I-beam bottom flange (Williams and Choudhuri 2010)

Figure 2-1. PSC box- and I-beam distresses

2.3 DETERIORATION OF PRESTRESSED/REINFORCED CONCRETE COMPONENTS

Prestressed/reinforced concrete components are subjected to conditions that impact durability and load capacity (Aktan et al. 2002). Figure 2-2 shows the common causes that lead to the degradation of prestressed/reinforced components (Raupach and Buttner 2014). Concrete degrades due to excessive loads, settlements, and physical and chemical attacks. Physical attacks are a result of freeze-thaw action and volume change loads coupled with internal and external constraints (Aktan et al. 2003). The chemical attacks include alkali-aggregate reaction (AAR), delayed ettringite formation (DEF), and the intrusion of deleterious chemical agents. Carbonation, chloride content, and lowered resistivity are the common causes of steel corrosion. The primary objective of this work is to diagnose, prognose, and mitigate concrete deterioration due to chemical reactions, mainly AAR and DEF. Therefore, deteriorations due to other mechanisms are not discussed in this report.

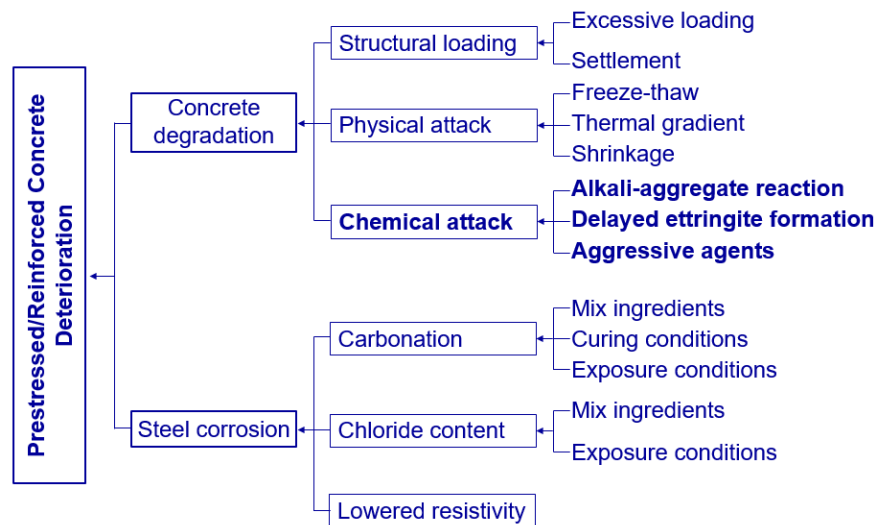


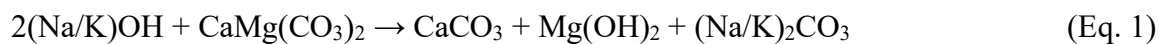
Figure 2-2. Typical causes of prestressed/reinforced concrete deterioration

2.3.1 Alkali-Aggregate Reaction (AAR)

A chemical reaction between certain minerals in aggregates and alkalis in the cement matrix is called AAR (Blight and Alexander 2010). Based on the type of reactive constituent in the aggregates, AAR is divided into three categories – (i) alkali-carbonate reaction (ACR), (ii) alkali-silicate reaction, and (iii) alkali-silica reaction (ASR) (Blight and Alexander 2010). Blight and Alexander (2010) documented the mechanisms of such deterioration types. Among these three categories, ASR is the most prominent deterioration mechanism.

2.3.1.1 Alkali-Carbonate Reaction (ACR)

The ACR is a reaction between small dolomite crystals in a clay matrix ($\text{CaMg}(\text{CO}_3)_2$) and the alkali hydroxide ($(\text{Na/K})\text{OH}$) present in the cement matrix. The chemical reaction produces calcite (CaCO_3), brucite ($\text{Mg}(\text{OH})_2$), and alkali carbonate ($(\text{Na/K})_2\text{CO}_3$). This process is known as dedolomitization due to the breakdown of the dolomite, as shown in Eq. 1. The extent of cracking due to dedolomitization depends on the micro-texture and the nature of the minerals. The exposed clay due to cracking swells in the presence of moisture leading to further degradation of the concrete matrix.



2.3.1.2 Alkali-Silicate Reaction

The reaction between alkali hydroxide and a combined form of phyllosilicates is known as alkali-silicate reaction. The product of this chemical reaction is not expansive in nature (Blight and Alexander 2010). This reaction is defined as ASR when the reaction products swell. According to the literature, it is still controversial as to whether or not this reaction can be separated from ASR.

2.3.1.3 Alkali-Silica Reaction (ASR)

The reaction between siliceous aggregates or minerals and alkali hydroxide produces an alkali-silica gel ($\text{Na}_2\text{SiO}_3 \cdot 2\text{H}_2\text{O}$) (Thomas et al. 2013a). This gel is hygroscopic and has a tendency to imbibe water and expand (Thomas et al. 2013a). Concrete may eventually crack when the tension generated from this expansive action exceeds the tensile strength capacity of the concrete. However, the timeline for ASR depends on the aggregate type, mineralogy, and exposure conditions (Sarkar et al. 2004).

The mineralogy of siliceous aggregates are mainly three types: Quartz, Chalcedony, and Opal. The atomic structures of these aggregates are crystalline, crypto-crystalline, and amorphous (or glassy), respectively (Sarkar et al 2004). Based on the aggregate mineralogy and the form of silica, aggregates are listed into three categories: non-reactive, reactive, and highly reactive. Table 2-1 shows a summary of different types of SiO_2 arrangements and which aggregate types belong to which category. As an example, the siliceous aggregate with quartz mineralogy and crystalline atomic structure is non-reactive.

Table 2-1. Mineralogy, Atomic Structure, and Reactivity Level of SiO₂ Arrangements

Mineralogy	Atomic structure	Reactivity level
Quartz	Crystalline	Non-reactive
Chalcedony	Crypto-crystalline	Reactive
Opal	Amorphous or glassy(non-crystalline)	Highly reactive

Two ASR gel components are produced based on the amount of calcium oxide (CaO) present in the pore-water solution. They are (i) non-expansive calcium-alkali-silicate-hydrate (C-(N/K)-S-H) that is known as CSH gel with alkali impurities and (ii) expansive alkali-silicate-hydrate ((N/K)-S-H). Figure 2-3 shows the ASR mechanism. During the *first stage*, the reactive silica undergoes depolymerization, dissolution, and swelling when the pore solution consists of water (H₂O), alkalis (Na⁺, K⁺), hydroxyl ions (OH⁻), and H₃SiO₄⁻ ions (the dissolution of silica provides the latter form). This volume change is not significant compared with the subsequent reactions, but it can damage the concrete. Also, the byproduct of cement hydration reaction, (Ca(OH)₂), dissolves during this stage, and the concentration of calcium ions depends on the alkali concentration since the dissolution of Ca(OH)₂ is inversely proportional to the alkali concentration. During the *second stage*, a non-expansive C-(N/K)-S-H gel is formed as the alkali and calcium ions diffuse into the swollen aggregates and react. The concentration of calcium (produced from dissolution) in the non-expansive gel depends on the alkali concentration. During the *third stage*, the pore solution diffuses into the silica through the porous layers of C-(N/K)-S-H gel. The production of expansive or non-expansive gel depends on the relative concentration of alkali and rate of diffusion. As shown in Figure 2-3, non-expansive gels will form only if the CaO amount is greater than or equal to 53% of anhydrous C-(N/K)-S-H gel by weight. Since an increase in alkali concentration hinders the solubility of Ca(OH)₂, the expansive (N/K)-S-H gel forms with little or no calcium. This low viscous expansive gel could easily diffuse away from the aggregate; it also expands in the presence of moisture and induces tensile stresses leading to cracking. These cracks are filled with ASR products that spread over a wide area under pressure.

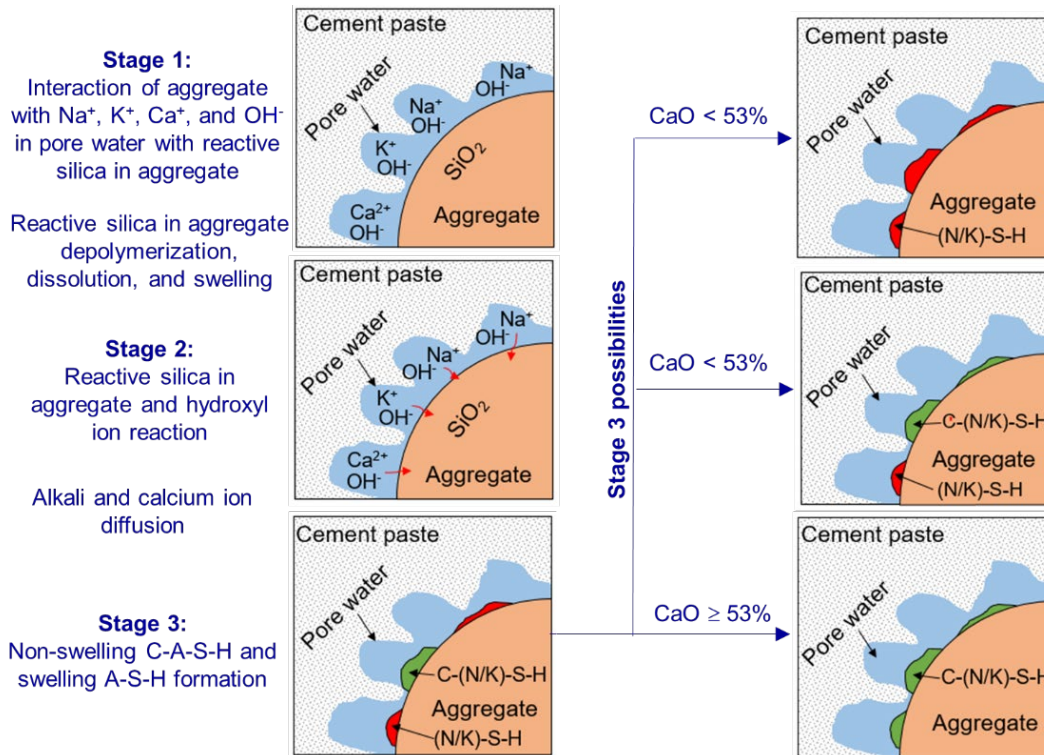


Figure 2-3. Stages of ASR and formation of swelling and non-swelling products

2.3.2 Delayed Ettringite Formation (DEF)

Tricalcium aluminate reacts with gypsum in the presence of water and produces ettringite (Kosmatka and Wilson 2011). This process is known as the primary ettringite formation at an early age. The primary ettringite converts to either monosulfate hydrate or a part of a solid solution series between monosulfate and hemisulfate for the molar ratio of sulfate to tricalcium aluminate from 0.7 to 1.2 (Kuzel 1996). The monosulfate hydrate possesses a complete crystalline structure (Hall et al. 1996). However, the primary ettringite could decompose at an early age due to a high curing temperature rather than converting to monosulfate hydrate. According to Hall et al. (1996), the primary ettringite decomposes at $237.2 \pm 32.9^\circ \text{F}$ and forms calcium aluminate monosulfate and bassanite. Diamond (1996) stated a much lower temperature of 126°F to observe decomposed primary ettringite. However, recent studies suggest that the ettringite can decompose at a temperature higher than 158°F (Tosun 2006). The calcium aluminate monosulfate and sulfate reacts in the presence of water and forms ettringite in the void space of hardened concrete (Kuzel 1996). This process is known as the delayed ettringite formation (DEF), as shown in Figure 2-4. The process creates a volumetric expansion leading to cracking and delamination in concrete (Mak et al. 2012).

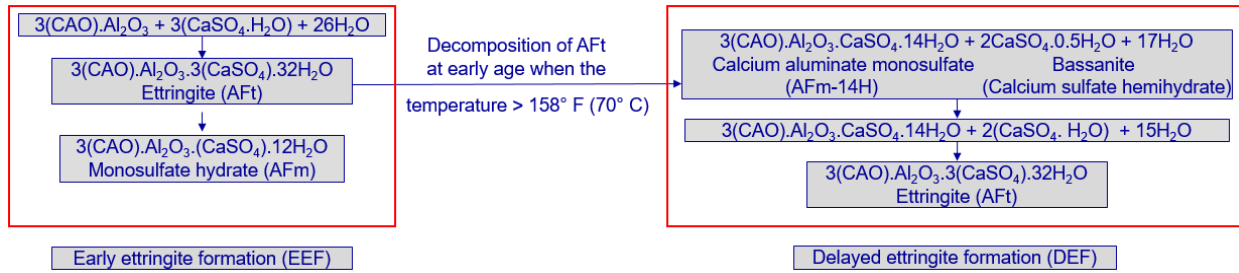


Figure 2-4. Early ettringite formation (EEF) and delayed ettringite formation (DEF)

The primary ettringite decomposes due to many reasons that are classified as primary, secondary, and tertiary factors (Mak et al. 2012). As shown in Figure 2-5, the primary factors are from the concrete mix. The fabrication process and service environment contribute to the secondary and tertiary factors. The elevated temperature used for accelerated curing plays a vital role in the delayed ettringite formation. Moisture is one of the tertiary factors that contributes to DEF and concrete degradation.

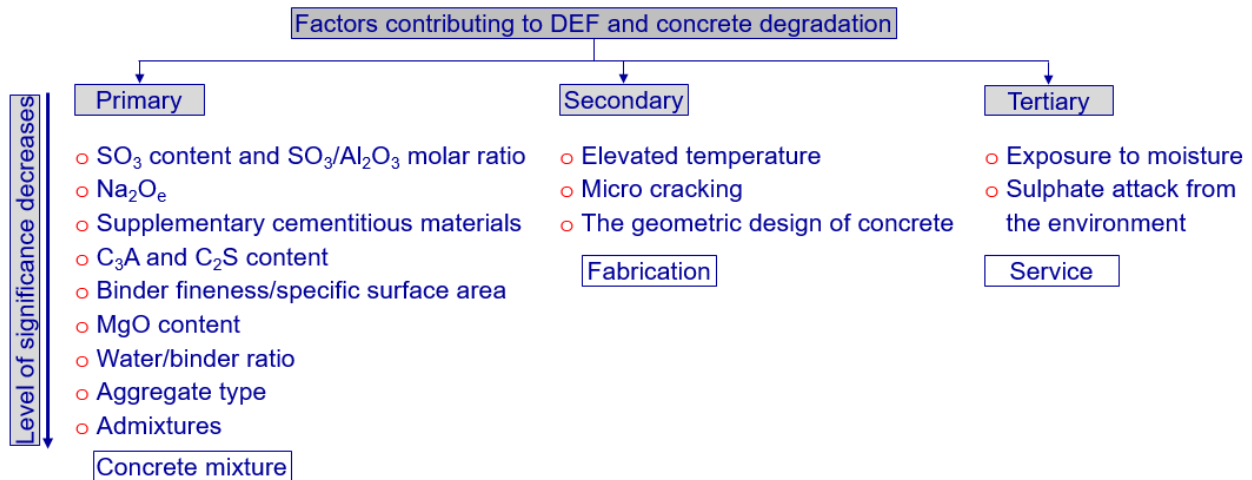


Figure 2-5. Factors contributing to DEF and concrete degradation

2.3.3 Cracking Due to ASR

The following are the two hypotheses related to the mechanism of concrete expansion due to ASR (Wigum et al. 2006):

- a) Expansion of concrete is caused by the gel.
- b) Solid expansion of aggregate causes the primary expansion of concrete while the gel intrusion into closed cracks causes the secondary expansion.

Gel composition is a major factor governing the rate of expansion and concrete cracking because the gel viscosity and porosity that control concrete expansion depend on the gel

composition. Concrete cracks when the tensile stress induced by this expansion exceeds the tensile strength of concrete. This explanation supports the first hypothesis. According to the second hypothesis, the ASR gel develops inside aggregate and expands by absorbing moisture through osmosis action to cause an expansion of aggregate. No cracking is observed in the cement matrix since the expansion is within the aggregate. The cement matrix eventually cracks when the tensile stress induced by the expansion of several neighboring aggregates exceeds the tensile strength. According to the second hypothesis, the expansion due to ASR develops map cracks with reactive aggregates as nodes. In the presence of prestressing strands, cracks develop parallel to the strands since the tensile stresses are developed perpendicular to the direction of confinement (Thomas et al. 2011).

The stresses developing in real structures are complicated as a result of the drying shrinkage. As shown in Figure 2-6, drying shrinkage generates tension at the exterior surface and compression in the interior (Helmuth 1993). The expansion due to ASR is negligible during this period. As a result, fine cracks are developed at the exterior surface. During the *second stage*, microcracks develop at the interior due to ASR expansion and a growth of surface cracking is observed. During the *third stage*, the rate of ASR reaction closer to the exterior surface decreases due to drying, but the surface cracks grow wider due to the continuation of ASR expansion at the interior (Helmuth 1993). However, a timeline for the initiation and growth of cracks is not given.

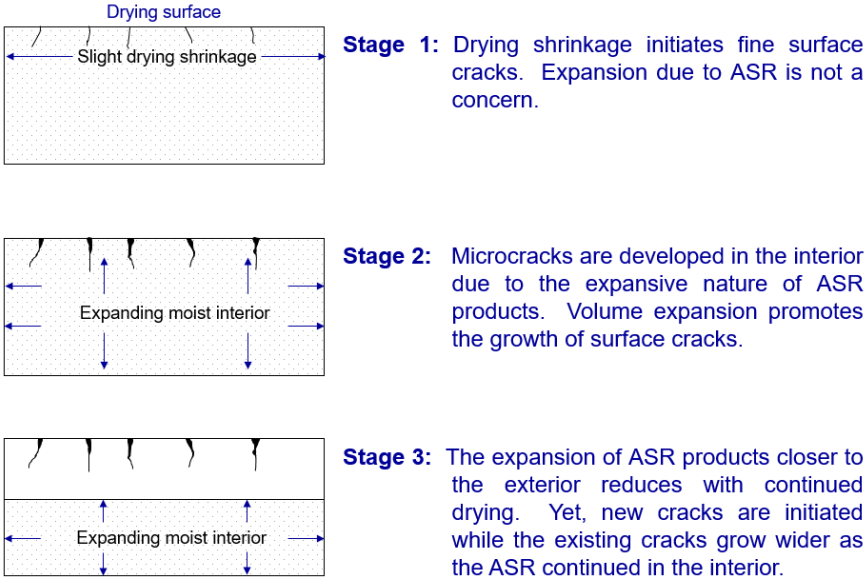


Figure 2-6. The role of drying shrinkage and ASR in developing surface cracking in concrete members (Helmuth 1993)

Figure 2-7 presents a timeline for the appearance of material related distress (Van Dam et al. 2002). Accordingly, ASR and ACR cracks could appear after 5 years from construction, whereas the cracking due to internal sulfate attack (i.e. DEF) could appear as early as one year from construction.

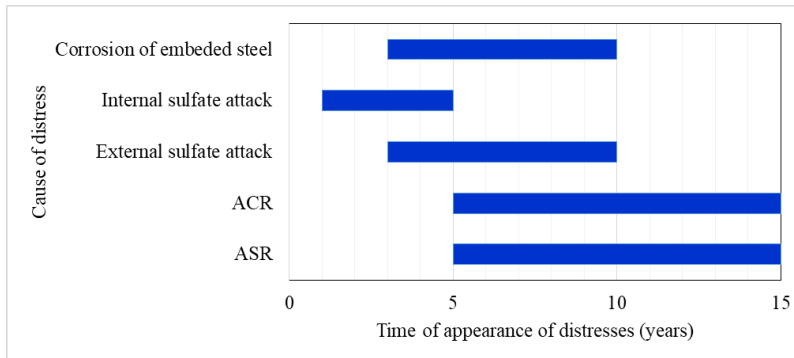


Figure 2-7. The time of appearance of material related distress in concrete (Van Dam et al. 2002)

2.4 PSC BOX- AND I-BEAM INSPECTION

The U.S. Federal-Aid Highway Act of 1968 was enacted following the historic collapse of the Silver Bridge over the Ohio river in 1967. The bridge was located between West Virginia and Ohio in the U.S., and the collapse resulted in over 40 casualties. The Act required the U.S. Secretary of Transportation to establish National Bridge Inspection Standards (NBIS) to ensure the safety of the travelling public (FR 2004). The NBIS establishes minimum qualifications of inspectors, identifies the types of bridges to be inspected, defines inspection frequency, and classifies the information to be collected and reported. Finally, load rating is included as part of the NBIS to ensure safety (Hartle et al. 2002). Revisions were needed to address perceived ambiguities in the NBIS by clarifying the NBIS language, reorganizing the NBIS into a more logical sequence, and making the regulation easier to read and understand (FR 2004). Inspection procedures, rating systems, and documentation formats have evolved throughout the years to enhance bridge management decisions. The current practice is to use component-level inspection, element-level inspection, or a hybrid version of those two methods.

The AASHTO Manual for Bridge Element Inspection (MBEI) is the national standard (AASHTO MBEI 2019) for bridge element inspection. The Michigan Bridge Element Inspection Manual (MiBEIM) is the agency standard that provides condition state information for bridge owners and inspectors for the element level inspections performed within the State of Michigan (MiBEIM 2017). Element level inspection procedures were developed with a much broader

vision. As an example, documentation of crack widths, spacing, intensity, etc., can be accomplished in the future with the availability of Unmanned Aerial Vehicles (UAV) and Artificial Intelligence (AI) enabled inspection systems. On the other hand, MDOT needs to have practically implementable procedures with the available technology and human resources, since it is not practical for inspectors to document distress types and extent at the level described in the AASHTO MBEI during biennial inspections. Since documenting specifics on distress types and their extents of deterioration is not mandatory, agencies follow their own policies and procedures when assigning a condition state to an element.

The following section describes the national and agency specific inspection guidelines and their limitations for evaluating the condition of PSC box- and I-beams with specific distress types.

2.4.1 National and Agency Specific Guidelines

2.4.1.1 Evolution of Bridge Element Inspection

Bridge deck, superstructure, and substructure are the three primary components rated during routine safety inspections as reported to the Federal Highway Administration (FHWA) for analysis of bridge condition on a national scale. These components are also recorded in the National Bridge Inventory (NBI). A rating scale of 9 (excellent and/ or new condition) to 0 (failed condition and/ or out-of-service) is used. In the past, the rating has been assigned without identifying the deterioration process or the extent of deterioration. As a rating was assigned based on multiple distress symptoms observed on a component or a localized problem at the time of inspection, a significant variability has been observed between the ratings assigned by bridge inspectors (Washer et al. 2019). Also, the NBI General Condition Rating (GCR) data has been primarily used at the Federal level to indicate large-scale functional and geometric characteristics of bridges to present an overall performance within a state or among states, rather than using such data for bridge management purposes at the state level. Since the NBI GCR data is not comprehensive enough to provide adequate information to make performance-based assessments and decisions (including the selection of cost-effective repair, rehabilitation, or replacement alternatives), highway agencies included additional components in their bridge management databases. In addition to assigning a rating, inspectors include a description of observations in their reports. As an example, the Michigan Department of Transportation (MDOT) bridge management database includes inspector comments recorded since the early 1990s. However, the information collected

as inspector comments cannot be effectively used in a Bridge Management System (BMS). Additional refinements to the data collection, documentation, and rating procedures are still needed to improve the effectiveness of bridge management decisions, to evaluate the interdependency of bridge elements on distress initiation, and to measure the rate of deterioration.

Since the granularity of NBI GRC data is inadequate for making maintenance decisions or conducting research, the Pontis Bridge Management System (BMS) was developed by the FHWA and Caltrans, during 1990-91, by incorporating a menu of 160 elements with a greater level of detail. Utilizing the experience of early adopters of the Pontis BMS, a task force created in 1993 (under the patronage of the FHWA) developed a new standard called the Commonly Recognized (CoRe) elements with a set of 108 standardized elements (Thompson and Shepard 2000). The development of the CoRe element manual and adoption of it in 1995 (as an official AASHTO manual) is significant since the manual incorporated the definitions of each element, the unit of measurement, the definition of a set of standardized condition states ranging from 3 to 5, and a list of typical feasible actions for each condition state. Since the condition states defined from CoRe element inspection were different from the NBIS rating, the FHWA developed and accepted a translator algorithm in 1997 to convert CoRe element condition data into NBIS condition rating for Federal level analysis. The CoRe element specification allows adding sub-elements and non-CoRe elements. Thompson and Shepard (2000) listed the guidelines for consideration when defining sub-elements and non-CoRe elements.

A major drawback of the CoRe element approach was the lack of granularity in certain element descriptions to fully capture all the condition defects present within a bridge. As an example, the wearing surface was incorporated in the definition of the deck element, and they were rated together. Further, the CoRe element manual had no major revisions for 15 years since its introduction in 1994, except for two minor changes. As a result, several changes were made to the CoRe element manual by the AASHTO Subcommittee on Bridge and Structures (SCOBS) to develop the AASHTO Bridge Element Inspection Guide Manual (BEIGM) in 2010. These revisions involved changes in the measurement units of decks and slabs to square area measurements, development of separate elements for wearing surfaces and protective coatings, standardization of the number of element condition states to four, incorporation of smart flags into the condition state language, and enhancement of element commentary to guide the bridge inspectors (Newton 2010). The original element language of the CoRe element manual was

modified to capture multiple distresses present within a defined condition state for an element (AASHTO BEIGM 2010, AASHTO MBEI 2019). Introduction of these changes provided the flexibility to adapt this manual by both large- and small-scale agencies.

The first edition of the Manual for Bridge Element Inspection (MBEI) was published in 2013, with an interim update in 2015 (AASHTO MBEI 2014). The second edition was published in 2019 (AASHTO MBEI 2019). The manual provides two element types identified as National Bridge Elements (NBEs) or Bridge Management Elements (BMEs). It also provides guidance for defining Agency-Developed Elements (ADEs), with or without ties to the elements defined in the manual. The latest edition of the manual includes deck, superstructure, substructure, culverts, bearings, and bridge rail as NBEs, along with joints, protective systems, and approach slabs as BMEs. In addition, material defects are listed under steel, prestressed concrete, reinforced concrete, timber, other materials, masonry, wearing surfaces, concrete reinforcing steel, steel protective coatings, and concrete protective coatings. The manual defines four Condition States (CSs) for NBEs and BMEs, describes material defects that bridge inspectors can use for deciding a specific condition state of an element or a defect, and provides pictures showing some condition states.

2.4.1.2 Recording Bridge Element Inspection

Considering the scope of this study, the content of this section is limited to PSC I-beams and box-beams in side-by-side or spread box-beam bridges. The NBEs 104 and 109 are defined in AASHTO MBEI (2019) for PSC box-beams and open web girders such as I-beams, respectively. An ADE 823 is defined by MDOT for box-beams in side-by-side and spread box-beam bridges considering their dominance in the state; the ADE 823 also considers the unique design, inspection, and maintenance challenges associated with side-by-side box-beam bridges (MiBEIM 2017).

Figure 2-8 shows a part of an MDOT safety inspection report prepared for a PSC I-girder bridge (i.e. STR 426). The CS numbers assigned for the PSC I-girders (NBE 109) are shown within the red box. CS2 is due to cracks or delamination at several beam ends near the sole plates and horizontal cracking on the web of beams 2, 3, and 4 (south) near the west abutment. CS3 is due to spalls that exposed steel reinforcement or prestressing strands (i.e. STS – spall to steel) at beam ends over the pier bearings and high-load-hits (HLH's) on several beams. The contribution of defects to CS2 and CS3 are 2% and 1% with respect to the total length of the girders.

STR 426		SAFETY INSPECTION REPORT - AASHTO ELEMENTS			S07-06111		
Facility	Latitude / Longitude	MDOT Structure ID	Structure Condition				
STERLING ROAD	44.0332 / -84.058	08108111000S070	Fair Condition(5)				
Feature	Length / Width / Spans	Owner					
I-75	384 / 32.4 / 6	Region: Bay(4)					
Location	Built / Recon. / Paint / Ovly.	TSC	Operational Status				
2.0 MI W OF STERLING	1968 / / 1968 / 2012	Bay City(2)	A Open, no restriction(A)				
Region / County	Material / Design	Last NBI Inspection	Scour Evaluation				
Bay(4) / Arenac(6)	5 Prestressed Concrete / 32 Multi Str Comp	09/24/2020 / 08LE	N Not Over Waterway				
NBI INSPECTION							08LE
Inspector Name	Agency / Company Name	Insp. Freq.	Insp. Date				
	MDOT Bay Region	24	09/24/2020				
AASHTO ELEMENTS							(English Units)
Element Number	Element Name	Total Quantity	Unit	Good CS1	Fair CS2	Poor CS3	Severe CS4
Superstructure							
109	Pre Opn Conc Girder/Beam	1920	ft	1858 97%	47 2%	15 1%	0 0%
CS2: Crks/delam at several beam ends near sole plates and horiz crk on web of Bm 2-4S near W abut. / CS3: STS on beam ends over piers at bearings and HLH's on Bms 3, 4, 5S of Span 5W and Bms 4 & 5S of Span 2W.							

Figure 2-8. A bridge safety inspection report showing the CSs of PSC I-beams

A condition state for PSC box- and I-beams is assigned based on the severity of observed defect types. For box- and I-beams (ADE 823 and NBE 109), these defects are defined based on their material type (i.e. prestressed concrete) and are given in the CS Table 2, as shown in Figure 2-9 (MiBEIM 2017). The condition state descriptions given in the CS Table 2 of MiBEIM (2017) and the AASHTO MBEI (2019) are similar. However, the fourth line of the CS Table 2, footnote 1, needs to be updated as “...*prestressed* concrete cracks less...” instead of “...reinforced concrete cracks less...”. Defining cracks as insignificant (crack width < 0.004 in.), moderate (0.004 in. < crack width < 0.009 in.), and wide (crack width > 0.009 in.) in the MiBEIM (2017) and the AASHTO MBEI (2019) is similar. Moderate and heavy pattern cracking discussed under defect 1110 are not explicitly defined in the MiBEIM (2017). The AASHTO MBEI (2019) classifies pattern (map) cracks as moderate and heavy, based on the spacing between the cracks. The crack spacing of moderate pattern cracks ranges from 1 to 3 ft. Heavy pattern cracks have a crack spacing of, at most, 1 ft. The MiBEIM (2017) provides a pictorial illustration of three condition states (CS2, CS3, and CS4) of PSC elements below the CS Table 2 (see Figure 2-9). Unlike in the AASHTO MBEI (2019), where the condition states are specifically illustrated based on the defect type, the photos in the MiBEIM (2017) are rather generalized.

CS TABLE 2 – PRESTRESSED CONCRETE

Defects	Condition State 1 GOOD	Condition State 2 FAIR	Condition State 3 POOR	Condition State 4 SEVERE
Spalls/ Delaminations/ Patch Areas (1080)	None.	Delaminated. Spall 1 in. or less deep or less than 6 in. diameter. Patched area is sound.	Spall greater than 1 in. deep or greater than 6 in. diameter. Patched area is unsound or showing distress. Does not warrant structural review.	The condition warrants a structural review to determine the effect on strength or serviceability of the element or bridge; OR a structural review has been completed and the defects impact strength or serviceability of the element or bridge.
Exposed Rebar (1090)	None.	Present without section loss.	Present with section loss that does not warrant structural review.	
Exposed Prestressing (1100)	None.	Present without section loss.	Present with section loss that does not warrant structural review.	
Cracking ⁽¹⁾ - PSC (1110)	Insignificant cracks or moderate-width cracks that have been sealed.	Unsealed moderate-width cracks or unsealed moderate pattern (map) cracking.	Wide cracks or heavy pattern (map) cracking.	
Efflorescence / Rust Staining (1120)	None.	Surface white without build-up or leaching without rust staining.	Heavy build-up with rust staining.	
Settlement - Substructure (4000)	None.	Exists within tolerable limits or arrested with effective actions taken to mitigate.	Exceeds tolerable limits but does not warrant structural review.	
Scour - Substructure (6000)	None.	Exists within tolerable limits or arrested with effective countermeasures.	Exceeds tolerable limits but is less than the limits determined by scour evaluation, and does not warrant structural review.	
Damage (7000)	Not applicable.	The element has minor damage caused by vehicular or vessel impact.	The element has moderate damage caused by vehicular or vessel impact.	The element has severe damage caused by vehicular or vessel impact.

(1) The inspector should use judgment when utilizing the condition state defect conditions, especially for concrete cracking. The crack defect description definitions describe generalized distress, but the inspector should consider width, spacing, location, orientation, and structure or nonstructural nature of the cracking. The inspector should consider exposure and environment when evaluating crack width. In general, reinforced concrete cracks less than 0.004 inches can be considered insignificant and a defect is not warranted. Cracks ranging from 0.004 to 0.009 inches can be considered moderate, and cracks greater than 0.009 inches can be considered wide.



Figure 2-9. CS Table 2 for PSC elements with supplemental information for inspectors (MiBEIM 2017)

The MiBEIM (2017) defines a few ADEs as a subset of PSC box- and I-girders. The condition state information of these ADEs is separately documented in addition to their respective NBEs. Figure 2-10 shows a part of an MDOT safety inspection report prepared for a PSC I-beam bridge (i.e. STR 426). The beam end condition states are assigned under ADE 826 in addition to NBE 109. Twenty (20) beam ends are assigned CS3. Sixteen (16) beam ends have temporary supports that are in good condition (CS1). The CS of temporary beam end supports is documented using ADE 845, in addition to NBE 109.

STR 424		SAFETY INSPECTION REPORT - AASHTO ELEMENTS			S05-06111		
Facility	Latitude / Longitude	MDOT Structure ID	Structure Condition				
LINCOLN ROAD	43.9985 / -84.0274	06106111000S050	Poor Condition(4)				
Feature	Length / Width / Spans	Owner					
I-75 SB	155.8 / 32.2 / 3	Region: Bay(4)					
Location	Built / Recon. / Paint / Ovly.	TSC	Operational Status				
2.4 MI S OF STERLING	1968 / / / 1968	Bay City(2)	A Open, no restriction(A)				
Region / County	Material / Design	Last NBI Inspection	Scour Evaluation				
Bay(4) / Arenac(8)	5 Prestressed Concrete / 02 Multi Str Non Comp	05/05/2021 / 6VHI	N Not Over Waterway				

NBI INSPECTION				6VHI			
Inspector Name	Agency / Company Name	Insp. Freq.	Insp. Date				
	MDOT Bay Region	12	05/05/2021				

AASHTO ELEMENTS								(English Units)	
Element Number	Element Name	Total Quantity	Unit	Good CS1	Fair CS2	Poor CS3	Severe CS4		
Superstructure									
109	Pre Opn Conc Girder/Beam	781	ft	675	46	60	0		
				86%	6%	8%	0%		
CS2: Cracks CS3: STS									
826	Beam End Deterioration	20	(EA)	0	0	20	0		
				0%	0%	100%	0%		
845	Beam End Temp Supp (SH)	16	(EA)	16	0	0	0		
				100%	0%	0%	0%		

Figure 2-10. A bridge safety inspection report showing the CSs of PSC I-beams and ADEs

As shown in Figure 2-11, ADE 826 is used to document the CS of beam ends based on the level of deterioration within 5 ft of bearing. The loss of section at each beam end is the only parameter included in the CS Table 9 because of its significance on girder end capacity. Beam end cracking is common and promotes girder end deterioration as documented in Aktan et al. (2002). Even though beam ends are encased by backwalls in semi-integral and integral bridges, cracking at beam ends is frequently documented in bridge safety inspection reports (Amunugama and Attanayake 2021). Amunugama and Attanayake (2021), Williams and Choudhuri (2010), Aktan et al. (2002), and Memberg et al. (2002) documented several other defects at the girder ends; these included hairline cracks, map cracks, efflorescence with/without rust stains, and exposed stirrups. The lack of information and data on girder end distresses hinders the investigation on the causes of deteriorations and prevents the development of effective maintenance strategies.

CS TABLE 9 – BEAM END (Deterioration, Contact, Temp Support)

Defects	Condition State 1	Condition State 2	Condition State 3	Condition State 4
	GOOD	FAIR	POOR	SEVERE
Beam End Deterioration (826)	Section loss to element has been repaired.	Section loss exists and has not been repaired. Structural analysis is not yet warranted.	Measurable section loss that warrants detailed inspection to determine remaining section.	The condition warrants a structural review to determine the effect on strength or serviceability of the element. A request for action (RFA) should be submitted requesting a structural evaluation and/or repairs.
Beam End Contact (844)	Beam ends have been modified to address contact.	Beam ends are in contact. No visible distress observed.	Beam ends are in contact, distress is observed.	
Beam End Temporarily Supported (845 SH, 846 FH)	Temporary support(s) in place and functioning as designed.	Minor section loss on temporary support.	Moderate section loss on temporary support.	

Figure 2-11. CS Table 9 with beam end condition state definitions (MiBEIM 2017)

It is evident from Figure 2-8 and Figure 2-10 that the MDOT practice is to list the defects contributing to the condition states below the respective element as inspector comments. Even though these inspector comments are very useful, inconsistent terminology and formats are a hindrance to the use of such information for assessing the causes of deterioration and bridge management decision-making. Even though additional resources are needed, an update to the current inspection format to record defect types that contribute to a condition state, along with the corresponding girder numbers and span numbers, would provide granular data for identifying the best combination of fixes for a specific condition.

In contrast to the MDOT practice of recording defect types that contribute to a certain condition state using inspector comments, a few other DOTs (Caltrans 2017 and NJDOT 2015) and AASHTO MBEI (2019) use designated defect numbers to indicate the contribution of specific defect(s) to a condition state. Figure 2-12 is an element inspection record format, presented in Appendix B2.2.3 of AASHTO MBEI (2019), for incorporating data on defect types that contribute to specific CS types of NBE or BME elements. Violet and blue background colors are used for NBEs and BMEs, whereas a white background is used for the defects. CS1 is assigned for the beams (NBE 109) since all the PSC I-beams are in good condition. CS3 is assigned to the reinforced concrete pier cap (NBE 234) with 18 ft (13.6%) of defects; these include 12 ft of exposed rebar (defect 1090) and 6 ft of efflorescence/rust staining (defect 1120). CS4 is assigned to the compression joint seal (BME 302) with 40 ft (30%) of defects; these include 40 ft (100%) of deteriorated or damaged adjacent deck or header (defect 2360).

Element Number	Element Description	Unit of Measure	Total Quantity	Condition State 1	Condition State 2	Condition State 3	Condition State 4
12	Reinforced Concrete Deck	ft ²	11,880	11,628	0	252	0
<i>1080</i>	<i>Delamination/Spall/Patched Area</i>	<i>ft²</i>	<i>252</i>	<i>0</i>	<i>0</i>	<i>252</i>	<i>0</i>
301	Pourable Joint Seal	ft	88	88	0	0	0
302	Compression Joint Seal	ft	132	92	0	0	40
<i>2360</i>	<i>Adjacent Deck or Header</i>	<i>ft</i>	<i>40</i>	<i>0</i>	<i>0</i>	<i>0</i>	<i>40</i>
330	Metal Bridge Railing	ft	540	540	0	0	0
515	Steel Protective Coating	ft ²	1,726	1,726	0	0	0
331	Reinforced Concrete Bridge Railing	ft	540	540	0	0	0
109	Prestressed Concrete Girder/Beam	ft	2,144	2,144	0	0	0
310	Elastomeric Bearing	each	64	64	0	0	0
215	Reinforced Concrete Abutment	ft	88	88	0	0	0
205	Reinforced Concrete Column	each	9	8	0	1	0
<i>1130</i>	<i>Cracking (RC and Other)</i>	<i>each</i>	<i>1</i>	<i>0</i>	<i>0</i>	<i>1</i>	<i>0</i>
234	Reinforced Concrete Pier Cap	ft	132	114	0	18	0
<i>1090</i>	<i>Exposed Rebar</i>	<i>ft</i>	<i>12</i>	<i>0</i>	<i>0</i>	<i>12</i>	<i>0</i>
<i>1120</i>	<i>Efflorescence/Rust Staining</i>	<i>ft</i>	<i>6</i>	<i>0</i>	<i>0</i>	<i>6</i>	<i>0</i>

Notes:

* See Figure B2-1 for defect locations
Violet background: National Bridge Element
Blue background: Bridge Management Element
Italic type: Defect

Figure 2-12. Element inspection record format showing the contribution of specific defect(s) to a condition state: PSC I-beam bridge inspection summary (AASHTO MBEI 2019)

As shown in Figure 2-9, CS Table 2 for PSC members documents all the crack types and their significance using only a single defect type provided by AASHTO (i.e. Cracking - PSC # 1110). With this approach, the presence of a specific crack type cannot be verified unless the inspector's comments provide additional information. The inspection practices followed by MiBEIM (2017) and AASHTO MBEI (2019) emphasize crack width and spacing over the cause or type of cracking. As an example, map cracks indicate material related distress or mix design and curing related issues depending on when they are documented during the life of a PSC beam. Also, diagonal cracks extending from the girder supports to girder top signify overloading or a lack of shear capacity. Whereas, the diagonal cracks extending from the girder top end to girder

bottom in beams with harped strands are due to the stresses developed in the beam due to the specific strand pattern. Also, as shown in Figure 2-11, ADE 826 documents girder end deterioration by providing CS numbers based on the significance of concrete spalling. Therefore, the inspection templates need to be updated to document the type, location, orientation, and structural or nonstructural nature of the cracks during field inspection.

Another limitation in the current practice is that the defect percentage of beams is calculated with respect to the total girder length. Because of this limitation, the conditions that are unique to certain beams in a bridge might not get the required attention. As an example, a significant level of longitudinal cracking on fascia beams, as shown in Figure 2-1f, was documented by Williams and Choudhuri (2010). Such cracking is sometimes limited to a few spans and one side of the bridge. Hence, the percentage of cracking calculated with respect to the total length of girders on the bridge could make such deteriorations unnoticeable. The MDOT practice is to highlight the presence of such cracking using inspector comments. This limitation can be eliminated by defining an ADE for fascia beams and calculating the percentage of crack length based on the total length of fascia beams.

2.5 STAINING TECHNIQUES FOR DETECTING ASR

So far, three staining techniques have been developed and evaluated to identify the presence of ASR in concrete. These stains include cuprammonium sulfate (Poole et al. 1988), uranyl acetate (Natesaiyer and Hover 1988, 1989), and sodium cobaltinitrite/rhodamine-B (Guthrie and Carey 1997, 1998, and 1999). However, only uranyl acetate and the combination of sodium cobaltinitrite/rhodamine B have shown the ability to highlight ASR gel in distinct colors (Van Dam et al. 2002). This section describes the fundamentals, application procedures, capabilities, and limitations of these two techniques.

2.5.1 Detection of ASR in Concrete

2.5.1.1 Ion Exchange Properties of Silica Gel

In the network of tetrahedron SiO_4 in silica gels shown in Figure 2-13, oxygen atoms are partially required to build the Si-O-Si bridges while the rest are free to bind with the ions in the solution where the gel is precipitated (Ahrlund et al. 1960a). An oxygen atom bound to two Si^{4+} has a high electron affinity, but the electron density around the oxygen atom is lower than an oxygen atom

bound to a metal atom. The electron pairs on the oxygen atoms connected to silicon atom are comparatively sluggish resulting in a moderately low basicity. Therefore, hydrogen ions bound to a Si-O group can be replaced rather easily by cations, and this cation swap can be possible even at comparatively low pH while an anion swap is not at all possible.

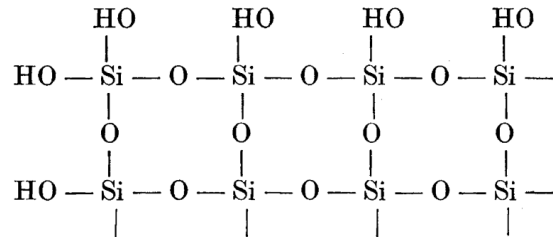


Figure 2-13. Structure of silica gel (Ahrland et al. 1960a)

The ion exchange properties of silica gel were evaluated considering adsorption by placing an accurately weighed amount of silica in a known amount of metal solution, which was deposited in a glass-stoppered flask previously filled with CO₂ free air. The system was shaken for a time that was greater than the time for equilibrium. The change in the solution concentration is determined by titration. Special attention was required to eliminate CO₂ interaction in every titration (Ahrland et al. 1960 a and b, Bartell and Fu 1929, Strazhesko et al. 1974, and Kolthoff and Stenger 1933 a and b). In 1925, Patrick and Barclay demonstrated that the adsorbed Na⁺ ions in silica gel could be replaced by Ag⁺, Cu²⁺, and Fe³⁺ by treating the gel with diluted solutions of corresponding metal salts. Bartell and Fu (1929) demonstrated that the inorganic bases were preferentially adsorbed by silica gels in the order of LiOH > NaOH > KOH > NH₄OH. Later, Kolthoff and Stenger (1933 a) proved that the adsorption of NaOH and KOH was identical. Also, Kolthoff and Stenger (1931 and 1933 b) showed that the Ca²⁺ and Cu²⁺ were strongly adsorbed by silica gel. Their study further showed that the adsorption of copper by silica gel from its ammonical solutions (Cu(NH₃)₄(OH)₂ and Cu(NH₃)₄SO₄) immediately resulted in an intense dark blue color gel (i.e. silica gel adsorbing ammonio copper ion, Cu(NH₃)₄²⁺). Ahrland et al. (1960a) investigated the adsorption of alkali, transitional, and rare earth actinide metals and presented their adsorption levels in the order of Zr⁴⁺ > U⁴⁺ ≈ Pu⁴⁺ > UO₂²⁺ > Gd³⁺ > Ca²⁺ ≈ Ba²⁺ ≈ Na⁺. The adsorption of the metal ions depends on the pH of the solution. Using the cation adsorption phenomenon presented by Patrick and Barclay (1925), Poole et al. (1988) and Natesaiyer and Hover (1988) developed two staining techniques to identify ASR in concrete. Poole et al. (1988) used a cuprammonium sulfate solution while Natesaiyer and Hover (1988) used a uranyl acetate

solution. However, further development of using a cuprammonium sulfate solution to identify ASR is not documented in literature. The most recent literature presents the application of a uranyl acetate solution and a combination of sodium cobaltinitrite ($\text{Na}_3\text{Co}(\text{NO}_2)_6$) and rhodamine B ($\text{C}_{28}\text{H}_{31}\text{N}_2\text{O}_3\text{Cl}$) to identify ASR in concrete (Van Dam et al. 2002). Therefore, only those two methods are further discussed in this section.

2.5.2 Uranyl Acetate Test

The principal of this test is to treat a specimen using uranyl acetate to replace the cations in ASR gel with UO_2^{++} ions to produce the characteristic yellowish-green color under a short-wave ultraviolet (UV) light with a wavelength between 180 nm and 280 nm (1800 Å and 2800 Å) (Natesaiyer and Hover 1988). The specimen is dampened with distilled water and observed under UV light to identify fluorescent particles on the surface before treating the surface with uranyl acetate. This step, called prescreening, allows for identifying the natural fluorescence present in the damp specimen to avoid misinterpretation of the observations on the uranyl acetate treated surface. During prescreening, non-fluorescent aggregates appear dark while the cement paste, slag, and certain aggregates produce a certain level of fluorescence (ASTM C856 2014).

After prescreening, the specimen is treated with uranyl acetate for a prescribed duration. Uranyl acetate solution preparation methods, treatment methods, treatment duration, observation time window to detect fluorescence after treatment, and the cited references are listed in Table 2-2. As shown in the table, the treatment practices vary. For example, Natesaiyer and Hover (1988) soaked the specimens for 10 minutes in a solution prepared by mixing 0.35 oz of reagent grade uranyl acetate powder in 3.4 fl oz of a 1.67N acetic acid solution. However, the ASTM C856-14 (2014) recommended wetting the surface using a squeeze bottle with a solution prepared by dissolving 0.18 oz of reagent grade uranyl acetate powder in 3.4 fl oz of 1N acetic acid solution. In addition, laboratory work performed by Igarashi et al. (2016) and Sanno et al. (2013) showed that specimens need to be soaked in a uranyl acetate solution (with uranium concentration of 0.00058%) for at least 30 minutes to observe a saturated fluorescence intensity. Natesaiyer and Hover (1988) recommended observing the specimen within an hour after treatment while the recommendation of Igarashi et al. (2016) was to provide adequate drying time to obtain the maximum fluorescence intensity. The ASTM C856-14 (2014) recommendation is to observe the specimen immediately after the treatment. Interestingly, a 254 nm wavelength UV light was used in all these studies.

One of the major challenges of implementing this method in the field is the interference of the ambient light while observing the unique fluorescent signatures using a UV light. The current practice for minimizing the ambient light interference is to use a sealed metal box with a UV light and an opening to view the treated surface. Another common approach is to use a dark cloth to cover the operator’s upper body and the treated area. The implementation of these methods in the field is risky and inconvenient, and could lead to misinterpretation of the results.

Table 2-2. Uranyl Acetate Solution Preparation, Treatment, and Observation Methods

Solution preparation procedure	Treatment method	Treatment duration (min.)	Observation time window	Source of information
Mix 0.35 oz (10 g) of reagent grade uranyl acetate powder in 3.4 fl oz (100 ml) of a 1.67N acetic acid solution.	Immersion	10	Within an hour	Natesaiyer and Hover (1988)
Mix 0.18 oz (5 g) of reagent grade uranyl acetate powder in 6.8 fl oz (200 ml) of an 0.44N acetic acid solution.	Wetting the specimen using a squeeze bottle or a spray	Momentary application of solution to adequately wet the surface	3 to 5 minutes after treatment	Stark (1991)
Mix 0.18 oz (5 g) of reagent grade uranyl acetate powder in 3.4 fl oz (100 ml) of a 1N acetic acid solution.	Wetting the specimen using a squeeze bottle	1	Immediately after treatment	ASTM C856-14 (2014)
Uranyl acetate solution with uranium concentration of 0.00058%	Immersion	30 ¹	Need to provide adequate drying time	Igarashi et al. (2016). Sanno et al. (2013)

¹ Optimum soaking period to obtain the best color contrast

2.5.2.1 Color Signature Development

Natesaiyer and Hover (1988) presented the following observations after conducting several experiments using (i) chromatographic grade silica gel pretreated with NaOH, (ii) innocuous and reactive aggregates (Chert and Opal) untreated or immersed in 1N NaOH solution at room temperature for three months, and (iii) cross-sections of mortar bars prepared with innocuous and reactive aggregates (20% Opal or 30% Chert):

1. Untreated and uranyl acetate treated chromatographic grade silica gels pretreated with NaOH were observed using a short-wave UV light, and a bright fluorescence was detected only on the uranyl acetate treated specimen because of the replacement of Na⁺ ions with UO₂⁺⁺.
2. The Chert and Opal aggregates immersed in 1N NaOH for three months at room temperature and subsequently treated with uranyl acetate produced the brightest yellowish-green fluorescence under short-wave UV light because of the strongest adsorption of UO₂⁺⁺ into

the ASR products. The reactive aggregates treated only with uranyl acetate had a dull fluorescence under the UV light as a result of UO_2^{++} replacing the adsorbed cations in the disordered or amorphous silica surfaces.

3. Only Opal showed its natural dull green fluorescence among the untreated aggregates, while Chert did not show any fluorescence.
4. The Opal aggregates in the mortar bars could be identified with their natural fluorescence under the UV light. Each aggregate particle was surrounded by a bright reaction rim representing UO_2^{++} adsorbed by the ASR products. A limited reaction was observed in the bars with 30% Chert. The fluorescence was not visible in the specimens with innocuous aggregates.

As shown in Figure 2-14a and b, the yellowish-green color is observed along the reaction rims and the cracks with ASR products in reactive aggregates and the concrete matrix. The images with the yellowish-green color need to be carefully interpreted since the ettringite filled cracks and air voids also produce similar color signatures, as shown in Figure 2-14c. The other limitations of uranyl acetate testing include the following: exposure to uranium-containing solutions and solids, the uranyl ion bonding to negatively charged surfaces, and the requirement of a dark environment to support clear observations (Guthrie and Carey 1997).

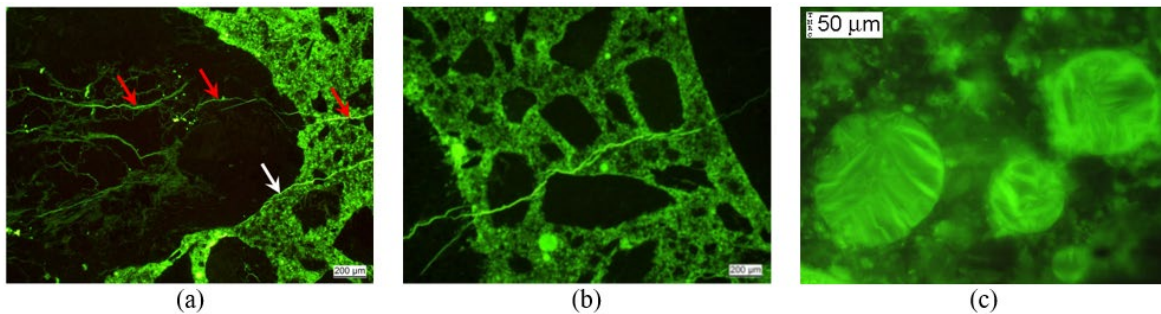


Figure 2-14. Fluorescent micrography observations (a) microcracks - one crack is running from the aggregate into the paste (red arrows) while another one travels along the interface between aggregate and paste before running into the paste (white arrow), (b) a crack running from one large aggregate to another by cutting through a small aggregate in between (Leemann and Griffa 2013), and (c) air voids filled with ettringite showing similar fluorescence (Peterson 1999)

Igarashi et al. (2016) evaluated (a) specimen exposure duration to uranyl acetate in developing detectable ASR gel fluorescence, (b) the effect of uranyl acetate drying time on the detectable ASR gel fluorescence intensity, and (c) the impact of storage duration in a high humidity environment on the exudation of ASR gel onto the saw-cut specimen surface. Figure 2-15 shows the impact of specimen exposure duration to uranyl acetate on detectable ASR gel fluorescence.

After evaluating the exposure duration, Igarashi et al. (2016) identified 30-minute exposure as the optimum duration to achieve a near saturation condition in fluorescence intensity. Figure 2-16 shows the impact of drying time on the ASR gel fluorescence intensity. The total duration from exposure to uranyl acetate until the end of the drying period is shown under each image, while the drying period is shown within the brackets. As shown in the figure, uranyl acetate color overshadows the characteristic yellowish-green color with an extended drying period. To minimize the possible misinterpretation of results, in the presence of uranyl acetate color, ASTM C856-14 (2014) recommends observing the surface under a UV light immediately after cleaning the uranyl acetate treated surface.

The application of chemicals on a freshly broken surface produces better results. Other surface preparation methods such as wet sawing, polishing, and cleaning removes ASR gel and/or contaminates the surface with ASR gel. This poses many challenges to identifying the unique signatures expected from an ASR damaged concrete (Guthrie and Carey 1998). To overcome this challenge, Igarashi et al. (2016) recommended storing specimens under high humidity conditions for several days after saw cutting and/or polishing the surface to promote exudation of the ASR gel, as shown in Figure 2-17. This approach is possible when the results are not immediately required.

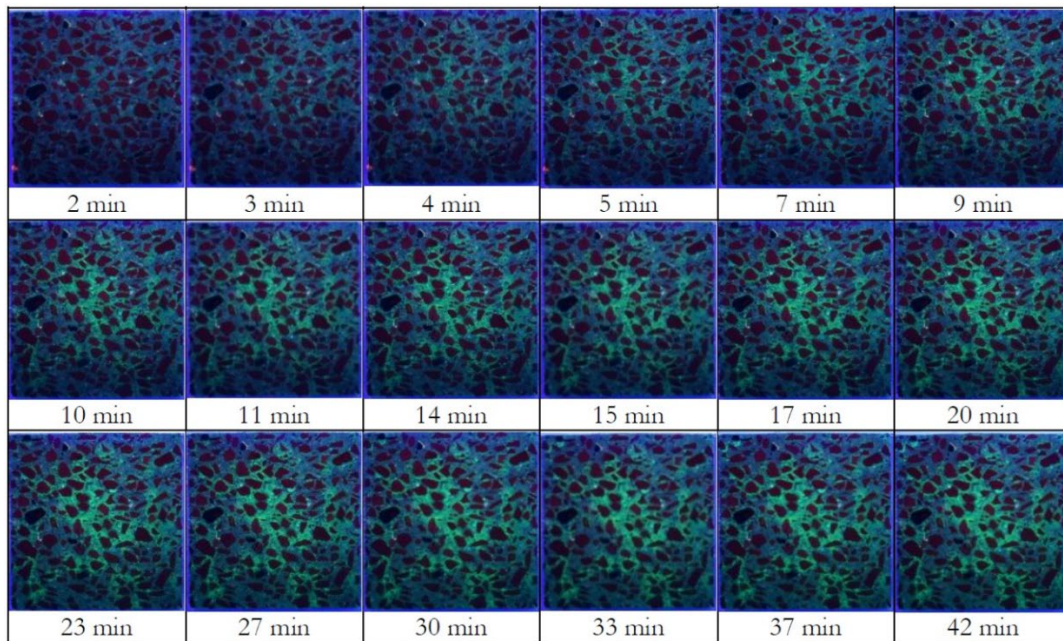


Figure 2-15. Impact of specimen exposure duration to uranyl acetate on detectable ASR gel fluorescence (Igarashi et al. 2016)

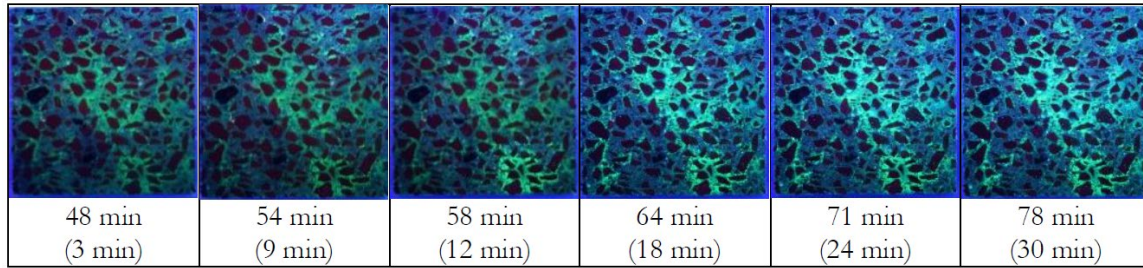


Figure 2-16. Impact of drying time (in brackets) on ASR gel fluorescence intensity (Igarashi et al. 2016)

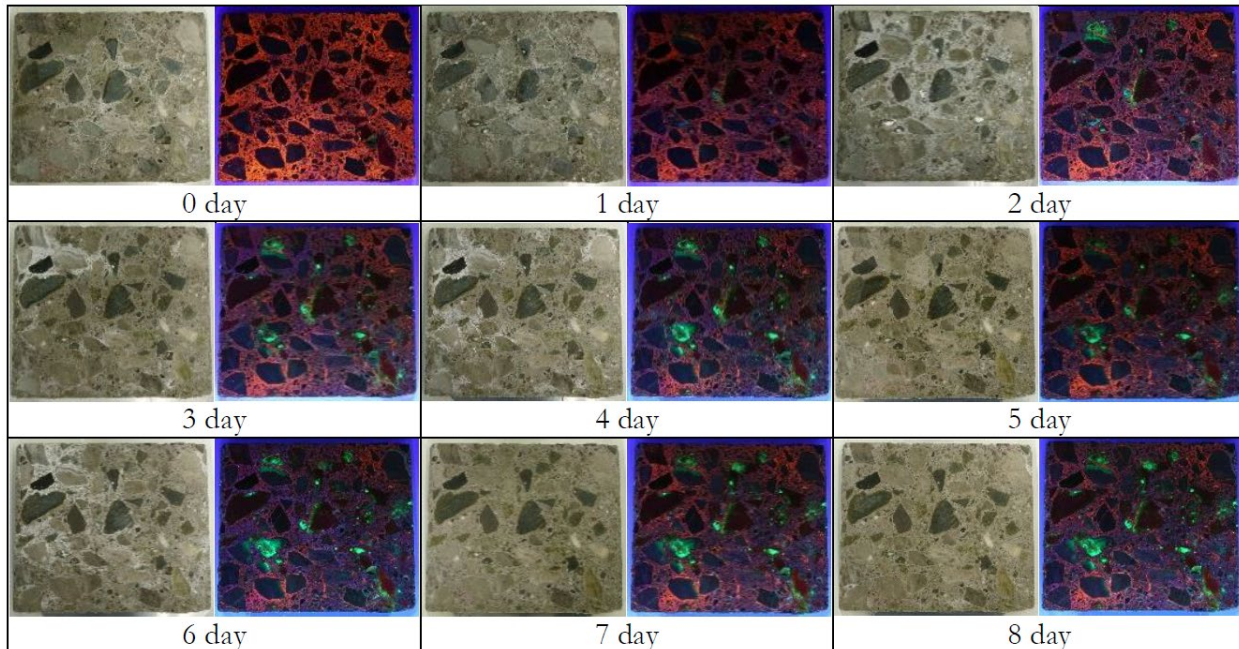


Figure 2-17. Impact of storage duration to exudation of ASR gel onto the specimen surface in the presence of high relative humidity (Igarashi et al. 2016)

2.5.3 Sodium Cobaltinitrite/Rhodamine B Test

Guthrie and Carey (1997 and 1998) developed a dual staining technique to identify ASR gel with K^+ and Ca^{2+} . This staining technique uses two chemical compounds: (i) sodium hexanitrocobaltate ($Na_3Co(NO_2)_6$), which is commonly referred to as sodium cobaltinitrite, and (ii) rhodamine B ($C_{28}H_{31}N_2O_3Cl$), which is known as a “geochemical” due to its dependency on the geological and chemical compositions of ASR gels (Guthrie and Carey 1997, 1998, and 1999). Among these two chemical reagents, sodium cobaltinitrite is a well-known product used in analytical chemistry to determine the K^+ content of a solution. The chemical reaction between the dissolved sodium cobaltinitrite and potassium forms a yellowish precipitate ($K_2NaCo(NO_2)_6 \cdot 6H_2O$). Section 2.3.1.3. describes two ASR gel compounds that are developed in mortar and concrete based on two forms of CaO concentration in the pore solutions: (i) the non-expansive calcium-alkali-silicate-hydrate

(C-(N/K)-S-H), known as the C-S-H gel with alkali impurities or the Ca^{2+} rich ASR gel, and (ii) the expansive alkali-silicate-hydrate ((N/K)-S-H). Even though both K^+ and Na^+ behave similarly in ASR, this staining technique is capable of detecting only the K^+ - and Ca^{2+} -rich ASR gels.

The application procedure requires lightly washing the surface with distilled water to make it damp and remove dust before the application of sodium cobaltinitrite, the “yellow” solution. The contact between the specimen and yellow solution is maintained for about 30 – 60 seconds before washing the surface using distilled water. The yellow stain highlights the areas with ASR gels rich in K^+ . The degree of reactivity can be diagnosed based on the extent of the yellow stain. The typical rock forming minerals like feldspars, micas, and illite remain unstained since there is no cation-exchange to react with sodium cobaltinitrite. However, certain aggregates such as K-rich smectites and K-rich zeolites may appear yellow. The color intensity increases as the surface dries up (Guthrie and Carey 1997, 1998, and 1999).

After washing the surface following the application of sodium cobaltinitrite, rhodamine B, the “pink” solution, can be applied at any point to detect Ca^{2+} distribution (Guthrie and Carey 1998, Frybort et al. 2020). As the Ca^{2+} concentration increases, the color changes from yellow, orange, to light purple-red (Frybort et al. 2020). The contact between the specimen and pink solution is maintained for about 30 – 60 seconds before washing the surface using distilled water. Even though the concrete without visible deterioration is not expected to show pink stains, rhodamine B could stain not only the Ca^{2+} -rich ASR gel (i.e., nonexpansive ASR) but also the semipermeable regions associated with carbonation and paste deterioration (Guthrie and Carey 1997 and 1999). The areas with small amounts of K^+ - and Ca^{2+} -rich ASR gels or the semipermeable areas are highlighted in an “orangish color” due to overlapping of yellow and pink colors (Guthrie and Carey 1998). Figure 2-18 shows two cores treated with sodium cobaltinitrite and rhodamine B. The second core has more K^+ -rich ASR since the intensity of yellow color is greater in Figure 2-18e than in Figure 2-18b. Since orange and light purple-red color areas cover most of the core 2 section, Figure 2-18f, most of the ASR gels in core 2 are Ca^{2+} -rich non-expansive gels.

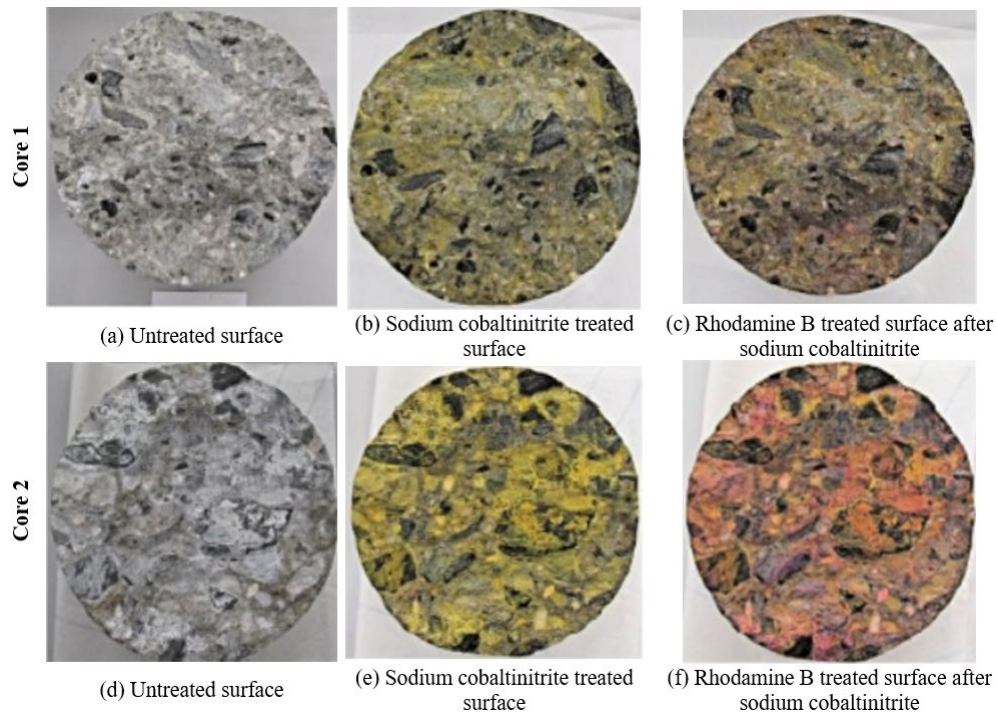


Figure 2-18. Cores treated with sodium cobaltinitrite (b and e) and rhodamine B (c and f) reagents; core 2 shows a higher probability of having non-expansive ASR gels (Frybort et al. 2020)

2.5.4 Summary

Three staining techniques have been developed to identify ASR in concrete. However, only two methods, the uranyl acetate method and the sodium cobaltinitrite/rhodamine B combination method, have shown promising results to detect ASR in concrete.

The uranyl acetate test was well developed over the years. Different scholars used different uranyl acetate concentrations, treatment methods, and durations. The recent laboratory experiments demonstrated that the fluorescence could reach to saturation when a specimen is immersed in uranyl acetate solution for 30 minutes. The limitations of this method include the following: (i) ettringite filled cracks and air voids producing yellowish-green fluorescence, (ii) exposure to uranium-containing solutions and solids, (iii) the uranyl ion bonding to negatively charged surfaces, and (iv) the requirement of a dark environment to observe the fluorescence.

Unlike the testing with uranyl acetate, the sodium cobaltinitrite/rhodamine B combination can be used to evaluate the presence of ASR under ambient exposure conditions. The primary concern is that the method is limited to identifying K^+ -rich ASR gels. Also, the lack of published literature on this method limits the experience and available color signatures for effective implementation and results interpretation.

2.6 LOAD RATING OF PSC BEAMS/BRIDGES

MDOT uses Load Factor Rating (LFR) and Load and Resistance Factor Rating (LRFR) methods. The LFR method is used for older structures, while the LRFR method is used for post-2010 structures. The load rating is reported using a rating factor (RF) calculated following a relevant rating method (i.e. LFR or LRFR); an $RF \geq 1$ represents a safe structure to support the loads. An $RF < 1$ requires remedial actions such as load posting, repair, and replacement. The RF multiplied by the rating vehicle weight (in tons) presents the rating of the structure in tons.

2.6.1 LFR Method

Inventory and operating ratings are calculated.

2.6.1.1 Inventory Rating

The inventory rating factors are calculated using Eq. 2 to Eq. 6.

$$\text{Concrete tension:} \quad RF = \frac{6\sqrt{f'_c} - (F_D + F_P + F_S)}{F_L} \quad (\text{Eq. 2})$$

$$\text{Concrete compression:} \quad RF = \frac{0.6f'_c - (F_D + F_P + F_S)}{F_L} \quad (\text{Eq. 3})$$

$$\text{Concrete compression:} \quad RF = \frac{0.4f'_c - \frac{1}{2}(F_D + F_P + F_S)}{F_L} \quad (\text{Eq. 4})$$

$$\text{Prestressing steel tension:} \quad RF = \frac{0.8f_y - (F_D + F_P + F_S)}{F_L} \quad (\text{Eq. 5})$$

$$\text{Flexural and shear strength:} \quad RF = \frac{\phi R_n - (1.3D + S)}{2.17L(1 + I)} \quad (\text{Eq. 6})$$

where,

- D = unfactored dead load moment
- f'_c = concrete compressive strength
- f_y = prestressing steel yield strength
- F_D = unfactored dead load stress
- F_L = unfactored live load stress including impact
- F_P = unfactored stress due to prestress force after losses
- F_S = unfactored stress due to secondary prestress forces
- I = impact factor

- L = unfactored live load moment
- RF = rating factor
- R_n = nominal resistance (M_n for moment)
- S = unfactored prestress secondary moment
- ϕ = load factor design (LFD) resistance factor

2.6.1.2 Operating Rating

The operating rating factors are calculated using Eq. 7 to Eq. 8.

$$\text{Prestressing steel tension: } RF = \frac{0.9f_y - (F_D + F_P + F_S)}{F_L} \quad (\text{Eq. 7})$$

$$\text{Flexural and shear strength: } RF = \frac{\phi R_n - (1.3D + S)}{1.3L(1+I)} \quad (\text{Eq. 8})$$

2.6.2 LRFR Method

The design load inventory rating, design load operating rating, legal load rating, and permit load rating are calculated using relevant limit states.

2.6.2.1 Strength I and II Limit States

The design load inventory rating, design load operating rating, legal load rating, and permit load rating factors are calculated using Eq. 9. The primary difference is the reliability levels implemented for each rating using different live load factors, γ_{LL} .

$$RF = \frac{C - (\gamma_{DC})(DC) - (\gamma_{DW})(DW) \pm (\gamma_P)(P)}{(\gamma_{LL})(LL + IM)} \quad (\text{Eq. 9})$$

where,

- C = capacity
= $\phi_c \phi_s \phi R_n$ for the strength limit states, with $\phi_c \phi_s \geq 0.85$
- DC = dead load effect due to structural components and attachments
- DW = dead load effect due to wearing surface and utilities
- IM = dynamic load allowance
- LL = live load effect
- P = permanent loads other than dead loads
- RF = rating factor
- R_n = nominal member resistance (as inspected)

- γ_{DC} = load and resistance factor design (LRFD) load factor for structural components and attachments
- γ_{DW} = LRFD load factor for wearing surfaces and utilities
- γ_{LL} = evaluation live load factor
- γ_P = LRFD load factor for permanent loads other than dead loads = 1.0
- ϕ = LRFD resistance factor
- ϕ_c = condition factor
- ϕ_s = system factor

2.6.2.2 Service I Limit State

An optional Service I limit state check is performed for the permit load rating. Under permit loads, the stress in prestressing steel nearest to the extreme tension fiber of a member should be less than 90% of the prestressing steel yield strength ($0.9f_y$).

2.6.2.3 Service III Limit State

The service III limit state is checked under the design load inventory rating and optionally under the legal load rating using Eq. 10. The service III limit state evaluates the limiting concrete tensile stress under service loads.

$$RF = \frac{C - (\gamma_{DC})(f_{DC}) - (\gamma_{DW})(f_{DW})}{(\gamma_{LL})(f_{LL+IM})} \quad (\text{Eq. 10})$$

where,

- C = capacity = f_R for service limit states
- f_{DC} = dead load stress due to structural components and attachments
- f_{DW} = dead load stress due to wearing surface and utilities
- f_{LL+IM} = live load stress with dynamic load allowance
- f_R = allowable stress specified in the LRFD code

2.6.3 Load Rating Parameters Impacted by Distresses

Even though multiple parameters are in the RF calculation equations, only a handful of these parameters would be affected by beam distresses, as shown in Table 2-3. The following assumptions were used when defining the impact of distress on rating parameters:

- The deck is assumed to be in a satisfactory condition.
- The beam distresses are localized towards the bottom flange (i.e. parameters associated with the top flange and the compression reinforcement are not affected).
- The presence of non-prestressed reinforcement is neglected.

Table 2-3. Load Rating Parameters Impacted by Beam Distress

Load rating parameter	LFR method	LRFR method
Prestressing steel:		
Number of strands/ area of prestressing steel	√	√
Prestressing steel yield strength	√	√
Concrete material properties:		
Concrete compressive strength	√	√
Concrete modulus of rupture and tensile strength	√	√
Concrete elasticity modulus	√	√
Beam section properties:		
Cross-sectional area (composite/noncomposite)	√	√
Section moduli (composite/noncomposite)	√	√
Cracked moment of inertia	-	√
Live load and barrier load distribution	√	√
Condition factor (ϕ_c)	-	√

Load rating is performed using a simple hand calculation, an in-house spreadsheet calculation program, or a load rating software. Any of these methods or tools should be able to incorporate the parameters listed in Table 2-3 with necessary modifications to account for the type and degree of deterioration when load rating a deteriorated PSC beam. Since MDOT uses the AASHTOWare Bridge Rating (BrR), its capabilities and limitations for load rating of distressed PSC box- and I-beams were reviewed and summarized in the following section.

2.6.4 AASHTOWare BrR for Load Rating of Distressed PSC Beams

State highway agencies, the Federal Highway Administration (FHWA), and bridge rating consultants use AASHTOWare BrR, formerly known as Virtis, for load rating (AASHTOWare 2018). The capacity of a distressed beam can be evaluated using AASHTOWare BrR as an individual member (using a single line model) or as part of a bridge superstructure (using a grillage model). Irrespective of the analysis model complexity, material properties, section properties, prestressing strand layout, stress limits, and load distribution need to be defined. Load rating output is obtained at program defined and/or user defined points of interest along the beam length.

The material properties and the girder section properties representing distresses can be defined as input to AASHTOWare BrR. The following sections describe the options available in AASHTOWare BrR version 6.8.4.3001 (the academic version) to incorporate beam distresses for load rating.

2.6.4.1 Concrete and Prestressing Steel Material Properties

Figure 2-19 shows the concrete material property data input window. Concrete properties can be imported from a library or defined by the user. Certain concrete material properties, such as the modulus of elasticity, can be calculated as per the Standard Specifications for Highway Bridges (AASHTO SSHB 2002) (for the LFR method) or the LRFD Bridge Design Specifications (for the LRFR method). For example, the modulus of elasticity calculated as per the Standard Specifications for Highway Bridges is defined as the *Std Modulus of Elasticity (E_c)*, whereas the modulus of elasticity calculated according to the LRFD Specifications is defined as the *LRFD Modulus of Elasticity (E_c)*. These two elasticity moduli are highlighted in Figure 2-19 using a red box. Basically, AASHTOWare BrR provides flexibility to customize material properties as needed. However, *defining material properties for a part of the cross-section is not possible since this is not a general-purpose 3D finite element software. This limitation affects the program capabilities to automatically calculate the effective section properties.*

Figure 2-20 shows the prestressing steel material property data input window. Since the prestressing steel material properties can be imported from a library or defined by the user, the *ultimate tensile strength (F_u)*, *yield strength (F_y)*, and *modulus of elasticity (E)* can be defined to represent the condition of strands. However, *assignment of custom material properties to each individual strand is not practical with the current setup. This limitation affects the program capabilities to automatically calculate the effective number of strands and eccentricities.*

Bridge Materials - Concrete

Name: Description:

Compressive strength at 28 days (fc) = ksi

Initial compressive strength (f'ci) = ksi

Coefficient of thermal expansion = 0.0000060000 1/F

Density (for dead loads) = kcf

Density (for modulus of elasticity) = kcf

Std Modulus of elasticity (Ec) = ksi

LRFD Modulus of elasticity (Ec) = ksi

Std Initial modulus of elasticity = ksi

LRFD Initial modulus of elasticity = ksi

Poisson's ratio = 0.200

Composition of concrete = Normal

Modulus of rupture = ksi

Shear factor = 1.000

Splitting tensile strength (fct) = ksi

Copy To Library... Copy from Library... OK Apply Cancel

Figure 2-19. Concrete material property data input window

Bridge Materials - PS Strand

Name: Description:

Strand diameter = in

Strand area = in²

Strand type = Low Relaxation

Ultimate tensile strength (Fu) = ksi

Yield strength (Fy) = ksi

Modulus of elasticity (E) = ksi

Transfer length (Std) = in

Transfer length (LRFD) = in

Unit load per length = lb/ft

Epoxy coated

Copy To Library... Copy from Library... OK Apply Cancel

Figure 2-20. Prestressing steel material property data input window

2.6.4.2 Concrete Stress Limits

Concrete stress limits, as per the *LFD* and *LRFD* methods, are defined using the data input window shown in Figure 2-21. The stress limits are either user-defined or automatically generated as per the LFD or LRFD Specifications.

	LFD	LRFD
Initial allowable compression:	<input type="text"/> ksi	<input type="text"/> ksi
Initial allowable tension:	<input type="text"/> ksi	<input type="text"/> ksi
Final allowable compression:	<input type="text"/> ksi	<input type="text"/> ksi
Final allowable tension:	<input type="text"/> ksi	<input type="text"/> ksi
Final allowable DL compression:	<input type="text"/> ksi	<input type="text"/> ksi
Final allowable slab compression:	<input type="text"/> ksi	<input type="text"/> ksi
Final allowable compression: (LL + 1/2(Pe + DL))	<input type="text"/> ksi	<input type="text"/> ksi

Figure 2-21. Concrete stress limits data input window

2.6.4.3 Beam Cross-Section Properties

Two options are available to define beam cross-sections: cross-section based and schedule based. The cross-section based option allows for defining different cross-sections along the selected locations of the beam length. Even though this option provides flexibility to define customized sections incorporating deteriorations at specific locations along the beam span, this option is available only for steel beams. For PSC I- and box-beams, section properties are defined using a schedule-based entry. With this option, the same cross-section is assigned for the entire beam length. Figure 2-22 and Figure 2-23 show the section property data input window for a PSC I-beams. A similar data input window is available for PSC box-beams. Two options are available to define section properties: (1) define girder dimensions using the *Dimensions* tab (see Figure 2-22) and use the *Compute* option under the *Properties* tab (see Figure 2-23) to calculate section properties, or (2) define input section properties under the *Properties* tab (see Figure 2-23).

Since the AASHTOWare BrR does not have an option to define PSC I-beam cross-sections with deteriorations, the resultant section properties can be calculated using an external tool, such as MathCAD, after accounting for the loss of a section (due to distresses) and inputting the results under the Properties tab (see Figure 2-23). Interestingly, only the major axis moment of inertia is allowed, limiting the analysis only to the major axis bending. Therefore, major damages that require bi-axial bending analysis cannot be performed using AASHTOWare BrR.

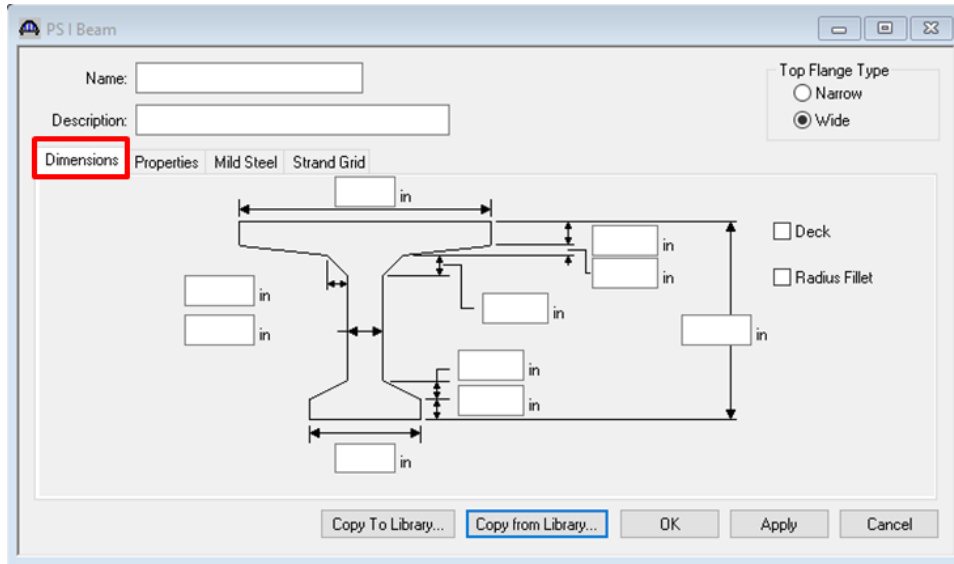


Figure 2-22. Dimensions tab in the PSC I-beam section property data input window

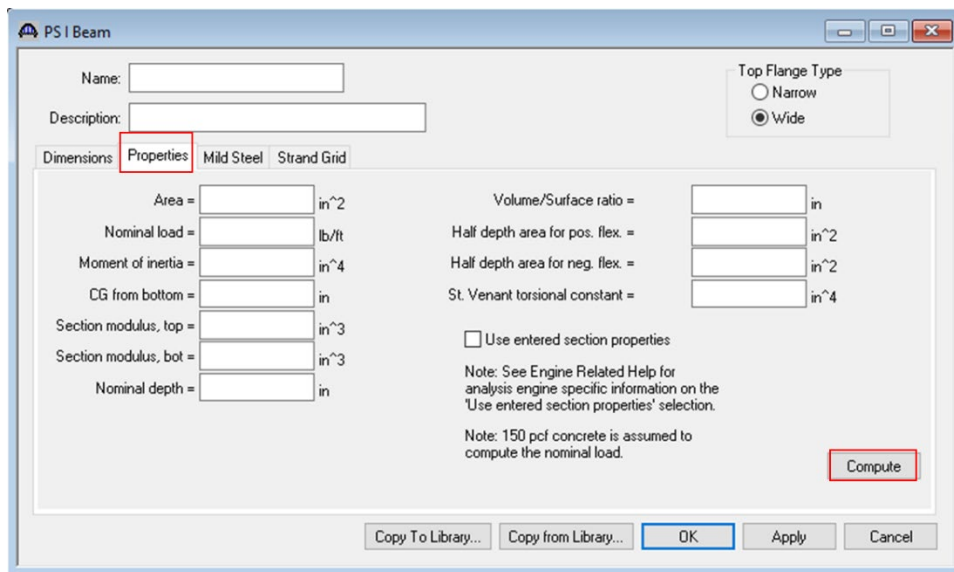


Figure 2-23. Properties tab in the PSC I-beam section property data input window

2.6.4.4 Prestressing Strand Layout

Before developing a prestressing strand layout, a prestressing strand grid is defined. As shown in Figure 2-24, the strand grid is developed by defining the number of rows of prestressing steel (*Row No.*), the number of strands in each row (*No. of Strands*), the vertical distance to each row from the beam bottom (*Vertical Distance from bottom*), and the horizontal spacing between the strands in a row (*Horizontal Spacing*).

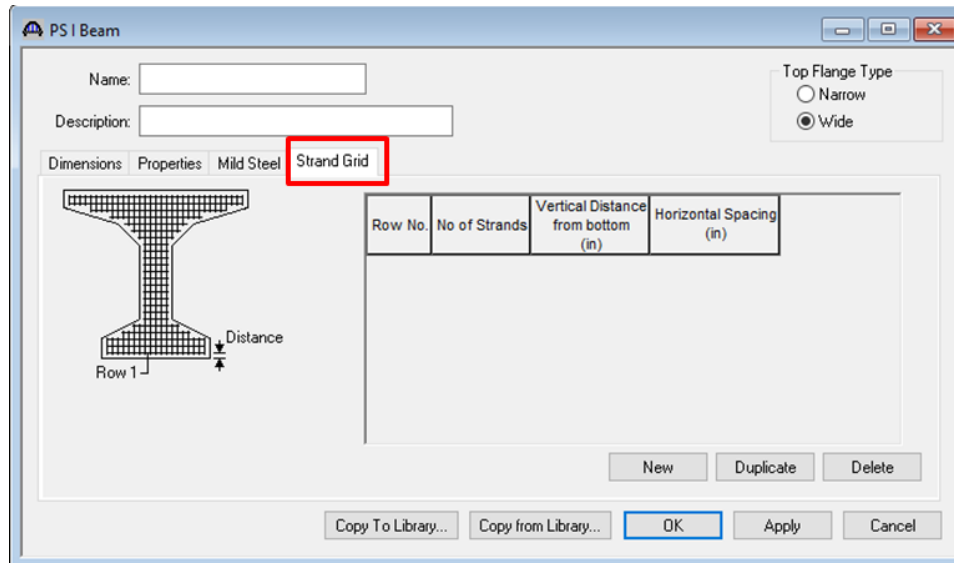


Figure 2-24. *Strand Grid* tab in the PSC I-beam section property data input window

The *strand layout* window, shown in Figure 2-25 and Figure 2-26, is used to define the effective number of prestressing strands for a given beam section. The observed and estimated level of damage to the beam and the strands needs to be considered when developing the strand layout. *P and CGS only* (see Figure 2-25) and *Strands in rows* (Figure 2-26) are the two options available to define a strand layout. In the *P and CGS only* option, the resultant force in the strands (*P*) with the center of gravity of the strands (*CGS*) is separately calculated and assigned. In the *Strands in rows* option, the individual strands are defined on the grid. The light grey crosses in Figure 2-26 denote the strand grid. A user can manually choose the grid locations to define the strand layout. The total *Number of strands* in the girder section and *CG of strands* (center of gravity) are automatically calculated based on the defined strand layout.

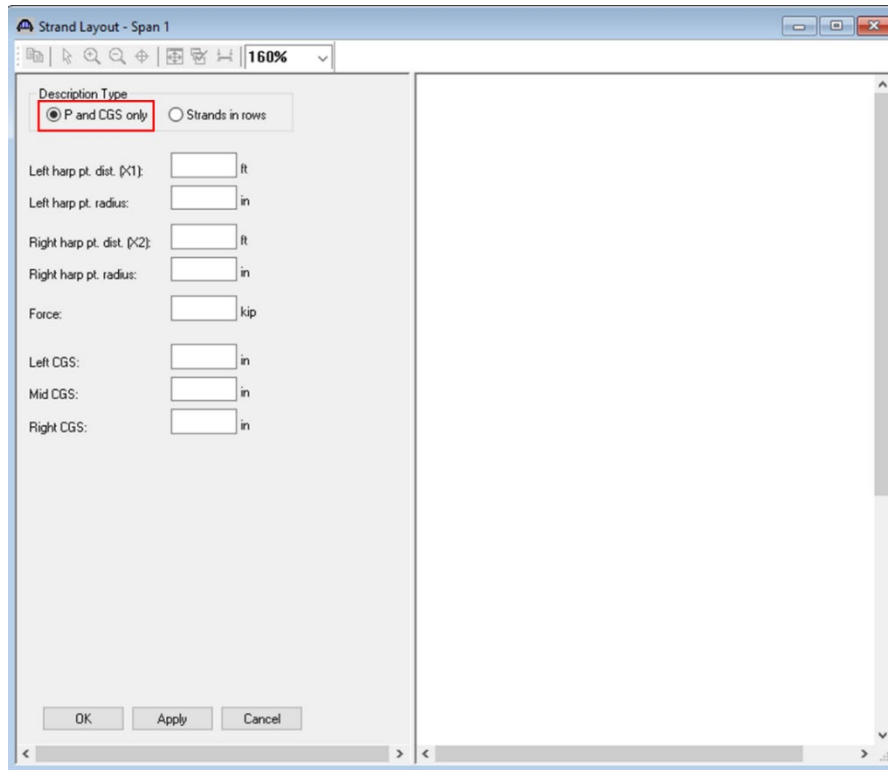


Figure 2-25. Strand layout data input window with *P and CGS* option

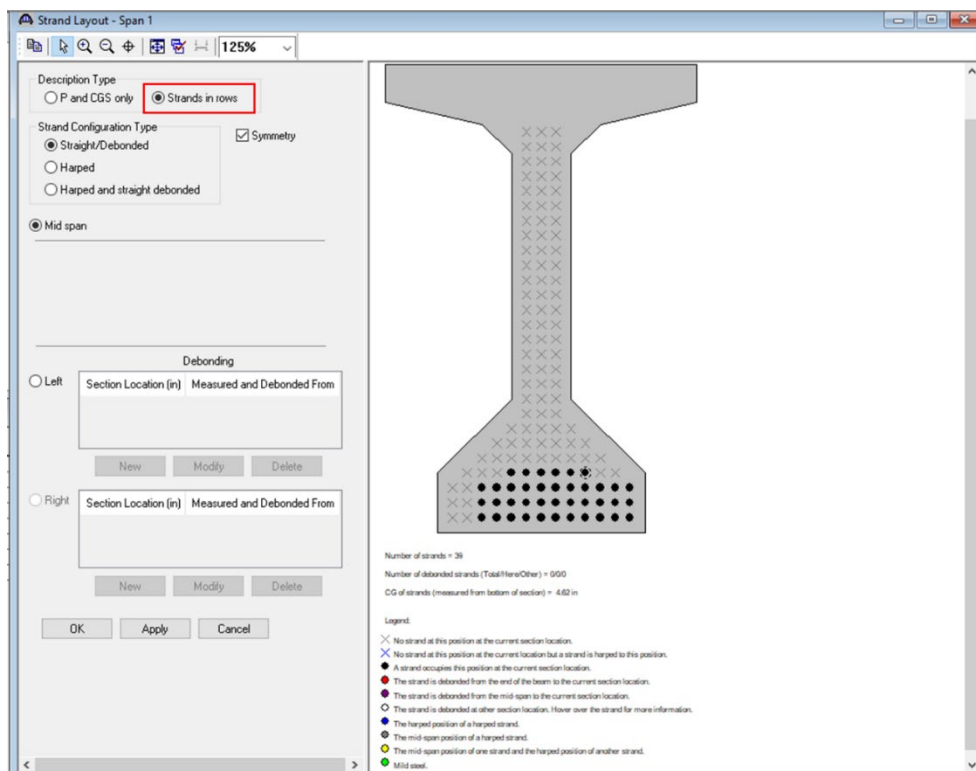


Figure 2-26. Strand layout data input window with *Strands in rows* option

2.6.4.5 Live Load Distribution Factors

Two options are available to analyze a distressed beam in a bridge superstructure: the distressed beam can be analyzed as a member of the superstructure model (Girder System Superstructure), or as a single line element model of the beam itself (Girder Line Superstructure). There are two options to define live load distribution factors for the Girder System Superstructure model: (1) select the *Compute from Typical Section* button to use the defined sections for the superstructure (see Figure 2-27 and Figure 2-28), or (2) define live load distribution factors as a direct user input. Figure 2-27 and Figure 2-28 show the dialog boxes to define live load distribution factors for LFD (*Standard*) and *LRFD* methods, respectively. If the distressed beam is modeled as a Girder Line Superstructure, live load distribution factors can only be defined as a user input using dialog boxes similar to Figure 2-27 and Figure 2-28.

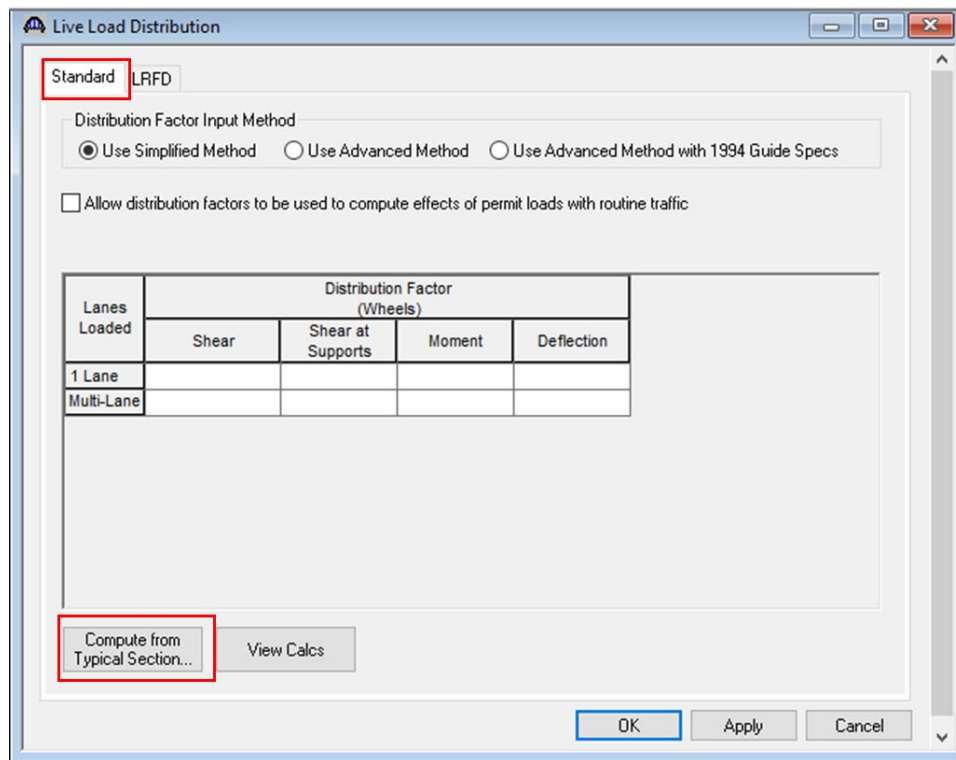


Figure 2-27. Dialog box to define live load distribution factors for the LFD (*Standard*) method when the superstructure is modeled as a Girder System Superstructure

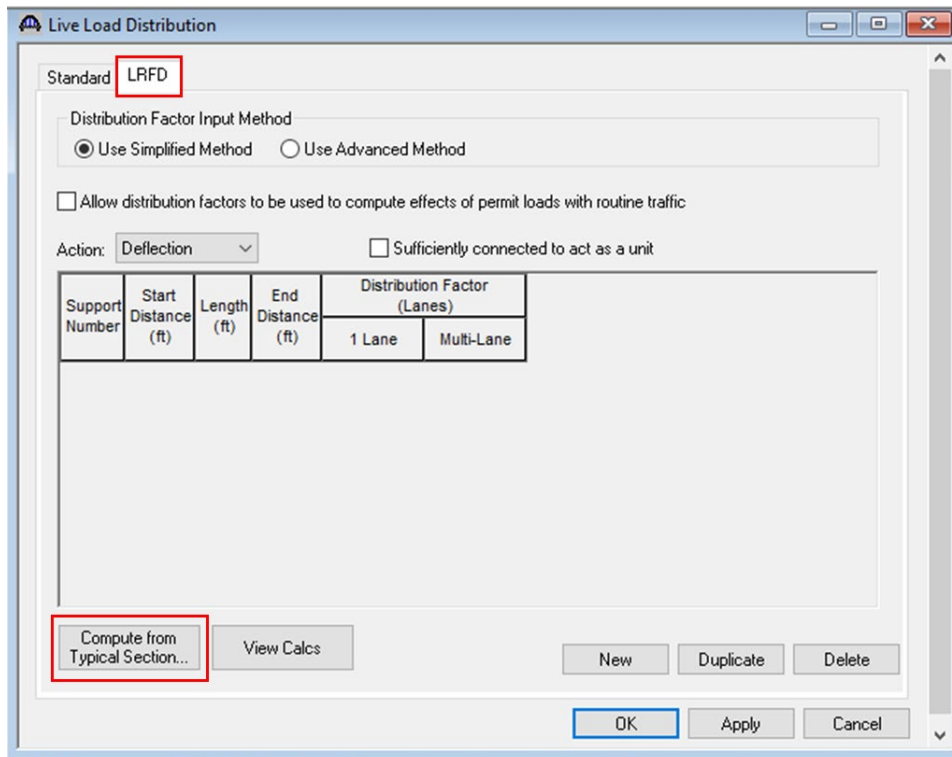


Figure 2-28. Dialog box to define live load distribution factors for the *LRFD* method when the superstructure is modeled as a Girder System Superstructure

2.6.4.6 Condition Factor (ϕ_c)

A condition factor (ϕ_c) is required to compute rating factors using LRFR strength limit states. For a selected member, the condition factor can be defined as shown in Figure 2-29. Based on the physical condition of the member, the condition factor can be selected as *Good or Satisfactory*, *Fair*, or *Poor*.

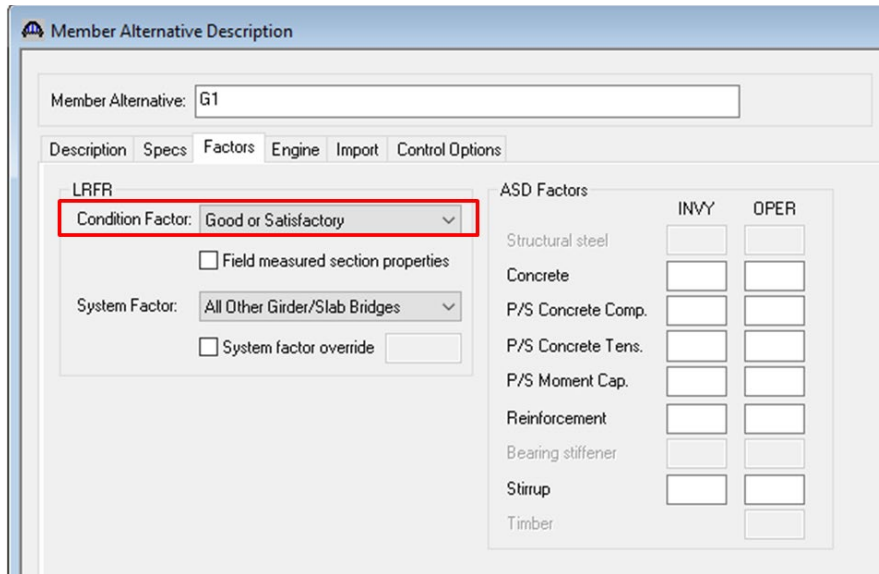


Figure 2-29. Dialog box to assign a beam condition factor

2.6.4.7 Points of Interest (POIs) for Analysis Results

The load rating output can be collected at the points of interest (POIs) using the *Control Options* available for a member, as shown in Figure 2-30. These POIs can be generated at locations that are predefined in the software program at *tenth points except at supports, at support points, at support face and critical shear points, and at section change points*. The software program also allows for specifying *user-defined points* (see Figure 2-30). To obtain the load rating output at a damaged location of a beam, a user-defined POI can be established. Figure 2-31 shows the dialog box for assigning user-defined POIs with respect to the *distance from the leftmost support*, or as a *fraction* of the span length measured from the left or right end of the span.

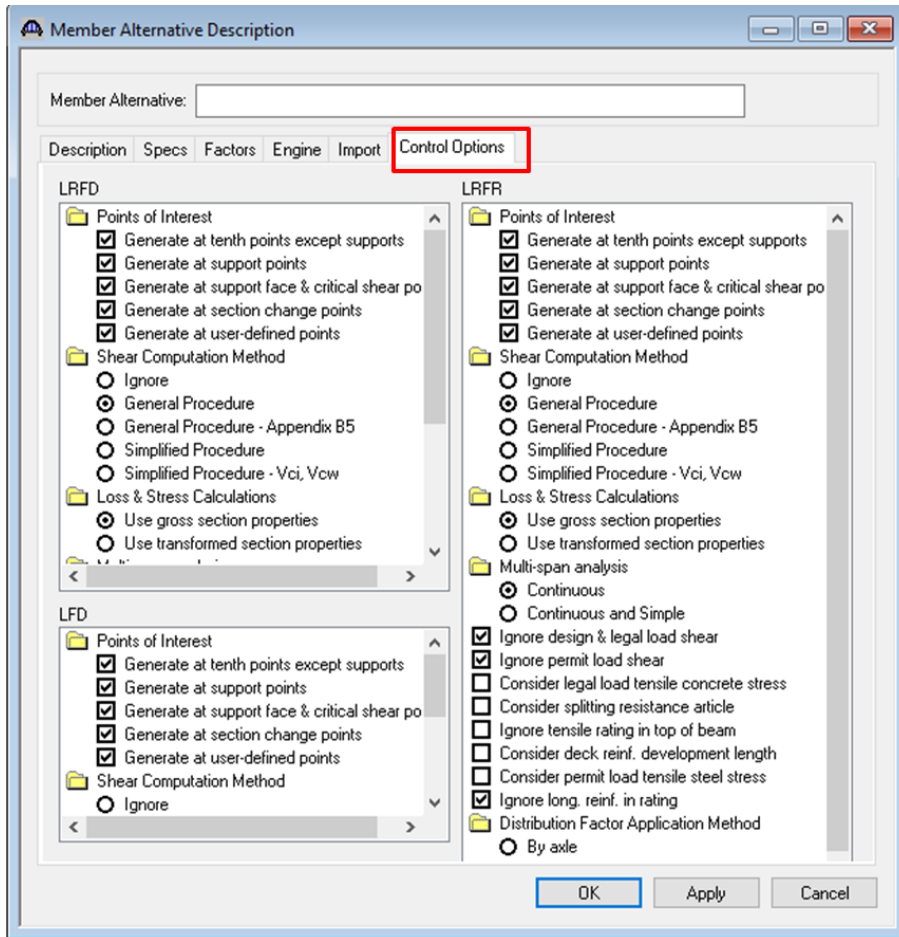


Figure 2-30. Control options selection window

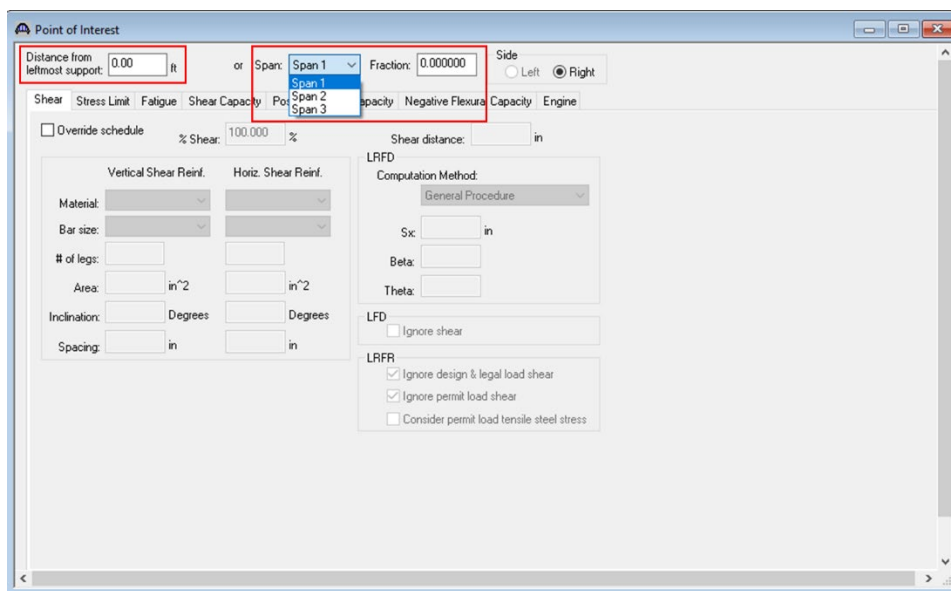


Figure 2-31. Dialog box to assign user-defined points of interest

2.6.4.8 Override Option in AASHTOWare BrR

According to Aktan et al. (2005), Williams and Choudhuri (2010), and Tabatabai and Nabizadeh (2019), the residual capacity of a beam depends on the damage magnitude and the damage location within the beam cross-section. Typically, the material properties, section properties, stress limits, and the strand layout defined for a beam in AASHTOWare BrR are automatically applied over the entire span length. The override option in AASHTOWare BrR can be used to assign user-defined stress limits and section capacities at the corresponding distress location(s) on a PSC beam, as shown in Figure 2-32 and Figure 2-33.

Figure 2-32 shows the override option for stress limits. The stress limits defined for a beam span can be overridden with different stress limits at a user defined POI. For example, consider a beam cross-section with heavy bottom flange deterioration with a questionable tensile capacity. *The damage location can be first defined as a POI. Using the options in the dialog box shown in Figure 2-32, a reduced tensile stress limit or zero tensile stress limit can be defined as the allowable tension at the defined POI. This new stress limit overrides the program-defined allowable tensile stress only at the damage location.*

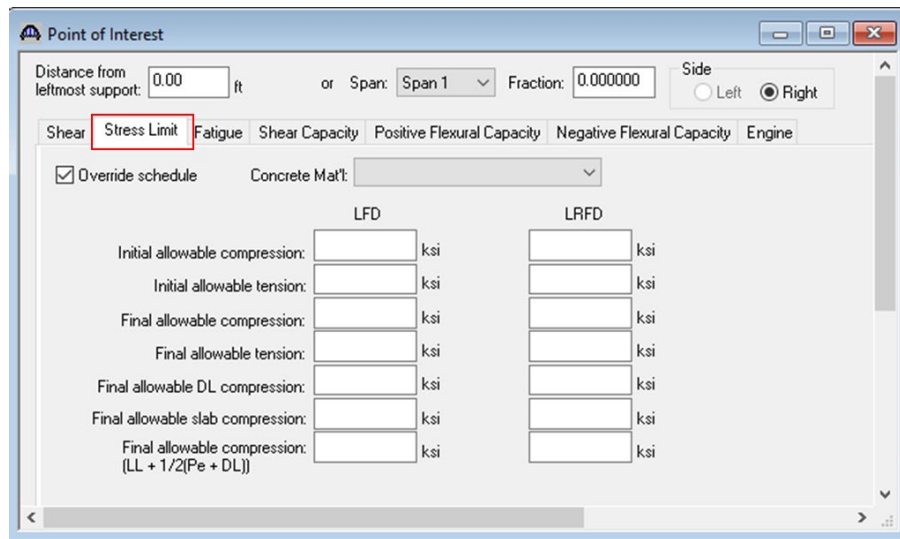


Figure 2-32. Stress limit override option in AASHTOWare BrR

Figure 2-33 shows the override options for positive flexural capacities. The program-calculated capacity at a location can be overridden with a user-defined moment capacity and the factor, phi, for a selected load rating method (*LFD* or *LRFR*). For the LRFR method, the override option is available for each limit state.

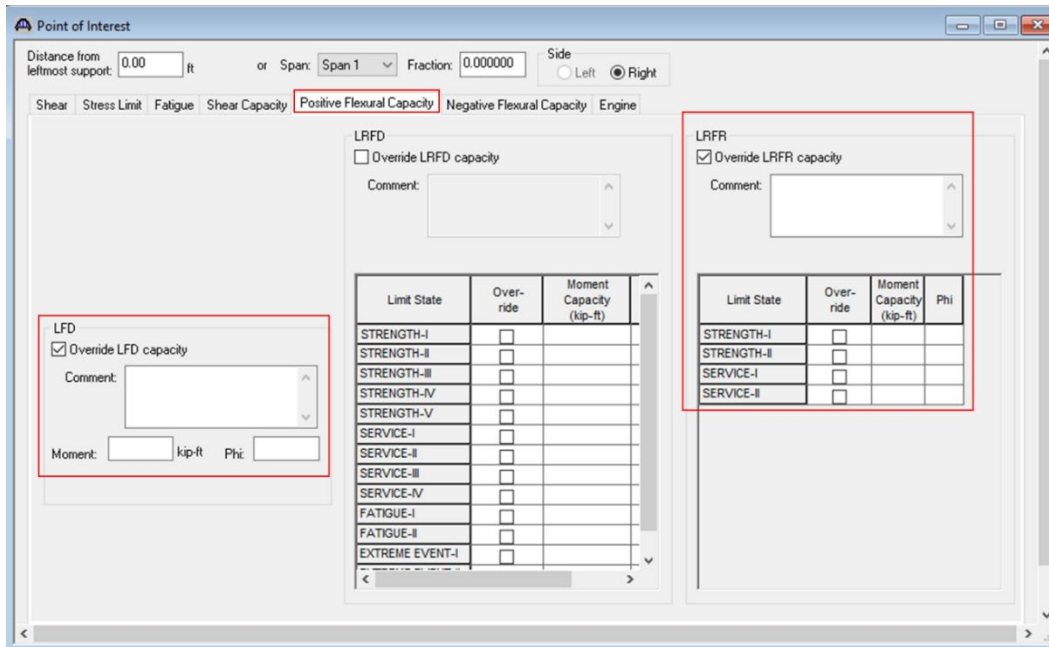


Figure 2-33. Positive flexural capacity override option in AASHTOWare BrR

In summary, the degradation of material and section properties, damages to prestressing steel, and live load distribution with distressed PSC beams need to be quantified and defined in AASHTOWare BrR to evaluate load ratings. The following sections present a comprehensive summary of literature on deteriorated PSC beams. The summary includes (1) concrete and prestressing steel properties of deteriorated PSC beams, (2) guidelines for calculating beam section properties, (3) guidelines for deciding the number of effective prestressing strands, (4) redevelopment of damaged prestressing strands, (5) distress quantification methods, (6) crack depth evaluation techniques, and (7) live load distribution with distressed beams.

2.7 CONCRETE DEGRADATION IN PSC BEAMS

Since a cracked section is used for calculating beam capacity under strength limit states, the degradation of concrete mechanical properties below the neutral axis is not a concern. However, the impact of concrete deterioration on mechanical properties (i.e. tensile strength, modulus of rupture, and elasticity modulus) is important when evaluating the service limit states. The following sections present the impact of concrete deterioration on compressive strength, elastic modulus, and tensile strength. Since ultrasonic pulse velocity (UPV) through concrete is used as a nondestructive method to assess concrete quality and calculate concrete mechanical properties, the impact of concrete deterioration on UPV is discussed. As a concrete deterioration mechanism,

ASR is considered primarily in this report. The rate of ASR and its impact on UPV and mechanical properties depend on several parameters such as alkali load in the mix, concrete mix ingredients and proportions, aggregate reactivity, curing conditions (temperature and relative humidity), exposure conditions, along with loads and boundary conditions (Abd-Elssamad et al. 2020). The Institution of Structural Engineers (ISE) presents lower-bound residual compressive strength, tensile strength, and modulus of elasticity as functions of the percentage of free expansion (ISE 1992). The ISE recommended residual mechanical properties are based on the data from unrestrained ASR-affected concrete, normalized with reference to unaffected properties at 28 days of curing. Esposito et al. (2016), Kawabata et al. (2017), and Martin et al. (2017) present several empirical models to calculate mechanical properties of ASR-affected concrete with different reactive aggregates, concrete compositions, restraint conditions, curing conditions, and loading conditions.

2.7.1 Compressive Strength

Figure 2-34 shows the variation of the normalized concrete compressive strength with ASR expansion. Each data set in Figure 2-34 was normalized with respect to the 28-day compressive strength of sound concrete. The envelope shown in the figure was developed by Abd-Elssamad et al. (2020) using data from 15 previous studies representing different loading conditions, concrete mix proportions, reactive aggregates, and curing regimes. The envelope developed by Abd-Elssamad et al. (2020) includes data from Jones and Clark (1996), Swamy and Al-Asali (1988), Fan and Hanson (1998), Ahamad et al. (2003), Batic et al. (2004), Multon et al. (2005), Ben Haha (2006), Giaccio et al. (2008), Giannini and Folliard (2012), Hafci (2013), Sanchez (2014), Esposito et al. (2016), Gautam (2016), Na et al. (2016), and Sanchez et al. (2016). The average trend in the variation of compressive strength with ASR expansion is represented by the dashed line. Figure 2-34 also shows the lower bounds of normalized residual compressive strength defined in the ISE (1992).

As shown in Figure 2-34, *the maximum average reduction in compressive strength of concrete is relatively insignificant due to ASR (about 15% at 0.35% expansion). The compressive strength tends to increase initially until the expansion reaches about 0.15%. The continued cement hydration or the transformation of ASR gel in the cracks into a more calcium-rich gel*

resembling the C-S-H gel compensate for the compressive strength loss due to ASR (Multon et al. 2005, Na et al. 2016, Gautam 2016, and Hayes 2020).

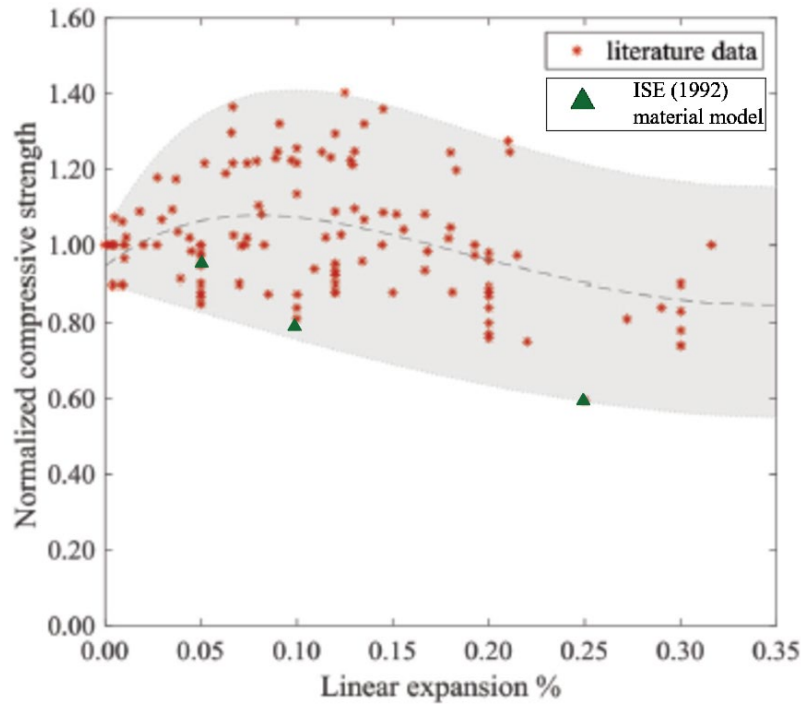


Figure 2-34. Variation of normalized concrete compressive strength with % expansion due to ASR (Abd-Elssamad et al. 2020 and ISE 1992)

A large volume of published literature describes the impact of ASR on the compressive strength of concrete. Each study had its own criteria in selecting a concrete mix for the control specimens. Swamy and Asali (1988), Fan and Hanson (1998), Ahmad et al. (2003), Smaoui et al. (2004a and 2004b), Multon et al. (2005), Giaccio et al. (2008), Sargolzhahi et al. (2010), Gianni and Folliard (2012), Sanchez (2014), and Gautam (2016) used the same composition in all the specimens, but they used nonreactive aggregates in the controls. Hafci (2013), Esposito et al. (2016), Hayes (2020), and Kongshaug et al. (2020) used the same composition in all the specimens, including the controls, but they used different curing conditions to control expansion; the control specimens were kept under room conditions, while the reactive specimens were subjected to high temperature and relative humidity to promote ASR. Since the type of coarse aggregate and curing conditions influence concrete strength differently, the prudent approach is to correlate data from specimens with reactive and nonreactive aggregates, cured under an elevated temperature and at room temperature, before using the strengths for normalizing the strength of ASR-affected specimens. Esposito et al. (2016) suggest using reference values at 0.05% expansion, as the value

used to discriminate between nonreactive and potentially reactive concrete. The data presented in Figure 2-34 can be considered as the general trend since the composition and curing conditions of the specimens used by Abd-Elssamad et al. (2020), for the 28-day compressive strength, is unclear. Nevertheless, *the lower-bound residual strengths recommended in ISE (1992) provide conservative estimates for assessment purposes.*

Esposito et al. (2016) used data from 12 experimental studies, including their own, to develop the variation of normalized mechanical properties of concrete with expansion due to ASR. The normalized data were fitted to a continuous piecewise linear curve and an S-shaped curve to develop two empirical models: Eq. 11 and Eq. 12. These equations represent the variation of a normalized material property (P/P_{ref}) as a function of ASR-induced expansion (ϵ).

Continuous piecewise linear function:

$$\frac{P}{P_{ref}} = \begin{cases} q_1 + m_1\epsilon & \epsilon \leq 0.05\% \\ q_m + m_m\epsilon & 0.05\% < \epsilon \leq 0.10\% \\ q_h + m_h\epsilon & 0.10\% < \epsilon \leq 0.50\% \\ q_e + m_e\epsilon & \epsilon > 0.50\% \end{cases} \quad (\text{Eq. 11})$$

where,

P = concrete property of interest

P_{ref} = 28-day undamaged concrete property

q_m = $q_l + (m_l - m_m) \times 0.05$

q_h = $q_m + (m_m - m_h) \times 0.10$

q_e = $q_h + (m_h - m_e) \times 0.50$

Please refer to Table 2-4 for q_l , m_l , m_m , m_h , and m_e .

S-shaped curve:

$$\frac{P}{P_{ref}} = \beta_0 - (\beta_0 - \beta_\infty) \frac{1 - \exp\left(-\frac{\epsilon}{\epsilon_c}\right)}{1 + \exp\left(-\frac{\epsilon - \epsilon_l}{\epsilon_c}\right)} \quad (\text{Eq. 12})$$

where,

β_0 = normalized concrete property at zero expansion

β_∞ = normalized concrete property at asymptotic expansion

ϵ_l = latency expansion (i.e., expansion at which the material property starts degrading)

ϵ_c = characteristic expansion

Please refer to Table 2-4 for β_0 , β_∞ , ϵ_l , and ϵ_c .

Table 2-4. Fitting Coefficients and Standard Deviations (Esposito et al. 2016)

Data	Piecewise linear curve						S-shaped curve				
	q_1	m_1	m_m	m_h	m_e	σ (%)	ϵ_c (%)	ϵ_1 (%)	β_0	β_∞	σ (%)
E	1.07	-1.06	-1.78	-0.98	-0.23	7	0.37	1.13×10^{-9}	1.06	0.19	7
E_{st}	1.04	-0.46	-1.89	-1.08	-0.21	9	0.42	2.27×10^{-14}	1.05	0.11	9
E_{dyn}	1.08	-1.43	-1.75	-0.91	-0.26	6	0.31	6.89×10^{-12}	1.07	0.29	6
f_c	0.89	2.36	2.06	-0.37	-0.18	13	0.07	1.13	1.00	0.64	15
f_t	1.01	-0.15	0.20	-0.83	-0.08	15	5.24×10^{-04}	0.51	1.00	0.59	15
$f_{t,sp}$	1.01	-0.25	-0.15	-0.86	-0.04	8	0.11	0.35	1.01	0.60	8
MOR	1.06	0.53	0.04	-1.54	-0.14	20	0.07	0.37	1.05	0.34	20
$f_{t,dir}$	0.97	2.23	-0.68	0.20	-0.18	13	0.10	2.15	1.05	0.70	12

E - Modulus of elasticity considering E_{st} and E_{dyn} together
 E_{dyn} - Dynamic modulus of elasticity
 f_t - Tensile strength of concrete
MOR - Modulus of rupture

E_{st} - Static modulus of elasticity
 f_c - Compressive strength of concrete
 $f_{t,sp}$ - Splitting tensile strength of concrete
 $f_{t,dir}$ - Direct tensile strength

As shown in the 4th row of the table, a piecewise linear curve results in the least error of 13% and is recommended for calculating the concrete strength of ASR damaged concrete.

2.7.2 Modulus of Elasticity

Figure 2-35 shows the reduction in the concrete modulus of elasticity with the expansion due to ASR. Abd-Elssamad et al. (2020) developed this envelope using static and dynamic modulus of elasticity data from 15 previous studies. The dashed line represents the average trend. The data points in the figure represent different concrete mix proportions, reactive aggregates, and curing and exposure conditions. However, it is unclear if the 28-day reference values are taken from the specimens with reactive or nonreactive aggregates. The figure also includes the lower bounds from the ISE (1992) material model. Even though the average trend shows a continuous reduction of the modulus with the expansion, the ISE (1992) recommendation is not to consider a degradation of the property for up to 0.05% expansion. *As per Esposito et al. (2016), the elasticity modulus is the most sensitive material property to ASR expansion.* This is represented by the very small values assigned for the latency expansion in the S-shaped material property degradation curve defined in Eq. 12 and Table 2-4. *As shown in Table 2-4, both piecewise linear and S-shaped curves are suitable to represent the modulus of elasticity of ASR-damaged concrete.*

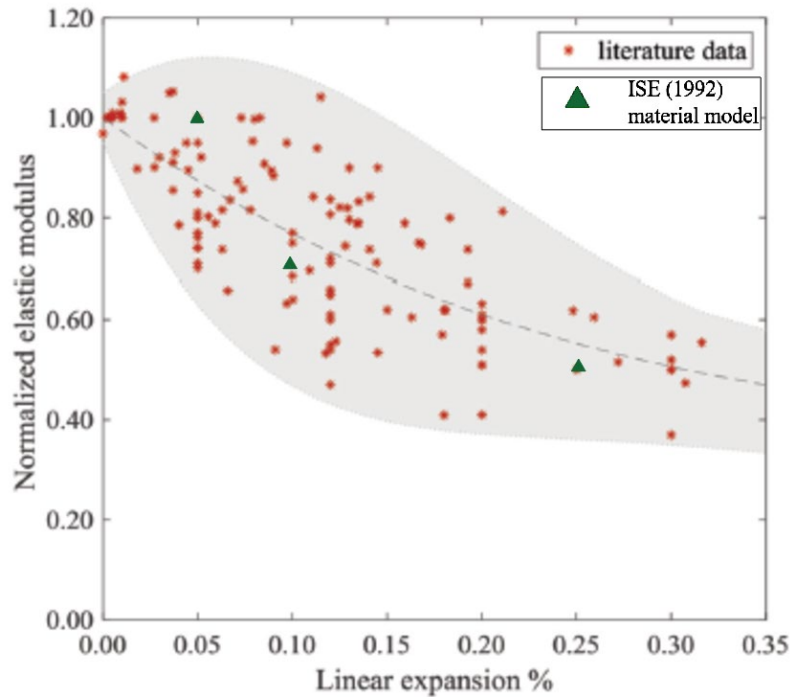


Figure 2-35. Variation of normalized concrete elasticity modulus with ASR expansion (Abd-Elssamad et al. 2020 and ISE 1992)

A large volume of published literature describes the impact of ASR on the concrete elasticity modulus. Figure 2-36 compares the variation of the residual concrete modulus of elasticity with concrete expansion due to ASR using the empirical models proposed by ISE (1992), Esposito et al. (2016), Kawabata et al. (2017), Martin et al. (2017) and Nguyen et al. (2019). The ISE (1992) and Kawabata et al. (2017) models show a drastic reduction of the elasticity modulus at and beyond 0.1% expansion, with about 70% reduction at 1.0% expansion.

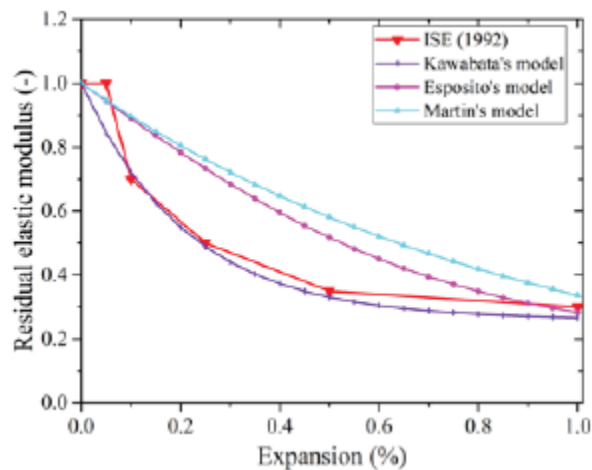


Figure 2-36. Residual elasticity modulus variation with concrete expansion due to ASR (Nguyen et al. 2019)

2.7.3 Tensile Strength

Splitting tensile strength (indirect tensile strength), direct tensile strength, and modulus of rupture (MOR) are the indicators of concrete tensile strength. Figure 2-37 shows the reduction in the concrete splitting tensile strength with the ASR expansion (Sanchez 2014). The graph used data from 20 concrete mixes with different reactive aggregates. The tensile strength reduction is the ratio of the value obtained at a selected expansion level against the value obtained on sound concrete specimens at the same maturity. The ISE (1992) model presents conservative values.

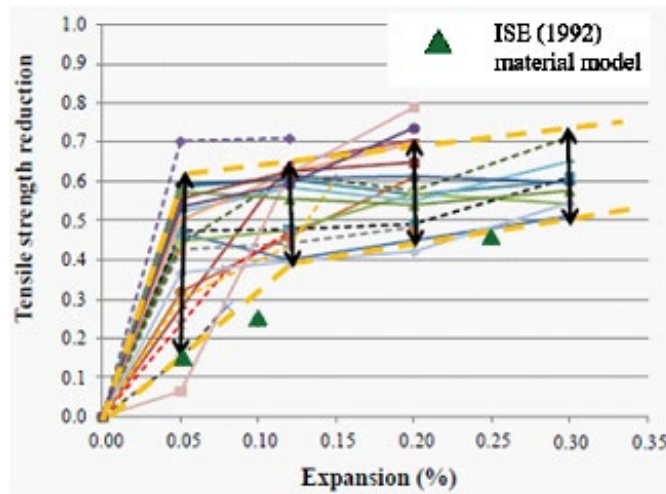
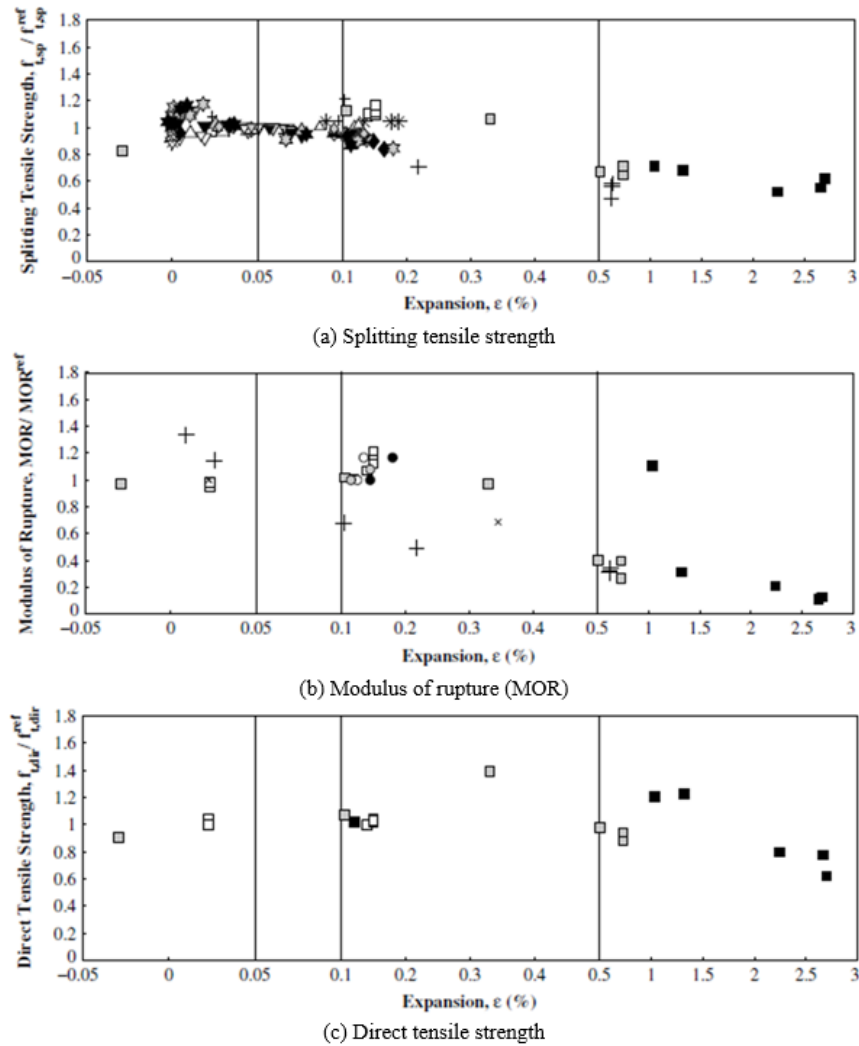


Figure 2-37. Reduction in normalized splitting tensile strength due to ASR (Sanchez 2014 and ISE 1992)

Esposito et al. (2016) developed the variation of normalized tensile strength of concrete with ASR expansion. The normalized tensile strength was calculated in terms of splitting tensile strength (see Figure 2-38a), MOR (see Figure 2-38b), and direct tensile strength (see Figure 2-38c). The tensile strength at a 0.05% expansion was used as the reference. This 0.05% is the expansion threshold specified by RILEM AAR-0 to identify reactive concrete mixes (Sims and Nixon 2003). According to Figure 2-38, all three strengths show a negligible reduction in strength for expansion levels less than 0.1%. When the expansion levels exceed 0.5%, the reduction in the splitting tensile strength, MOR, and direct tensile strength is about 40, 70, and 10%, respectively. As shown in Table 2-4, tensile strength is less sensitive to concrete expansion. This is evident from the larger values listed in Table 2-4 for the latency expansion when compared to the modulus of elasticity. As shown in Table 2-4, both piecewise linear and S-shaped curves are suitable to represent the tensile strengths and MOR of ASR-damaged concrete. However, except for the splitting tensile strength, the error percentage of the calculated values using Eq. 11 and Eq. 12 can be as high as 13% to 20%.



Note: A nonuniform scale is used to represent the percent expansion

Figure 2-38. Variation of normalized splitting tensile strength, modulus of rupture (MOR), and direct tensile strength with ASR expansion (Esposito et al. 2016)

2.7.4 Ultrasonic Pulse Velocity (UPV)

Since UPV is used to calculate the dynamic modulus of elasticity, the variation of UPV with concrete expansion is expected to emulate the trends shown in Figure 2-35 and Figure 2-36. According to Swamy and Al-Asali (1988), Ahmed et al. (2003), and Gautam (2016), a significant reduction in UPV was observed in concrete specimens with ASR at early stages of the reaction, even before any visible cracks appeared or an expansion was noted. However, several other studies contradict the findings and concludes that the UPV is less sensitive in detecting ASR-related damages in concrete, except at greater expansion levels (Rivard and Saint-Pierre 2009, Sargolzahi et al. 2010). Rivard and Saint-Pierre (2009) evaluated UPV on laboratory specimens with reactive

aggregates and on field cores extracted from ASR-affected structures using compression (P) and shear (S) waves. Both laboratory and field data showed less sensitivity of S-waves compared to P-waves in detecting material degradation due to ASR.

2.7.5 Impact of Concrete Deterioration (Other than ASR) on Mechanical Properties

Harries (2006) evaluated compressive strength of three corrosion damaged PSC box-beams (one interior beam and two exterior beams) using a Schmidt hammer and cores extracted from the beams. In 2005, one of the exterior beams infamously collapsed from the Lakeview bridge in Pennsylvania. The in-situ compressive strength of concrete evaluated with the Schmidt hammer test, around the fractured area of the failed beam, was 16% more than its 28-day design compressive strength. The average compressive strength of the other two beams (interior and exterior beams), evaluated with the Schmidt hammer, exceeded their 28-day design compressive strength by 31% and 21%, respectively. The average compressive strength of extracted cores from all three beams exceeded the 28-day design compressive strength by 24%. Alfailakawi et al. (2020) extracted cores from three corrosion damaged PSC I- and three box-beams that were scheduled for demolition. The compressive strength of PSC I- and box-beams was 45% and 40% more than their design strengths. Attanayake and Aktan (2011) evaluated the compressive strength of a 50-year-old distressed double-cell box-beam that was removed from an in-service bridge. The beam had two full-length longitudinal cracks at the bottom flange with heavy leaching. The compressive strength was 58% more than its design strength.

2.7.6 Effective Section Properties

Stiffness reduction in ASR-damaged concrete requires the use of a transformed section. While the ASR damage is observed at the bottom flange and not considered for cracked section properties for most cases, the evaluation of service limit states and stress redistribution due to damages require transformed section calculation. Besides material degradation, section properties are altered mainly due to spalling. Since a majority of the spalls are localized at the bottom flange, the location of the neutral axis of the damaged beam section shifts up towards the beam top flange. Accordingly, the cross-section area, moments of inertia, depth to the neutral axis, and the section moduli need to be revised for load rating.

An interactive tool was developed by Tabatabai and Nabizadeh (2019) to calculate the flexural strength of damaged, undamaged, and repaired sections of PSC I-beams. The bottom flange damage due to impact loads and the top flange damage due to deck removal were considered. A discretized beam cross-section was defined in an Excel spreadsheet with each cell representing a 0.5×0.5 in. block making up the beam cross-section. Each cell included properties of the respective material (i.e. beam concrete, deck concrete, prestressing strands, etc.) The loss of concrete due to spalls was modelled by eliminating the cross-sectional elements at the damaged area. Figure 2-39 shows the modeling of a WI Type 72W beam with three levels of damages. Each cell defines a strain assuming a linear strain behavior. The stress in each cell is calculated using the stress-strain relation of the corresponding material. This stress was multiplied by the cell area to determine the force in each cell. The Prestressed Bridge Assessment, Repair, and Strengthening (PreBARS) program calculates the neutral axis of the section using an iterative procedure by balancing the compression and tension forces in the section.

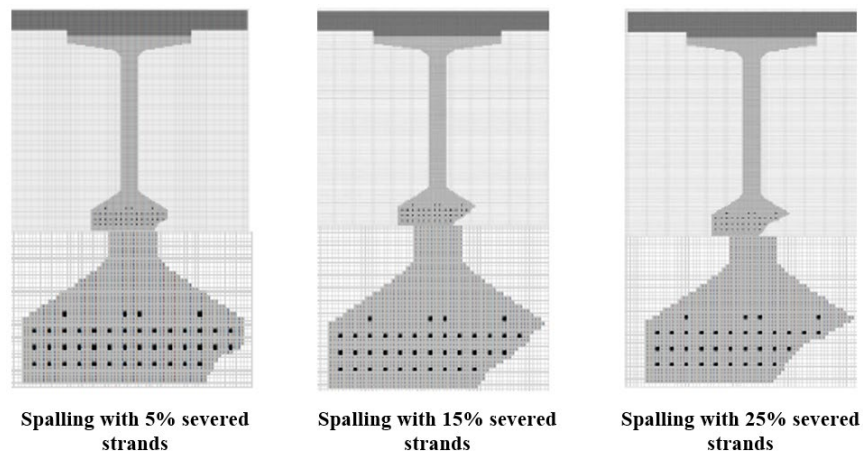


Figure 2-39. Modeling of beams with spalled concrete and severed strands (Tabatabai and Nabizadeh 2019)




In a composite prestressed concrete beam-slab system, the dead loads (such as the weight of beam, haunch, and slab) and the prestress loads are resisted by the noncomposite section. Any damage to a composite prestressed beam would redistribute the stresses developed under noncomposite dead loads and prestress into both the beam and the slab. The procedure presented in Tabatabai and Nabizadeh (2019) was implemented in the load rating calculation sheets included in this report. This procedure requires calculating composite, transformed section properties of a damaged section.

2.8 PRESTRESSING STRANDS

2.8.1 Material Properties

Naito et al. (2011) examined seven beams salvaged from three decommissioned adjacent box-beam bridges in Pennsylvania. Cracks, delamination, spalls, and strand condition were recorded by inspecting the beams at “arm’s length”. The strand condition at the bottom layer (first level) and the second layer were recorded and classified as no corrosion, light corrosion, pitting, heavy pitting, wire loss, or wire fracture. Table 2-5 shows the relative strength of the strands for three levels of corrosion (light corrosion, pitting, heavy pitting). Compared to light corrosion, pitting and heavy pitting reduced strand tensile strength by 20.1% to 28.6%, respectively.

Table 2-5. Strength of Corroded Strands (Naito et al. 2011)

Strand condition	Condition	Relative strength	Comment(s)
Light corrosion		100%	None
Pitting		79.9%	Pitting corresponds to a section loss < 20%
Heavy pitting		71.4%	Heavy pitting corresponds to a section loss > 20%

Naito et al. (2011) evaluated the condition and strength of strands located adjacent to or above the longitudinal crack(s) observed in PSC box-beams. The results are presented in Table 2-6. As shown in the table, the strands located above a longitudinal crack had the highest reduction in tensile strength.

Table 2-6. The Impact of Cracks on Strand Condition and Strength (Naito et al. 2011)

Strand and crack location	Corrosion or damage probability (%)						Average strength
	No corrosion	Light corrosion	Pitting	Heavy pitting	Wire loss	Wire fracture	
Strand at Level 1, above crack	29.6	8.7	17.4	34.8	7.8	1.7	77.5%
Strand at Level 1, adjacent to crack	69.5	6.3	8.4	11.6	4.2	0.0	91.0%
Strand at Level 2, above crack	53.1	9.4	6.3	12.5	9.4	9.4	77.0%
Strand at Level 1, no crack	89.7	3.8	2.4	3.4	0.6	0.2	97.8%
Strand at Level 2, no crack	85.5	9.1	1.8	1.8	1.8	0.0	97.4%

Frosch et al. (2020b) evaluated the condition of prestressing strands in distressed box-beams of a few Indiana bridges. The corroded strands had an adequate capacity but not an appreciable level of ductility. Frosch et al. (2020b) recommended the following:

- Limit corroded strand strain to 0.01 due to lack of ductility.
- For strands with surface corrosion and minor pitting, use 75% of the strand strength (f_{pu}) and limit the strain to $0.75f_{pu}/E_{ps}$, where E_{ps} is the strand elasticity modulus.
- Disregard strands with severe corrosion or fractured wires.

Considering the practical difficulties to assess the degree of corrosion, the typical practice is to disregard the corroded strands during the capacity evaluation. The additional guidelines for deciding the number of damaged strands are discussed in Section 2.8.2.

2.8.2 Number of Effective Prestressing Strands

The capacity of a deteriorated beam is calculated after eliminating damaged or heavily corroded prestressing strands. Tabatabai and Nabizadeh (2019) presented a calculation process to account for the stress redistribution due to beam damage. Typically, the condition of the strands at the bottom layer is easier to document. Harries (2006) and Frosch et al. (2020b) documented corrosion in the strands adjacent to the corroded and exposed strands. A saw cut inspection performed by Harries (2006) documented 6 severely corroded strands, 2 broken strands, and several strands with mild corrosion (Figure 2-40). Out of the 6 severely corroded strands, 4 were exposed due to concrete spalling, while 2 strands located at the 2nd row were concealed. This example shows the challenges of assessing prestressing strand condition in PSC beams. The challenges are highlighted by Attanayake and Aktan (2011), who showed the condition of strands located at and near the longitudinal cracking in PSC box-beams. Unlike at the spalls, the damages to prestressing strands at or near longitudinal cracks are unpredictable.

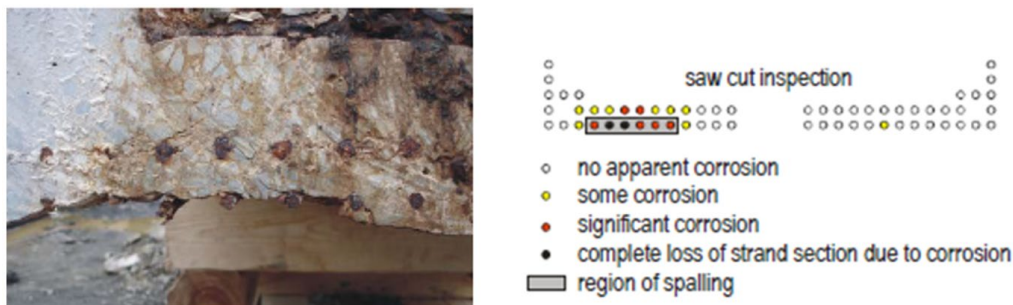


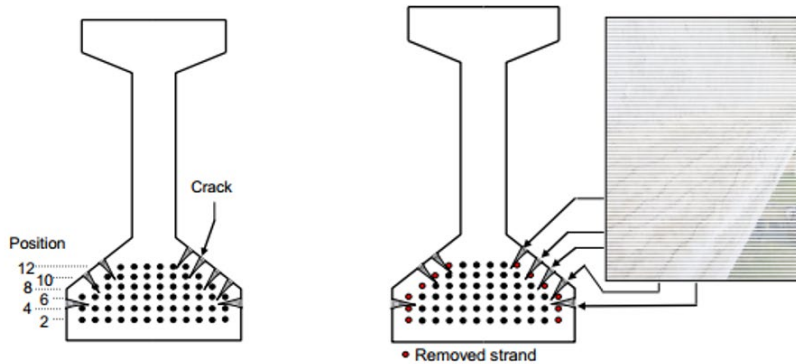
Figure 2-40. Saw cut surface of a box-beam showing strand conditions (Harries 2006)

IDOT (2004), PennDOT (2010), and UDOT (2017) have guidelines for estimating the number of effective strands in deteriorated PSC beams. IDOT's (2004) procedure for the evaluation of damaged PSC deck beams is in their standard document titled "*Guidelines for Estimating Strand Loss in Precast Prestressed Concrete (PPC) Deck Beam Bridges (February 2004)*". The conditions considered are longitudinal cracks; exposed reinforcement (prestressing strands, wire mesh, stirrups, and bars); and delaminated, wet, or stained areas. Additionally, the presence of corrosion or unsound areas adjacent to these distresses is considered. In response to a survey administered by the PennDOT (Harries and Miller 2012), IDOT described their practice as, "If strands are intact, determine section modulus change due to concrete loss. If strands are damaged, run in-house developed spreadsheets to determine capacity loss due to loss of prestress." PennDOT's (2010) procedure for the evaluation of distressed adjacent noncomposite PSC box-beams is described in their standard document titled "*Publication 238 Part 1E, Chapter 3 – Inspection*". This procedure considers the distress type, location, and intensity. The UDOT Bridge Management Manual (2017) outlines procedures for eliminating strands in PSC I- and box-beams to account for the prestressed strands subjected to corrosion in exposed beam sections. Refer to Appendix A for more details.

The work by Harries (2006), Harries et al. (2009, 2012a, 2012b), and Naito et al. (2010) contributed to the development of PennDOT guidelines. Alfaiakawi et al. (2020) evaluated the recommendations of Naito et al. (2010) for a project sponsored by VDOT that load tested 6 corrosion damaged PSC beams to failure. Three AASHTO Type II and three 27 × 48 in. box-beams were included in the study. In addition to following Naito et al.'s (2010) recommendations, a modified approach was used to predict the residual flexural capacity of the corrosion damaged PSC I-beams. The modified approach is listed in Appendix A. After comparing the load test results with the two capacity calculation methods, Alfaiakawi et al. (2020) recommended the procedures in Naito et al. (2010) to the VDOT's Structure and Bridge Division for load rating of corrosion damaged PSC box- and I-beams.

Williams and Choudhuri (2010) proposed a methodology to assess the capacity of PSC I-beams due to ASR. The methodology focused mainly on the potential loss of prestressing steel due to strand deterioration and the loss of strand to concrete bond at locations of major horizontal cracking in the beam bottom flange. Figure 2-41a shows the details of a severely deteriorated PSC I-beam. As shown in Figure 2-41a, the beam exhibited crack widths up to 3/8 in. and crack lengths

along the entire span of fascia beams. Figure 2-41b shows the strands neglected during the capacity evaluation. The strands closer to the surface and adjacent to the cracks were disregarded.



(a) Bottom flange longitudinal cracking (b) Strands removed from capacity calculation

Figure 2-41. Deteriorated strands in an I-beam (Williams and Choudhuri 2010)

2.8.3 Redevelopment of Severed Prestressing Strands

The typical practice is to completely disregard the contribution of a severed strand(s) when assessing the capacity of a PSC beam. However, more rational procedures are available to determine the effectiveness of strands (UDOT 2017). When a crack parallel to a bonded strand exists at a beam end and the concrete is in sound condition, the effectiveness of the strand is considered beyond the crack. When a crack parallel to a bonded strand exists within the span, the effectiveness of the strand is not considered for a length equal to the crack length because of the unknown condition of the strand. Figure 2-42 shows the redevelopment of a severed strand in a region away from the distress region. In the figure, f_{pe} is the effective stress after losses, f_{ps} is the stress when the section reaches its nominal capacity, l_{tr} is the transfer length, and l_d is the development length (AASHTO 2017). The development length of a bonded strand is calculated using Eq. 13:

$$l_d \geq \kappa (f_{ps} - 0.66 f_{pe}) d_b \quad \text{Eq. 13}$$

where, κ = 1.0 for pretensioned members with a depth less than or equal to 24 in.

= 1.6 for pretensioned members with a depth greater than 24 in.

d_b = nominal strand diameter

f_{pe} = effective stress in the prestressing steel after losses

f_{ps} = average stress in prestressing steel at the time for which the nominal resistance of the member is required

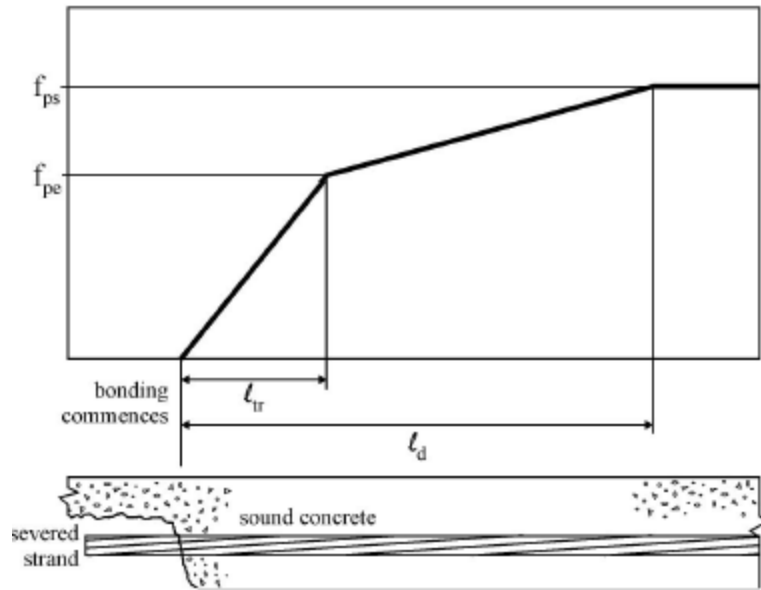


Figure 2-42. Concept of the redevelopment of a severed strand (Kasan and Harries 2011)

Kasan and Harries (2011) evaluated the strand redevelopment by monitoring the prestressing strand strain in a decommissioned box-beam. Strands were intentionally cut at specific distances, and the strain was measured on the same strands at a distance away from the severed locations. Kasan and Harries (2011) concluded that the AASHTO (2017) specified value of $60d_b$ for the transfer length is conservative since the effective prestress was developed in the severed strands at a distance greater than $35d_b$. However, the development length was not evaluated.

2.9 DISTRESS QUANTIFICATION

Even though the testing of cores provides the most accurate information to quantify material properties, coring of PSC beams is not allowed. The data presented in Figure 2-34 through Figure 2-38 can be used to estimate mechanical properties when the percent expansion of an ASR affected component is known. Because of the practical challenges of measuring concrete expansion of in-service structural components for years under the field conditions, the literature documents several attempts to correlate the characteristics of cracks to concrete expansion, the depth of degradation, and material properties. Crack density, damage rating index (DRI), and crack index (using crack mapping) are used to assess concrete damage due to ASR and AAR (Godart et al. 1992, Smaoui et al. 2004a and 2004b, Sanchez 2014, Sanchez et al. 2017, Sagradyan and Ogura 2021).

2.9.1 Crack Density

The crack density is defined as the total area of cracks [i.e. $\Sigma(\text{crack width} \times \text{length})$] per unit surface area. Even though Sanchez (2014) developed a graph showing the variation of crack density vs. concrete expansion, such information has very little practical significance since the crack density was documented over specimen cross-sections rather than the surface of field specimens. Sagradyan and Ogura (2021) evaluated the cracking of PSC cube specimens, but the data is not useful for the assessment of PSC beams.



2.9.2 Damage Rating Index (DRI)

The DRI is calculated by taking the summation of the products of distress characteristics per unit area and their corresponding weighing factors. Shrimmer (2015) presents a DRI developed by considering distress characteristics such as reaction rims, cracks in aggregate, cracks in aggregate-containing ASR gel, air voids containing ASR gel, cracks in paste, cracks in paste containing ASR gel, debonded aggregate, and corroded aggregate. Table 2-7 shows the DRI-based classification system developed by Shrimmer (2015) to determine the degree of ASR in concrete. Later, Shrimmer (2019) used cores from four in-service structures to assess their condition; the structures comprised a dam in the Pacific Northwest of USA; a dam in the Eastern U.S.; a river wall in Ontario, Canada; and a highway bridge in the Pacific Northwest of the U.S. Table 2-8 presents the correlated DRIs to the surface condition recorded from the dam in the Pacific Northwest and the river wall in Ontario. As shown in Table 2-8, the exposed surfaces exhibited comparatively higher damages.

Table 2-7. DRI-Based Classification System for ASR Damaged Structures (Shrimmer 2015)

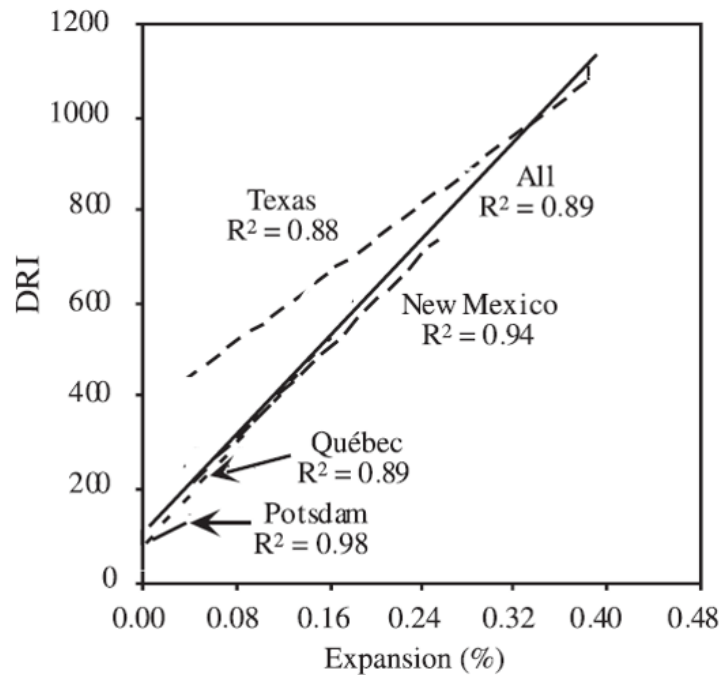
DRI	Degree of ASR
0 - 40	Negligible
40 – 125	Minor
125 – 300	Moderate
300 – 500	Significant
500 – 600	Serious
> 650	Very serious

Table 2-8. Correlation of Field Observations to DRI (Shrimer 2019)

Structure	Core location	Field observation	DRI	Degree of ASR
<p>Dam, Pacific Northwest, USA</p>  <p>Radial gate wall showing a well-developed crack pattern, efflorescence, and discoloration along cracks</p>	Gravity section	Moderate to significant damage, frequent map cracking/staining	387	Significant
	Spillway wall, inside face, mid-height	Moderate to serious, map cracking ranges from minor to frequent	184	Moderate
	Spillway wall, outside face	Minor to serious, map cracking ranges from none to frequent and open	238	Moderate
	Spillway wall, inside face, upper	Moderate to serious, map cracking and staining common	185	Moderate
	Spillway wall, inside face, upper	Serious cracking common	321	Significant
	Forebay wall, top	Minor to moderate, occasional cracks	246	Moderate
<p>River wall, Ontario, Canada</p>  <p>A section of the riverside face of the wall</p>	River-face exposed wall, upper	Significant damage, frequent map cracking/staining and efflorescence	425	Significant
	River-face exposed wall, mid-level	Significant damage, map cracking ranging from moderate to frequent	401	Significant
	Exposed wall, lee side of river	Moderate map cracking, staining and efflorescence	288	Moderate
	Buried wall, 3.25 ft below grade	Very minimal cracks, overall good condition	42	Minor

Studies have developed relationships between the crack density and damage rating index (DRI) to the ASR expansion (Rivard et al. 2002, Smaoui et al. 2004a and 2004b, Bérubé et al. 2005, Thomas et al. 2013b and 2013c, Sanchez 2014, Sanchez et al. 2015 and 2017, Gautam et al. 2017, Martin et al. 2017, Shrimer 2019). Smaoui et al. (2004a and 2004b) developed correlations between DRI and ASR expansion using concrete cylinders fabricated with four different reactive aggregates (Texas sand, New Mexico gravel, Québec City limestone, and Potsdam sandstone). They exposed the aggregates to high temperature and humidity conditions. The DRI was evaluated at 5 expansion levels for Texas sand and New Mexico gravel, 6 expansion levels for Québec City limestone, and 3 expansion levels for Potsdam sandstone. The specimens were split in half along

the longitudinal axis and a single 4 in. by 8 in. section was used to calculate the DRIs. Figure 2-43 shows the relationship between the DRI and ASR expansion for each aggregate type and when all four aggregate types combined. At an expansion of 0.08%, Québec City limestone and New Mexico gravel resulted in a DRI of around 300, whereas Texas sand corresponds to a DRI of about 520. Therefore, a single correlation between DRI and ASR expansion would produce a considerable error based on the type of reactive aggregate. Bérubé et al. (2005) used concrete cores to evaluate the validity of the correlations obtained in Figure 2-43 for Québec City limestone. The concrete cores were extracted from ASR affected in-service concrete elements (foundations, columns, beams, pile cap, and an abutment wall). The DRI from the cores were more than 550 and greater than that recorded from the test specimens. This may be due to the difference in the petrographic features contributing to the DRI for laboratory and field concrete. The higher DRI values resulted in greater expansion rates from the data presented in Figure 2-43. However, the expansion rates seem unrealistic when compared to the observed damages of the in-service elements.



Québec City limestone	:	$\text{DRI} = 62.9 + 2738 \times \text{expansion} (R^2 = 0.89)$
New Mexico gravel	:	$\text{DRI} = 101.7 + 2479 \times \text{expansion} (R^2 = 0.94)$
Texas sand	:	Not given
Potsdam sandstone	:	$\text{DRI} = 68.8 + 1297 \times \text{expansion} (R^2 = 0.98)$

Figure 2-43. DRI vs. ASR expansion for concrete cylinders (Smaoui et al. 2004a and 2004b)

Sanchez et al. (2017) conducted a laboratory study using concrete specimens prepared with several reactive aggregate types to develop a DRI-based classification system to evaluate the significance of ASR damage at various expansion levels. Also, the impact of expansion on the mechanical properties was evaluated. All the specimens were allowed free expansion. The results are summarized in Table 2-9. They indicate the sensitivity of tensile strength and elasticity modulus to the damage due to ASR. Even though the results are valuable, the findings cannot be used for practical applications since the members of in-service structures are subjected to various degrees of constraint and other deterioration mechanisms. Sanchez et al. (2017) proved the challenges of using laboratory data for field applications by evaluating the condition of the 50-year-old Robert-bourassa/charest overpass in Quebec, Canada.

Table 2-9. Damage Classification of ASR Affected Concrete (Sanchez et al. 2017)

DRI	ASR damage classification	Expansion (%)¹	Reduction in elasticity modulus (%)	Reduction in compressive strength (%)	Reduction in tensile strength (%)
100-155	Negligible	0.00 to 0.03	-	-	-
210-400	Marginal	0.04 ± 0.01	5 to 37	-10 to 15	15 to 60
330-500	Moderate	0.11 ± 0.01	20 to 50	0 to 20	40 to 65
500-765	High	0.20 ± 0.01	35 to 60	13 to 25	45 to 80
600-925	Very high	0.30 ± 0.01	40 to 67	20 to 35	-

¹ - These expansion levels should not be considered as strict limits between the various classes of damage degree but more as indicators/reference levels for which comparative analysis of petrographic and mechanical data was carried out allowing to highlight significant damage levels in concrete due to the progress of ASR.

2.9.3 Crack Index

Both crack density and DRI use internal damages documented at a petrographic level. The crack index, on the other hand, measures the surface crack widths over time to quantify the rate of ASR expansion (Wehrle et al. 2010, Buford 2013). This technique is sometimes referred to as crack mapping. The crack index is the summation of crack widths per unit length, typically expressed per foot or meter. The crack index can be presented along predefined coordinate axes or for a zone by taking the average of the crack indices along the axes (Godart et al. 1992). Table 2-10 shows a classification of the extent of damage proposed by Godart et al. (1992) based on the cracking index. This classification provides a qualitative indication of the extent of damage, not the degree of true damage in a structure (Godart et al. 1992).

Table 2-10. Cracking Index Based Damage Classification (Godart et al. 1992)

Cracking index (in/ft)	Extent of damage
0 to 0.006	Negligible
0.006 to 0.012	Low
0.012 to 0.024	Moderate
0.024 to 0.060	High
0.060 to 0.120	Very high
> 0.120	Considerable

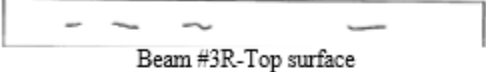
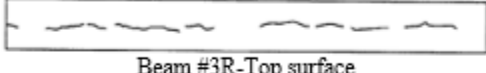
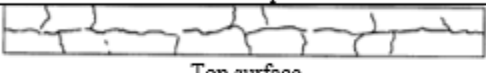
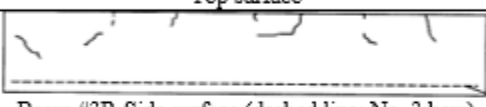
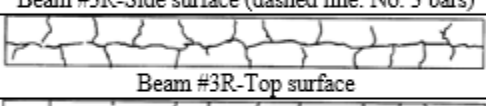
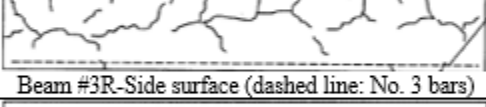
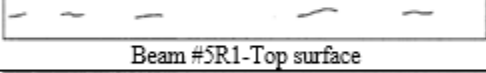
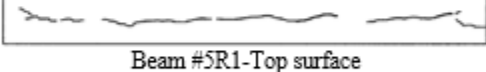
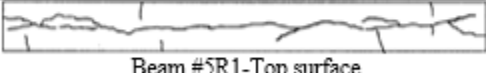

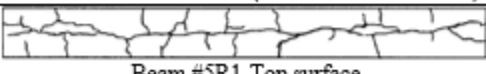
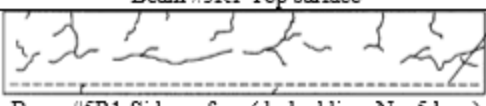
Bérubé et al. (2005) found more damages over the surfaces exposed to outdoor conditions. The crack index cannot be universally applied to all the structures to assess the ASR damage since the crack patterns are dependent on the component size, location, exposure conditions, reinforcement details, and the internal and external constraints (Smaoui et al. 2004a and 2004b, Bérubé et al. 2005, and Buford 2013). Further, several other mechanisms (such as drying shrinkage, freezing and thawing, etc.) contribute to near surface damages making the cracking index less reliable to evaluate the interior conditions.

2.9.4 Depth of Degradation

To assess the capacity of PSC beams, the depth of degradation from the exposed surfaces needs to be evaluated. Since the degradation of material properties is related to the level of expansion, the possibility of using distress features observed on the surface of a distressed structure, preferably the cracks, to predict the level of expansion needs to be evaluated. Fan and Hanson (1998) evaluated the development of surface cracking on 6 × 10 × 60 in. reinforced concrete beams immersed in a 0.5 N NaOH solution and subjected to heating and cooling cycles between 100° F and room temperature. Table 2-11 shows the development of cracks on the top and side surfaces of the beams against the duration of exposure to the NaOH solution. The #3R and #5R1 labels in the table represent the beams with two #3 bars and two #5 bars, respectively. The table also presents the longitudinal expansion at the top surface, transverse expansion, and the longitudinal expansion at the reinforcement level. The longitudinal expansion at the reinforcement level is always lower than the longitudinal expansion at the beam top, which is an indication of the impact of restraints. The top surface cracking initiated at about 0.080% expansion at the beam top. With the increase in expansion, the cracks further developed and connected to form the pattern cracks. The dominant cracks are oriented in the direction of reinforcement. Even though the beam with smaller reinforcement had more cracking at the end of the 8-month exposure, both beams

developed similar crack patterns at the end of the 12-month exposure. Another important observation is the development of significant expansion due to ASR within 12 months of 100° F of exposure. However, this study did not correlate crack width to the crack depth to evaluate the depth of degradation.

Table 2-11. Propagation of Cracks with Expansion (Fan and Hanson 1998)

Duration of exposure to alkali solution (months)	Observed crack patterns	Max. crack width (in.)	Longitudinal expansion at top (%)	Transverse expansion (%)	Longitudinal expansion at rebar (%)
6	 Beam #3R-Top surface	Hairline cracks	0.0800	0.0489	0.0444
7	 Beam #3R-Top surface	0.004	0.0956	0.0667	0.0556
8	 Top surface	0.008	0.1067	0.0800	0.0644
8	 Beam #3R-Side surface (dashed line: No. 3 bars)	Hairline cracks	0.1067	0.0800	0.0644
12	 Beam #3R-Top surface	0.022	0.1444	0.1111	0.0844
12	 Beam #3R-Side surface (dashed line: No. 3 bars)	0.006	0.1444	0.1111	0.0844
6	 Beam #5R1-Top surface	Hairline cracks	0.0933	0.0622	0.0511
7	 Beam #5R1-Top surface	0.006	0.1200	0.0800	0.0622
8	 Beam #5R1-Top surface	0.010	0.1289	0.0911	0.0711
8	 Beam #5R1-Side surface (dashed line: No. 5 bars)	Hairline cracks	0.1289	0.0911	0.0711
12	 Beam #5R1-Top surface	0.024	0.1644	0.1133	0.0733
12	 Beam #5R1-Side surface (dashed line: No. 5 bars)	0.006	0.1644	0.1133	0.0733

Bérubé et al. (2005) estimated concrete expansion in three bridges: the Du-Vallon bridge, the Père-Lelièvre bridge, and the St-David bridge. The expansion was estimated by measuring surface crack widths on a set of selected distressed members. The crack widths intersecting two perpendicular lines were measured. Typically, 3.25 ft long horizontal and vertical lines are used for this purpose. The expansion in one particular direction and the 3D expansion of certain components are calculated as follows:

$$\text{Percent expansion} = \frac{\sum \text{crack width intersecting the measurement line}}{\text{Length of the measurement line}} \times 100$$

Volume expansion in columns, foundations, and abutment walls






$$= (2 \times \text{horizontal expansion} + \text{vertical expansion})/3$$

Volume expansion in beams

$$= (\text{horizontal expansion} + 2 \times \text{vertical expansion})/3$$

Table 2-12 shows the level of distress observed and the estimated expansion. As shown in the table, the vertical expansion in the column and abutment wall are less than the horizontal expansion due to axial loads and constraints. The longitudinal (horizontal) expansion in the PSC beam is lower than the vertical expansion due to prestress. Therefore, the use of crack width measurements to estimate concrete expansion is not practical for the real structures. Further, these studies did not correlate surface crack width to crack depth to estimate the depth of degradation.

Table 2-12. Member Distress and the Average Expansion (Bérubé et al. 2005)

Bridge	Distressed member	Distress description	Horizontal expansion (%)	Vertical expansion (%)	Volume expansion (%)
Du-Vallon bridge	Concrete foundations (Degradation due to alkali-reactive - frost-susceptible aggregate)		0.140	0.111	0.130
Du-Vallon bridge	Columns (spalling and steel corrosion on the exposed surfaces to salt-water spray from the traffic)		0.100	0.035	0.078
Père-Lelièvre bridge	Beams (Major cracks parallel to prestressing strands)		0.020	0.058	0.045
Père-Lelièvre bridge	Beams and pile caps (Map cracking at the surface)		0.015	0.058	0.044
St-David bridge	Abutments (Map cracking, exudation of siliceous gel, signs of steel corrosion and localized spalling)		0.067	0.073	0.069

According to Fournier and Bérubé (2000), 1 to 2 in. deep surface cracks are typically observed due to AAR. Miki et al. (2013) evaluated the depth of cracks induced by ASR. Figure

2-44 shows the crack patterns at four depths from the surface: 1) at the surface, 2) 0.079 in. (2 mm), 3) 0.236 in. (6 mm), and 4) 0.394 in. (10 mm). The crack widths were documented as less than 0.0039 in. (0.1 mm), between 0.0039 and 0.0079 in. (0.1 and 0.2 mm), and larger than 0.0079 in. (0.2 mm). The cracks wider than 0.0079 in. (0.2 mm) extended at least 0.394 in. (10 mm) from the surface, whereas the cracks thinner than 0.0039 in. (0.1 mm) extended up to 0.236 in. (6 mm) from the surface.

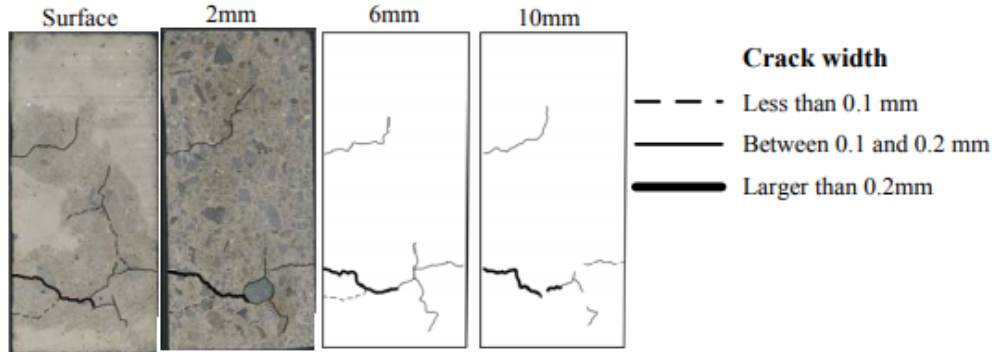
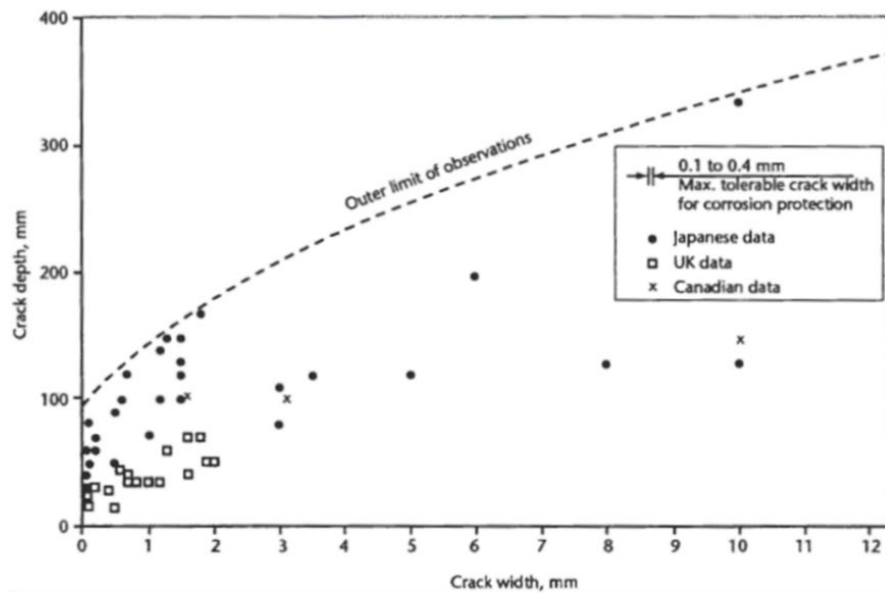


Figure 2-44. Crack patterns at different depths from the surface (Miki et al. 2013) (1 mm = 0.0394 in)

Figure 2-45 shows the crack depth vs. crack width relationship defined by the CSA International (2000) for reinforced concrete structures. The outer limit was established using the data from the Institution of Engineers (ISE 1992) and Durand (1995). A similar relationship for PSC members is not available.



Note: British and Japanese data from Institution of Structural Engineers 1992; Canadian data from Durand 1995.

Figure 2-45. Crack depth vs. width variation in reinforced concrete members (CSA 2000) (1 mm = 0.0394 in.)

2.10 CRACK DEPTH EVALUATION USING NON-DESTRUCTIVE TECHNIQUES

Ultrasonic pulse velocity (UPV) based test methods are a popular nondestructive evaluation (NDE) technique for assessing concrete quality and uniformity (ASTM 2016). Bungey et al. (2006), Pinto et al. (2010), Kalyan and Kishen (2014), and Baehaki et al. (2019) evaluated the capabilities and limitations of using UPV-based test methods to determine the depth of surface cracks in concrete. In ultrasonic testing, stress waves are generated by a transducer placed on the concrete surface. This transducer is referred to as the transmitter. The stress waves reflected from various reflectors within the concrete mass are captured by another transducer called the receiver. The ultrasonic pulse velocity (UPV) is calculated using the length of wave travel path and the travel time of the wave between transmitters and receivers (Time of Flight or TOF). Pulse velocity is typically used to assess the quality of concrete (ASTM 2016). Also, by knowing the wave velocity and the travel time, the location of certain reflectors (i.e. defects or component boundaries) is determined.

Basically, three types of stress waves are generated by a transmitter: longitudinal waves, shear waves, and surface waves. Longitudinal waves excite and displace particles parallel to the direction of wave travel path. Shear waves displace particles perpendicular to the direction of wave travel path. Surface waves displace particles in an elliptical orbit closer to the surface. Compression (P) waves are a type of longitudinal waves. Rayleigh (R) waves are a type of surface waves. Since the particle motion for a surface wave is restricted near the surface, the depth of penetration of the surface waves is smaller compared to the other two types of waves. Based on their particle motion, longitudinal waves are the first to arrive at the receiver, whereas the surface waves are the last (Bungey et al. 2006, Tesfamariam and Martín-Pérez 2010). Even though compression waves are faster, the amplitude and energy of shear waves are comparatively greater (Popovics and Abraham 2010).

When evaluating the surface crack depth using UPV methods, the transmitter(s) and receiver(s) are placed on either side of the crack. The idea is that the wave path from the transmitter to the receiver is altered due to the wave refraction occurring at the crack tip. As a result, the time of flight observed for a concrete specimen with a surface crack would be greater than that for a concrete specimen without a surface crack. Commercially produced UPV devices have been used to estimate the surface crack depth in concrete structures. These commercially available UPV devices can be categorized into two types based on their transducer configuration. The first configuration, which is the most basic, has two transducers with one acting as the transmitter and

the other acting as the receiver. The second configuration has an array of transducers in which the transducers act as transmitters and receivers in a sequential mode. The following sections describe the use of these transducer configurations to estimate the depth of surface cracks.

2.10.1 Two-Transducer Method

A typical, portable, two-transducer UPV system available in the market is shown in Figure 2-46. These transducers are designed to generate and capture longitudinal waves. An effective implementation of this system requires establishing a good contact between the specimen surface and transducers. This is accomplished by using a thin layer of coupling agent. As needed, the surface is ground to remove irregularities.

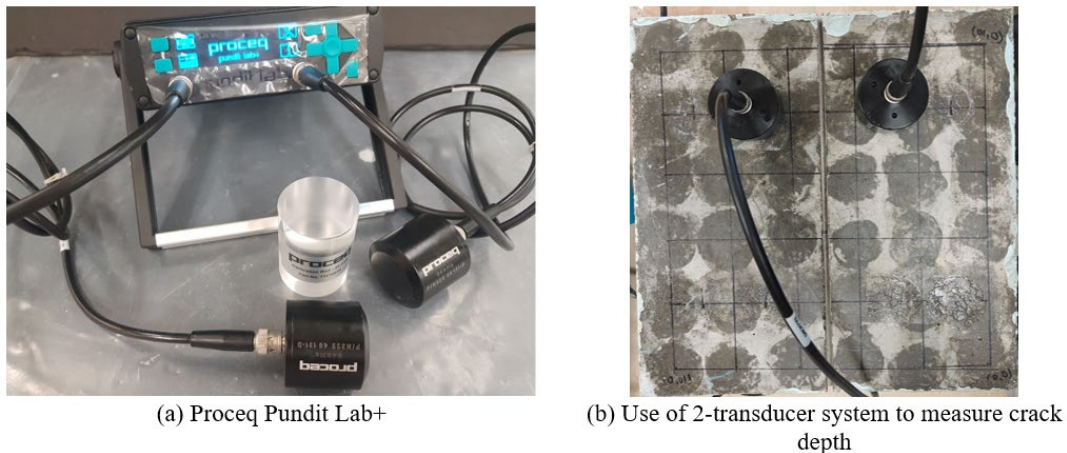


Figure 2-46. The two transducer TOF measurement system to measure crack depth

Several transducer arrangements are proposed in literature to measure the travel time for estimating the depth of a surface crack. Five such arrangements are presented in Figure 2-47.

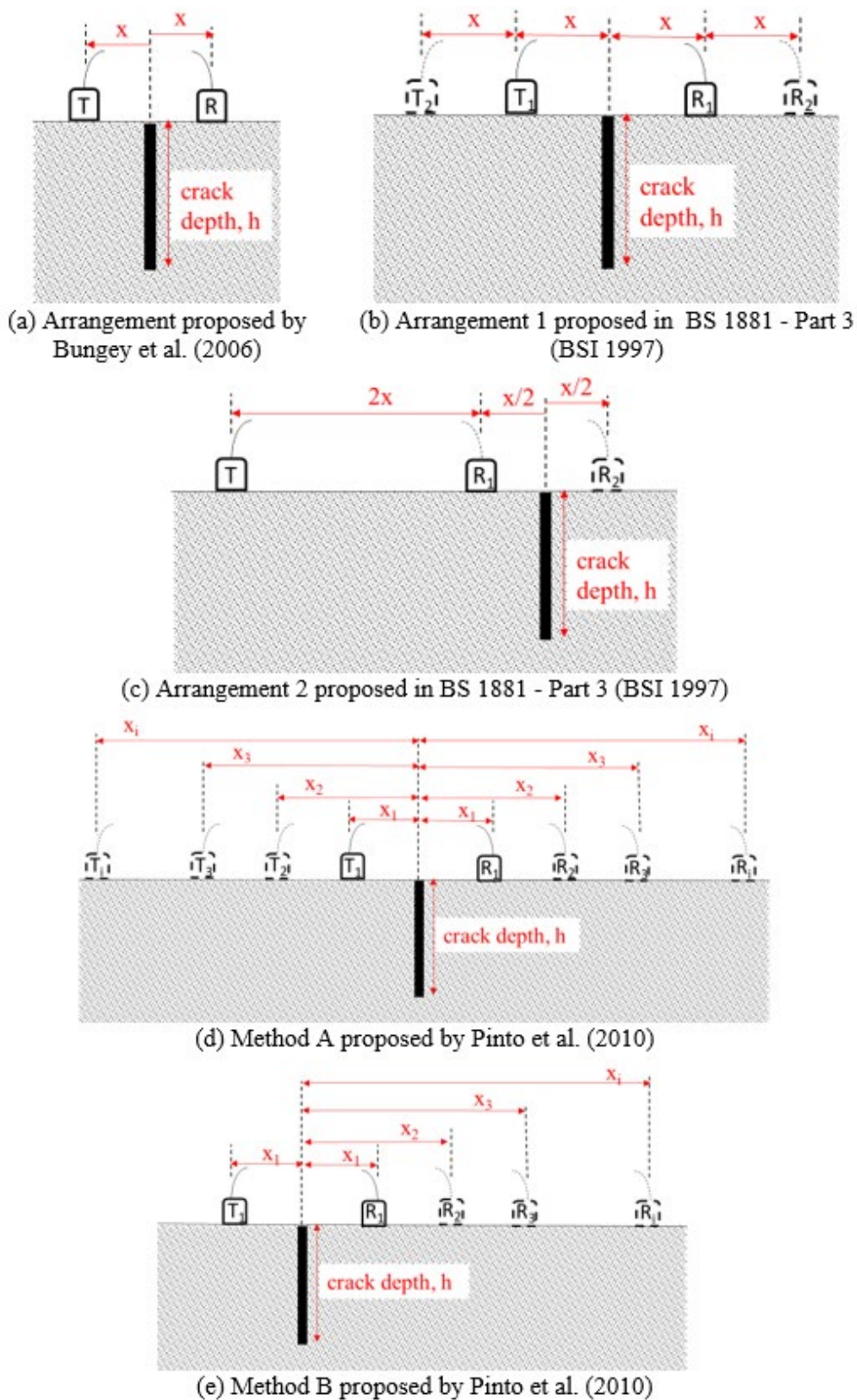


Figure 2-47. Transducer arrangements to measure surface crack depth (T = transmitter and R = receiver)

Eq. 14 is used to calculate the crack depth (h) when the crack is located equidistant from the transmitter and the receiver as shown in Figure 2-47a (Bungey et al. 2006). This procedure requires making two sets of measurements. During the first set of measurements, the transducers are placed at $2x$ spacing in a region with sound concrete, and the travel time (t_s) is measured. During the second set of measurements, the transducers are placed on either side of the crack at $2x$ spacing, as shown in Figure 2-47a, and the travel time around the crack (t_c) is measured.

$$h = x \sqrt{\frac{t_c^2 - t_s^2}{t_s^2}} \quad \text{Eq. 14}$$

where:

t_c = travel time around the crack when transducers are placed at a spacing of $2x$, μs

t_s = travel time measured at a location on the same specimen without cracks by placing transducers at a spacing of $2x$, μs

x = distance to the transmitter or receiver measured perpendicular to the crack, in.

The crack depth (h) is calculated using Eq. 15 when the travel time is measured with the transducer arrangement shown in Figure 2-47b for Arrangement 1 in BS 1881 – Part 3 (BSI 1997). The travel time (t_1) is recorded with transducers at T_1 and R_1 positions with respect to the crack. The travel time (t_2) is recorded with transducers at T_2 and R_2 positions with respect to the crack.

$$h = x \sqrt{\frac{4t_1^2 - t_2^2}{t_2^2 - t_1^2}} \quad \text{Eq. 15}$$

where:

t_1 = travel time when the transmitter and receiver are placed at T_1 and R_1 positions, μs

t_2 = travel time when the transmitter and receiver are placed at T_2 and R_2 positions, μs

x = distance to the transmitter or receiver measured perpendicular to the crack when the transducers are placed at T_1 and R_1 positions, in.

For arrangement 2 in BS 1881 – Part 3 (BSI 1997), the crack depth (h) is calculated using Eq. 16 when the travel times are measured with the transducer arrangement shown in Figure 2-47c. This procedure requires placing the transmitter stationary at a distance of $2.5x$ from the center of the crack. The travel times t_1 and t_2 are measured by placing the receiver at $2x$ and $3x$ distances from the transmitter towards the direction of the crack.

$$h = \frac{x}{2} \sqrt{\left(\frac{3t_1^2 + 2t_2^2}{t_1 t_2}\right)^2 - 25} \quad \text{Eq. 16}$$

where:

t_1 = travel time when the receiver is at a distance of $2x$ from the transmitter, μs

t_2 = travel time when the receiver is at a distance of $3x$ from the transmitter, μs

x = distance as defined in Figure 2-47c, in.

As an enhancement to the BS 1881 - Part 3 arrangement 1 shown in Figure 2-47b, Pinto et al. (2010) proposed Method A shown in Figure 2-47d. This method results in more than two data sets across the crack and allows developing a linear relationship between x_i^2 and t_i^2 , as shown in Eq. 17. The crack depth (h) is calculated by taking the square root of the intercept of the best fit line. The first measurement is recorded when the crack is located equidistant from the transmitter and the receiver. The subsequent measurements are recorded by moving the transmitter and receiver at fixed increments.

$$x_i^2 = V^2 \frac{t_i^2}{4} - h^2 \quad \text{Eq. 17}$$

where:

t_i = travel time when the receiver and the transmitter are at a distance of x_i from the crack, μs

V = wave velocity, in./s

x_i = distance from the center of crack to the transmitter or the receiver, in.

In Method B shown in Figure 2-47e, the transmitter is held stationary while the distance to the receiver is incrementally changed along a straight line perpendicular to the crack (Pinto et al. 2010). The initial measurement is recorded when the crack is located equidistant from the transmitter and the receiver. The subsequent measurements are recorded by moving the receiver at fixed increments. This method also results in more than two data sets across the crack and allows for developing a linear relationship between x_i^2 and $(t_i - t_1/2)^2$, as shown in Eq. 18. The crack depth (h) is calculated by taking the square root of the intercept of the best fit line.

$$x_i^2 = V^2 \left(t_i - \frac{t_1}{2}\right)^2 - h^2 \quad \text{Eq. 18}$$

where:

t_1 = travel time when the transmitter and the receiver are at a distance of x_1 from the center of crack, μs

t_i = travel time when the receiver is at a distance of x_i from the center of crack, μs

V = wave velocity, in./s

x_i = distance from the center of crack to the receiver, in.

The transducer arrangements shown in Figure 2-47 provide alternatives to select the most suitable method for evaluating the depth of cracks in concrete members with various space constraints. All the measurements use the indirect transmission, which is considered less reliable than the direct transmission due to poor signal strength, scattering due to discontinuities, the near surface influence, and travel path uncertainties (Bungey et al. 2006). BS 1881 - Part 3 (BSI 1997) states that the wave velocity calculated based on the indirect transmission is about 5 to 20% less than velocity from the direct transmission. According to Kalyan and Kishen (2014), the presence of surface cracks in concrete contributed more to the change in wave travel path than internal cracks. The effect of surface cracks on wave velocity was prominent when the indirect transmission was used over the direct transmission (Kaylan and Kishen 2014).

Recommendations for transducer spacing are provided in literature to improve the reliability of the UPV readings acquired through indirect transmission. According to BS 1881-Part 3 (BSI 1997) and Proceq (2017), a minimum distance of 4 in. (100 mm) and 6 in. (150 mm) was recommended between the transducers for concrete with a maximum aggregate size of $\frac{3}{4}$ in. (20 mm) or less and for concrete with a maximum aggregate size between $\frac{3}{4}$ in. (20 mm) and 1.5 in. (40 mm), respectively. Yaman et al. (2001) proposed a minimum of four measurement points with the first receiver location being at least two times the wavelength (λ) and the subsequent distances increasing by at least one-half wavelength (i.e. 2λ , 2.5λ , 3λ , and 3.5λ). When a minimum of four measurement points were used, a maximum of 2% error was observed by Yaman et al. (2001) for the UPV measured using the indirect transmission. This error further decreased with the increase in number of measurement points (Yaman et al. 2001). The maximum aggregate size of the concrete specimens used to measure UPV by Yaman et al. (2001) was 1 in. Yaman et al. (2001) used a minimum transducer spacing of 8 in. (200 mm) in their UPV measurements, which is more than the minimum spacing specified in BS 1881 – Part 3 for 1 in. maximum aggregate size (BSI 1997).

Pinto et al. (2010) evaluated the reliability of the four transducer arrangements shown in Figure 2-47a, b, d, and e to calculate the surface crack depth. Concrete prisms with four known surface crack depths (i.e. 2 in., 3 in., 4 in., and 6 in.) and three crack widths (i.e. 0.02 in., 0.079 in.,

and 0.236 in.) were used for this study. A minimum of four transducer locations were used for the two graphical methods (Method A and B) following the recommendations by Yaman et al. (2001). The average UPV measured using indirect transmission at several locations on this concrete was about 12959 ft/s (3950 m/s). For an average UPV of 12959 ft/s with two 54 kHz transducers, the wavelength through concrete would be approximately 2.88 in. The first receiver location was at 8 in., which is more than two times the wavelength ($2\lambda = 5.76$ in.) recommended by Yaman et al. (2001). The subsequent distances were increased by 2 in.; this is more than one-half wavelength ($\lambda/2 = 1.44$ in.) that Yaman et al. (2001) recommend. The calculated crack depth was compared with the actual crack depth to evaluate the error percentage. The comparison of the estimated and the actual crack depths using the four transducer arrangements evaluated by Pinto et al. (2010) is shown in Figure 2-48. Method A, shown in Figure 2-47d, produced the least mean error of about 10% for the estimated crack depth (considering all four crack depths). It should be noted that the spacing recommendation by Yaman et al. (2001) was made for concrete without surface cracks. The impact of crack width on the crack depth calculation was inconclusive.

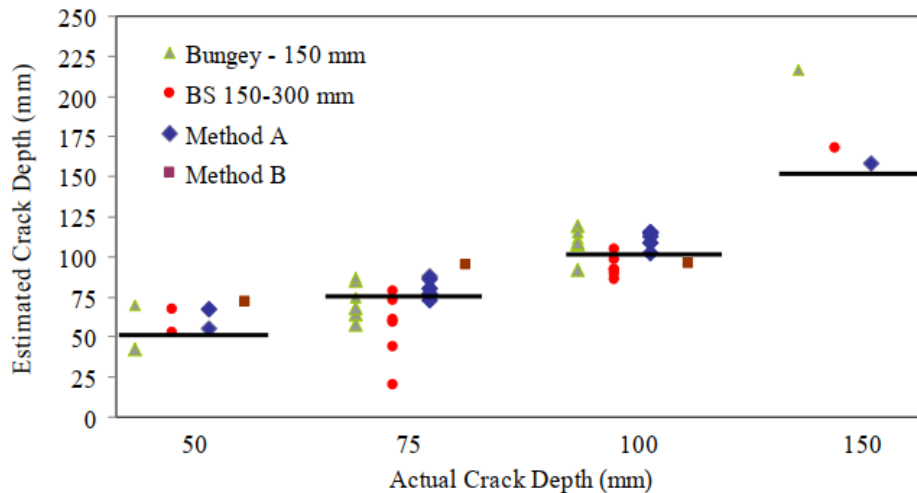


Figure 2-48. Estimated and actual crack depths for four transducer arrangements (Pinto et al. 2010)

Baehaki et al. (2019) calculated the depth of three simulated cracks (i.e. 0.79 in., 1.58 in., and 2.36 in.) using the data collected from transducer Arrangement 1 in BS 1881 – Part 3, as shown in Figure 2-47b. The distance to the transducers from the crack (x) was changed to evaluate the impact of transducer spacing on the crack depth calculation. Data was collected with x as 1.18 in., 2.36 in., 3.54 in., and 4.72 in. Baehaki et al. (2019) observed that the calculated crack depth error percentage increased with the reduction in transducer spacing from the crack. The least error for

the calculated crack depth was observed when the transducers were placed at 4.72 in. from the crack (i.e. transducer spacing = 9.44 in.). The average error for the calculated crack depth considering all three crack depths was about 15% when the transducer spacing was 9.44 in. This 9.44 in. distance is greater than the recommended spacing of two times the wavelength (5.9 in. or 150 mm), assuming a pulse velocity of 13123 ft/s (4000 m/s) (Yaman et al. 2001). The average errors for the calculated crack depth when the transducer spacing was 9.44 in. were 29.04%, 1.39%, and 0.623%, for the 0.79 in., 1.57 in., and 2.36 in. crack depths, respectively. Accordingly, the error percentage of calculated crack depth using arrangement 1 in BS 1881 – Part 3 decreased with the increase in crack depth.

Proceq Pundit Lab and PL-200 are commercially available tools that use the same principal as arrangement 1 in BS 1881 - Part 3 to calculate crack depth using UPV measurements (Proceq 2017). Figure 2-49 shows the Proceq Pundit PL-200 measurement window with a transducer arrangement and the results. For the crack shown in Figure 2-49, the travel times were 74.5 μs (t_1) and 113.5 μs (t_2) when the spacing between transducers was 2.36 in. (0.060 m) and 4.72 in. (0.120 m), respectively. The crack depth (d) at the measured location was calculated and displayed as 2.68 in. (0.068 m).



Figure 2-49. Crack depth calculation using Proceq Pundit PL-200 data (Proceq 2014)

The transducer arrangements shown in Figure 2-47 are only applicable for the cracks that are perpendicular to the surface. According to BS 1881- Part 3, the perpendicularity of a crack is verified by a simple check. First, the transmitter and the receiver are placed symmetrically on either side of the crack, as shown in Figure 2-47a. Then, each transducer is moved away from the crack in turn at similar distances, as shown in Figure 2-50a and Figure 2-50b, and the respective travel times are measured. When the receiver is moved away from the center of crack as shown in Figure 2-50a, the travel time (t_1) is calculated using Eq. 19. When the transmitter is moved

away from the center of crack as shown in Figure 2-50b, the travel time (t_2) is calculated using Eq. 20.

$$t_1 = \frac{\left(\sqrt{\left(x_1 + \frac{h}{\tan \alpha}\right)^2 + h^2}\right) + \left(\sqrt{\left(x_1 + x_2 - \frac{h}{\tan \alpha}\right)^2 + h^2}\right)}{V} \quad \text{Eq. 19}$$

$$t_2 = \frac{\left(\sqrt{\left(x_1 + x_2 + \frac{h}{\tan \alpha}\right)^2 + h^2}\right) + \left(\sqrt{\left(x_1 - \frac{h}{\tan \alpha}\right)^2 + h^2}\right)}{V} \quad \text{Eq. 20}$$

where:

α = slope of the crack, deg

h = crack depth, in.

t_1 = travel time when the transmitter and receiver are placed at T_1 and R_2 positions, μs

t_2 = travel time when the transmitter and receiver are placed at T_2 and R_1 positions, μs

x_1 = distance from the center of crack to the transmitter or receiver when the transmitter and receiver are placed at T_1 and R_1 positions, in.

x_2 = distance moved by the receiver from R_1 to R_2 positions or, distance moved by the transmitter from T_1 to T_2 positions, in.

V = wave velocity, in./s.

When x_1 and x_2 are always larger than the crack depth (h), travel time t_1 will be less than t_2 . This reduction in the travel time is observed with the movement of the transducer away from the crack tip (BSI 1997).

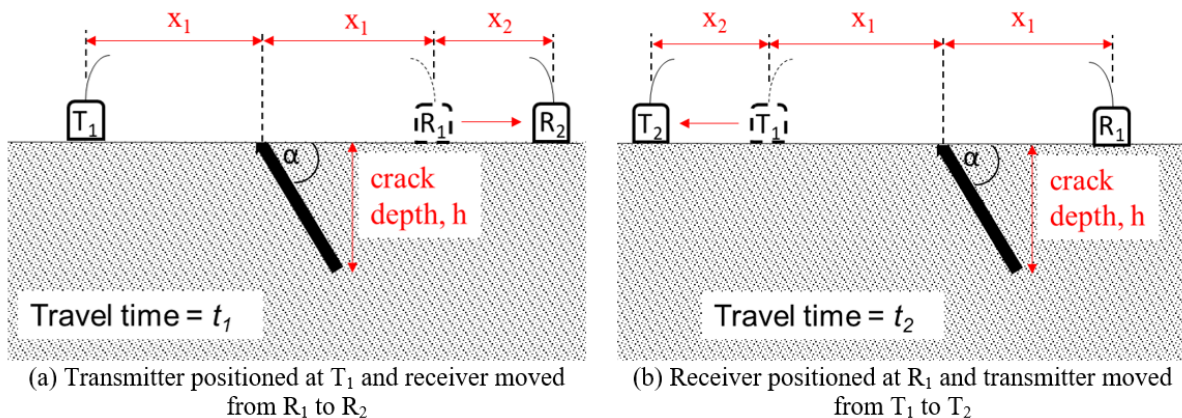


Figure 2-50. Check for slope direction of an oblique crack (BSI 1997)

2.10.2 Application of Multi-Array Transducers

In contrast to the basic transducers used in two transducer systems, multi-array transducer units, or the so-called tomography equipment, includes an array of transducers capable of transmitting and receiving stress waves. The currently available tomography equipment uses shear waves, provides a wide aperture, and produces A- and/or B-scans. Shear waves result in lower signal attenuation and backscattering compared to the longitudinal waves. Also, because of having an array of transducers (with 24 or 48 transducers), multiple measurements made at a single location using shear waves improve accuracy compared to a single measurement with a typical compression wave transducer system (Lee and Oh 2016). Figure 2-51a shows a commercially available ultrasonic shear wave tomography equipment, MIRA A1040 (ACS 2021). This device has a 4 by 12 array of dry-point contact transducers. The unit displays both A- and B-scans of a single measurement (Figure 2-51c). The data collected on a grid can be used to generate B-, C-, and D-scans (Figure 2-51d). The fundamentals of data analysis and post-processing procedures are discussed in Mayer et al. (2008), Mayer et al. (2012), and Attanayake et al. (2018).

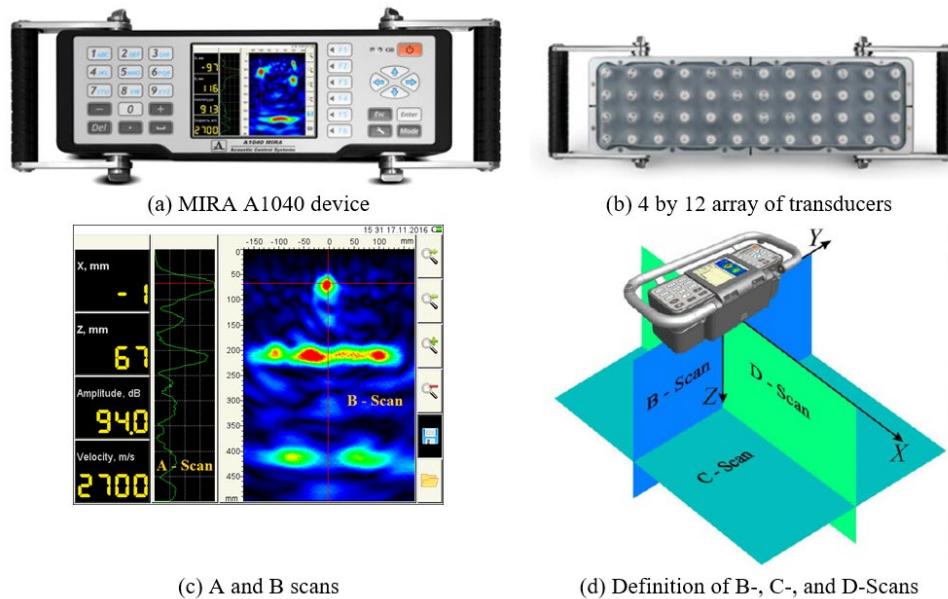


Figure 2-51. MIRA A1040 - Commercially available linear array system (ACS 2021)

In comparison to the application of two-transducer devices, limited studies have been conducted using multi-array transducer devices to estimate the depth of surface cracks. Helmerich et al. (2015) evaluated the feasibility of using MIRA A1040 to detect surface crack depths. Initial trials were conducted using a slab with a notch. The data was collected by placing the excitation

direction parallel to the notch (i.e., placing the device perpendicular to the notch) as shown in Figure 2-52a. The presence of the notch reduced the strength of backwall reflections compared to the backwall reflection observed on a specimen without a crack as shown in Figure 2-52b. Signal disturbances were observed around the tip of the notch, but significant reflections were absent in the B-scans to accurately estimate the depth (see Figure 2-52c).

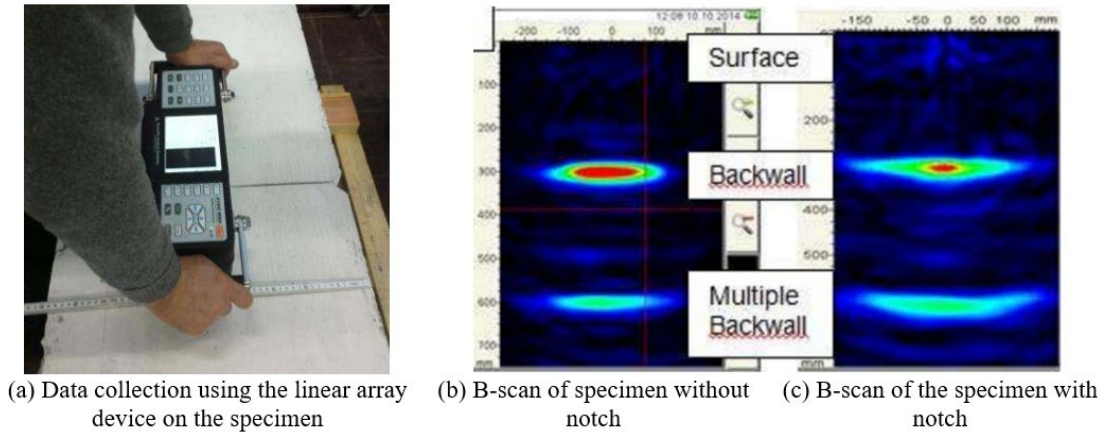


Figure 2-52. Evaluation of surface cracks using a linear array device (Helmerich et al. 2015)

With the experience gained by scanning the notched specimen, Helmerich et al. (2015) used the same device to scan a slab specimen with a longitudinal crack on the top surface under laboratory conditions. This longitudinal crack was a result of a corroded rebar embedded within the specimen as shown in Figure 2-53a. An array of measurements with the excitation direction parallel to the longitudinal crack was recorded to reconstruct a B-scan. The backwall reflection was visible in the B-scan as shown in Figure 2-53b. The surface wave transmission was hindered when the crack was located directly below the array (see Figure 2-53b). However, Helmerich et al. (2015) could not estimate the depth of the longitudinal crack.

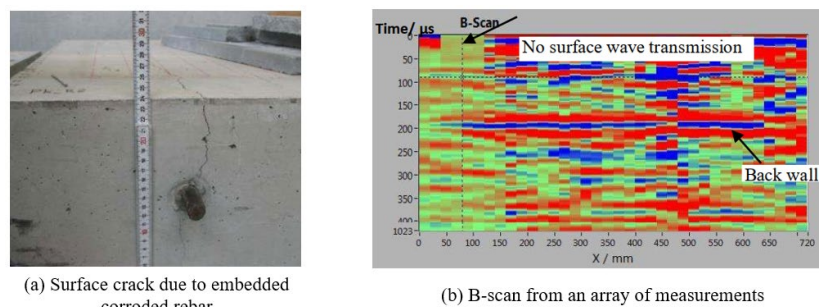


Figure 2-53. Evaluation of surface cracks using a linear array device (Helmerich et al. 2015)

Popovics et al. (2017) used MIRA A1040 to scan a 10 in. thick concrete slab with a simulated open crack. This crack was located at the center of the top surface of the slab and the

crack depth varied from 0.4 in. to 5.9 in. MIRA B-scans were recorded at three crack depths: 0.4 in., 3.0 in., and 5.9 in. For each crack depth, two MIRA scanning configurations were evaluated: scanning position directly above the crack (see Figure 2-54a) and scanning position with the MIRA device offset from the crack (see shown in Figure 2-54b).

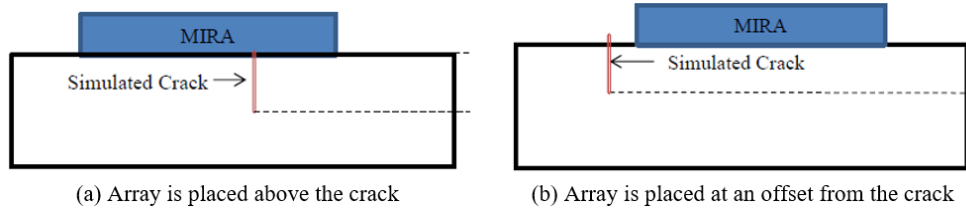


Figure 2-54. Positions of MIRA A1040 w.r.t the surface crack (Popovics et al. 2017)

Figure 2-55 shows B-scans recorded with the array placed above the crack. Two scans were recorded at each crack depth. A partial reflection was observed at the 0.4 in. deep crack. Almost zero reflections were observed at the 5.9 in. deep crack. Compared to 0.4 in. and 5.9 in. deep cracks, much better reflections were observed at the 3.0 in. deep crack. The broken yellow line represents the position of actual crack depths. The results show that the measurements were sensitive to the depth of cracks.

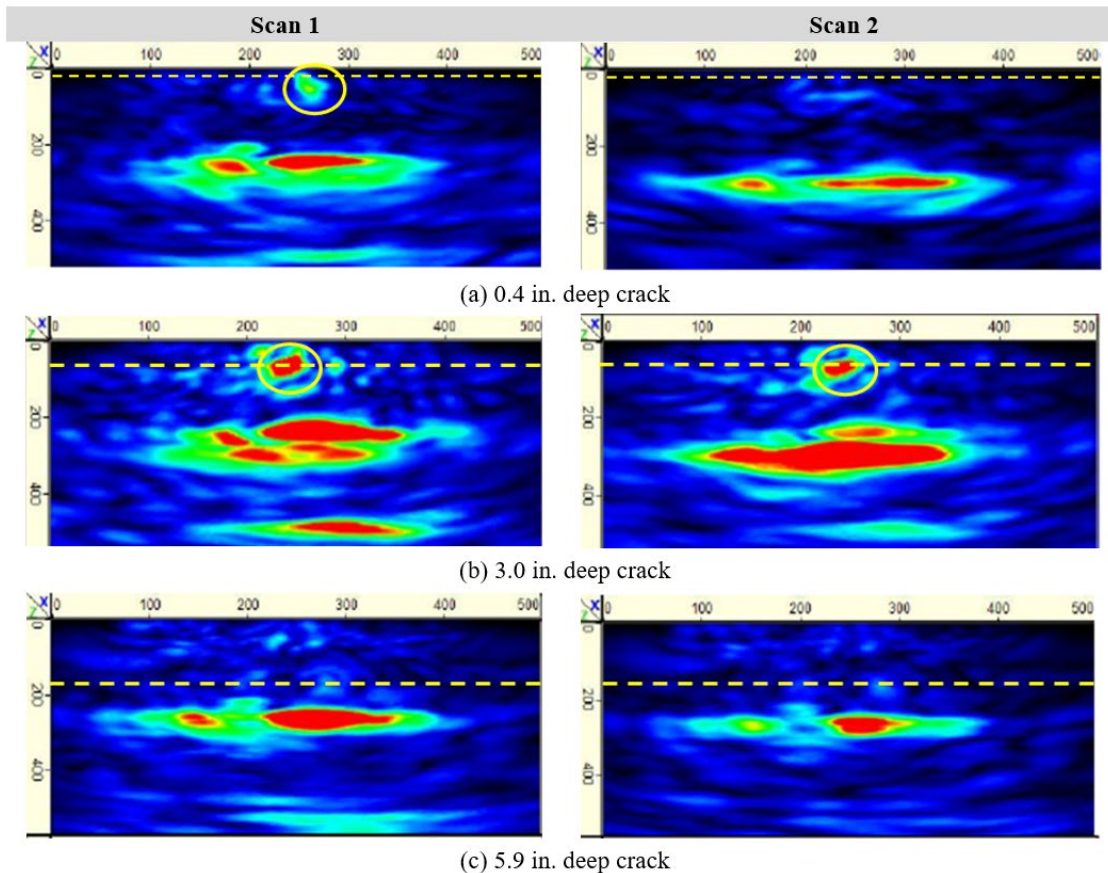


Figure 2-55. B-scans recorded with the unit placed above the crack (Popovics et al. 2017)

Figure 2-56 shows B-scans recorded with the device placed at an offset from the crack. As shown, all the crack tips are visible and, as expected, the crack tip reflections are slightly offset [at about 3 in. (80 mm)] from the vertical centerline of the B-scan. Both 0.4 in. and 3.0 in. deep cracks showed better reflections compared to the 5.9 in. deep crack. The broken yellow line represents the position of actual crack depths. The results show that (i) the measurements are sensitive to the depth of cracks and (ii) the measurements with the array offset from the crack yield better results.

In addition to the use of laboratory specimens with simulated cracks, Popovics et al. (2017) evaluated the performance of the MIRA device under field conditions using 8 concrete pavement panels with visible cracks. Strong back wall reflections were observed from 7 panels. However, the detection of surface cracking on these panels was challenging.

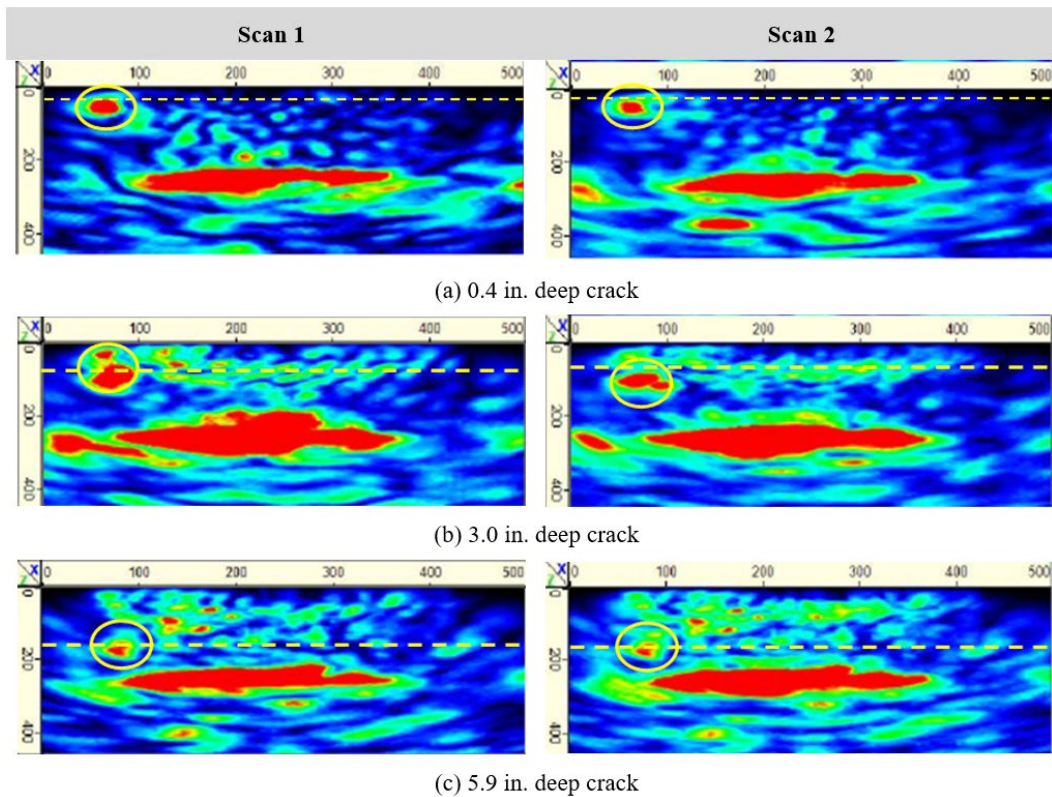


Figure 2-56. B-scans recorded with the unit offset from the crack (Popovics et al. 2017)

2.11 UNIAXIAL VS. BIAXIAL SECTION ANALYSIS FOR DISTRESSED BEAM(S)

An application of an eccentric load, asymmetric loss of concrete and prestressing strands or a combination thereof could require considering flexure about two perpendicular axes to calculate resultant stresses (Kasan and Harries 2013). Figure 2-57a shows the position of the neutral axis

(NA) for a 33×36 in. PSC box-beam section with no section damage. Figure 2-57b shows the rotation of the NA by about 5° for the same section due to asymmetric loss of 3 prestressing strands at the bottom left corner. Depending on the magnitude of damages, the uniaxial section analysis may overestimate the beam capacity (Harries 2006, Harries et al. 2009, Kasan and Harries 2013). For PSC box-beams, a uniaxial sectional analysis provided approximate results to a biaxial analysis when the rotation of the NA is less than 9° (Harries 2006). In a majority of cases, biaxial analysis is required for fascia beams due to eccentric barrier loads and lack of transverse constraints. Irrespective of the damage level, the capacity of interior beams in side-by-side box-beam bridges with full-depth shear keys can be evaluated using uniaxial sectional analysis (Harries 2006).

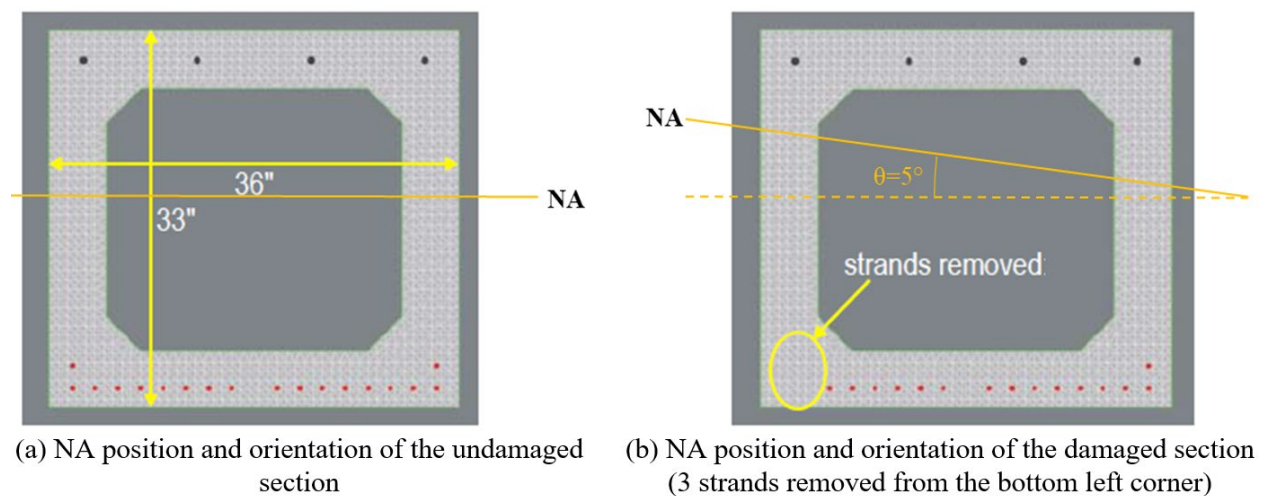


Figure 2-57. Rotation of the NA of a 33×36 in. box-beam-section due to an asymmetric loss of strands (Harries 2006)

2.12 LIVE LOAD DISTRIBUTION IN THE PRESENCE OF DISTRESSED PSC BEAMS

The fraction of live loads supported by an interior and exterior beam in multi-beam bridges is calculated as per the AASHTO LRFD specifications. The loss of material and/or the degradation of material properties reduces beam stiffness and alters live load distribution. Literature presents several studies on the live load distribution in bridges with damaged beams. The focus of such studies is on the impact of high-load-hits (Wipf et al. 2004, Kim 2006, Kim 2008, Froesch et al. 2020b).

Wipf et al. (2004) load tested three PSC I-beam bridges in Iowa, the southbound I-65 bridge near Altoona, the westbound IA-34 bridge near Osceola, and the westbound I-80 bridge near De Soto. In each bridge, beams with a significant section loss with at least one damaged prestressing

strand was recorded. Table 2-13 summarizes the damages in all three bridges and the live load distribution factors (DFs) calculated using strain and deflection data recorded during load testing. The load carried by the damaged beams is less than the design load estimated using the 1996 AASHTO LFD Bridge Design Specifications. When a bridge consists of damaged beams, the percentage of the load carried by the undamaged beams increases. In the Altoona bridge, the damaged second interior beam supported only about 50% of the design load since the rest of the load was redistributed to the undamaged beams. In the Osceola bridge, the damaged exterior beam supported only about 72% of the design load, whereas the damaged exterior beam in the De Soto bridge supported only about 68% of the design load (Wipf et al. 2004).

Kim (2006 and 2008) evaluated the live load distribution in the Main Street bridge in Winnipeg, Canada, with a distressed exterior beam. The distressed beam is a C-shaped prestressed beam as shown in Figure 2-58. The exterior beam had concrete spalling with two or three damaged prestressing strands. The damaged prestressing strands represented about 10-15% of the total prestressing strand area. The flexural capacity of the distressed beam was about 18% less than the design capacity. Even though the live load distribution factors for the bridge with undamaged beams were calculated using the AASHTO LRFD specifications, the load distribution with the damaged beams was calculated using a refined finite element model. The strand and concrete damages were simulated by removing the elements. Even though the live load distribution factors for interior beams did not change due to system redundancy, the damaged exterior beam carried about 10% lower load compared to an undamaged exterior beam.

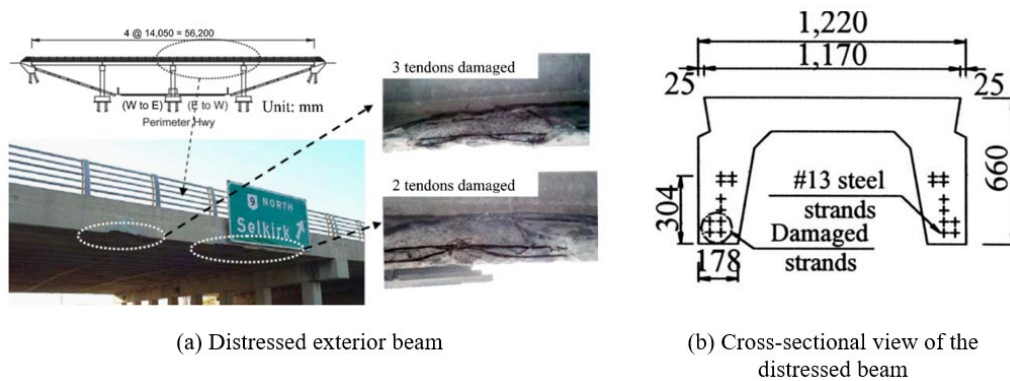


Figure 2-58. Detail of the distressed exterior beam in the Main Street Bridge in Winnipeg, Canada (Kim 2008) (Note: Dimensions are in mm)

Table 2-13. Live Load Distribution with Damaged Beams (Wipf et al. 2004)

Bridge details	Damage description	DF as per the 1996 AASHTO LRFD Specification	DF from strain measurements	DF from deflection measurements
Altoona Bridge (6 PSC I-beams with 2 main spans and 2 approach spans)	<ul style="list-style-type: none"> • West exterior beam: Spalling from the bottom flange with approximately 2.5 in. of concrete missing at the deepest point and one severed strand. • First interior beam: Spalling from the bottom flange with 4 in. of concrete missing at the deepest point with two severed strands and five exposed strands. • Second interior beam: Spalling from the bottom flange with approximately 2.5 in. of concrete missing at the deepest point with one severed strand. • Third interior beam: Spalling from the bottom flange with approximately 2.0 in. of concrete missing at the deepest point and one partially exposed strand. • Fourth interior beam: Spalling from the bottom flange with approximately 2.5 in. of concrete missing at the deepest point and one severed strand. • East exterior beam: Spalling from the bottom flange with approximately 2.0 in. of concrete missing at the deepest point and one exposed and partially severed strand. 	Second interior beam = 0.66	Second interior beam = 0.31	Second interior beam = 0.27
Osceola Bridge (8 PSC I-beams with 2 main spans and 2 approach spans)	<ul style="list-style-type: none"> • Exterior beam: Two severed strands in the bottom layer. Hollow area around the severed strands. • First interior beam: Spalling from the bottom flange with 2.5 in. of concrete missing at the deepest point and two to three partially exposed strands. • No damage to other 6 beams. 	Exterior beam = 0.39	Exterior beam = 0.28	Not Available
De Soto Bridge (9 PSC I-beams with 2 main spans and 2 approach spans)	<ul style="list-style-type: none"> • Exterior beam: One severed strand in bottom layer and one exposed strand at the north end. Three exposed strands with concrete spalling at the south end. • No damage to other 8 beams. 	Exterior beam = 0.44	Exterior beam = 0.30	Not Available

Frosch et al. (2020b) evaluated the live load distribution of adjacent box-beam bridges in Indiana. The aim of the study was to evaluate the load distribution in the absence of properly functioning shear keys. The as-built bridges had a wearing surface over the beams. Load testing was conducted on a 40 ft long, single span bridge with 7 beams. Only two exterior beams had deteriorations. Exterior beam 1 had three exposed prestressing strands near the support and two rust-stained longitudinal cracks, approximately 5 ft long, near the mid span. Exterior beam 2 had minor longitudinal cracking. The load testing was performed under four conditions: 1) as built, 2) after removal of the wearing surface, 3) after the shear keys were disabled by saw cutting along the entire length of all the joints, and 4) with the installation of a 5 in. thick, reinforced concrete deck. The study revealed that the presence of a 5 in. thick, reinforced concrete deck restored the load distribution in the absence of shear keys.

2.13 FINITE ELEMENT (FE) ANALYSIS OF DAMAGED PSC BEAMS

The documented distresses are incorporated into finite element models by adjusting geometric and/or material properties of the damaged beams (Aktan et al. 2005, Mayans 2014, and Yazdani and Montero 2016). Aktan et al. (2005) evaluated the capacity of a PSC box-beam under three different distress levels. A gradual reduction of the concrete modulus of elasticity was defined to represent the spalls or the material degradation. The reduction in the concrete modulus varied from the surface to a predetermined depth of distress. A maximum reduction of 99.975% of the modulus was defined at the surface. In the case of a broken strand, the effective distress length was increased by the transfer length. At the end of this length, the prestressing force was restored to its full value.

Mayans (2014) modeled an impact damaged beam with a reduced moment of inertia to represent concrete spall. Yazdani and Montero (2016) created a 3D refined finite element model of an I-beam using the Abaqus general purpose finite element program to represent a beam with high-load-hit. Concrete spall and 9 severed strands were recorded at the damaged location. The concrete spall was modeled by removing the concrete elements in the FE model even though doing so is not the best practice as the removal of elements creates artificial stress concentrations. The best practice is to define a gradual change in concrete modulus, as demonstrated in Aktan et al. (2005). Tabatabai and Nabizadeh (2019) investigated the stress distribution in a PSC beam before and after a damage at the midspan. The damage at the mid span of the beam was simulated by

removing the corresponding concrete elements from the model at the damage location even though that is not considered as the best practice (Aktan et al. 2005).

2.14 CONCRETE SURFACE COATINGS

AAR/ASR and DEF have contributed to the initiation and/or acceleration of concrete deterioration in PSC beams. The damages due to ASR has been mostly reported on the fascia beams that are subjected to frequent wetting/drying and temperature cycles to promote the rate of reaction and swelling of ASR gel to initiate/promote concrete cracking. The interior beams might not show the same rate of deterioration because of not reaching the moisture and temperature thresholds to promote the reaction. Once the surface cracks are initiated, other mechanisms (such as steel corrosion and freeze-thaw) promote the rate of concrete deterioration. The moisture from the internal sources (i.e. remnant moisture) depends on many parameters including concrete mix design, curing durations and conditions, and exposure conditions. The wind-driven rain and snow, drained chloride-laden water from bridge decks, etc., are the external sources of moisture to PSC bridge beams. Since controlling surface temperature is difficult, controlling moisture is an option to retard the development of ASR related damages in concrete (Reed 2016). EN 1504 recommends controlling moisture by applying a coating or sealer to control concrete degradation (The Concrete Society 2009). The Illinois Department of Transportation (IDOT) applies protective coatings to (i) all the surfaces at the end of the beam, except for the top surface of the top flange and the bottom surface of the bottom flange, and (ii) fascia beams on all the surfaces of the side exposed to view for the entire length of the beam and the bottom surface of the bottom flange. The coating is applied as early as the 4th calendar day, counted from the day of casting, if short term crack growth has subsided and the crack width is less than 0.007 in. (IDOT 2020). A study conducted by the Northeast Prestressed Products, LLC, and the Pennsylvania Department of Transportation (PennDOT) demonstrated the possibility of applying Si-Rex03 Silicon Resin Emulsion paint with Primer on prestressed beams with 24 hours of concrete placement (personal communication). These records highlight the possibility of applying coatings at the fabrication yard to protect beams and the need for a close working relationship with the product manufacturers to develop application guidelines. Wehrle et al. (2010) demonstrated the impact of using a breathable surface coating to hinder ASR- and DEF-related concrete deterioration. Therefore, the need is for a protective system with hydrophobic and breathable properties to control moisture in PSC beams.

This section describes the impacts of surface treatments on concrete durability, guidelines for crack sealing and repair, along with a performance-based procedure for concrete surface coating selection.

2.14.1 Impact of Surface Coatings on Concrete Durability

Concrete coatings are used for aesthetic purposes, controlling moisture, and protecting from exposure elements (Nixon 2002, Kriha 2016). Protective coatings consist of several components, primarily categorized into two phases: continuous or vehicle and discontinuous. Binders and solvents belong to the continuous phase and are responsible for protecting the coated surface and dictating the methods of application. The discontinuous phase consists primarily of pigments and extenders in developing the desired aesthetic qualities, weatherability, and corrosion resistance. Additives are included to enhance anticipated properties and to mitigate coating defects (Kriha 2016).

The effectiveness of surface treatments depends on their physical and chemical properties, substrate condition, surface preparation, type and use of primers, application procedures, and exposure conditions. To extend the service life of concrete structures, these coatings need to satisfy various functional requirements. Even though many studies are documented in literature, the use of data to compare and evaluate coating performance is challenging because of the variability in concrete mixes, specimen types, curing conditions, and exposure conditions used in those studies. As a result, the coating performance was documented by using normalized values of water absorption and reduction in chloride diffusivity with respect to the untreated/control specimens. The results are documented in Table 2-14 columns (b) and (c), respectively. Columns (d) and (e) list two other performance parameters: adhesion to the substrate and crack bridging ability. For example, concrete coated with acrylic absorbed only 5% to 29% of water compared to the amounts absorbed by the uncoated ones. The specimens coated with acrylic reduced chloride diffusivity by 23% to 89% compared the untreated specimens (Almusallam et al. 2003 and Medeiros and Helen 2009). As documented in columns (d) in row 2, the average bond strength of acrylic coatings is 507 psi. Also, the acrylic coatings can bridge cracks as wide as 0.34 in. (Delucchi and Cerisola 2005 and Delucchi et al. 2002 and 2004). As presented in Table 2-14, acrylic coatings can significantly reduce water absorption and chloride diffusivity while having a good crack bridging ability. The crack bridging ability of a coating depends on the physical and chemical properties of the coating, coating thickness, and exposure conditions (Delucchi and

Cerisola 2005 and Delucchi et al. 2002 and 2004). In addition, Wehrle et al. (2010) showed that the acrylic coatings, silane resins, and a combination of silane and acrylic coatings effectively reduced the ASR expansion by 29.76%, 34.52%, and 22.62%, respectively, when compared with untreated specimens.

Table 2-14. Water Absorption and Chloride Diffusivity of Surface Treated Concrete and Adhesion and Crack Bridging Ability of Coatings

Surface treatment (a)	Relative water absorption (b)	Relative reduction in chloride diffusivity (c)	Adhesion (psi) (d)	Crack bridging ability (in.) (e)	Reference ¹ (f)
Acrylic	0.05 – 0.29	0.23 – 0.89	507	< 0.34	(1), (2), (4), (5), (10)
Bacterial carbonate precipitation	0.5 – 0.8				(11)
Chlorinated rubber	0.15 – 0.21	0.52 – 0.56			(1)
Epoxy resin	0.05 – 0.26	0.60 – 0.87	493	< 0.08	(1), (3), (5)
Ethyl silicate	0.21 – 0.73				(7), (8), (12)
Fluorinated polymer	0.33				(14)
Magnesium fluosilicate	0.5				(9)
Modified cementitious mortar coating	0.5				(6)
Nano-silica	0.9				(8)
Polymer emulsion coating	0.67	0.17 – 0.56			(1)
Polyurethane resin coating	0.04 – 0.38	0.86 – 0.91	507	< 0.11	(1), (3), (10)
Silicon resin	0.375				(13)
Sodium silicate	0.38 – 0.67				(7), (8)
Super-hydrophobic paper sludge ash	0.014 – 0.2				(14)

¹ - (1) Almusallam et al. 2003; (2) Delucchi and Cerisola 2005; (3) Delucchi and Cerisola 2012; (4) Delucchi et al. 2002; (5) Delucchi et al. 2004; (6) Diamanti et al. 2013; (7) Franzoni et al. 2014; (8) Hou et al. 2014; (9) Jia et al. 2016; (10) Medeiros and Helen 2009; (11) Muynck et al. 2008; (12) Pigino et al. 2012; (13) Wehrle et al. 2010; (14) Wong et al. 2015

2.14.2 Guidelines for Crack Sealing and Repair

The primary objective of crack sealing and repair are to improve the functional performance of components, concrete surface appearance, and durability while retarding material degradation and steel corrosion (ACI 2014). Various highway agencies, ACI, and PCI have established crack width limits for deciding upon sealing or repair actions (ACI 2014, PCI 2016). As an example, ACI (2014) suggested repairing 0.002 to 0.250 in. wide cracks using epoxy injection. However, Rooke (2018) highlighted that only the cracks wider than 0.004 in. can be sealed effectively using epoxy injection. Figure 2-59 shows the crack width limits used by highway agencies and various other

guidelines to decide crack sealing and repair needs. Most of these guidelines are for concrete components and do not specifically address PSC. Only a few agencies require sealing cracks narrower than 0.002 in. A personal communication with a fabricator indicated that the Indiana DOT requires applying penetrating sealants on PSC beams at the plant and before loading. However, the Indiana DOT requires a 28-day waiting period before the application of concrete surface sealers (INDOT 2013). Agencies like Alabama DOT (ALDOT) and Illinois DOT (IDOT) provide guidelines for the repair of cracks in precast/prestressed members. Several other agencies like Michigan DOT (MDOT) and Ohio DOT (ODOT) documented the general procedures to treat cracks. As an example, MDOT Construction Manual (MDOT 2022a) Section 712-3.9 recommends pressure injection of 0.002 in. or wider cracks. MDOT recommends using sealer when the width is less than 0.002 in., whereas IDOT recommends using protective coatings when the crack width is less than 0.007 in. Appendix A4: Concrete Standard Repair Program in the MDOT Structural Fabrication Quality Manual (MDOT 2021a) recommends using healer sealers for the repair of non-structural cracks. Even though the fabrication manual includes pressure injection procedures, crack width limits are not given. The crack width limits given in Figure 2-59 for MDOT are from the Construction Manual Section 712-3.9 (MDOT 2022a).

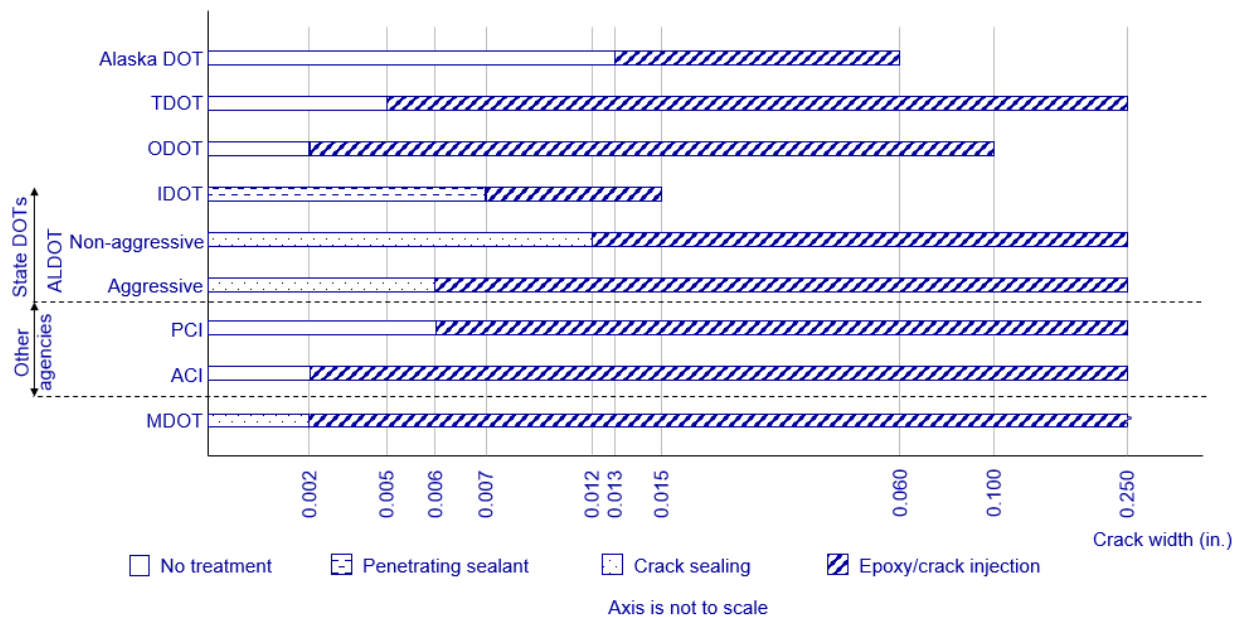


Figure 2-59. Practices of state highway and other agencies

As shown in Figure 2-59, Ohio DOT (ODOT), Tennessee DOT (TDOT), and Alaska DOT do not require treating cracks narrower than 0.002, 0.005, and 0.013 in., respectively. The IDOT

requirement is to apply a protective coating or a concrete penetrating sealer for beam ends and the visible surfaces of the fascias when the cracks are narrower than 0.007 in. and the short-term visible crack growth has subsided. ALDOT defines the crack repairing methods based on the exposure condition. As shown in Figure 2-59, ALDOT recommends using a low viscosity epoxy to seal cracks narrower than 0.012 in., when they are exposed to a non-aggressive conditions, or 0.006 in., when they are exposed to aggressive conditions. ALDOT (2015) uses epoxy injection to treat cracks wider than the above limits. Even though several DOTs define an upper limit for crack widths, MDOT does not have such limits. Also, ALDOT recommended assessing the structural competence and the durability of the cracked concrete when the crack widths are between 0.013 and 0.060 in. (DOT&PF 2020).

2.14.3 Performance-Based Selection

Table 2-15 lists fifteen (15) acrylic-based concrete surface coatings in the MDOT special provisions for concrete surface coatings (20RC710(A285)) (MDOT 2021b). The coating performance parameters are listed in column (a). Column (b) lists standard or the minimum limits in the special provision for each performance parameter. The performance data from the manufacturer's technical datasheet are listed in the rest of the columns. For example, the 1st row lists bond strength as the performance parameter; the MDOT requirement is that the bond strength is greater than or equal to 100 psi, and the bond strength of Thorolastic is 210 psi. As noted in column (b), the coatings should at least achieve 200% tensile elongation when tested to conform to ASTM D2370 (MDOT 2018a). As mentioned in column (e), Colorlastic reached 300% tensile elongation (ChemMaster 2019). However, according to the information provided in the technical datasheet (TDS), the test was performed in compliance with ASTM D412 (2021). ASTM D2370 evaluates the tensile properties of organic coatings while ASTM D412 evaluates the tensile properties of vulcanized rubber and thermoplastic elastomers. These two standards utilize different apparatus, test specimens, and exposure conditions. The performance data that are not available in the technical data sheets are noted in the table using "NA." Similarly, concrete surface coatings in the other highway-agency approved product lists were evaluated as per the MDOT requirements. The coatings satisfying MDOT requirements are listed in Table 2-16.

Crack bridging ability, hydrophobicity, and breathability were selected as the most important performance parameters for concrete coatings. The coatings that satisfy the MDOT

requirements for those three performance parameters are identified in Table 2-15 and Table 2-16 with green highlights. Selected products include the following: Colorlastic, Sherwin Williams concrete texture coating smooth B97-160 series, Decra-flex 300, Elastocolor, Benjamin Moore super spec masonry 100% acrylic elastomeric coating flat 056, Tammolastic, Thorocoat, Thorolastic, Elastocolor Coat (Smooth), Masterprotect C 350, Masterprotect HB 400 DOT, and Si-Rex 03. Personal communication with a contractor confirmed that Thorocoat (i.e. MasterProtect® HB 400) and Sherwin Williams B 97-160 (i.e. Concrete Texture Coat) are commonly used in MDOT bridges.

Figure 2-60 shows the concrete surface coating performance chart that was developed using coating flexibility and water vapor permeance (WVP) as the performance parameters. Based on the WVP evaluated as per the ASTM E96 Procedure A (i.e. desiccant method), the International Building Code (ICC 2018) provides three vapor retarder classes as follows:

Class I	$WVP \leq 0.1$ perms	Vapor impermeable
Class II	$0.1 \text{ perms} < WVP \leq 1$ perms	Vapor semi-impermeable
Class III	$1 \text{ perms} < WVP \leq 10$ perms	Vapor semi-permeable
	$10 \text{ perms} > WVP$	Vapor permeable

Table 2-15. Performance Parameters and Limits for the MDOT Approved Coatings

Performance parameters	MDOT requirements (12SP-710A-05)	Carbocyclic 3350	Colorcoat	Colorlastic	Concrete texture coating smooth B97-160 series	Decra-flex 300	Elastocolor	Perma-crete pitt-flex elastomeric coating 4-110	Permacoat	Sikagard 550w elastic	Super color coat	Super spec masonry 100% acrylic elastomeric coating flat 056	Tammolastic	Thorocoat	Thorolastic	O' leary 1375 elastomeric
(a)	(b)	(c)	(d)	(e)	(f)	(g)	(h)	(i)	(j)	(k)	(l)	(m)	(n)	(o)	(p)	(q)
Pull-off strength ASTM D4541 (psi)	≥ 100	NA ¹	NA	NA	NA	NA	NA	NA	NA	NA	NA	NA	NA	NA	210	NA
Ultimate elongation ASTM D2370 (%)	≥ 200	NA	NA	300 ²	NA	300	625 ²	429	NA	NA	NA	200	290 ²	NA	344 ²	284 ²
Ultimate tensile strength @ 75 °F ASTM D412 (psi)	≥ 100	NA	NA	200	NA	NA	200	406	NA	NA	NA	520	200	NA	220	133
Crack bridging (in.)	≥ 0.016	NA	NA	0.03	0.004	0.016	0.03	NA	NA	NA	NA	0.031	0.004	0.03	0.03	0.06
Flexibility ASTM D522 (%)	> 6.75	NA	NA	28	3.3	28	NA	NA	NA	NA	NA	NA	28	3.3	28	28
Water vapor permeance (VWP) ASTM D1653 (perms)	≥ 4	NA	>3	10.5	9	30.0	14.5	13.0	NA	NA	NA	32.0	11.0	13.0	12	4.0
Salt spray resistance @ 300 hours ASTM B117	Pass	NA	NA	Pass	Pass	Pass	NA	NA	NA	NA	NA	NA	Pass	Pass	Pass	NA
Freeze-thaw durability ASTM C666 (Cycles)	ND ³	NA	100	300	50	5	NA	NA	NA	NA	NA	NA	300	Pass	60	NA
Scaling resistance @ 50 cycles ASTM C672 (Scaling mass)	ND	NA	NA	0	NA	NA	NA	NA	NA	NA	NA	NA	0	NA	NA	NA

¹-Not available ²-ASTM D 412 ³- Not defined

Table 2-16. Approved Products in Other Highway Agency Lists

Performance parameter (a)	MDOT requirements (12SP-710A-05) (b)	Elastocolor Coat (Smooth) (c)	Masterprotect C 350 (d)	Masterprotect HB 200 (e)	Masterprotect HB 400 DOT (f)	Si-Rex 03 (g)
Pull-off strength ASTM D4541 (psi)	≥ 100	NA ¹	500	NA	NA	710
Ultimate elongation ASTM D2370 (%)	≥ 200	269	NA	NA	NA	NA
Ultimate tensile strength @ 75 °F ASTM D412 (psi)	≥ 100	398	NA	NA	NA	NA
Crack bridging (in.)	≥ 0.016	0.047	0.03	0.03	0.036	0.004
Flexibility ASTM D522	> 6.75%	NA	6.75%	3.3%	3.3%	13.8%
Water vapor permeance ASTM D1653 (perms)	≥ 4	24.8	20	25	13	38.13
Salt spray resistance @ 300 hours ASTM B117	Pass	Pass	NA	Pass	Pass	Pass
Freeze-thaw durability ASTM C666 (Cycles)	ND ²	NA	NA	50	Pass	50
Scaling resistance @ 50 cycles ASTM C672 (Scaling mass)	ND	NA	NA	NA	NA	NA

¹Not available ² - Not defined

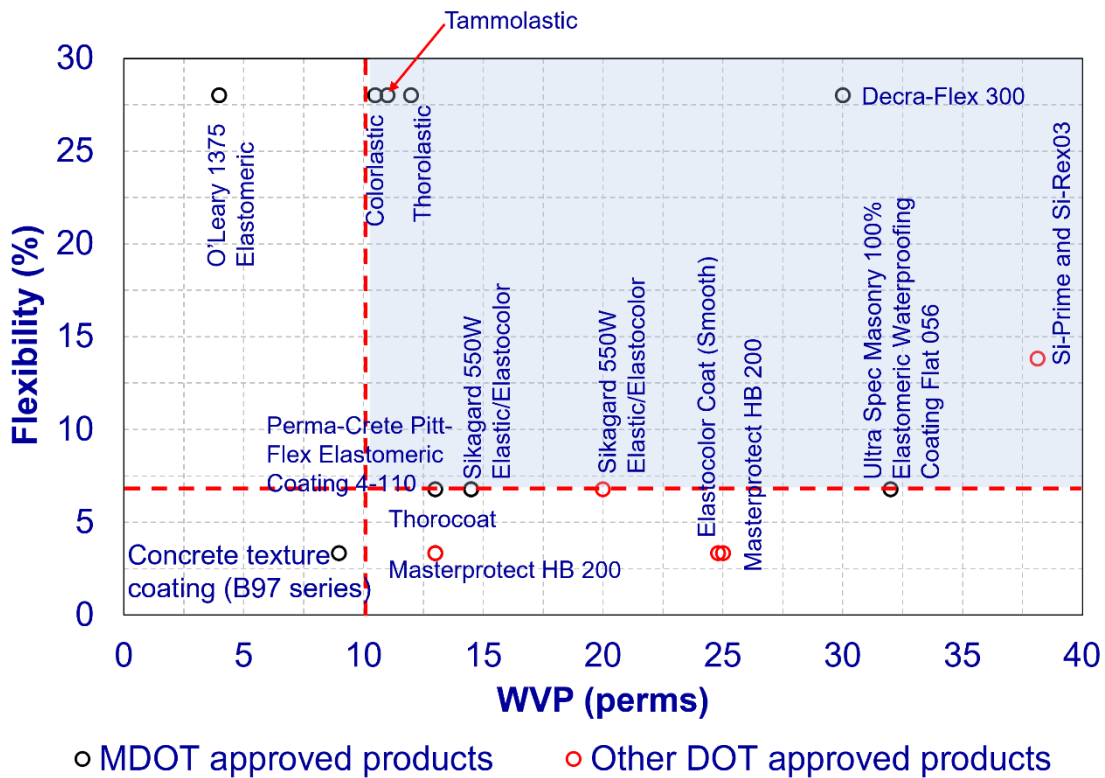


Figure 2-60. Concrete surface coating performance chart

The coating with the highest WVP and crack bridging capability is expected to be the best for protecting PSC beams. As a result, a feasibility range for coating selection is established based on WVP and flexibility of the coatings. Despite the minimum requirement of MDOT, a minimum limit of VWP is selected as 10 perms to confirm to the International Building Code. The minimum flexibility limit was selected from the MDOT special provision for warrant on concrete surface coatings (12SP-710A-05) (MDOT 2018a). Moreover, the coatings in the highlighted area in Figure 2-60 satisfy both WVP and flexibility requirements. Si-Rex 03 has the greatest breathability of 38.13 perms while Benjamin Moore super spec masonry 100% acrylic elastomeric coating flat 056 has the second-highest water vapor permeance of 32 perms. However, personal communication with the agent confirmed that Benjamin Moore super spec masonry 100% acrylic elastomeric coating flat 056 is no longer available and was replaced with Benjamin Moore ultra-spec masonry elastomeric waterproofing coating flat 0359. According to the information in the technical data sheets, both these coatings have similar performance. Thus, Benjamin Moore ultra-spec masonry elastomeric waterproofing coating flat 0359 and Si-Rex 03 are selected for further evaluation.

2.15 PENETRATING SEALANTS

The MDOT Materials Source Guide that was published in 2020 (MDOT 2020) did not have an approved list of penetrating sealants. The products listed in Table 2-17 were compiled using the information provided in the following MDOT documents:

- Materials Source Guide, October 2018 Edition (MDOT 2018b)
- Materials Source Guide, October 2019 Edition (MDOT 2019a)
- *Special Provision for Silane Treatment for Bridge Barriers on Job Number 115752* (MDOT 2017)
- *Special Provision for Silane Treatment for Concrete Bridge Surface on Job number 202704* (MDOT 2018c)
- *Special Provision for Silane Treatment for Bridge Barriers and Deck Fascias* (MDOT 2019b)

After reviewing manufacturer technical data sheets, the type of sealant (water-based or solvent-based) and silane content were included in the table. The penetrating sealant performance parameters listed in the October 2019 edition of the MDOT Materials Quality Assurance Procedures Manual (MDOT 2019c) includes the reduction in water absorption, resistance to chloride intrusion, moisture vapor transmission (MVT), and the depth of penetration. Except the resistance to chloride intrusion, the other three parameters are important to reduce the adverse effects of AAR, DEF, and freeze-thaw. Reduction in permeability reduces the rate of ASR and carbonation (AT 2008). Alberta Transportation (AT) is a longtime proponent of using penetrating sealants for reducing concrete permeability. This is evident from the wide acceptance and adoption of Alberta Transportation's evaluation methods by other highway agencies. The Best Practice Guidelines for Selecting Concrete Bridge Deck Sealers (AT 2008), published by Alberta Transportation, recommends using Type 1c penetrating sealers on precast concrete that is steam cured for 1 to 5 days. Since one of the objectives of this project is to identify the products that are suitable for protecting precast, prestressed concrete (PSC) beams from moisture intrusion while allowing moisture vapor transmission (MVT), the products that are listed in the Alberta Transportation Approved Product List for Bridge Concrete Sealers (AT 2020) (published on April 08, 2020) were reviewed. The products highlighted in Table 2-17 are MDOT approved and are also classified as Type 1c in the Alberta Transportation approved product list.

Table 2-17. MDOT Approved Penetrating Sealants

Product name (a)	Manufacturer (b)	Type (c)	Silane content (%) (d)	Sources (e)
Aquapel Plus 20% silane	L & M Construction Chemical, Inc.		20	MDOT (2018b) MDOT (2019a)
Barracade Silane 40	Euclid Chemical Co.		40	
MasterProtectH200	BASF Construction Chemical	Water-based	20	
MasterProtectH400	BASF Construction Chemical	Water-based	40	
Power Seal 40	Vexcon Chemicals	Water-based	40	
Stifel S	Nox-Crete Chemicals			
Aquanil™ Plus 100	ChemMaster, Inc.	Solvent-based	100	MDOT (2017) MDOT (2018c) MDOT (2019b) AT (2020)
Baracade Silane 100C	The Euclid Chemical Company	Water-based	100	
Certi-Vex® Penseal 244	Vexcon Chemicals	Solvent-based	100	
KlereSeal® 9100-S	Pecora Corporation		100	
Master Protect H 1000 (Hydrozo 100)	BASF Construction Chemical	Solvent-based	100	
Protectosil®BH-N	Evonik Degussa Corporation	Water-based	100	
Sikagard® 750L	Sika Corporation	Water-based	99	
Sil-ACT™ ATS -100	Advance Chemical Technologies	Solvent-based	100	
Xiameter® OFS-6403	Dow Corning Corporation	Solvent-based	98	

The MDOT product qualification process is described in section 5.06 of the Material Quality Assurance Procedure Manual (MDOT 2019c). Table 2-18 shows the performance parameters and evaluation methods listed in this MDOT Manual. The products are evaluated using a Grade D structural concrete mix with a 0.45 water-cementitious material ratio (w/c). Reduction in chloride intrusion, reduction in water absorption, and reduction in chloride absorption based on southern and northern exposure are evaluated using the NCHRP Report 244 Series II and IV test procedures. The resistance to chloride ion penetration is evaluated using AASHTO procedures. The waterproofing after abrasion and MVT performance limits listed in MDOT (2019c) are for Type 1b sealers defined in Alberta Transportation Specification B388 (AT 2010). As discussed previously, Type 1c sealers are recommended for precast concrete (AT 2008). Hence, the performance limits defined in B388 for Type 1c sealers are also incorporated into the table.

As per BT010 (AT 2000b), the performance of Type 1b sealers is evaluated using a concrete mix with a 0.5 w/c ratio while the Type 1c sealer performance is evaluated using a concrete mix with a 0.35 w/c ratio. BT001 (AT 2000a) specifies the application of Type 1b and 1c sealants on concrete specimens with different maturity levels. As an example, concrete cubes used for evaluating Type 1b need to be cured a minimum of 60 days while the cubes for Type 1c evaluation need to be cured for a minimum of 8 days and a maximum of 183 days. Also, the

required moisture content (or relative humidity, RH) for sealant application is different. For Type 1b, the cubes need to be dried to $70 \pm 2\%$ RH within 14 to 21 days. For Type 1c, the cubes need to be dried to $80 \pm 2\%$ RH within 6 to 8 days. Also, the sandblasting requirements are different. For Type 1b, 0.420 ± 0.035 oz (12 ± 1 grams) per side and 2.54 ± 0.07 oz (72 ± 2 grams) per cube need to be removed. For Type 1c, 0.85 ± 0.035 oz (24 ± 1 grams) per side and 5.08 ± 0.07 oz (144 ± 2 grams) per cube need to be removed. *Because of these different requirements for the selection and evaluation of penetrating sealants for precast members, the evaluation methods listed in the current MDOT specifications need to be revised to reflect the requirements for Type 1c sealer.* OHD L-40 procedures for the evaluation of sealant penetration depth is equally applicable for cast-in-place and precast concrete. However, with lower w/c used in precast concrete, the depth of penetration can be very small and could lead to greater inaccuracies in the assessment of penetration depths.

Table 2-18. Penetrating Sealant Performance Parameters and Limits

Performance parameter	Evaluation method	Performance limit
Reduction in chloride intrusion	NCHRP Report 244, Series II with a 5-day air drying period	$\geq 85\%$
Reduction in water absorption	NCHRP Report 244, Series II with a 5-day air drying period	$\geq 85\%$
Reduction in absorbed chloride, southern exposure	NCHRP Report 244 Series IV	$\geq 95\%$
Reduction in absorbed chloride, northern exposure	NCHRP Report 244 Series IV	$\geq 90\%$
Resistance to chloride ion penetration	AASHTO T259 & T260	$\frac{Cl^{-1} \text{ content of sealed specimen}}{Cl^{-1} \text{ content of unsealed specimen}} < 0.55$ Chloride content should be measured at a depth of $\frac{1}{2}$ in. and adjusted for baseline chloride content.
Waterproofing after abrasion	Alberta Transportation B388 Specification	$\geq 86\%$ (Type 1b Sealer) with 72 g abrasion $\geq 85\%$ (Type 1c Sealer) with 144 g abrasion
Moisture vapor transmission (MVT)	Alberta Transportation B388 Specification	$\geq 70\%$ (Type 1b Sealer) $\geq 85\%$ (Type 1c Sealer)
Depth of penetration	OHD L-40	≥ 0.15 in. (3.8 mm)

Even though many experimental parameters were not consistent, published data was compiled to evaluate the reduction in chloride concentration in concrete after sealant application. The compiled data is presented in Figure 2-61. Protectosil®BH-N performs much better than many other sealants. Even though SIL-ACT®ATS-100 did not perform well, considering its wide use in Michigan, Protectosil®BH-N and SIL-ACT®ATS-100 were selected for this project.

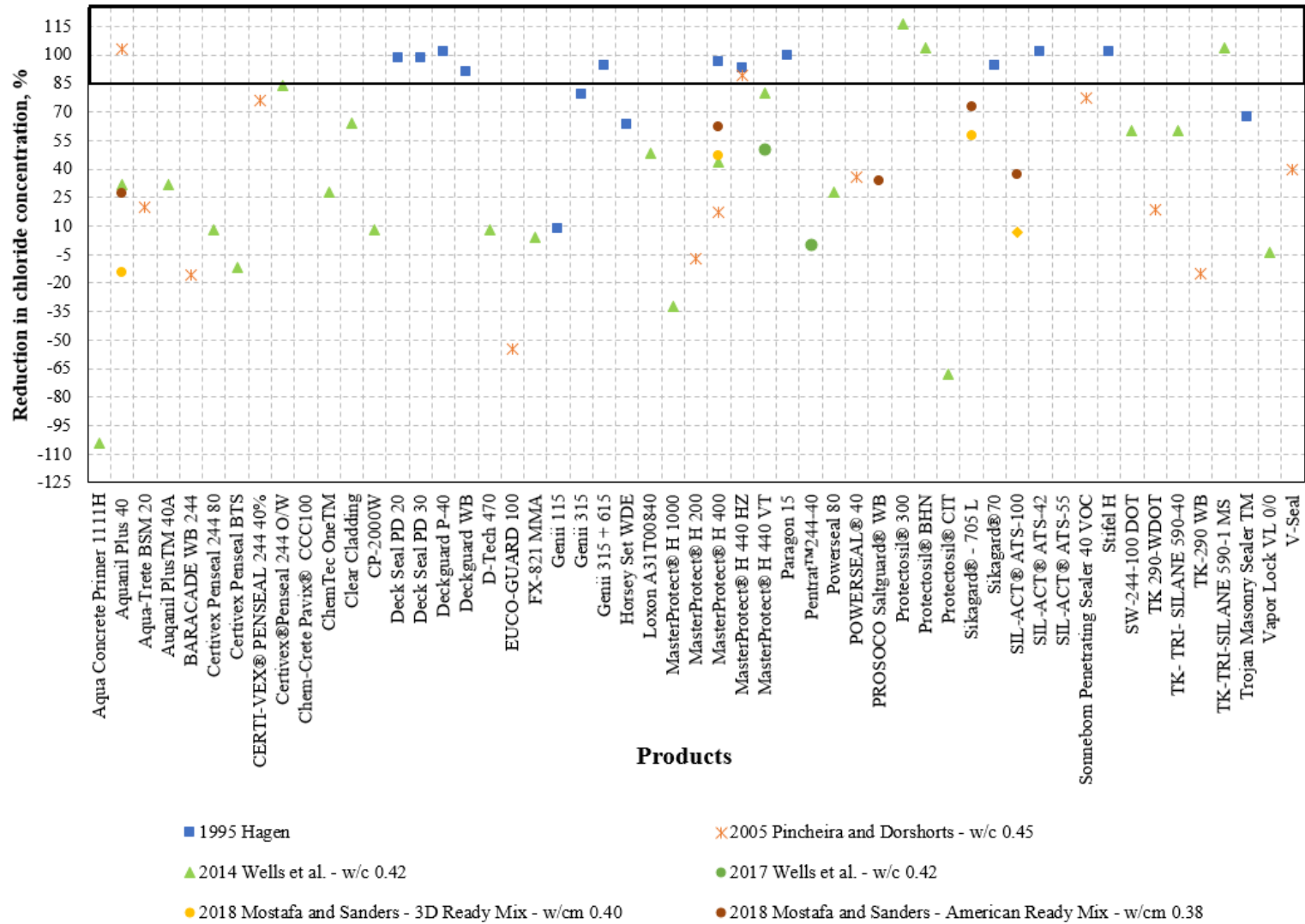


Figure 2-61. Performance of concrete treated with penetrating sealants

3 CONCRETE DETERIORATION IN PSC BRIDGE BEAMS

3.1 OVERVIEW

One of the project tasks is to assess the extent of AAR and other similar deterioration mechanisms of in-service MDOT PSC bridge beams. To identify such bridges, regional bridge engineers were surveyed, and a list of bridges with specific deterioration types in respective regions (Bay, Grand, Metro, North, South, Superior, and University) was developed. Appendix B presents the surveys and responses. Table 3-1 shows the total number of bridges in each region and the number of bridges listed in the survey with the cracking in beams. Column (a) lists the regions. Column (b) lists the total number of I-beam bridges in each region and the number of bridges with longitudinal cracking in the beams. As shown in the table, the Superior Region has 37 I-beam bridges, but none of them have longitudinal cracking. Similarly, Column (c) and (d) show the number of spread box-beam bridges and side-by-side box-beam bridges in each region. As shown in the table, survey responses from Superior, North, and Bay Regions did not indicate the number of spread and side-by-side box beam bridges with longitudinal cracking in the beams.

Since the University Region has the highest number of bridges with longitudinal cracking in I-beams, inspection reports of those bridges were reviewed, and the girder condition rating and distress types documented in the inspector comments were summarized. The analysis of data indicated clusters of bridges with specific distress types located along a couple of corridors. This observation indicated the challenges of using statistical sampling to predict the bridge population with specific distress types in the MDOT inventory. Also, the lack of granularity in the MiBRIDGE database to extract information related to map and longitudinal cracking required extracting information from inspector comments documented in all the inspection reports. Considering the challenges of reviewing inspection reports of all the PSC bridges, only PSC I-beam bridges were selected to identify the population of bridges with specific distress types. Also, the experience of our team and the response to the surveys show that the presence of longitudinal cracking in most of the box beams is not due to concrete deterioration. The subsequent sections describe the data analysis procedures and the results.

An extensive inspection and experimental study were conducted using specimens collected from two bridges to evaluate the causes of concrete deterioration. Also, the depth of longitudinal cracks in two PSC I-beams was evaluated. Finally, the process and the results are described in this chapter. A summary of findings is described in this chapter with details provided in appendices.

Table 3-1. Bridges in Each Region and the Numbers Identified from the Survey

MDOT Region (a)	PSC – I: Total/Survey (b)	Spread-box: Total/Survey (c)	Side-by-side box: Total/Survey (d)
Bay	254/5	75/NR ¹	670/NR
Grand	221/21	74/2	413/11
Metro	242/28	61/9	225/27
North	63/6	13/NR	172/NR
Southwest	122/15	27/1	278/15
Superior	37/None ²	8/NR	260/NR
University	198/127	54/24	537/43
Total bridges	1137/202	312/36	2555/96

¹ Responses were not provided in the survey

² No PSC I-beam bridges with longitudinal cracking

3.2 DATA ANALYSIS

The entire PSC I-beam bridge inventory was analyzed to identify the population of bridges with specific distress types. The following steps were implemented in the data analysis:

- i. Extract data and information from inspection reports.
- ii. Develop distress charts.
- iii. Develop scatter plots.
- iv. Map the geographic distribution of bridges with map and longitudinal cracks on beams.
- v. Identify bridges to investigate the causes of deterioration.

3.2.1 Data and Information from Inspection Reports

A list of bridges in each region was developed with the *structure number*, *year built*, *year reconstructed*, and *year painted*. The list was populated with the condition rating and inspector comments regarding stringers. The MiBRIDGE database includes inspection reports leading back to 1994. This study used data from 1994 to June 2020. A view of the MiBRIDGE database is shown in Figure 3-1, which shows the inventory data and a list of available inspection reports for a specific bridge (Structure Number 10962). Figure 3-2 shows the layout of the spreadsheet with a sample dataset.

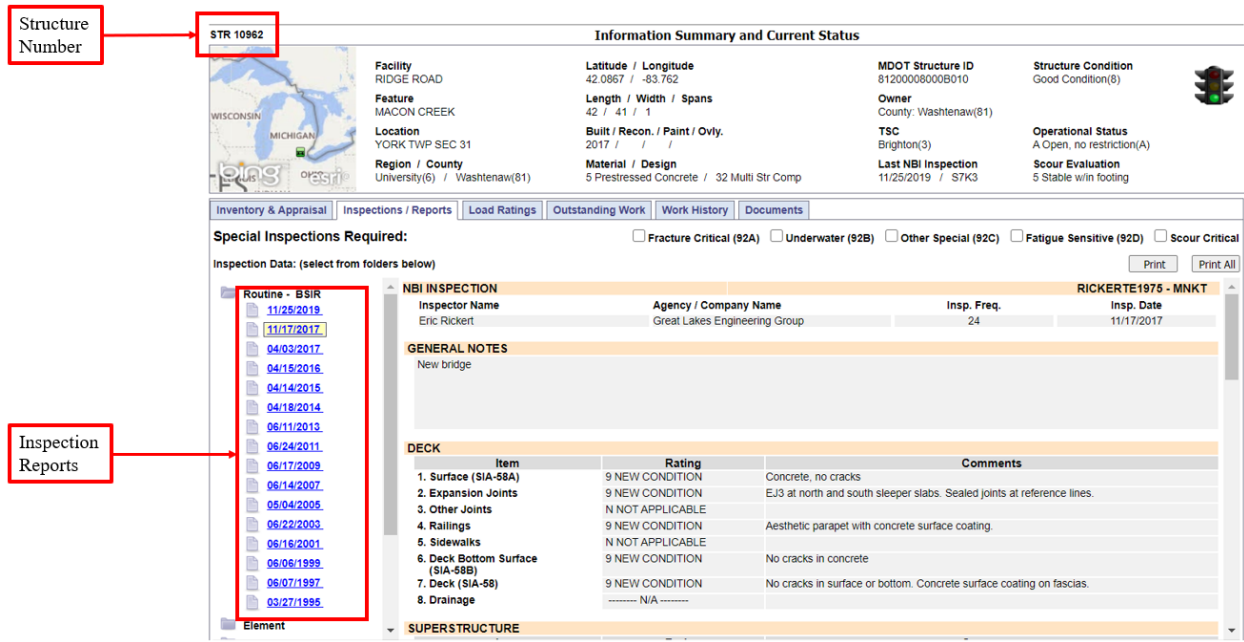


Figure 3-1. MiBRIDGE database showing bridge information and inspection reports

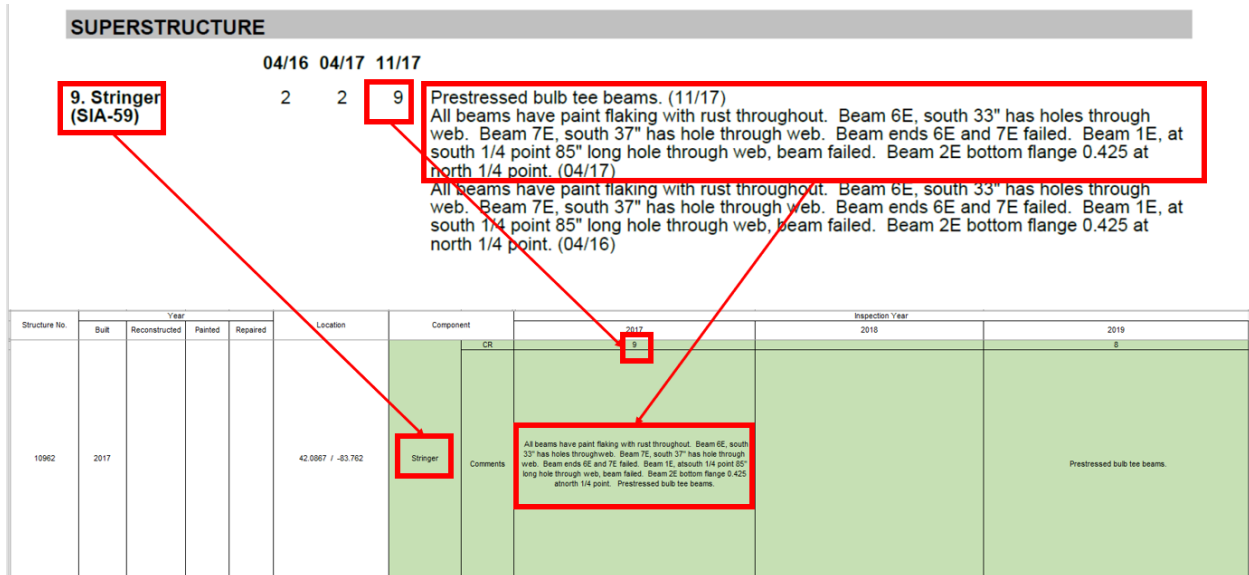


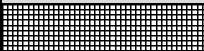









Figure 3-2. Spreadsheet with the data extracted from inspection reports

3.2.2 Distress Charts

The objective of this study is to identify PSC beams with concrete deterioration and the causes of deterioration. The primary focus is on the material related distress. Map cracks and longitudinal cracks are reported due to material related distress, such as ASR and DEF. Hence, map cracks anywhere within the beam and longitudinal cracks within the span were given the highest priorities when assigning color codes to distress types or condition ratings. Beam end cracks are observed

at the fabrication plants, as described in the fabrication inspectors’ survey responses given in Appendix B. Since concrete deterioration may not be the only reason for the beam end cracking observed in in-service bridges, a greater priority is assigned to the longitudinal cracking within the span. Table 3-2 shows concrete distress and stringer condition rating, priority level, and the color code assigned to each distress or condition rating. Even though the ‘movement’ was documented as a separate distress type, inspection reports of only two bridges noted it.

Table 3-2. Distress or Condition Rating, Priority Level, and Color Code

Distress or condition rating	Priority level	Color code
Map cracks	1	
Longitudinal cracks within the span	2	
Longitudinal cracks at girder end	3	
Spall	4	
Movement	5	
Delamination/popout	6	
Other (vertical, diagonal, and unspecified)	6	
Condition rating ≥ 7	7	
Condition rating 5 – 6	7	
Condition rating ≤ 4	7	

The data compiled from the inspection reports are presented in three formats, with respect to *structure number*, *year built*, and the *age from year built*. During the development of these charts, ratings and comments were documented progressively starting from the oldest record available in the MiBRIDGE database. When *year reconstructed* was given, the condition rating given in that specific year was checked. If the condition rating was 9 or 8 (New or Good Condition), the rating and the comments were documented from *year reconstructed*. If the condition rating was 7 or below, the bridge was not considered as a “new” structure, and the ratings and comments were documented starting from the oldest available inspection report. The rating from the most recent date of inspection was documented if two or more ratings were given in the same inspection year.

All comments were thoroughly reviewed to identify the distress types developed over the years. Key details such as distress type, distress location, extent of distress and any significant repairs noted in the inspector comments were highlighted using “red fonts” (Figure 3-3). Any noteworthy points or specific issues identified during the documentation process were recorded

under “Remarks”. For example, if the type of cracks were not described within the inspector comments, it was noted under “Remarks” as a reminder to check the images in the database.

The presentation of distress and condition rating with respect to *year built* is helpful to identify the performance of bridge beams with the same age. The data was rearranged by removing the inspector comments as shown in Figure 3-4. The figure shows the performance of beams in bridges that were built in the same year. Similarly, it is possible to identify the age of beams at which a specific distress type has developed to a detectable level when the data is rearranged with respect to the age of the beams, as shown in Figure 3-5. The age was calculated from the *year built*, instead from the girder fabrication due to the lack of access to such data. The figure shows a cluster of bridges with similar distress. As an example, a group of bridges built in 1989 had their map cracking first noted in inspection reports 16 years after construction. Also, several bridges built in 1993 and 1994 had their longitudinal cracking first noted in inspection reports 14 to 20 years after construction.

STRC_NUM	YEAR_BUILT	Component	Inspection Year																	Inspector Comments											
			1994	1995	1996	1997	1998	1999	2000	2001	2002	2003	2004	2005	2006	2007	2008	2009	2010		2011	2012	2013	2014	2015	2016	2017	2018	2019		
1801	1988	Stringer			3	3	3	3	3	3	3	3																			PCI(2000). PCI(2002). PCI(2004). Shrinkage cracks(2006). Concrete I beams with light shrinkage cracks(2008). Concrete I beams with tight vertical and horizontal cracks near beam ends(2010).
1856	1989	Stringer	3	3	3	3	3	3	3	7	7	7	7	7	7	7	7	7	7	7	7	7	7	7	7	7	7	7	7	HAIR LINE CRACKS ON FASCIA BEAMS(2000). Minor spalling on top Flanges at joints(2002). Minor spalling on top flanges at joints. Honeycombing throughout. Minor spalls in backwalls at some beam ends(2004). Honeycombing throughout. Small spalls in beam ends near bearing plates typical(2006). Honeycombing throughout. Small spalls in beam ends near bearing plates	
1857	1989	Stringer	3	3	3	3	3	3	3	7	7	7	7	7	7	7	7	7	7	7	7	7	7	7	7	7	7	7	7	STS ON TOP FLANGE B1, S1, PIER2, BAY1 FEW TIGHT CRACKS IN DIAPHRAM(2000). Few minor spalls on beam ends at joints(2002). Few minor spalls & cracks on beam ends at joints and in backwalls at beam ends(2004). Few small spalls in beam ends at bearing plates(2006). Few small spalls in beam ends at bearing plates(2008). Concrete I beams. Few small spalls in beam ends at bearing plates. 1sft spill top of beam 6x span 2w at pier 1w from water leaking through deck delam at joint. Rust stains(1999). Rust stains(2001).	
2262	1989	Stringer	3	3	3	7	7	7	7	3	3	3	3	3	3	3	3	3	3	3	3	3	3	3	3	3	3	3	3	Small, shallow spill in web of BMS at south backwall - west side of beam(2003). Light shrinkage cracks and honeycombing thruout(2005). Light shrinkage cracks and honeycombing thruout(2006). Concrete "I" beams with shrinkage cracks and honeycombing thruout. Tight diagonal cracking at beam ends in backwalls(2007).	
2263	1989	Stringer	3	3	7	7	7	7	7	3	3	3	3	3	3	3	3	3	3	3	3	3	3	3	3	3	3	3	3	Light small spill in backwall @ bearing on W. Light map cracking on W. backwall(1999). Light shrinkage cracks thruout. Areas of honeycombing(2005). Light shrinkage cracks thruout. Areas of honeycombing(2006). Concrete "I" beams with shrinkage cracks thruout. Small spalls and cracks at beam ends in backwalls. Light shrinkage cracks thruout. Areas of honeycombing(2007). Concrete I beams with shrinkage cracks(2009).	

Figure 3-3. Example of a distress chart organized with respect to structure number

3-6. The table includes data related to longitudinal cracks (LC), vertical cracks (VC), diagonal cracks (DC), map cracks (MC), delamination (DEL), spall, movement, popout, and other cracks. The *other cracks* include the type of cracks that were not specified in the inspection reports. Photographs were reviewed to confirm the accuracy of information before documenting data under *other cracks*. Figure 3-7 shows the scatter plot developed using the data in the table.

The scatter plot was used to identify the distribution of distresses at the girder end and within the span, along with the age range of a specific distress cluster. As an example, map cracks were documented on beams that were in service for a little more than 6 years. Two distinct clusters of bridges with map cracks within the span are shown in Figure 3-7, one with an age range of 6 to 20 years and the other around 50 years. Map cracking at the beam end is widespread and show three clusters: between 6 to 20 years, 22 to 28 years, and 35 to 52 years.

Longitudinal cracking at the beam ends has been observed just after construction. Unfortunately, the inspection data documented at the fabrication yard is not available to verify the presence of cracks at the yard. However, observation of cracking at that young age confirms that the causes of such cracking are not due to concrete deterioration. The longitudinal cracking within the span was observed after 6 years.

Structure No.	Year Built/Reconstructed	PSC I-beam age at the first observation of distress (yrs)															
		End									Within the span						
		LC	VC	DC	MC	DEL	Spall	Other cracks	Movement	LC	VC	DC	MC	DEL	Spall	Popout	Other cracks
1785	1962	38	54	44		50	38	39									
1786	1962	50	40			50	38	38									
1789	2007					5	5						5	5			
1790	2007					5	1							1			
1792	1962	38				38	38			54					38	40	
1801	1988				18		30								30		
1819	1994	14	20								20						
1829	1993	13		7	9	23		23		13							
1830	1993	7		7				21									
1837	1993	19			13					19			13				
1838	1993	13					23										
1839	1993				13								13				
1840	1993		11		11	19		7									
1841	1994	6	20		8						20		8				
1842	1994	18	18		18	24		22					18				22
1843	1994	12	18		18		8	20		24							
1856	1989		23		25	23	13	11			27						11
1857	1989		30		23	30	13	15			30						
1863	1981	23					23										
1889	2004																

Figure 3-6. A data set showing the age at which a distress was first observed on beams

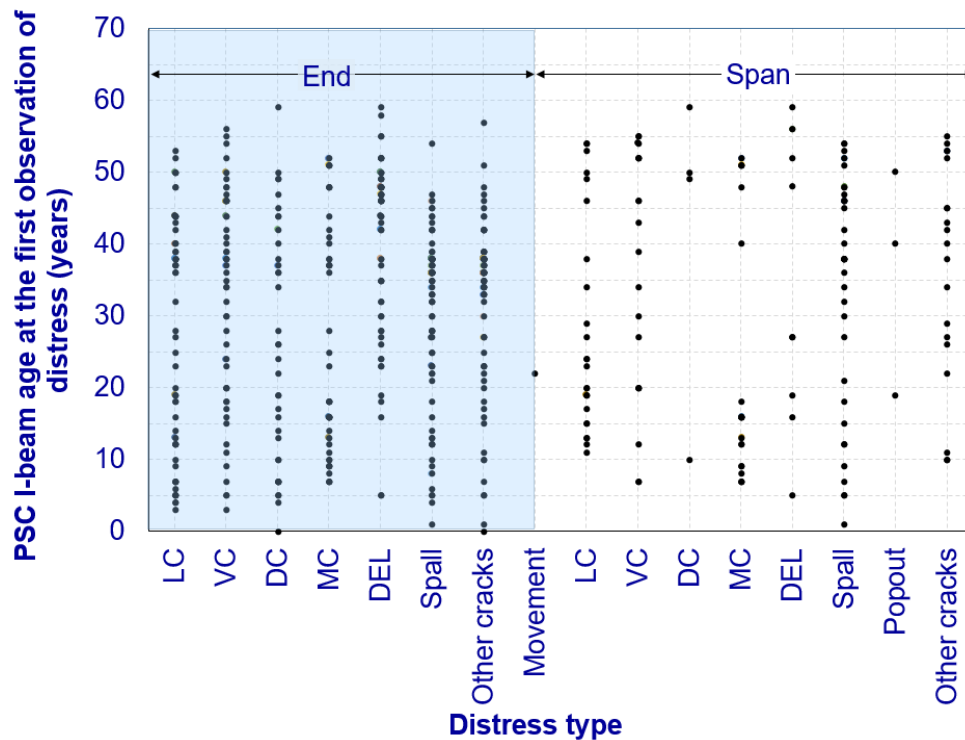


Figure 3-7. Scatter plot showing the age at which a distress was first observed on beams

3.2.4 Geospatial Distribution of Bridge Clusters

Figure 3-5 shows a rearranged distress chart based on the *Age* of the beams. To identify the beams with concrete deterioration, the map cracks anywhere within the beam and the longitudinal cracks only within the span were considered. This study selected bridges with map and/or longitudinal cracks documented in more than two consecutive inspection reports, along with or without other deteriorations such as diagonal cracks, spalls, or delamination in the subsequent years. The geospatial distribution of bridge clusters was studied by plotting them on an ArcGIS map (Figure 3-8). As shown in the figure, several clusters are located on specific corridors. Several bridges were inspected to document the condition and perform uranyl acetate testing, a screening test to evaluate the presence of ASR.

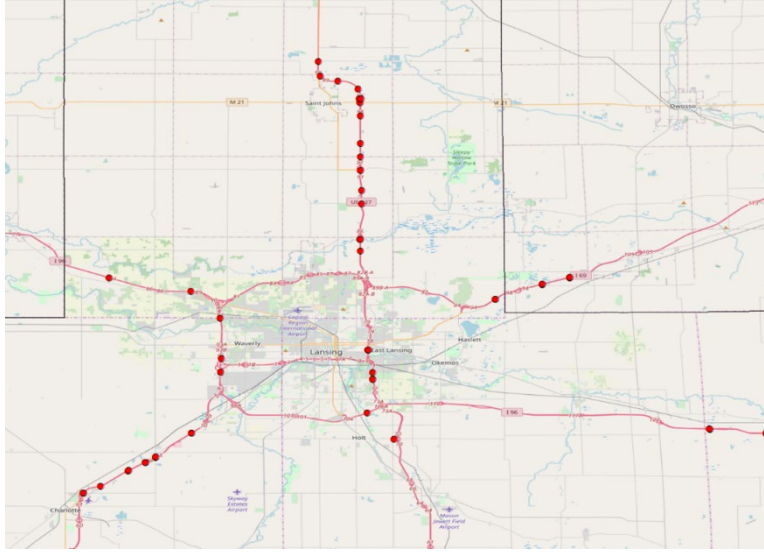


Figure 3-8. Location of bridges with concrete deterioration in PSC I-beams (an example)

3.3 DATA ANALYSIS CHALLENGES, ASSUMPTIONS, AND LESSONS LEARNED

The following sections describe the challenges during data compilation, interpretation of the findings, and the assumptions used throughout the process.

3.3.1 Challenges During Data Compilation

Certain inconsistencies were noted during the manual data extraction process, and the steps taken to standardize the procedure are discussed below.

3.3.1.1 *Inconsistent Vocabulary*

Multiple inspectors produce inspection reports for a single bridge over time. Even though Section 4.4 of the Bridge Inspector’s Reference Manual (Hartle et al. 2002) lists a set of abbreviations for inspectors, a majority of inspection reports included nonstandard abbreviations (e.g. “Efflorescence” as “effor / effl.”); this put forth a challenge to automate the data extraction process from a large volume of reports. Table 3-3 lists a set of abbreviations identified during the review of inspector comments. With the exceptions of “Abut”, “Eff”, “Delam” and “Cr”, the other abbreviations are not in the Bridge Inspector’s Reference Manual. These abbreviations were replaced with the respective words or phrases listed in the table to improve the consistency of information presented in inspector comments for further analysis.

Table 3-3. Abbreviated Terms in the Inspection Reports

Abbreviations in the inspection reports	Word/phrase
Abuts	Abutments
appr	Approach
bm	Beam
brgs	Bearing
Comp. seals	Completely sealed
CSC	Concrete surface coating
Crked	Cracked
Delam	Delamination
eb.	Eastbound
effor / effl.	Efflorescence
Exp jts	Expansion joints
HLH	High-load-hit
Incip	Incipient
Jt/Jts	Joints
LFT	Linear feet
longit	Longitudinal
NB	Northbound
PT	Posttensioned
Span 1S	South span 1
Span 2S	South span 2
SB/sb	Southbound
STS	Spall to steel
sft	Square feet
sm	Square meters
Wb	Westbound

3.3.1.2 Multiple Data Entry

Several inspection reports contained multiple comments and ratings for the same year. All relevant information was extracted to the spreadsheet, but only the most recent comments were considered for further analysis.

3.3.1.3 Year Built/Year Reconstructed

The age of a beam was calculated based on the *year built*. Certain bridges in the database included *year reconstructed* as the *year built*. However, the condition rating and inspector comments did not indicate the replacement of girders. Hence, the original *year built* was used for further analysis. In contrast, girder condition rating of certain bridges indicated that the bridges might have been reconstructed or replaced with new girders in a recent year even though the *year built* was not

recent. In such cases, the correct *year built* was identified from the National Bridge Inventory (NBI) database.

3.3.1.4 Distress Type and Location

The use of inconsistent terminology to describe types of cracks was a challenge. The following is a list of substitutes for the terminology used in the inspector comments:

- “Map crack” for “*shrinkage/alligator crack*”, “*random cracks*”
- “Vertical crack” for “*transverse crack*”
- “Longitudinal crack” for “*horizontal crack*”.

The distress location along the beam is not clearly defined in most of the inspection reports. The location of longitudinal cracking was assumed to be at the beam end if the location was not specified. The following phrases in the comments (shown below in *italics*) were used to assume the location of distress:

- *Deck drain area* → beam end
- *Entire length of span* → both beam end and span
- *Crack length < 5ft* → beam end
- *Crack length ≥ 5ft* → both beam end and span
- *Pier/Abutment* → beam end
- *Backwall* → beam end.

3.3.1.5 Multiple Beam Types

Certain bridges included multiple beam types. For example, bridge ID 10971 has adjacent box-beams in the north span and I-beams in the remaining six spans. In such cases, only the distresses observed on I-beams were considered. Also, a bridge in the Grand Region (S.N. 5199) has precast arches as fascias and was excluded from consideration.

3.3.1.6 Incorrect Beam Type

Certain adjacent box-beam bridges were listed as PSC I-beam bridges (i.e. 32- Multi-Stringer, W or I-Beam, Composite). For example, adjacent box-beam bridges S.N. 9994 and 9784 in the Bay Region are listed as I-beam bridges.

3.4 BRIDGES WITH CONCRETE DETERIORATION IN PSC BEAMS

3.4.1 Bridges with Map and/or Longitudinal Cracking in Beams

The data analysis process presented in Section 3.2 was implemented in all the regions to identify the number of bridges with PSC I-beam deterioration, possibly due to ASR or similar mechanisms. Table 3-4 lists the updated numbers. As shown in the table, the inspection reports of 28 bridges (i.e. 7 + 21) out of 253 bridges in the Bay Region documented map and/or longitudinal cracking in beams. For each of the 7 bridges listed in the 3rd column of the table, the inspectors documented the presence of map and/or longitudinal cracking only in one or two inspection reports that will be available as of June 30, 2021. The number of bridges with map and/or longitudinal cracks documented only in the most recent inspection report or in the last two inspection reports is noted within parentheses; this highlights the need for reviewing the subsequent inspection reports, as they become available, to confirm the progress of such distresses. As an example, out of the 7 bridges in the Bay Region noted in column 3 of the table, the last inspection report of one bridge and the last two inspection reports of 2 bridges documented map and/or longitudinal cracking in beams.

Table 3-4. Number of Bridges with Map and/or Longitudinal Crack in PSC I-Beams

Region	Total no. of I-beam bridges	Number of bridges with the frequency of observation of map and/or longitudinal cracks ≤ 2	Number of bridges with the frequency of observation of map and/or longitudinal cracks > 2
Bay	253	7 (3)	21
Grand	221	3 (2)	19
Metro	242	8 (4)	23
North	63	4 (4)	2
Southwest	122	0	20
Superior	37	0	1
University	198	11 (2)	53

3.4.2 Field Inspection - Summary of Observations

Twelve (12) bridges were selected to verify the presence of map and longitudinal cracking and their location documented in the inspection reports by visually inspecting the beams at an arm's length. These bridges are listed in Table 3-5. Even though the inspector comments did not indicate map or longitudinal cracking, bridges 424 and 12778 (highlighted in Table 3-5) were inspected since they are parallel structures to bridges 425 and 12779, respectively. Interestingly, fascia beams of both bridges (424 and 12778) had longitudinal cracking similar to the other structures. The possibility of having ASR in the deteriorated beams of 6 structures (424, 2273, 2618, 12775,

12778, and 12779) was evaluated using uranyl acetate testing, a screening test for ASR. As shown in Figure 3-9, map and longitudinal cracks are dominant over the bottom flange top surface of the fascia beams.

Table 3-5. Bridges Selected for Inspection

Structure No.	Year Built	Facility Carried	Feature Intersected	Region
424 ¹	1968	I – 75 SB	Lincoln Road	Bay
425	1968	I – 75 NB	Lincoln Road	Bay
10403	1983	M - 24	Wiscoggin Creek	Bay
2618	1992	M - 57	Flint River	Bay
143	1996	US-131	Kalamazoo River	Grand
12778 ¹	1998	US – 131 NB	MDOT RR Corridor	North
12779	1998	US – 131 SB	MDOT RR Corridor	North
2271	1989	I – 69 NB	Lansing Road	University
2272	1989	I – 69 SB	Lansing Road	University
2273	1989	I – 69 NB	M – 100	University
2282	1989	I – 69 SB	M – 100	University
1857	1989	I – 69 WB	Peacock Road	University
12772	1993	Price Road	US – 127	University
12775	1993	Townsend Road	US – 127	University

¹ - Selected for inspection because the inspection reports of the parallel structures documented cracking.



Figure 3-9. Map and longitudinal cracks in PSC I-beams

Figure 3-10 shows the fascia beam condition of structure 2273. Longitudinal and map cracks are dominant over the bottom flange top surface of the beam. The map cracks are superficial. Consequently, two locations were selected and cleaned by grinding. The first location was cleaned to remove map cracks and screened for ASR using uranyl acetate. As shown in the figure, ASR was not observed. However, when the surface of the 2nd location was lightly cleaned and screened for ASR, the characteristic yellowish-green color was observed over fine particles under UV light, indicating a minor level of ASR.

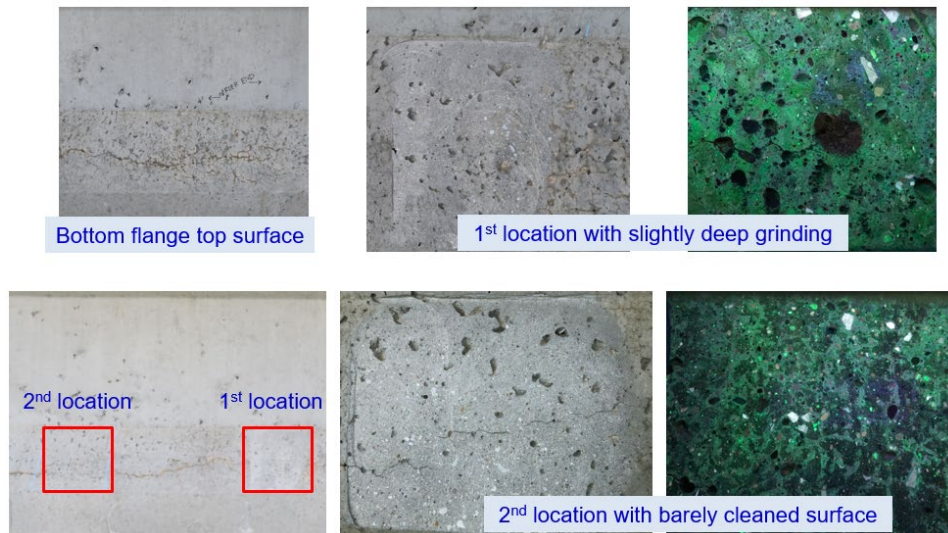


Figure 3-10. Structure 2273 fascia beam: Surface condition and fine aggregate ASR

Figure 3-11 shows the fascia beam condition of the structure 12775. The surface coating was not effective at protecting concrete in the presence of a 0.06 in. wide crack. Uranyl acetate testing indicated a significant level of ASR in fine aggregate. The other bridges screened for ASR either did not show any activity or had a minimum level similar to the structure 2273. Therefore, ASR cannot be considered as the primary reason for the initiation of map and longitudinal cracking. Another concern is the integrity of surface coatings in providing the expected protection for fascia beams. As shown in Figure 3-12, damaged concrete surface coatings could trap moisture promoting concrete deterioration. As seen in Figure 3-11, the 0.06 in. wide longitudinal crack is exposed to the elements, and a significant level of ASR was observed closer to the coated surface.

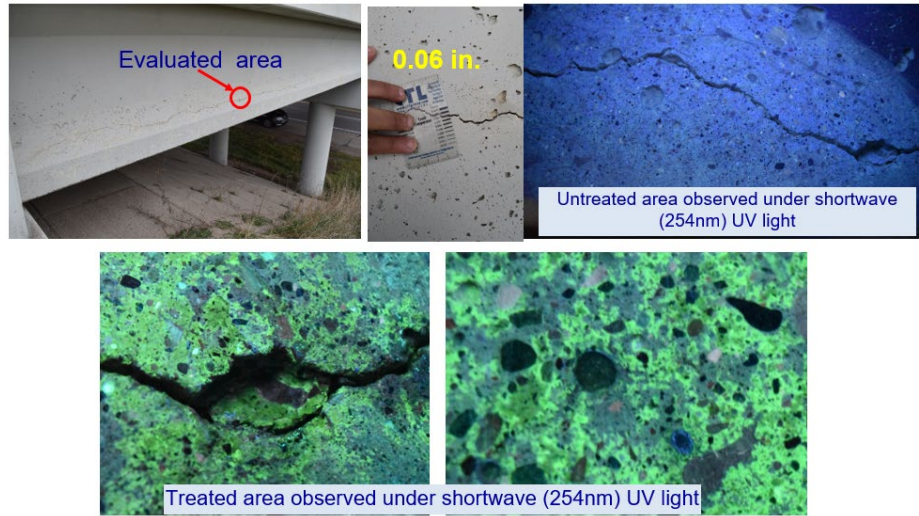


Figure 3-11. Structure 12775 fascia beam: Surface condition and fine aggregate ASR



Figure 3-12. Concrete surface coating damage and lack of crack bridging ability

Another key observation is the dominance of map and longitudinal cracking in the fascia beams that are exposed to direct sunlight. The best example is the bridge (S.N. 2618) that carries M-57 over the Flint River in the Bay Region. As shown in Figure 3-13, since the bridge is parallel to the east-west direction, the outside surface of the south fascia beam bottom flange is exposed to sunlight for a considerable duration during a day. As shown in the figure, longitudinal cracks are located within the zone exposed to sunlight. Similar cracking is not observed in the north fascia beams. Further, the temperature gradient across the width and height of the beam draws moisture towards the heated surface developing favorable conditions for certain deterioration mechanisms such as ASR (Attanayake and Mazumder 2021). As shown in Figure 3-14, similar conditions are recorded at other bridges. Hence, the use of breathable coatings and sealants are required to protect

concrete. Since the moisture is drawn from inside to outside when a temperature gradient exists towards the exterior surface, all the exposed surface need to be sealed. Even though sealants and coatings can be conveniently applied on new beams at the fabrication yards, the effective service life needs to be considered when selecting the products. According to Radlinska et al. (2014), the effective service life of penetrating sealants, coatings, and protective systems ranges from 6 to 10 years, 11 to 15 years, and 16 to 20 years, respectively. However, the effectiveness of these applications depends on the quality of the substrate and application parameters.



(a) Plan view of the bridge (image credit: Google.com)

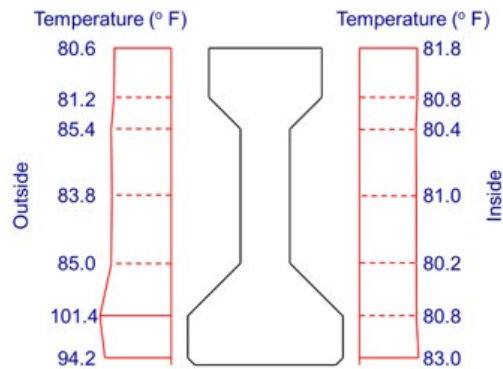


(b) Bottom flange of south fascia beam



(c) Bottom flange showing longitudinal cracks

Time: 16.01
Ambient Temperature = 88° F



(d) Surface temperature

Figure 3-13. Orientation and exposure of the bridge carrying M-57 over Flint River



(a) Plan view of the bridge (image credit: Google.com)

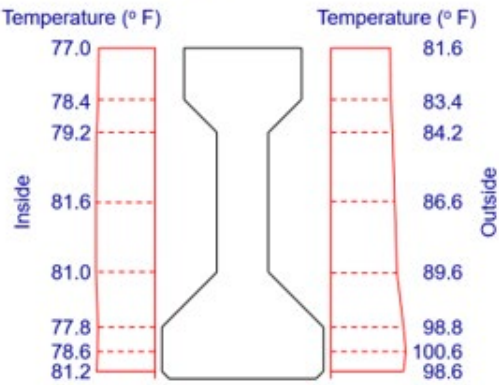


(b) East fascia beam (image taken from the south end)



(c) Outside surface of the bottom flange

Time: 11.51
Ambient Temperature = 84° F



(d) Surface temperature

Figure 3-14. Orientation and exposure of the bridge carrying Lincoln Road over I-75

Since most of the longitudinal and map cracks are dominant over the bottom flange, bridge inventory data was further analyzed to identify bridges with such cracking. Hence, the bridges listed in Table 3-6 are recommended to be inspected at arm’s length to develop maintenance and repair strategies. Figure 3-15 shows the geographic distribution of those bridges. An interactive ArcGIS map is provided as a deliverable of this project for MDOT to find necessary information about these bridges.

Table 3-6. Number of Bridges Showing Concrete Deterioration in PSC I-Beams

Region	Total no. of PSC I-beam bridges	No. of bridges with possible material distress in girders	Percentage of bridges with possible material distress in girders (%)
Bay	253	21 (3) ¹	8.30
Grand	221	15 (2)	6.79
Metro	242	25 (4)	10.33
North	63	6 (4)	9.52
Southwest	122	17	13.93
Superior	37	0	0
University	198	52 (2)	26.26
Total	1136	136	11.97

¹ The number of bridges with map and/or longitudinal cracks documented only in the most recent inspection report or the last two inspection reports.

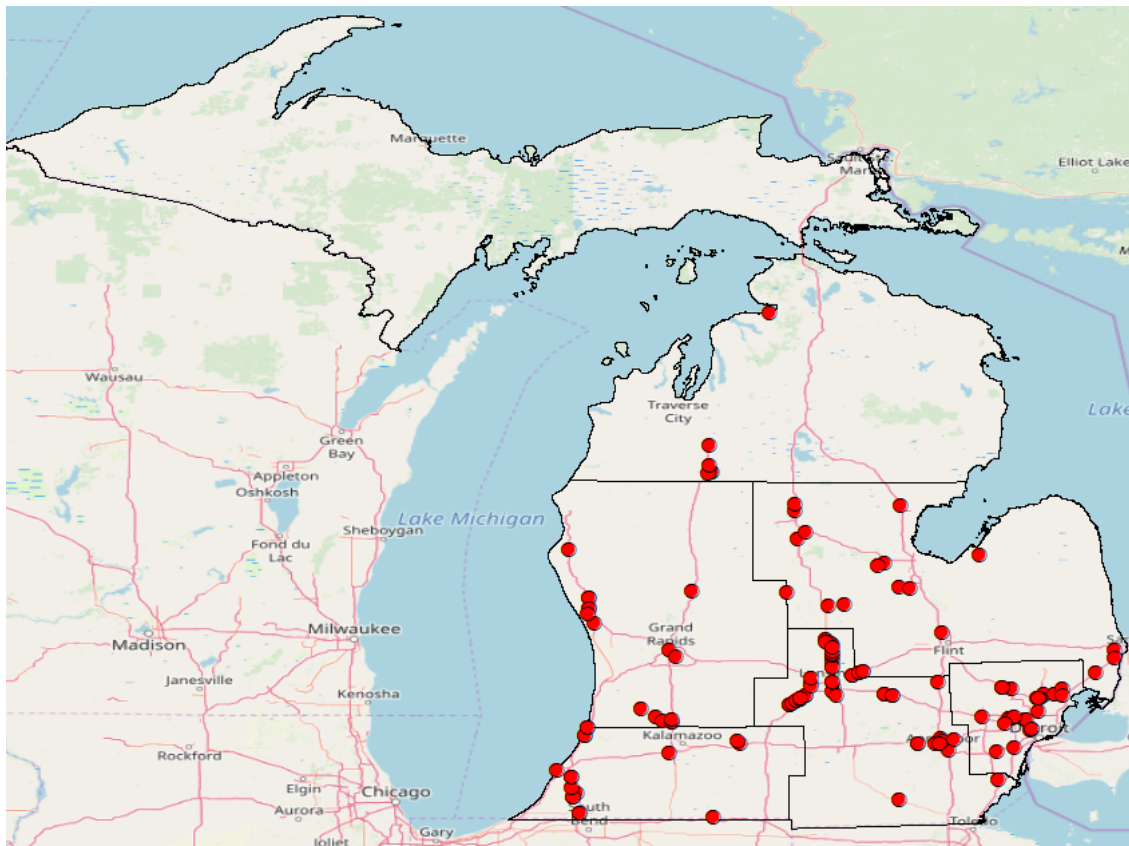


Figure 3-15. Geospatial distribution of bridges with potential material distress in I-beams

3.4.3 Concrete Deterioration in the Kalamazoo River Bridge Beams

The three-span, PSC I-beam bridge (S.N. 143) that carries US-131 SB over the Kalamazoo River is located in Allegan County, Michigan. The bridge was built in 1996. Each span consists of nine PSC I- beams. The latest inspection reported superficial map cracking and longitudinal cracking along the entire length of the fascia beams. The longitudinal cracks were on the top of the bottom flange along with scattered horizontal cracks on the outside of the bottom flange. Most of the cracks were epoxy injected and repaired. Even though the fascias were surface coated in 2013, the paint is cracked and peeled, exposing the cracks. A piece of concrete was collected from the south end of the east fascia beam and used for thin section petrography, Scanning Electron Microscopy (SEM) and Energy Dispersive X-ray Spectroscopy (EDS) analyses, along with a uranyl acetate ASR screening test to determine the causes of deterioration. Appendix C presents bridge details, beam condition, specimen details, along with the advanced analysis conducted for causal evaluation of concrete deterioration. The investigations revealed the presence of (i) adequate amount of entrained air, (ii) a very small portion of ASR susceptible fine aggregate, (iii) shallow microcracks extending inward along the flat, formed and painted side of the specimen; and (iv) deterioration mechanisms other than ASR.

3.4.4 Concrete Deterioration in the Brady Street Bridge Beams

The bridge (S.N. 12314) that carried Brady Street over the lower branch of the Rouge River was a single span with side-by-side box-beams located in Wayne County, Michigan. The bridge was built in 1994. This bridge comprised a total of 16 single cell, 39 in. deep and 36 in. wide box-beams. Due to significant deteriorations in the beams, this bridge was demolished during the last week of March 2020, after being in service for 26 years. The latest inspection reports indicated typical deteriorations such as widespread longitudinal cracking at the bottom flange of many beams. These cracks were mostly concentrated towards the north end of the bridge and extended up to 1/4th of the span. In addition to longitudinal cracking, concrete spall, corroded and broken strands, exposed strands, and efflorescence were documented. An inspection of beam soffits at “arm’s length” showed severe deteriorations with significant random cracking towards the north end of the beams. Significant scaling on box beam webs and ends was observed after removing the beams. Such cracking and deterioration are atypical to prestressed beams. Specimens collected during bridge demolition were used to prepare concrete prisms and evaluate the potential for

having ASR and DEF. Also, a thin section petrography and SEM-EDS analyses were conducted. Appendix D presents bridge details, beam condition, specimen details, along with experimental procedures and findings.

Concrete prisms taken from beam webs eliminated any concerns related to the impacts of DEF. Uranyl acetate testing on specimens extracted from beam ends showed ASR in fine aggregate. The ASR potential of fine aggregate was confirmed by measuring the expansion of concrete prisms taken from beam webs under 1N NaOH exposure at 176° F, and subsequent uranyl acetate testing. The petrography analysis results confirmed the presence of ASR in fine aggregate. Another major contributor to concrete deterioration was the low air content, 2 to 3%, as per the petrography analysis report. Significant scaling was observed at the north ends of the beams and concealed webs, an indication of freeze-thaw damage. North ends of beams were exposed to surface water due to the road profile. However, the concerns regarding salt scaling of beam ends were eliminated since EDS analysis did not find Cl⁻ in the collected specimens. Water seeped through the longitudinal joints, accumulated inside the airpockets in the grouted shear keys, and contributed to the freeze-thaw damage of beam webs. Even though salt scaling could be another mechanism to cause similar damages, verification testing was not conducted using beam web specimens during this investigation. SEM-EDS results confirmed the presence of ettringite at the severely deteriorated beam ends. Freeze-thaw is identified as the most probable primary concrete deterioration mechanism. Once the beam end concrete was severely cracked, ettringite filled the cracks.

The findings highlight the need for enhancing inspection guidelines to identify bridges with similar deteriorations, improving concrete quality control to assure an adequate amount of entrained air in hardened concrete, encouraging the use of fine aggregate with a good record of performance against ASR, and protecting girders from surface runoff.

3.5 DEPTH OF CRACKS IN PSC I-BEAMS

The depth of longitudinal cracks in two PSC I-beams was evaluated. Before implementing the technology under field conditions, the capabilities and limitations of ultrasonic shear wave tomography (also known as the linear array technique) and synthetic aperture focusing technique (SAFT) to detect the depth of cracks in concrete elements were evaluated. To accomplish this, a type of commercially available ultrasonic shear wave tomography equipment, the Proceq Pundit

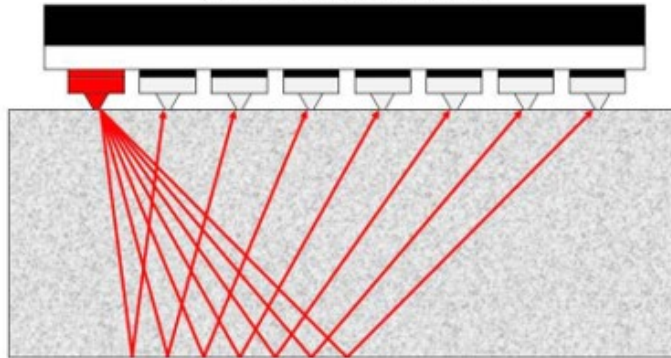
250 Array, was used to collect data on three concrete slabs with simulated cracks. The data was processed using the *InterSAFT* (Interactive Synthetic Aperture Focusing Technique) software of which the fundamentals, capabilities, and limitations are discussed in Mayer et al. (2008), Mayer et al. (2012), and Attanayake et al. (2018). A process for data collection and analysis was developed based on the experience gained by working with the simulated cracks; it was then implemented on two PSC I-beams to estimate crack depth under field conditions.

3.5.1 Device Description

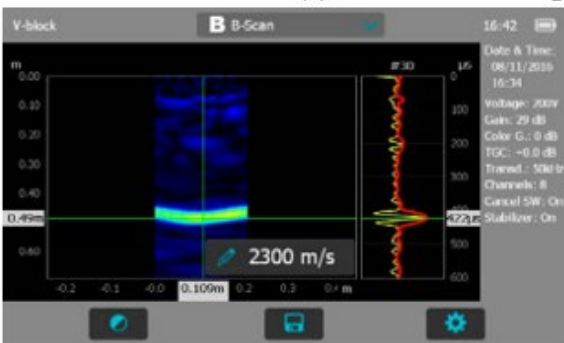
The Pundit 250 Array (shown in Figure 3-16a) has 3 rows and 8 columns of dry-point contact transducers with a total of 24 transducers. When one column transmits, the echoes are received by the remaining seven columns, as shown in Figure 3-16b. Each column transmits sequentially in return, except the last one. Each cycle produces a total of 28 A-scans. These 28 A-scan signals are processed using the synthetic aperture technique to develop B-scans, as shown in Figure 3-16c. B-scans are displayed in real-time on the measurement screen. In addition, a panorama B-scan can be created by stitching individual B-scans together to make a larger image. Panorama B-scans are used to identify the extent of defects within structures. For panorama B-scans, the instrument is moved along a single line with or without an overlap at the borders. Figure 3-16d shows a panorama B-scan constructed using 8 individual B-scans with overlap corresponding to two channels. Table 3-7 shows the technical specifications of the Pundit 250 array.



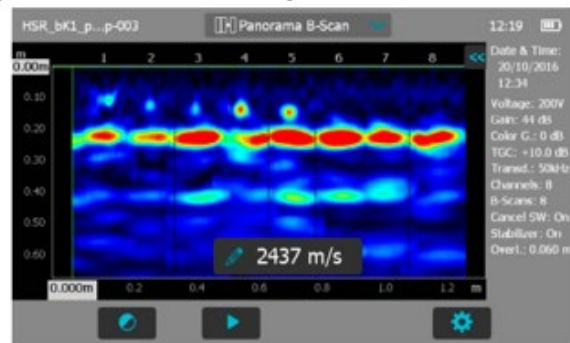
(a) Proceq Punit 250 array



(b) Transducer scanning configuration of Punit 250 array



(c) Real-time B-scan



(d) Panorama B-scan

Figure 3-16. Proceq Punit 250 array unit (Proceq 2017)

Table 3-7. Technical Specifications of the Pundit 250 Array (Proceq 2017)

Gain (dB)	0 – 80
Analog bandwidth (kHz)	15 – 100
Nominal transducer frequency (kHz)	50 (shear wave)
Range (μ s)	0 – 1000
Resolution (μ s)	1
Pulse voltage (V)	+/-150
Pulse shape	Rectangle
Pulse delay (ms)	8 – 200
Number of channels	8 (can be extended to 16)
Transducers per channel	3
Wave type	Shear wave, horizontally polarized
Center frequency (kHz)	Approximately 45
Transducer bandwidth (%)	80 – 100
Channel distance (in.)	1.18
Aperture size (in.)	8.27×1.97
Battery lifetime (hrs)	7
Dimensions (in.)	$9.45 \times 10.75 \times 6.02$
Weight (lbs)	6.61
Operating temperature ($^{\circ}$ F)	14 to 122
Humidity (%)	< 95 RH, non-condensing

3.5.2 Crack Depth Evaluation Using Laboratory Specimens

3.5.2.1 Specimen Details

Three $12 \times 12 \times 5.5$ in. concrete slab specimens were used. A 12 in. long and 0.155 in. wide saw cut was made at the top surface of each specimen, as shown in Figure 3-17a. The saw cut depths were 0.5, 1.25, and 1.75 in. Figure 3-17a shows one of the specimens with a 2×2 in. measurement grid. Figure 3-17b shows the measurement grid with coordinates. The elevation view of the slab is shown in Figure 3-17c. The crack is centered on the scanning grid and located along the line $x = 5$.

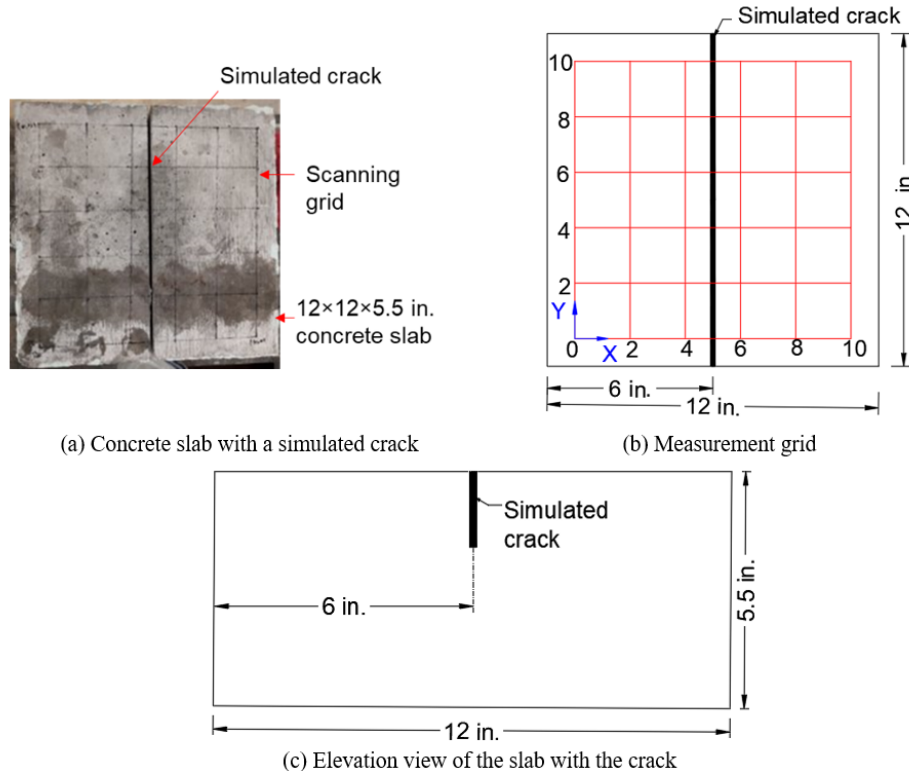


Figure 3-17. Concrete slab with a simulated crack

3.5.2.2 Data Collection Procedure

Data was collected by placing the array in three distinct arrangements:

1. *Arrangement-1*: the excitation direction was parallel to the crack, and the unit was placed symmetrically over the crack (Figure 3-18). The data was collected at two sections by placing the middle row of transducers along the lines $y = 3$ and $y = 7$.
2. *Arrangement-2*: the excitation direction was parallel to the crack, but the unit was placed offset from the crack (Figure 3-19). The data was collected at two sections by placing the middle row of transducers along the lines $y = 3$ and $y = 7$.
3. *Arrangement-3*: the excitation direction was perpendicular to the crack, and the unit was placed symmetrically over the crack (Figure 3-20). The data was collected only at one section by placing the middle row of transducers along the line $x = 5$.

The objective of all three scanning arrangements was to evaluate the impact of each arrangement on the calculation of crack depth. Unlike with the laboratory specimens, all the transducer columns may not be able to develop adequate contact with the measurement surface of field structures. As an example, the bottom flange of a PSC I-beam may not have an adequate width to support all 24 transducers of the Pundit 250 array. Hence, one must evaluate how the

absence of a set of transducers impacts data and results. Thus, *Arrangement-2* was used to evaluate the feasibility of estimating the crack depth with an instrument offset from the crack; it excluded data from a set of transducers.

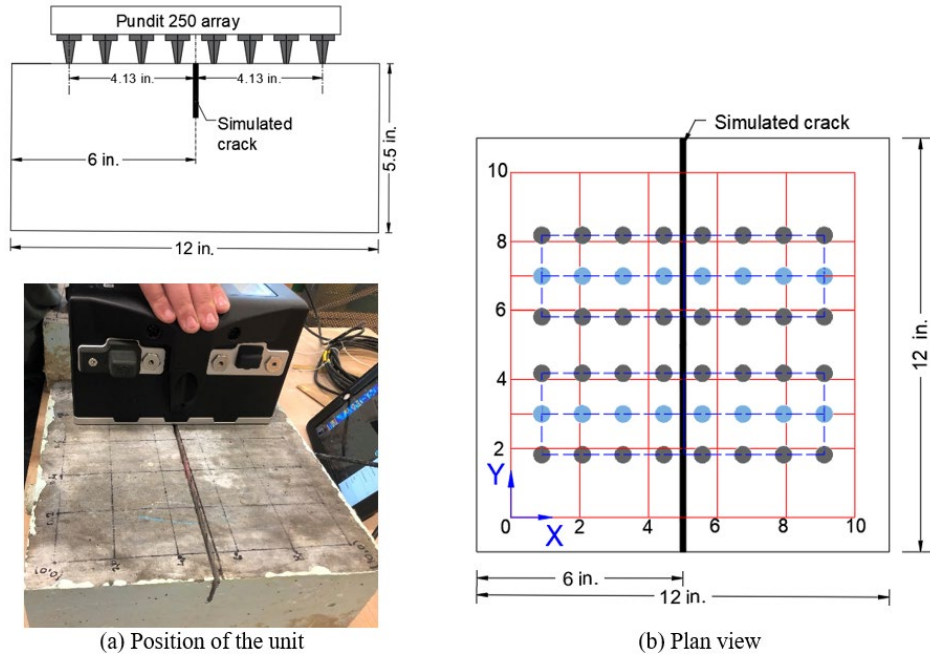


Figure 3-18. Arrangement-1: Excitation direction parallel to the crack and the unit placed symmetrically over the crack

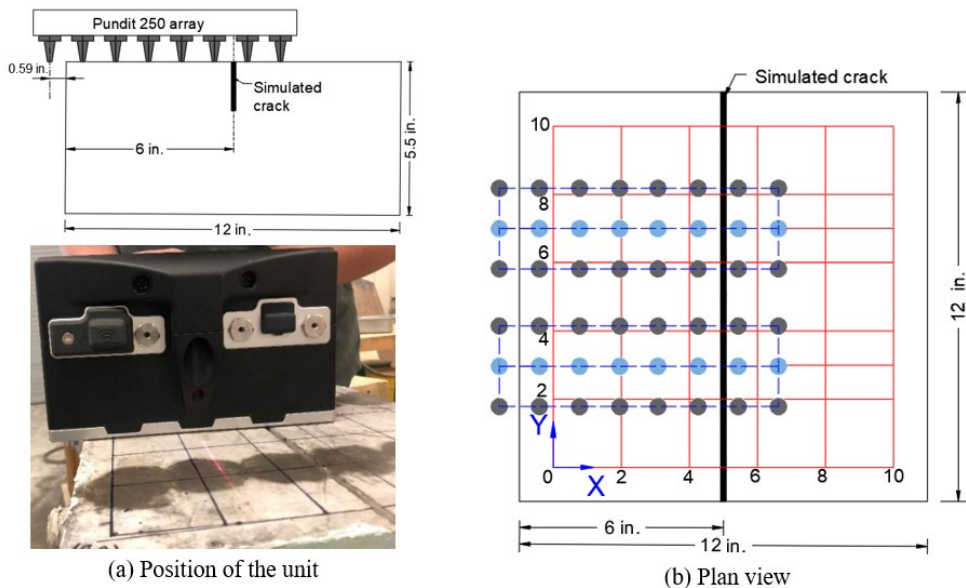


Figure 3-19. Arrangement-2: Excitation direction parallel to the crack and the unit placed offset from the crack

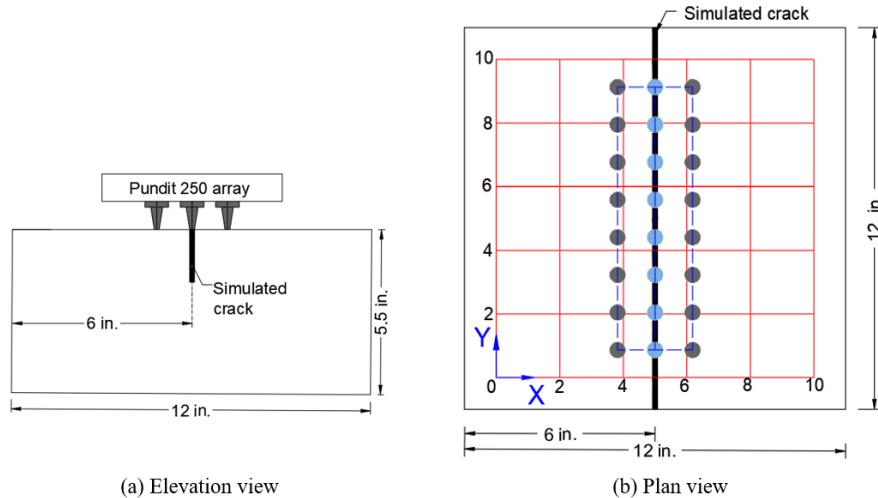


Figure 3-20. Arrangement-3: Excitation direction perpendicular to the crack and the unit placed symmetrically over the crack

3.5.2.3 Data Analysis

The data was processed to reconstruct B-scans and calculate crack depths. The data was analyzed using a propriety software, *InterSAFT* (Interactive Synthetic Aperture Focusing Technique), which is commercially available as Pundit Vision (Screening Eagle Technologies 2021). The raw data collected from the Pundit 250 array was converted from csv format to ghk format. The converted ghk data files were imported to *InterSAFT* to reconstruct the scan images. The software allows selecting groups of transducers as transmitters and receivers. This option allows duplicating the typical transmitter-receiver arrangement to measure a crack depth, but with an array of transmitters and receivers instead of single transducers. Further, this option provides a large aperture and an array of dry-point contact transducers to overcome the limitations of traditional methods. When processing the scans, a selected number of transducer columns was chosen as transmitters and receivers to obtain a particular set of data to construct B-scans. Figure 3-21 shows the available options for selecting transducer combinations.

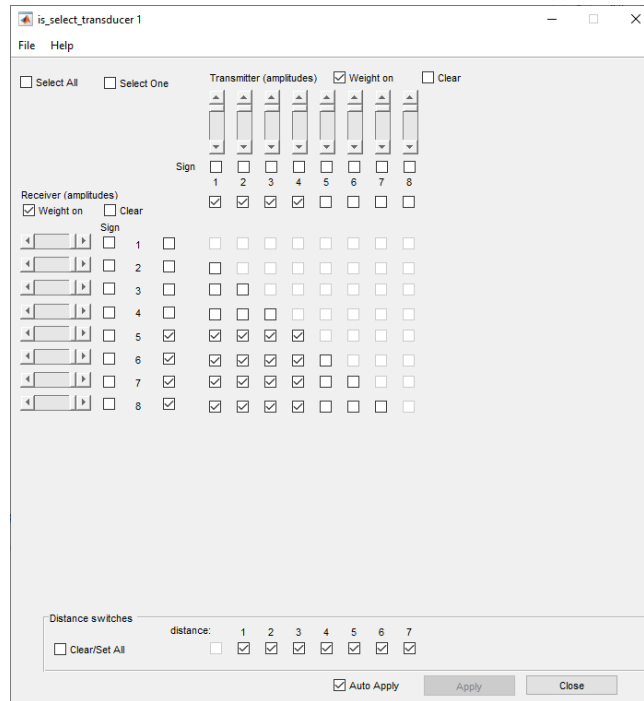
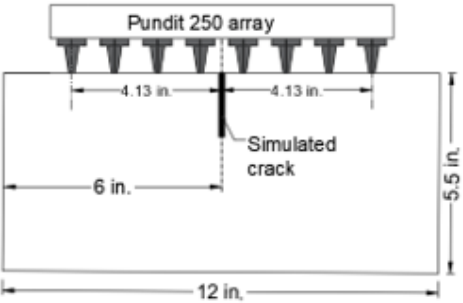
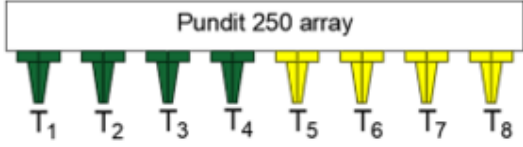
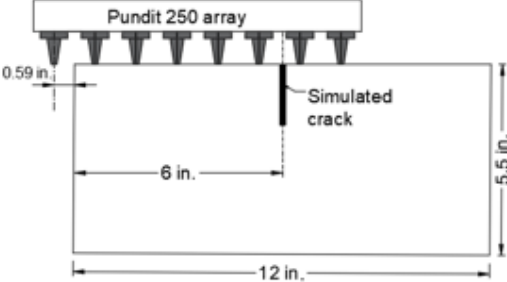
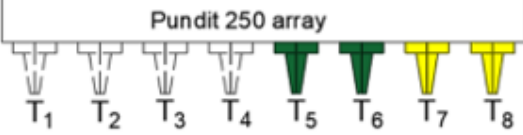
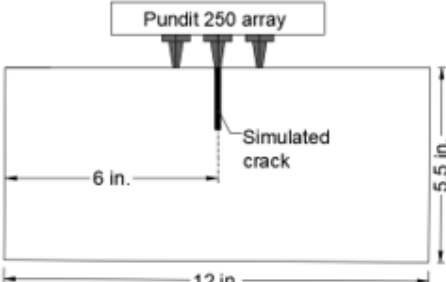
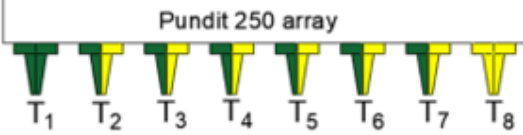



Figure 3-21. The options available in *InterSAFT* to select transducer combinations

Table 3-8 lists the selection of transducers for the analysis of data collected using three distinct arrangements of the array with respect to the crack. As an example, two sets of transducers were selected as transmitters and receivers to analyze the data collected using *Arrangement-1*. To develop the 1st set of transmitter-receiver combinations, T₁ to T₄ columns and T₅ to T₈ columns were selected as transmitters and receivers, respectively. To develop the 2nd set of transmitter-receiver combinations, T₃ and T₄ columns and T₅ and T₆ columns were selected as transmitters and receivers, respectively. To analyze the data collected using *Arrangement-2*, T₅ to T₆ columns and T₇ to T₈ columns were selected as transmitters and receivers, respectively. For the *Arrangement-3*, T₁ to T₇ columns and T₂ to T₈ columns were selected as transmitters and receivers, respectively. Figure 3-21 shows the selection of T₁ to T₄ columns and T₅ to T₈ columns as transmitters and receivers, respectively.

The pulse velocity was estimated using the surface wave module. The estimated pulse velocity was used as the starting velocity during the reconstruction process. This starting velocity was increased or decreased until the backwall reflections were observed at the depth of the slab specimens (5.5 in. or 139.7 mm). The reconstructed scans were further refined using deconvolution and filtering techniques.

Table 3-8. Transducer Groups Selected for the Reconstruction of B-Scans

Array placement	Selection of transducer columns for data analysis
<p><i>Arrangement-1:</i></p> 	 <p>Transmitters: T₁ to T₄ Receivers: T₅ to T₈</p>
<p><i>Arrangement-2:</i></p> 	 <p>Transmitters: T₃ to T₄ Receivers: T₅ to T₆</p>
<p><i>Arrangement-3:</i></p> 	 <p>Transmitters: T₁ to T₇ Receivers: T₂ to T₈</p>
<p>Legend:</p>  <p>Transmitter Receiver Transmitter/Receiver</p>	

3.5.2.4 Results and Discussion

The *surface waves* module in *InterSAFT* allows calculating shear wave velocity at the surface. Also, the graphical output indicates the presence of disturbances to the waves. Figure 3-22a shows a contour plot with straight, horizontal color bands indicating the presence of undisturbed shear waves at the surface. The presence of a surface crack disturbs surface wave propagation. The level of disturbance can be evaluated by analyzing surface wave profile around a crack. Figure 3-22 shows the impact of crack depth and transducer arrangement on surface wave propagation. As indicated by the discontinued color bands in Figure 3-22b, deeper cracks (1.25 in. and 1.75 in.) significantly impacted the propagation of shear waves at the surface when the transducer array was placed symmetrically over the crack with the excitation direction parallel to the crack. The influence of the shallower crack (0.5 in.) is minimal. As shown in Figure 3-22c, irrespective of the crack depth, undisturbed shear waves are present at the surface when the unit was placed symmetrically over the crack with the excitation direction perpendicular to the crack. The results show that the transducer array needs to be placed symmetrically over the crack with the excitation direction parallel to the crack for the detection of cracks. Since the shallow cracks (with a depth of about 0.5 in.) have a minimum influence on the shear waves at the surface, the calculated depth of such cracks will not be that accurate. The impact of crack width on measurements is unknown since a constant crack width of 0.155 in. was maintained in all three slabs.

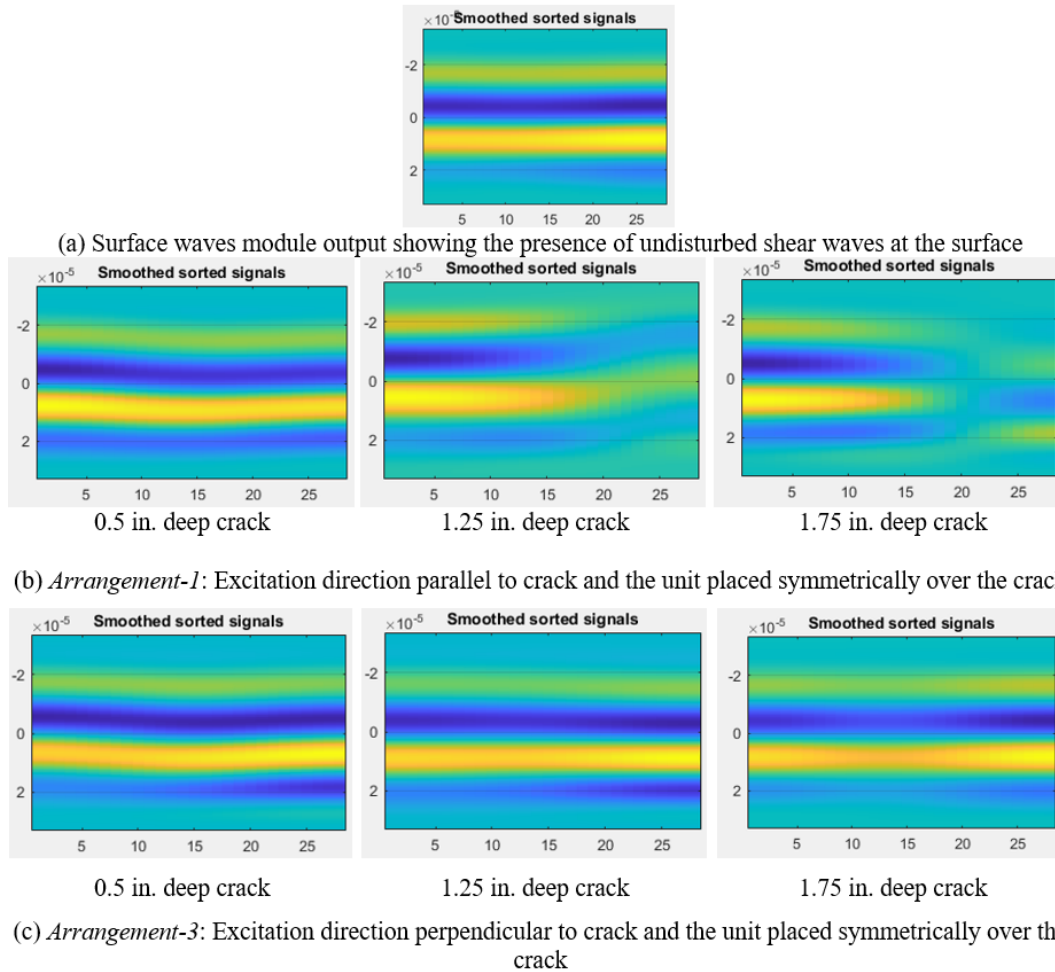


Figure 3-22. The impact of crack depth and transducer arrangement on surface wave propagation

The selection of a set of transducers as transmitters and receivers impacts the quality of B-scans produced from the UPV data collected across a crack. As indicated by the discontinued color bands in Figure 3-22b, the 1.25 and 1.75 in. deep cracks impact the propagation of shear waves at the surface when the data was collected using *Arrangement-1*. Therefore, two transmitter-receiver combinations were selected to process the data collected using *Arrangement-1* and produce B-scans, as shown in Figure 3-23. The selection of T₁ to T₄ columns of transducers as transmitters and T₅ to T₈ columns of transducers as receivers (see Figure 3-23b) produced better reflections at the actual crack tip location: as compared to the selection of T₁ to T₇ columns of transducers as transmitters and T₂ to T₈ columns of transducers as receivers (see Figure 3-23a). The results show that having transmitters on one side of the crack and receivers on the other side, depicting the traditional transmitter-receiver arrangement across a crack, produces better B-scans to estimate crack depth.

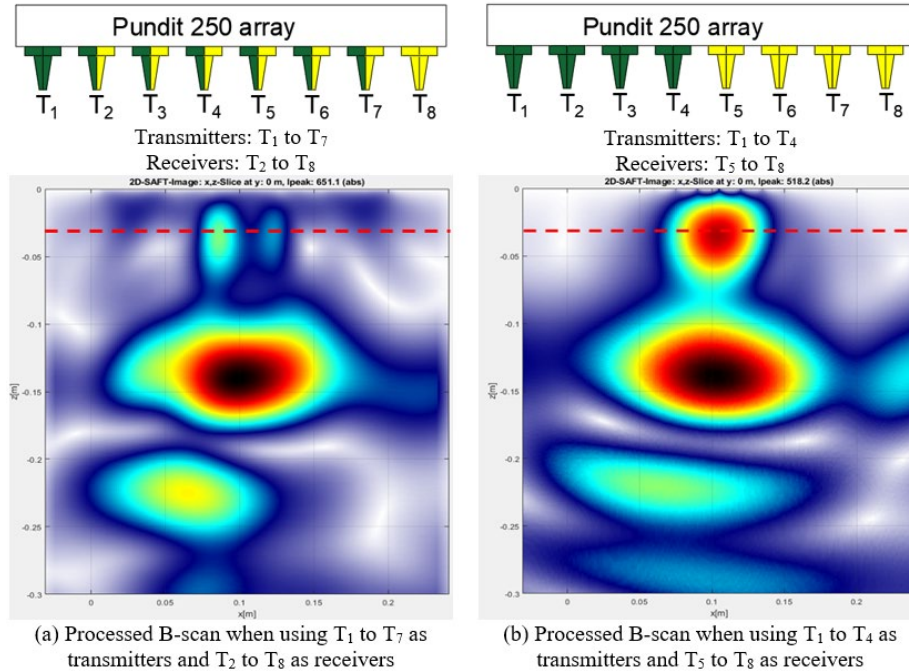


Figure 3-23. Processed B-scans using *Arrangement-1* data with two transmitter-receiver combinations for the slab with a 1.25 in. deep crack

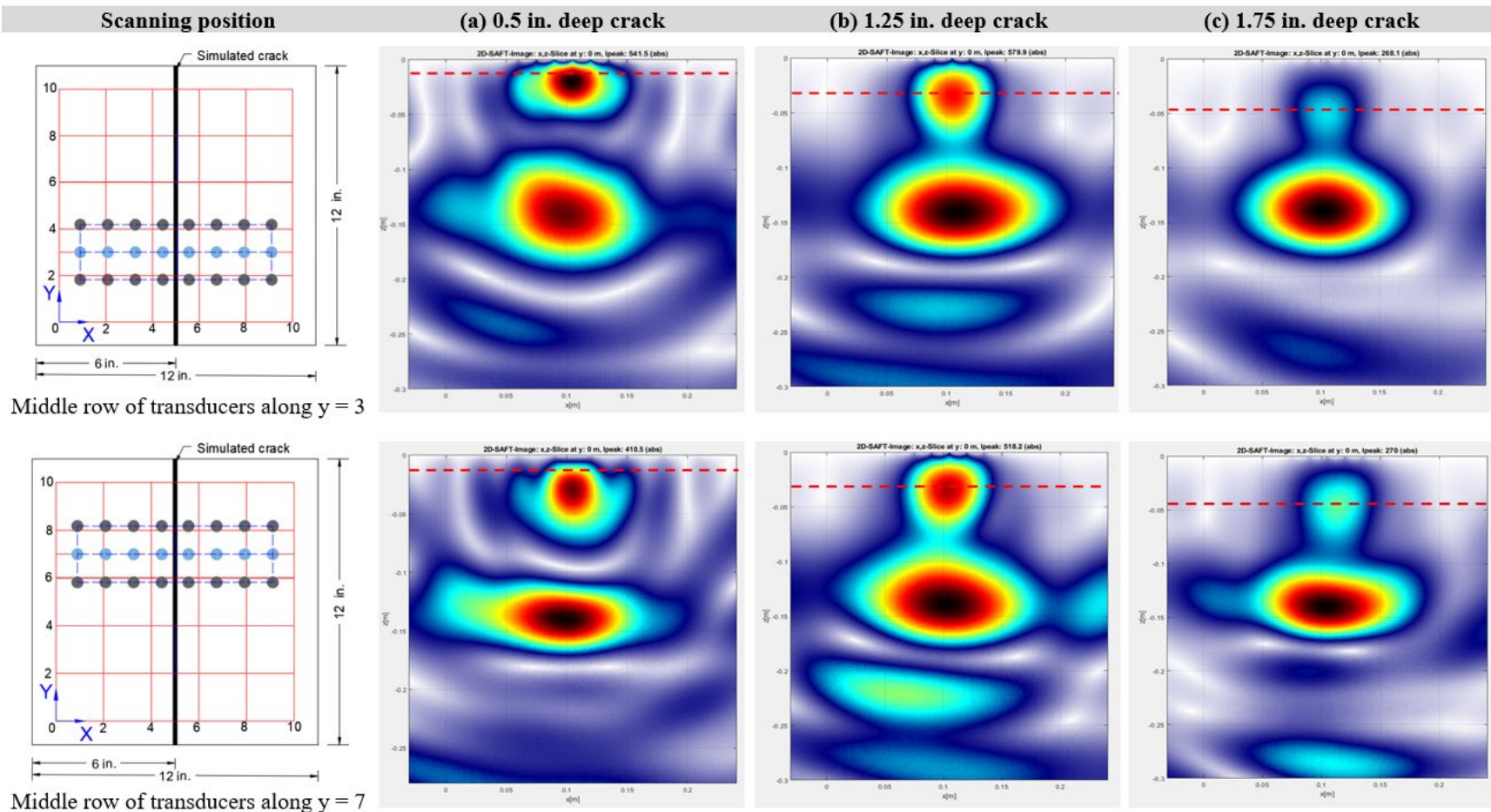
(The red dashed line shows the crack tip location at 1.25 in. or 31.75 mm.)

The reconstructed B-scans were analyzed to estimate the depth of cracks in each specimen and compared with the crack depth measured with a Vernier caliper. The data collected using *Arrangement-1* with T₁ to T₄ as transmitters and T₅ to T₈ as receivers was analyzed to produce the B-scans shown in Figure 3-24. The figure shows the processed B-scans for the slabs with 0.5 in., 1.25 in., and 1.75 in. deep cracks. The physical location of the crack tip in each slab is indicated by a red dashed line. As shown in Figure 3-24, the scans produced using the data from two scanning positions are similar for all three slabs. The backwall reflection is observed at the 5.5 in. (139.7 mm) depth. The signal strength around the tips of 0.5 in. and 1.25 in. deep cracks is stronger (see Figure 3-24a and Figure 3-24b). The 1.75 in. deep crack resulted in a low-intensity reflection at the crack tip (see Figure 3-24c). These reflections are observed at the vertical centerlines of the B-scans (i.e. about $x = 0.1$ m). As shown in Figure 3-24a, the reflection around the crack tip locations observed in the slab with a 0.5 in. deep crack is slightly offset vertically towards the backwall. The reflections observed in the slabs with 1.25 in. and 1.75 in. deep cracks are centered about their corresponding crack tip locations in the slabs (see Figure 3-24b and Figure 3-24c).

The data collected using *Arrangement-1* with T₃ to T₄ as transmitters and T₅ to T₆ as receivers was analyzed to produce the B-scans shown in Figure 3-25. The figure shows the

processed B-scans for the slabs with 0.5 in., 1.25 in., and 1.75 in. deep cracks. The physical location of the crack tip in each slab is indicated by a red dashed line. As shown in Figure 3-25, the scans produced using the data from two scanning positions are similar for all three slabs. The backwall reflection is observed at the 5.5 in. depth. A weak backwall reflection is observed in the slab with a 0.5 in. deep crack. The signal strength around the tips of the 0.5 in. and 1.25 in. deep cracks are stronger (see Figure 3-25a and Figure 3-25b). The 1.75 in. deep crack resulted in a low-intensity reflection at the crack tip (see Figure 3-25c). These reflections are observed at the vertical centerlines of the B-scans (i.e. about $x = 0.1$ m). As shown in Figure 3-25a, the reflection around the crack tip locations observed in the slab with 0.5 in. deep crack is slightly offset vertically towards the backwall. The reflections observed in the slabs with 1.25 in. and 1.75 in. deep cracks are centered about their corresponding crack tip locations in the slabs (see Figure 3-25b and Figure 3-25c).

The data collected using *Arrangement-2* with T_5 to T_6 as transmitters and T_7 to T_8 as receivers was analyzed to produce the B-scans shown in Figure 3-26. The figure shows the processed B-scans for the slabs with 0.5 in., 1.25 in., and 1.75 in. deep cracks. As shown in Figure 3-26a, the scans produced at the two scanning positions are similar for the slab with a 0.5 in. deep crack. In all the slabs, the backwall reflection is observed at the 5.5 in. depth. The signal strength around the tips of 1.25 in. and 1.75 in. deep cracks is affected by the scanning position and requires additional testing to evaluate the reasons. The reflections are observed at an offset from the vertical centerline of the B-scans (i.e. between $x = 0.15$ m and $x = 0.2$ m), as expected from the offset of the transducer array used in *Arrangement-2*. In the slabs with 1.25 in. and 1.75 in. deep cracks, the bottom edge of the reflections corresponds to the physical locations of crack tips in the slabs (see Figure 3-26b and Figure 3-26c). As shown in Figure 3-26a, the reflection around the 0.5 in. deep crack is slightly offset vertically towards the backwall.



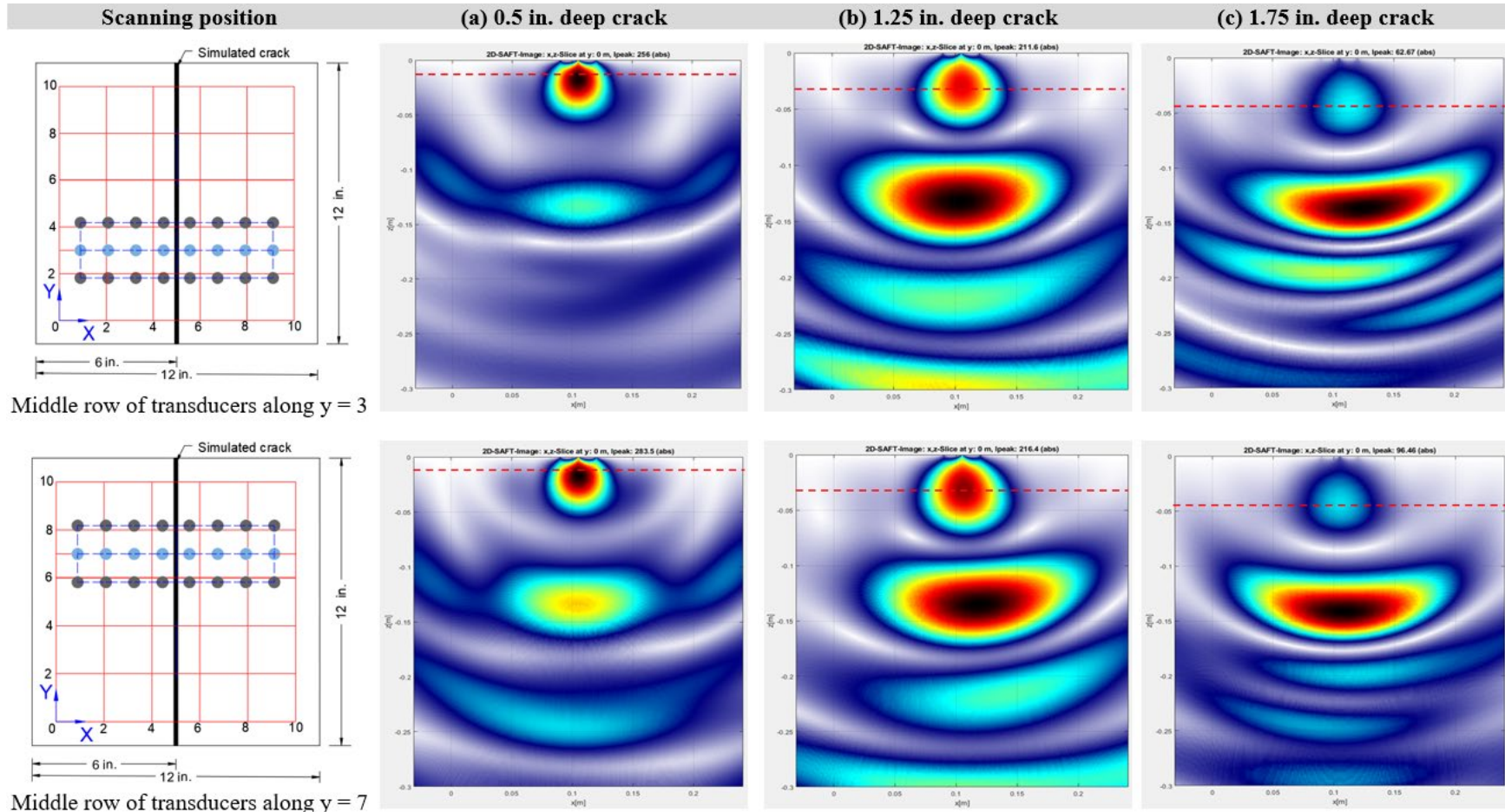


Figure 3-25. B-scans of slabs reconstructed using *Arrangement-1* data with T_3 to T_4 as transmitters and T_5 to T_6 as receivers
(The red dashed lines represent the crack tip locations in the slabs.)

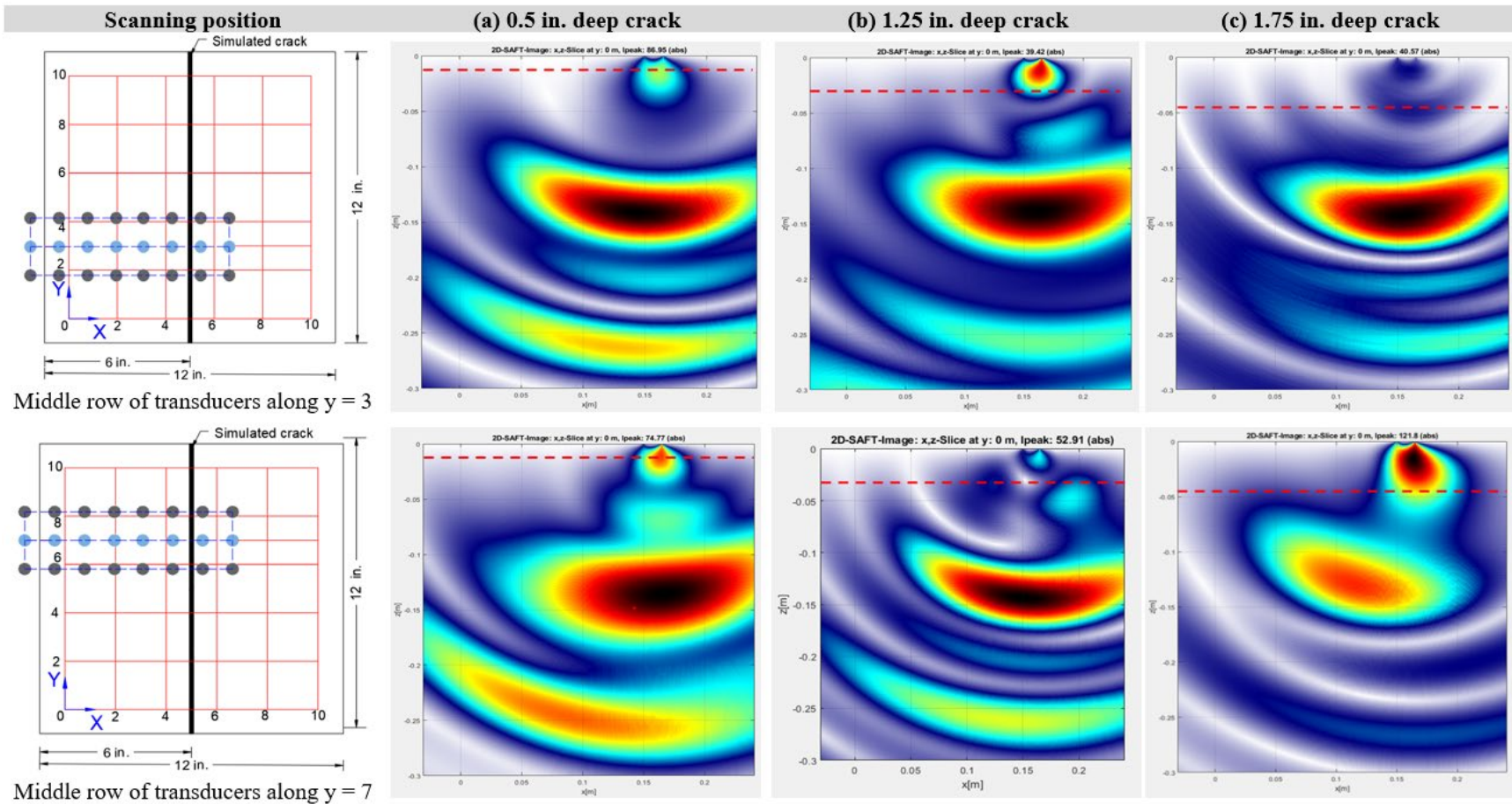


Figure 3-26. B-scans of slabs reconstructed using *Arrangement-2* data
 (The red dashed lines represent the crack tip locations in the slabs.)

The data collected using *Arrangement-3* with T_1 to T_7 as transmitters and T_2 to T_8 as receivers was analyzed to produce the B-scans shown in Figure 3-27. The figure shows the processed B-scans for the slabs with 0.5 in., 1.25 in., and 1.75 in. deep cracks. As shown in Figure 3-27a, the backwall reflection is only observed in the slab with a 0.5 in. deep crack. Establishing backwall reflections at the correct depth is necessary to calculate the pulse velocity required to produce calibrated B-scans. The lack of a backwall reflection makes it harder to accurately estimate a pulse velocity. Therefore, the initial velocity estimated using the surface wave module was used to produce B-scans shown in Figure 3-27b and c. Reflections were not observed around the 0.5 in. deep crack. The bottom edges of the high-intensity reflections observed with 1.25 in. and 1.75 in. deep cracks correspond to the crack tips in the slabs (see Figure 3-27b and c). Since B-scans were not calibrated, the results can only be used to indicate the presence of a possible crack.

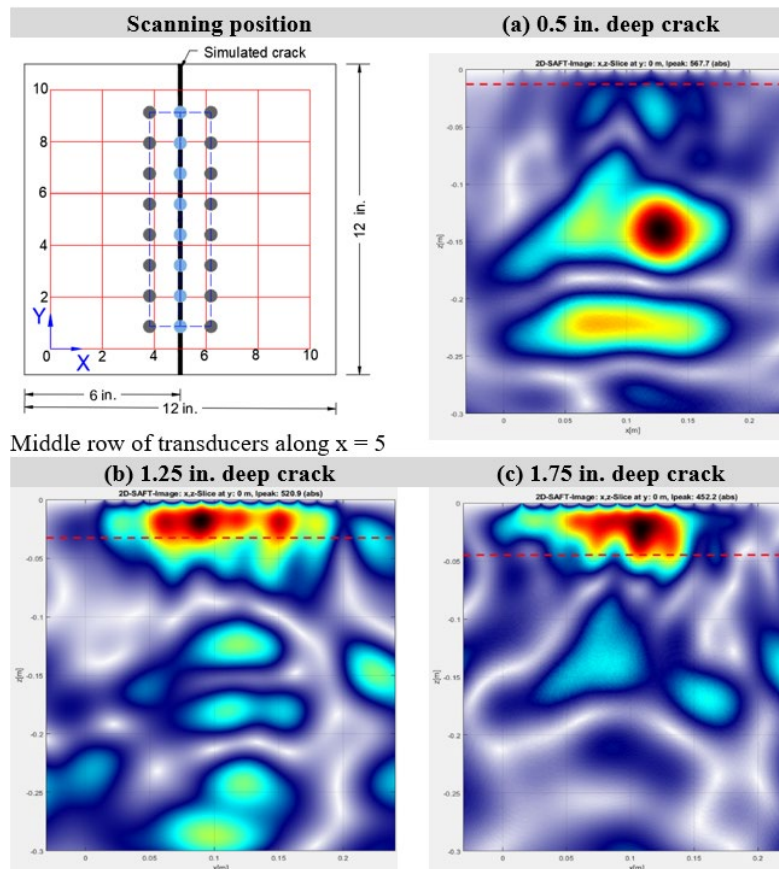


Figure 3-27. B-scans of slabs reconstructed using *Arrangement-3* data
(The red dashed lines represent the crack tip locations in the slabs.)

Based on the processed B-scans in Figure 3-24 to Figure 3-27, crack depths were estimated and are summarized in Table 3-9. The crack depth is estimated to the center of the reflections in the B-scans developed from the data collected with transducer *Arrangement-1*. The crack depth is estimated to the bottom of the reflections in the B-scans developed using the data collected with transducer *Arrangement-2* and 3. For deeper cracks (1.25 and 1.75 in.), all three transducer arrangements produced approximate results to the actual crack depth, compared to the shallower crack (0.5 in.). However, the most consistent results were obtained from the data collected using transducer *Arrangement-1* and analyzed using T₁ to T₄ as transmitters and T₅ to T₈ as receivers. *Arrangement-1* with T₁ to T₄ as transmitters and T₅ to T₈ as receivers represents the traditional single transmitter and receiver arrangement across a crack with compression waves; however, *Arrangement-1* has a large aperture and uses shear waves.

Table 3-9. Estimated Crack Depth in Slabs

Transducer arrangement	Position of the middle row of transducers	Estimated crack depth ¹ for		
		0.5 in. (12.7 mm) deep crack in. (mm)	1.25 in. (31.75 mm) deep crack in. (mm)	1.75 in. (44.45 mm) deep crack in. (mm)
<i>Arrangement-1:</i> Excitation direction parallel to crack and the unit placed symmetrically over the crack Transmitters: T ₁ to T ₄ Receivers: T ₅ to T ₈	Along y = 3	0.76 (19.28)	1.33 (33.83)	1.74 (44.10)
	Along y = 7	1.11 (28.27)	1.33 (33.83)	1.74 (44.10)
<i>Arrangement-1:</i> Excitation direction parallel to the crack and the unit placed symmetrically over the crack Transmitters: T ₃ and T ₄ Receivers: T ₅ to T ₆	Along y = 3	0.67 (17.14)	1.18 (29.98)	1.60 (40.68)
	Along y = 7	0.67 (17.14)	1.15 (29.12)	1.58 (40.25)
<i>Arrangement-2:</i> Excitation direction parallel to the crack with the unit placed offset to the crack Transmitters: T ₅ and T ₆ Receivers: T ₇ to T ₈	Along y = 3	1.01 (25.7)	0.94 (23.99)	NA ²
	Along y = 7	0.89 (22.7)	NA	1.65 (41.96)
<i>Arrangement-3:</i> Excitation direction perpendicular to the crack and the unit placed symmetrically over the crack Transmitters: T ₁ and T ₇ Receivers: T ₂ to T ₈	Along x = 5	NA	1.30 (33.00)	1.77 (44.95)

¹ – The most accurate estimated crack depth would be the value in mm. The values in mm were obtained from the processed B-scans and converted to inches.

² – Not available

3.5.3 Crack Depth Evaluation in PSC I-Beams

3.5.3.1 Fascia Beam of S.N. 424 Bridge

The Pundit 250 Array was used to scan a longitudinal crack on the inclined face of the bottom flange of an AASHTO Type III beam. This is the southern exterior beam of the bridge (S.N. 424) that carries Lincoln Road over I-75 southbound. Figure 3-28a shows the 4 × 4 in. measurement grid and the position of the longitudinal crack. The grid line $x = 0$ is at 84 in. from the backwall. As shown in Figure 3-28b, the unit was placed symmetrically over the crack with the excitation direction parallel to the crack (*Arrangement-1*). All the transducers were in contact with the measurement surface.

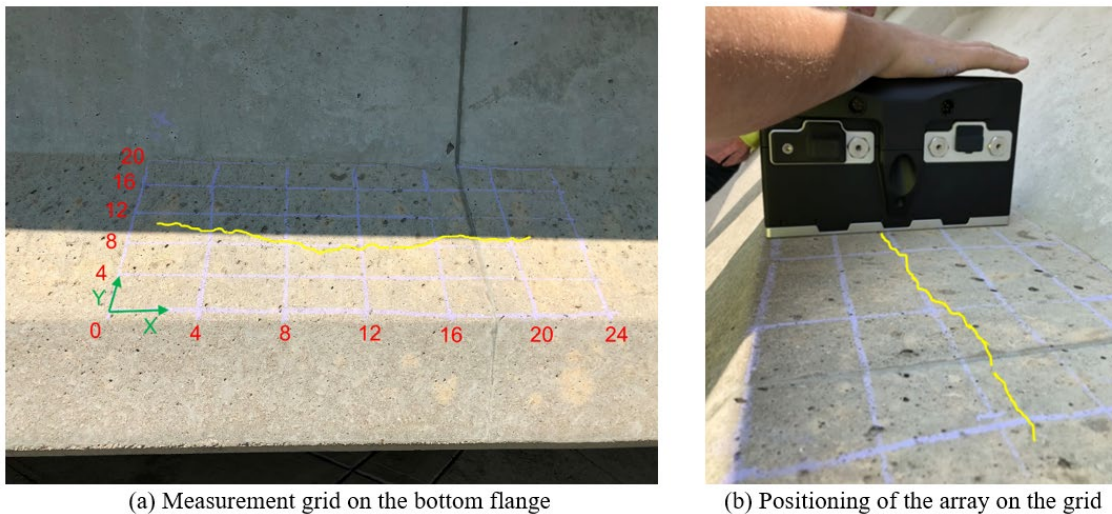


Figure 3-28. Measurement grid, crack location, and the array position on the fascia beam (S.N. 424)
(The yellow line shows the position of the longitudinal crack.)

The data was processed using the two transmitter-receiver combinations defined in Table 3-8 for *Arrangement-1*. Figure 3-29 and Figure 3-30 show the reconstructed B-scans with the middle row of transducers placed along the lines $x = 4$ to 20. The B-scans produced with the two transducer combinations were similar. As expected, a relatively lower intensity is observed in the B-scan reconstructed using T_3 to T_4 as transmitters and T_5 to T_6 as receivers, compared to using T_1 to T_4 as transmitters and T_5 to T_8 as receivers. The crack depth was estimated to the center of the significant reflection observed at the crack location and indicated by a red dashed line.

Table 3-10 shows the estimated depth at 5 locations along the crack and the measured crack widths at respective locations. Field verification of crack depth was not possible because the coring of in-service bridge beams is not allowed. Since laboratory studies using slabs yielded

accurate results with T₁ to T₄ as transmitters and T₅ to T₈ as receivers, the same transmitter-receiver combination was used to determine the most probable crack depths in the beam. Accordingly, as shown in column (c) of the table, the longitudinal crack depth in this beam varies between 0.99 in. (25.06 mm) and 2.24 in. (56.85 mm).

Table 3-10. The Depth of Longitudinal Cracking in a Fascia Beam (S.N. 424)

Position of the middle row of transducers (a)	Measured crack width in. (mm) (b)	Estimated crack depth¹ Transmitters: T₁ to T₄ Receivers: T₅ to T₈ in. (mm) (c)	Estimated crack depth¹ Transmitters: T₃ to T₄ Receivers: T₅ to T₆ in. (mm) (d)
Along x = 4	0.016 (0.406)	2.24 (56.85)	2.47 (62.84)
Along x = 8	0.013 (0.330)	1.70 (43.17)	1.78 (45.18)
Along x = 12	0.010 (0.254)	2.28 (57.85)	1.49 (37.87)
Along x = 16	0.010 (0.254)	0.99 (25.06)	1.07 (27.08)
Along x = 20	0.010 (0.254)	2.00 (50.85)	1.45 (36.87)

¹ – The most accurate estimated crack depth would be the value in mm. The values in mm were obtained from the processed B-scans and converted to inches.

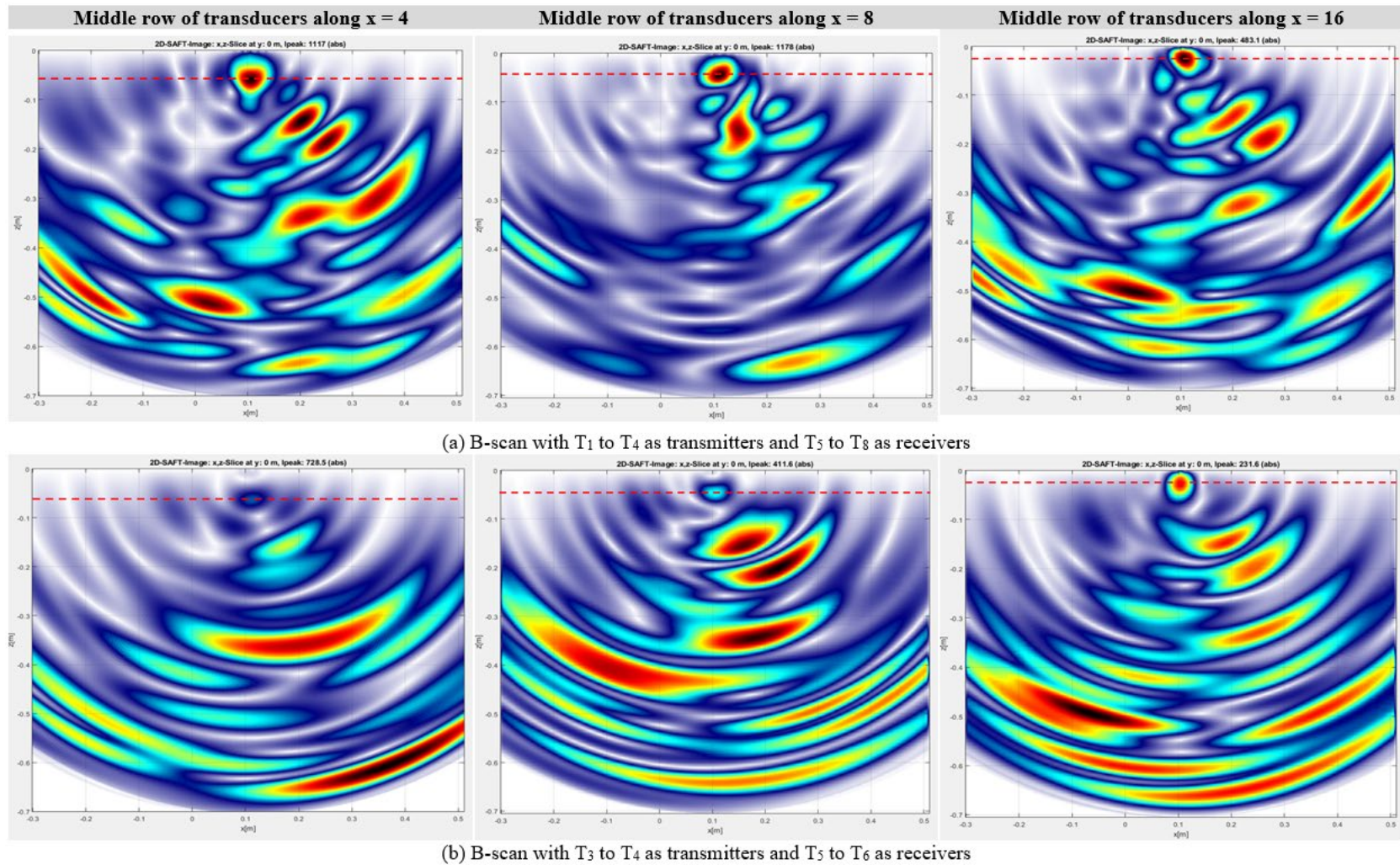


Figure 3-29. B-scans of the PSC I-beam of the S.N. 424 bridge reconstructed using transducer *Arrangement-1* data at lines $x = 4, 8,$ and 16 (The red dashed line represents the potential crack tip location.)

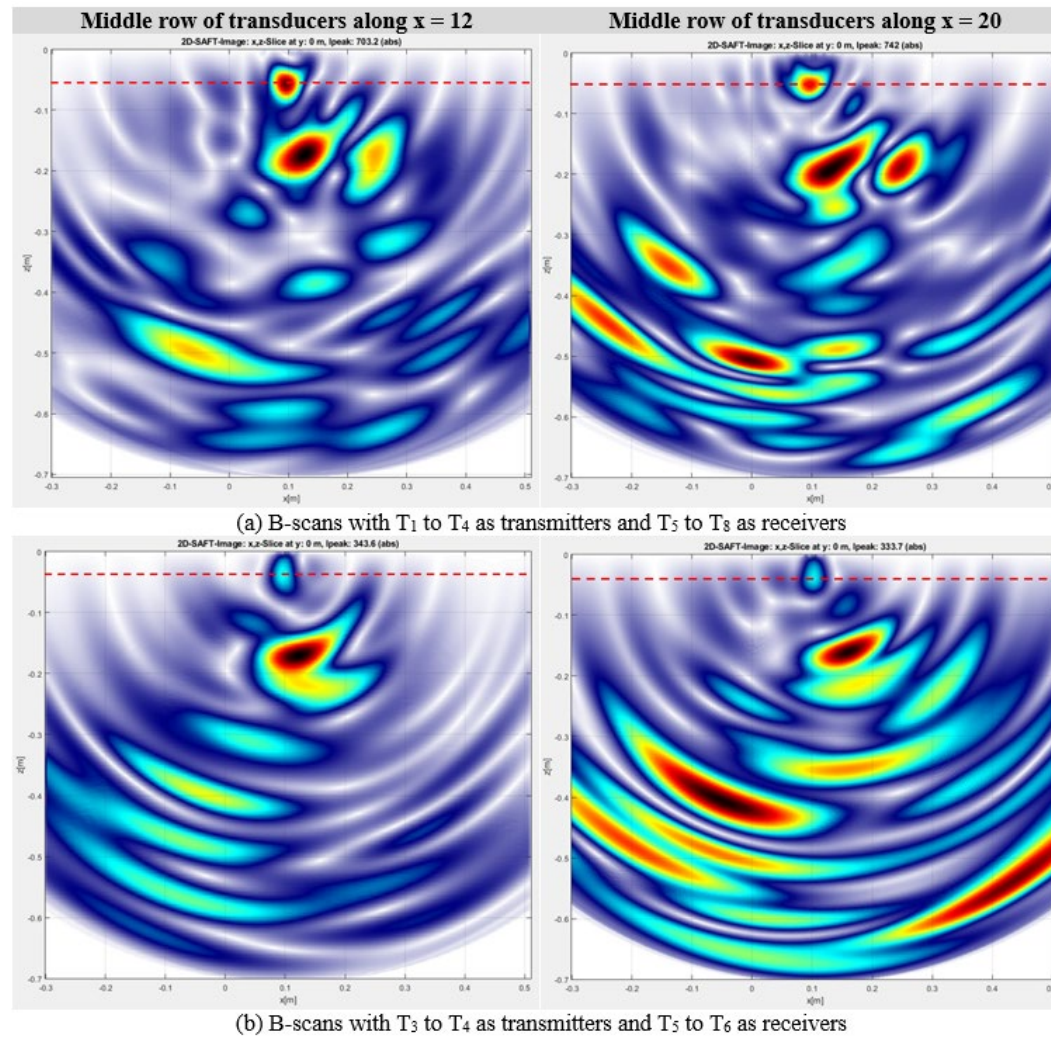


Figure 3-30. B-scans of the PSC I-beam of S.N. 424 reconstructed using transducer *Arrangement-1* data at lines $x = 12$ and 20 (The red dashed line represents the potential crack tip location.)

3.5.3.2 Fascia Beam of the S.N. 2618 Bridge

The S.N. 2618 bridge carries M-57 over the Flint River. The southern fascia beams have longitudinal cracking along the exterior inclined faces of the bottom flanges. The Pundit 250 Array was used to collect data over one of the dominant longitudinal cracks in these AASHTO Type III fascia beams. Figure 3-31a shows the 2×2 in. measurement grid and the position of the longitudinal crack. The grid line $x = 0$ is at 92 in. from the backwall. As shown in Figure 3-31b, the unit was placed symmetrically over the crack with the excitation direction parallel to the crack (*Arrangement-1*). The first transducer column (T_1 in Figure 3-31b) lost contact with the measurement surface since the longitudinal crack is located closer to the vertical face of the beam bottom flange.

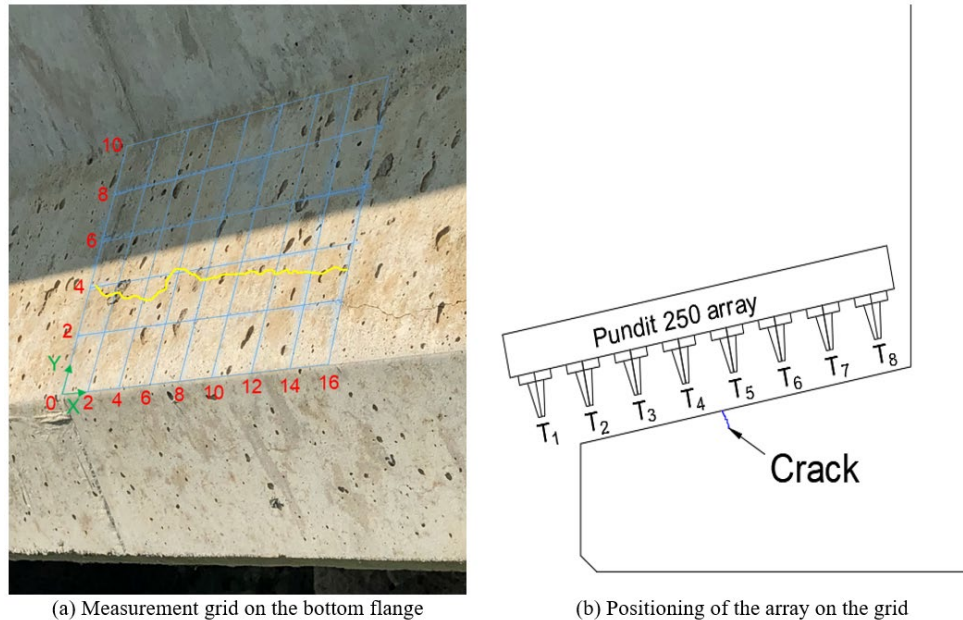


Figure 3-31. Measurement grid and array position on the fascia beam (S.N. 2618)

(The yellow line shows the position of the crack.)

The data was collected using the transducer *Arrangement-1* shown in Figure 3-18. The data was processed using the two transmitter-receiver combinations defined in Table 3-8 for *Arrangement-1*. Since the transducer column T_1 was not in contact with the concrete surface, data from column T_8 were also neglected in the analysis to maintain symmetry. The two transmitter-receiver combinations were (i) T_2 to T_4 as transmitters and T_5 to T_7 as receivers and (ii) T_3 to T_4 as transmitters and T_5 to T_6 as receivers. Figure 3-32 through Figure 3-34 show reconstructed B-scans with the middle row of transducers placed along the lines $x = 0$ to 16. The B-scans produced

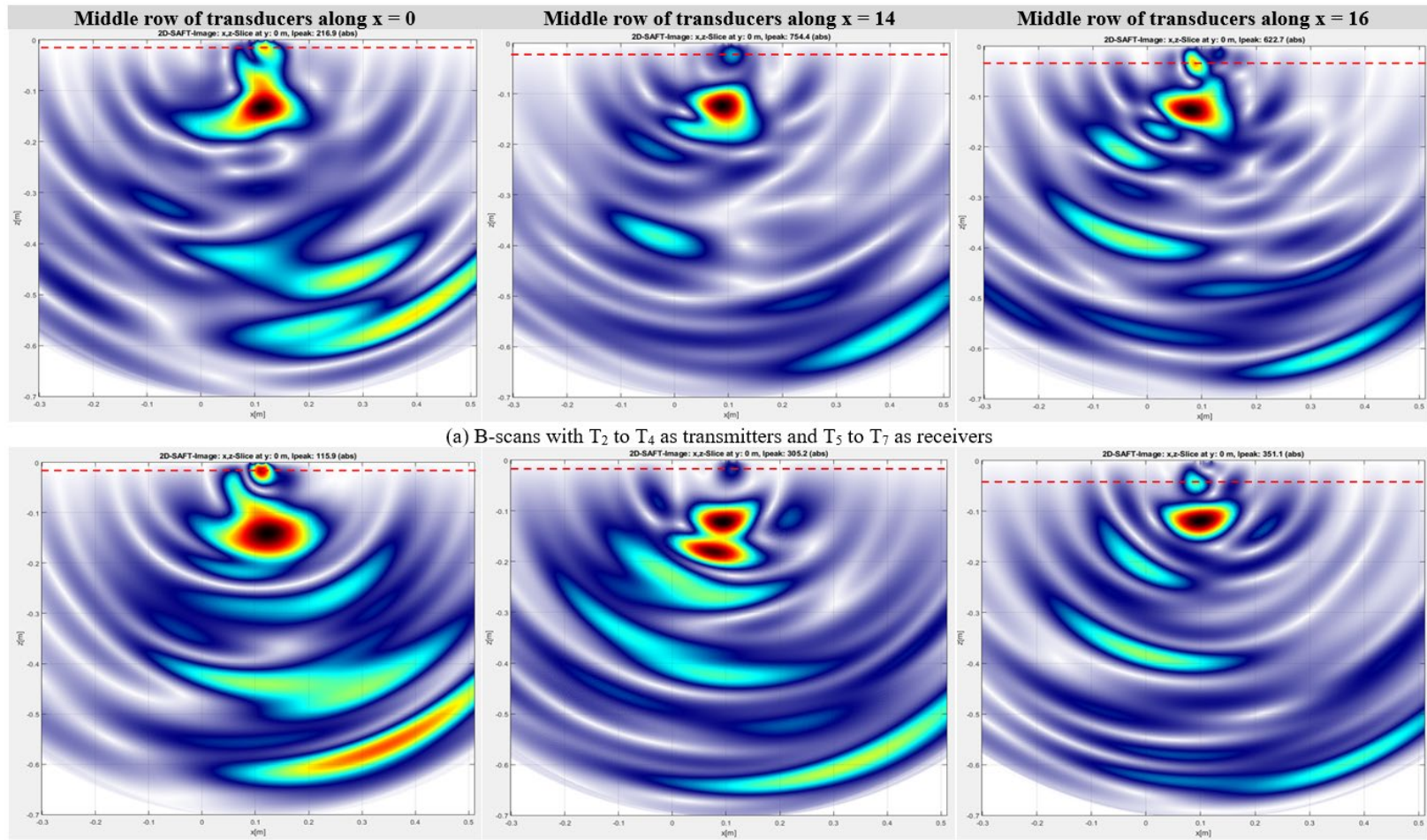
with the two transducer combinations were fairly similar. The crack depth was estimated to the center of the significant reflection observed at the crack location and indicated by a red dashed line. Table 3-11 shows the estimated crack depths with two different transducer combinations as transmitters and receivers. The measured crack width at each location is also given in Table 3-11. Field verification of crack depth was not possible because the coring of in-service bridge beams is not allowed. Using the results in column (c) of the table, the longitudinal crack depth was estimated to vary between 0.70 in. (17.89 mm) and 2.32 in. (58.85 mm).

Table 3-11. The Depth of Longitudinal Cracking in a Fascia Beam (S.N. 2618)

Position of the middle row of transducers (a)	Measured crack width in. (mm) (b)	Estimated crack depth¹ Transmitters: T₂ to T₄ Receivers: T₅ to T₇ in. (mm) (c)	Estimated crack depth¹ Transmitters: T₃ to T₄ Receivers: T₅ to T₆ in. (mm) (d)
Along x = 0	0.010 (0.254)	0.70 (17.89)	0.70 (17.89)
Along x = 2	0.010 (0.254)	NA ²	2.32 (58.85)
Along x = 4	0.010 (0.254)	2.32 (58.85)	2.91 (73.83)
Along x = 6	0.010 (0.254)	1.02 (25.88)	0.48 (12.9)
Along x = 8	0.010 (0.254)	2.28 (57.85)	2.31 (58.85)
Along x = 10	0.013 (0.330)	NA	NA
Along x = 12	0.013 (0.330)	NA	NA
Along x = 14	0.010 (0.254)	0.94 (23.89)	0.74 (18.89)
Along x = 16	0.010 (0.254)	1.33 (33.87)	1.69 (42.86)

¹ – The most accurate estimated crack depth would be the value in mm. The values in mm were obtained from the processed B-scans and converted to inches.

² – Not available



(b) B-scans with T_3 to T_4 as transmitters and T_5 to T_6 as receivers

Figure 3-32. B-scans of the PSC I-beam of the S.N. 2618 bridge reconstructed using transducer *Arrangement-1* data at lines $x = 0, 14$ and 16 (The red dashed line represents the potential crack tip location.)

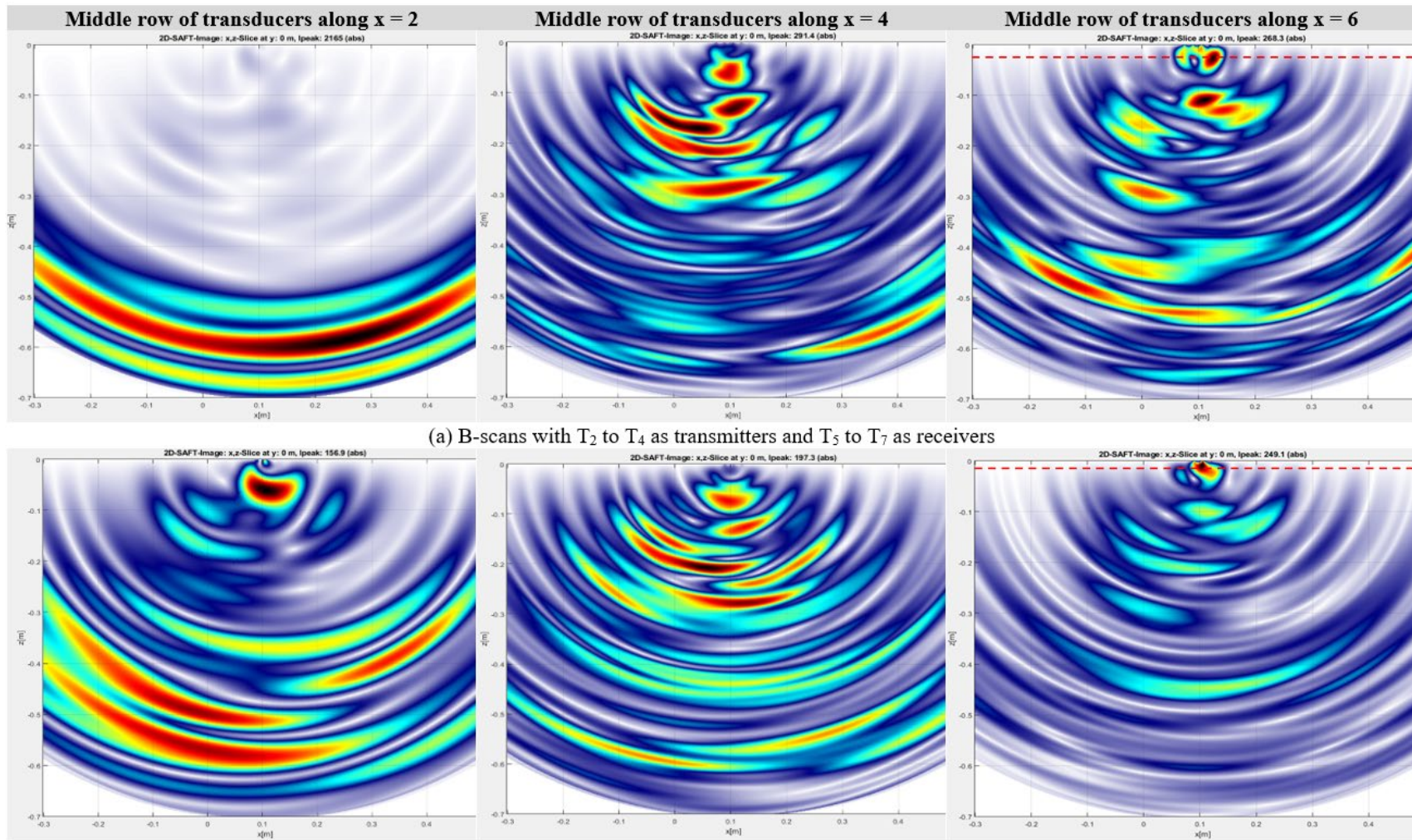


Figure 3-33. B-scans of the PSC I-beam of the S.N. 2618 bridge reconstructed using transducer *Arrangement-1* data at $x = 2, 4,$ and 6 (The red dashed line represents the potential crack tip location.)

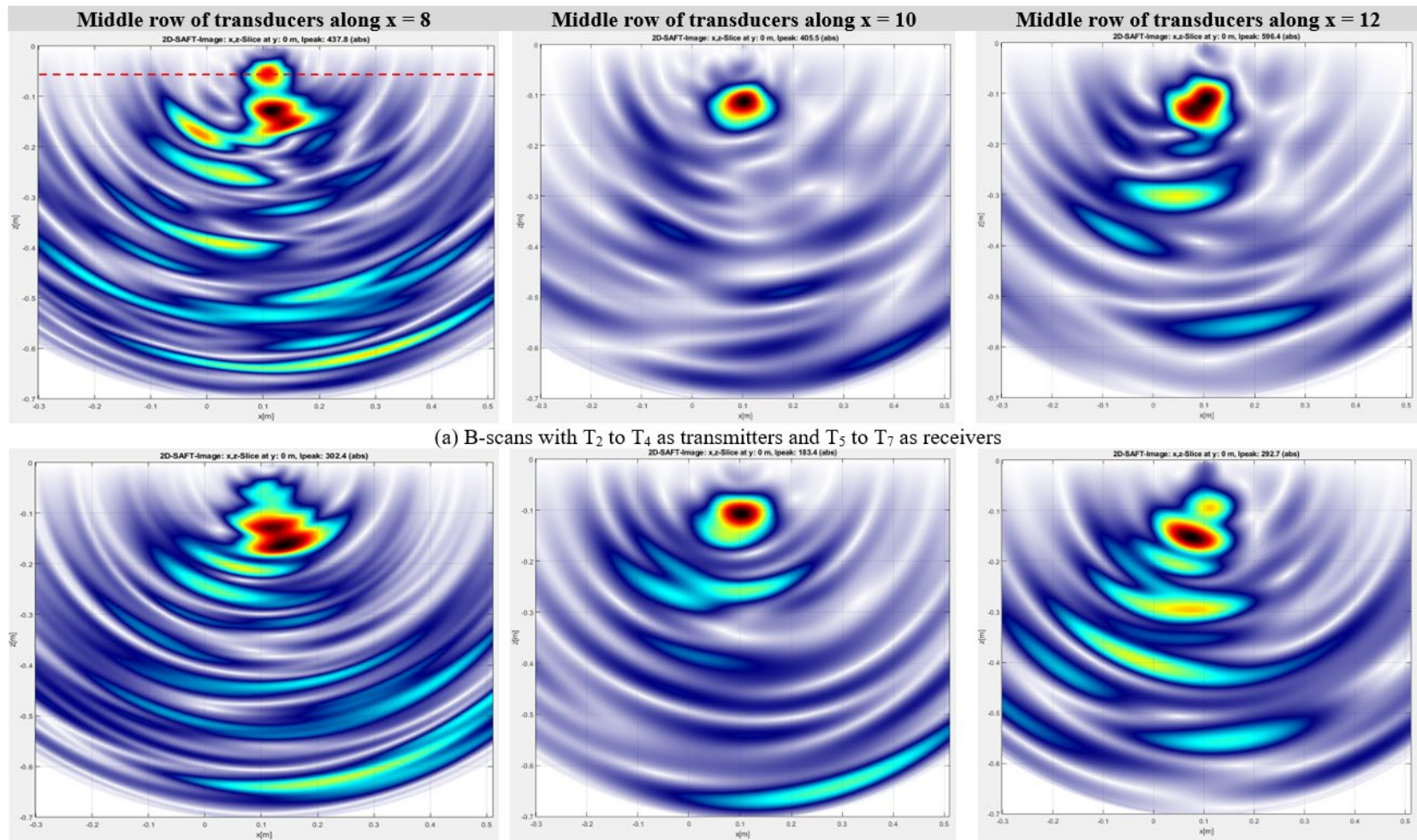


Figure 3-34. B-scans of the PSC I-beam of the S.N. 2618 bridge reconstructed using transducer *Arrangement-1* data at $x = 8, 10,$ and 12 (The red dashed line represents the potential crack tip location.)

3.5.4 Summary of Findings and Recommendations

Due to shortcomings in the indirect transmission of longitudinal waves used in two-transducer UPV devices, multi-array shear transducer devices are being evaluated to measure the depth of surface cracks. This study demonstrated the impact of various arrangements of a multi-array transducer device to collect data and the selection of transducer groups as transmitters and receivers to analyze data on the calculated surface crack depth in concrete specimens. Three concrete slab specimens with known crack depths (0.5 in, 1.25 in, and 1.75 in.) and two PSC I-beams of in-service bridges with longitudinal cracks were used for this purpose. The following conclusions were derived from the findings of this study.

- The multi-array unit and the data analysis procedures can be implemented under field conditions to estimate the depth of cracks in concrete components.
- The depth of 1.25 in. and 1.75 in. deep cracks in concrete slabs can be calculated with more than 90% accuracy using the B-scans reconstructed with the data collected by placing the excitation direction parallel to the crack and the unit placed symmetrically over the crack (*Arrangement-1*). Cracks with depths less than 1.25 in. can be identified, but the degree of accuracy needs to be further evaluated.
- The data collected with a limited number of transducers can be used to calculate crack depths due to space constraints and/or narrower dimensions of the components.
- Since the data collected on slabs with *Arrangements-1* and *2* resulted in backwall reflections, irrespective of the crack depths, the average wave velocity can be calculated and used to enhance the accuracy of the calculated crack depths.
- Even though the accuracy of calculated crack depth decreases when using the data collected by placing the unit with an offset from the crack (*Arrangement-2*), such an arrangement is useful at locations due to space constraints and/or narrower dimensions of the components.
- With the increase in crack depth, better indications of the crack tip locations were observed in the B-scans. However, reflections produced at the actual crack tip locations were distributed over a region. Hence, the prediction of a crack depth would be approximate and subjective. With *Arrangement-1*, the crack depth estimated to the center of the reflections produced crack

depths closer to the actual values. When the excitation direction is parallel to the crack with the unit placed offset from the crack (*Arrangement-2*), and when the excitation direction is perpendicular to crack and the unit is placed symmetrically over the crack (*Arrangement-3*), the crack depth estimated to the bottom of the reflections produced crack depths closer to the actual values. As the most reliable method, it is recommended to use *Arrangement-1*, where possible.

- Use of *Arrangement-1* on PSC I-beams with longitudinal cracks produced necessary data to estimate crack depths. However, the accuracy of crack depth was not verified since extracting cores from PSC beams of in-service bridges was not allowed. Also, the direction of the cracks into the concrete could not be assessed.
- The estimated crack depth in the PSC I-beam of S.N. 424 is between 0.99 in. (25.06 mm) and 2.24 in. (56.85 mm). The estimated crack depth in the PSC I-beam of S.N. 2618 is between 0.70 in. (17.89 mm) and 2.32 in. (58.85 mm). Even though not verified through coring, the estimated crack depth can be conservatively used to evaluate beam capacity.
- A consistent relationship was not observed between the measured crack width and the estimated crack depth in the PSC I-beams.
- The conclusions and recommendations of this study are based on a set of data collected from a limited number of specimens. Further, the depth of cracks in the PSC I-beam was not verified due to restrictions for extracting cores from in-service bridge beams. This study needs to be extended to develop implementation guidelines for various applications, to generate a large data set to enhance confidence, and to identify potential implementation challenges.

4 RECOMMENDED INSPECTION GUIDELINES FOR PSC BOX- AND I-BEAMS

4.1 OVERVIEW

Section 2.4 presents a lack of granularity in the current inspection data to identify bridge beams with specific deteriorations/distresses and the location of such conditions to ascertain the best methods of extending service life. In doing so, Chapter 3 describes the condition of fascia beams in several I-beam bridges and unique distresses documented on I- and box-beams that require special attention during maintenance and load rating.

A new Agency-Developed Element (ADE), as a superstructure element, is recommended to document exterior/fascia beam conditions since the fascia beams in more than 130 I-beam bridges had longitudinal cracking and/or map cracking along the bottom flange top surface. Further, the mix-of-fixes for fascia beams with such distresses is different from interior beams. Procedures to document the details of these distresses during biennial and scoping inspections are discussed. The element inspection report format is updated to include the ADE with a clear breakdown of the distress types contributing to condition states. A collection of pictures representing the types of distresses observed in PSC box- and I-beams is presented.

4.2 AGENCY-DEVELOPED ELEMENT (ADE)

A new ADE in the superstructure grouping is recommended to document fascia/exterior beam conditions. The identification number for this ADE has to be greater than 800, and it can be selected from 814, 827, 839, 848, 864 to 879, and 898. These numbers do not have a designated ADE listed in the MiBEIM (2017). This ADE, labeled in this report as ADE XXX, is defined as a new superstructure element, similar to NBE 104, 109, and 823. The condition state/s (CS/CSs) of ADE XXX is assigned as per the guidelines provided in the CS Table 2 - Prestressed Concrete. The percentages of defects contributing to CS of ADE XXX shall be based on the total length of exterior beams.

Table 4-1 shows the element description for the proposed fascia/exterior beam element (ADE XXX). The NBE 104, NBE 109, and ADE 823 shall record the CS for all the beams, while the proposed ADE XXX shall record the CSs for the exterior beams.

Table 4-1. Element Description for the PSC Fascia/Exterior Beam Element

No.	Name	CS Table	Description
XXX	Prestressed Concrete Fascia/Exterior Beam	2	Fascia/exterior pretensioned or post-tensioned concrete closed web girders and open web girders, including spread box or side-by-side with transverse post-tension. This is an ADE. When there is no deck and traffic rides directly on the girders, this element includes the web and bottom flanges only and the top flange is rated using NBE #15 (see pg. 10).
<p>Quantity Calculation: The quantity for these elements is the sum of all lengths of each fascia/exterior beam.</p> <p>Element Commentary: The girder evaluation is three dimensional in nature with the defects observed on all exterior and interior (if visible) surfaces.</p>			

Table 4-2 is updated with the new ADE and ready to be included in the MiBEIM. The details of the elements already in the MiBEIM are presented in black fonts while the proposed ADE XXX details are in red fonts.

Table 4-2. List of Girder Elements Updated with the New ADE XXX

GIRDERS (ft.)

Description: These elements transmit loads from the deck to the substructure. Elements listed include closed web (boxes) and open girders (I-sections) regardless of protective systems.			
No.	Name	CS Table	Description
102	Steel Closed Web/Box Girder	3	Steel box girders or closed web girders.
104	Prestressed Concrete Closed Web/Box Girder	2	Pretensioned or post-tensioned concrete closed web girders. When there is no deck and traffic rides directly on the girders the top flange is rated using NBE #15 (see pg. 10). For side-by-side or spread box beams use ADE 823 (see pg. 21).
105	Reinforced Concrete Closed Web/Box Girder	1	Reinforced concrete box girder or closed web girders. When there is no deck and traffic rides directly on the girders the top flange is rated using NBE #16 (see pg. 10).
106	Other Closed Web/Box Girder	6	Composite material or other material box girders or closed web girders that cannot be classified using any other defined closed web/box girder element.
107	Steel Open Girder/Beam	3	Steel open girders.
109	Prestressed Concrete Open Girder/Beam	2	Pretensioned or post-tensioned concrete open web girders. When traffic rides directly on the girders, the top flange is rated using NBE #15 (see pg. 10).
110	Reinforced Concrete Open Girder/Beam	1	Mild steel reinforced open web girders. When there is no deck and traffic rides directly on the girders, the top flange is rated using NBE #16 (see pg. 10).
111	Timber Open Girder	4	All timber open girders.
112	Other Open Girder/Beam	6	Composite material girders and open girder/beams that cannot be classified using any other defined element. Includes concrete encased steel girders.
823	Prestressed Concrete Box Beam	2	Pretension box beams, and includes side-by-side, transverse post-tensioned or spread box beams. This element is an ADE, and is a subset of NBE 104. When there is no deck and traffic rides directly on the girders, this element includes the web and bottom flanges only and the top flange is rated using NBE #15 (see pg. 10).
XXX	Prestressed Concrete Fascia/Exterior Beam	2	Fascia/exterior pretensioned or post-tensioned concrete closed web girders and open web girders, including spread box or side-by-side with transverse post-tension. This is an ADE. When there is no deck and traffic rides directly on the girders, this element includes the web and bottom flanges only and the top flange is rated using NBE #15 (see pg. 10).
<p>Quantity Calculation: The quantity for these elements is the sum of all lengths of each girder or girder section.</p> <p>Element Commentary: The girder evaluation is three dimensional in nature with the defects observed on all exterior and interior (if visible) surfaces.</p>			

4.3 DEFECT TYPES IN PSC BEAMS

4.3.1 Modifications to CS Table 2 of MiBEIM

Table 4-3 shows the updated definition of *Cracking-PSC* (defect 1110) in the CS Table 2. The Footnote 1 description in Table 4-3 is the same, except having “*reinforced*” replaced with “*prestressed*” since the table is for PSC. Map cracking is already included in defect 1110, but moderate and heavy pattern (map) cracking are not defined. Although the AASHTO MBEI (2019) includes definitions and pictures to describe map cracking, they are for reinforced concrete members. Therefore, several pictures depicting the condition of map cracks observed on PSC beams are provided as noted in Footnote 2. Accordingly, the CS Table 2 for PSC was updated and presented in Table 4-4. The updates are shown in red fonts.

Table 4-3. Updated Condition State Descriptions for the Cracking in PSC

Defects	Condition State 1 GOOD	Condition State 2 FAIR	Condition State 3 POOR	Condition State 4 SEVERE
Cracking ^(1,2) - PSC (1110)	Insignificant cracks or moderate-width cracks that have been sealed.	Unsealed moderate-width cracks or unsealed moderate pattern (map) cracking.	Wide cracks or heavy pattern (map) cracking.	The condition warrants a structural review to determine the effect on strength or serviceability of the element or bridge; OR a structural review has been completed and the defects impact strength or serviceability of the element or bridge.
<p>(1) The inspector should use judgment when utilizing the condition state defect conditions, especially for concrete cracking. The crack defect description definitions describe generalized distress, but the inspector should consider width, spacing, location, orientation, and structure or nonstructural nature of the cracking. The inspector should consider exposure and environment when evaluating crack width. In general, reinforced prestressed concrete cracks of less than 0.004 inches can be considered insignificant, and a defect is not warranted. Cracks ranging from 0.004 to 0.009 inches can be considered moderate, and cracks greater than 0.009 inches can be considered wide.</p> <p>(2) Use the pictures to describe the type of cracking and decide on the significance of pattern (map) cracking.</p>				

Figure 4-1 and Figure 4-2 present a set of box- and I-beam pictures depicting various defect types, ADE descriptions and numbers, and the respective CSs. Even though these defects are defined in the CS Table 2, and shown in Table 4-4, an adequate number of photographs was not provided in the MiBEIM (2017) to help bridge inspectors. Hence, the information provided in Figure 4-1 and Figure 4-2, once included in the MiBEIM after the CS Table 2, is expected to enhance the inspection process and the documentation of the CSs. The evaluation of the causes of concrete deterioration of the Brady Street Bridge indicated the possibility of freeze-thaw damage due to a very low amount of entrained air in beam concrete. The majority of beam ends and webs

were severely damaged. These concealed damages were identified during bridge demolition. Several beam soffits of that bridge had severe random cracking similar to what is shown in Figure 4-1e. All the defects shown in Figure 4-1 are typical to box-beams in side-by-side box-beam bridges, except the one shown in Figure 4-1e. Hence, finding bridges with box-beam cracking similar to the patterns shown in Figure 4-1e is very important since such conditions warrant further investigations to evaluate the box-beam conditions and a structural review to determine the effect on strength and/or serviceability of the element or bridge.

Figure 4-2 presents a set of I-beam pictures depicting various defect types. Light map cracking was observed on a majority of PSC I-beam webs. These cracks are superficial and not a concern unless the beam surface is exposed to repeated wet and dry conditions. However, observation of heavy map cracking on web, similar to what is shown in Figure 4-2a, requires further investigation since such cracking could develop into shear cracks, if present at beam ends, or longitudinal cracking within the span. The map cracking on the fascia beam's bottom flange easily develops into heavy or severe map cracking, as shown in Figure 4-2b, since the fascia is repeatedly exposed to environmental elements unless the beam is well protected with a surface coating. Repeated exposure to freeze-thaw conditions develops longitudinal cracking along the bottom flange, as shown in Figure 4-2c. These cracks can be repaired and sealed to extend the service life and thus, CS3 is assigned. End cracking of PSC beams is documented at the fabrication yard. These cracks, if not protected, could easily develop into longitudinal cracking as shown in Figure 4-2d under repeated exposure to environmental elements. Depending on the severity of cracking, CS4 is assigned since such conditions warrant further investigations to evaluate the number of corroded/damaged strands and a structural review to determine the impact on strength and/or serviceability of the bridge element.

Section 3.5.3 describes the measurement of the depth of longitudinal cracks in two fascia beams. These cracks were located within the span. The measured crack depths ranged from 0.70 in. to 2.32 in. The width of the cracks ranged from 0.010 in. to 0.016 in. Developing a crack width versus crack depth relationship for MDOT standard sections is recommended since knowing the depth of cracks allows for identifying the possible number of damaged strands, which is used to support load rating and maintenance decisions. The development of crack width and depth relation can be accomplished by collecting data from more than 100 bridges identified during this study with fascia beam deterioration. Having ADEs for fascia beams and beam ends will greatly enhance

the possibilities of identifying I-beams with longitudinal cracking, map cracking, and girder end distresses to support load rating and maintenance decisions.

As discussed in Chapter 3, after reviewing the entire MDOT I-beam inventory, typical defects in PSC I-beams were summarized by considering their locations along the span (i.e., end or span). Longitudinal cracks, vertical cracks, diagonal cracks, map cracks, delamination, spalls, and movement were observed at girder ends. Longitudinal cracks, vertical cracks, map cracks, flexural cracks, delamination, popout, and spalls were observed within the span. A majority of these defects are presented in Figure 4-1 and Figure 4-2. Figure 4-3 shows vertical cracking, diagonal cracking, and flexural cracking. Moreover, two types of diagonal cracks are documented at beam ends. As shown in Figure 4-3b, shear cracks radiate from beam end supports at an angle of about 45° from horizontal towards the top flange. Diagonal cracks also develop parallel to harped or draped strands, as shown in Figure 4-3c. A clear documentation of these crack types and their respective locations along a beam is very important in identifying the causes of cracking and developing the most effective mix-of-fixes. The location of these defects can be explicitly documented using the available NBEs for I- and box beams, the MDOT ADE for beam ends, and the proposed ADE for fascia beams.

According to the CS Table 2 of the MiBEIM (2017), delamination, spalls, and popout are already included under *Spalls/delaminations/patch areas (defect 1080)*, and the map cracks are already included under *Cracking-PSC (defect 1110)*. Therefore, the longitudinal cracks, vertical cracks, diagonal cracks, flexural cracks, and random cracking in PSC box-beam soffits need to be explicitly recorded during inspection to prevent the ambiguity of the generalized term “cracking”. The current data collection templates can be modified to improve inspection efficiency and eliminate the use of inconsistent terminology in inspector comments. One approach would be to provide a list of crack types as a drop-down list or as a list with checkboxes. Figure 4-4 shows an example of such a list that can be added to the current inspection template. If an inspector selects *Cracking-PSC (defect 1110)*, the template shown in Figure 4-4 shall be enabled to choose the type(s) of cracking. Photographs illustrating each crack type, along with the name of the crack type, are provided as a guidance for the inspectors. In addition, the presence of flexural cracks or diagonal cracks (from girder bottom to top), or random cracks at the box-beam soffit (shown in Figure 4-1e) should set a smart flag for immediate attention (i.e. the element or the portion of the

element is placed in CS4). If the creation of a custom form with the proposed drop-down list is difficult, different defect numbers can be assigned for each crack type.

Table 4-4. Updated CS Table 2

CS TABLE 2 – PRESTRESSED CONCRETE

Defects	Condition State 1	Condition State 2	Condition State 3	Condition State 4
	GOOD	FAIR	POOR	SEVERE
Spalls/ Delaminations/ Patch Areas (1080)	None.	Delaminated. Spall 1 in. or less deep or less than 6 in. diameter. Patched area is sound.	Spall greater than 1 in. deep or greater than 6 in. diameter. Patched area is unsound or showing distress. Does not warrant structural review.	The condition warrants a structural review to determine the effect on strength or serviceability of the element or bridge; OR a structural review has been completed and the defects impact strength or serviceability of the element or bridge.
Exposed Rebar (1090)	None.	Present without section loss.	Present with section loss that does not warrant structural review.	
Exposed Prestressing (1100)	None.	Present without section loss.	Present with section loss that does not warrant structural review.	
Cracking ^(1,2) - PSC (1110)	Insignificant cracks or moderate-width cracks that have been sealed.	Unsealed moderate-width cracks or unsealed moderate pattern (map) cracking.	Wide cracks or heavy pattern (map) cracking.	
Efflorescence/ Rust Staining (1120)	None.	Surface white without build-up or leaching without rust staining.	Heavy build-up with rust staining	
Settlement - Substructure (4000)	None.	Exists within tolerable limits or arrested with effective actions taken to mitigate.	Exceeds tolerable limits but does not warrant structural review.	
Scour – Substructure (6000)	None.	Exists within tolerable limits or arrested with effective countermeasures.	Exceeds tolerable limits but is less than the limits determined by scour evaluation, and does not warrant structural review.	
Damage (7000)	Not applicable.	The element has minor damage caused by vehicular or vessel impact.	The element has moderate damage caused by vehicular or vessel impact.	The element has severe damage caused by vehicular or vessel impact.

(1) The inspector should use judgment when utilizing the condition state defect conditions, especially for concrete cracking. The crack defect description definitions describe generalized distress, but the inspector should consider width, spacing, location, orientation, and structure or nonstructural nature of the cracking. The inspector should consider exposure and environment when evaluating crack width. In general, reinforced prestressed concrete cracks of less than 0.004 inches can be considered insignificant, and a defect is not warranted. Cracks ranging from 0.004 to 0.009 inches can be considered moderate, and cracks greater than 0.009 inches can be considered wide.

(2) Use the pictures to describe the type of cracking and decide on the significance of pattern (map) cracking.



(a) Spalls

(Spalls/ Delaminations/ Patch Areas 1080)

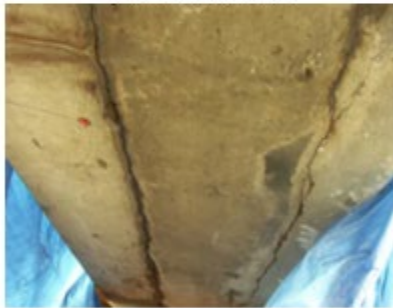
A Condition State is determined based on the significance as defined in CS Table 2



(b) Exposed prestressing with moderate spall
(Exposed Prestressing 1100)
Condition State 3



(c) Exposed prestressing with section loss
(Exposed Prestressing 1100)
Condition State 4



(d) Wide longitudinal cracking
(Cracking-PSC 1110)
Condition State 4



(e) Heavy random cracking
(Cracking-PSC 1110)
Condition State 4



(f) Leaching without rust staining
(Efflorescence / Rust Staining 1120)
Condition State 2



(g) Heavy build-up with rust staining.
(Efflorescence / Rust Staining 1120)
Condition State 3

Figure 4-1. PSC box-beam defect types and condition states



(a) Heavy map cracking on web
(Cracking-PSC 1110), Condition State 2



(b) Heavy map cracking on bottom flange
(Cracking-PSC 1110), Condition State 2



(c) Wide longitudinal cracking
(Cracking-PSC 1110), Condition State 3



(d) Wide longitudinal cracking
(Cracking-PSC 1110), Condition State 4
(Williams and Choudhuri 2010)

Figure 4-2. PSC I-beam defect types and condition states



(a) Vertical cracking



(b) Diagonal cracking – From girder bottom to girder top



(c) Diagonal cracking – From girder top to girder bottom



(d) Flexural cracking

Figure 4-3. Different crack types observed in PSC beams

Cracking-PSC (1110)

Longitudinal Cracks



Vertical Cracks



Diagonal Cracks
(Girder Bottom to Top)



Diagonal Cracks
(Girder Top to Bottom)



Flexural Cracks



Random Cracks
(Box-beam soffits)



Map Cracks



Figure 4-4. A template for documenting crack types under defect 1110

4.4 IMPLEMENTATION EXAMPLE

Figure 4-5 shows a sample format of the proposed update to the current MDOT safety inspection report, focusing mainly on the superstructure elements. The form includes an NBE (#109) and two ADEs (#826 and #XXX). ADE XXX is proposed for fascia/exterior beam elements. Violet and light green background colors represent NBEs and ADEs, respectively. Both NBE 109 and ADE XXX are parent elements. ADE 826 is a subset (or a child) of those parent elements. The defects contributing to the condition state of each NBE and ADE are recorded in italics underneath the respective elements. These defects are recorded with their designated element identification number. Additional details on the observed defects, such as the defect location (girder name, girder span, etc.) and crack type, are added as comments below the respective defect.

The example was prepared using data from the safety inspection report of STR 426 (see Figure 2-10). Please note that the breakdown of the distress quantities in Figure 4-5 is for illustration purposes only. As shown in Figure 2-10, the total length of this 6-span bridge is 384 ft. Each span has 5 PSC I-beams. NBE 109 represents all the beams, and ADE XXX represents the exterior beams. The total quantity of NBE 109 is 1920 ft (i.e. 384 ft \times 5) and the total quantity of ADE XXX is 768 ft (i.e. 384 ft \times 2). Distresses listed under NBE 109 or ADE XXX are the

distresses present within the entire length of beams (span and end) and contributed to a condition state. Accordingly, 47 ft contributed to the CS2 of NBE 109, of which 12 ft and 35 ft represent defect 1080 (spalls/delaminations/patch areas) and defect 1110 (cracking-PSC), respectively. The type of cracking contributed to the CS2 in NBE 109 is longitudinal cracking on the web of beams 2, 3 and 4S near the west abutment. This is added as a comment underneath the defect 1110 for NBE 109. Out of the 47 ft of distress contributed to the CS2 of NBE 109, 8 ft of defect 1080 (spalls/delamination/patch areas) was on the fascia beams (i.e. ADE XXX).

The beam end deterioration (ADE 826) is recorded as a subset of NBE 109 and ADE XXX. ADE 826, listed under NBE 109, includes all deteriorated beam ends. ADE 826, listed under the ADE XXX, includes only the deteriorated fascia beam ends. As recorded in the form, 20 ends of all the beams are at the CS2; of which 10 ends have defect 1080 (spalls/delamination/ patch areas) and the remaining 10 have defect 1110 (cracking – PSC). The 20 beam ends listed under NBE 109 includes 10 fascia beam ends. Of the 10 beam ends with CS2 assigned to ADE 826 and listed under ADE XXX, 5 ends have defect 1080, and the remaining 5 have defect 1110. As noted in the comments listed underneath defects 1080 and 1110, cracking/delamination near the sole plates of the exterior beams contributed to this condition state. When the proposed format is implemented and the inspectors are provided with adequately descriptive images, as shown in Figure 4-4, the data can be used for performing causal evaluation of concrete deterioration and selecting suitable maintenance strategies.

AASHTO ELEMENTS				(English Units)			
Element Number	Element Name	Total Quantity	Unit	Good CS1	Fair CS2	Poor CS3	Severe CS4
Superstructure							
109	Pre Opn Conc Girder/Beam	1920	ft	1858 97%	47 2%	15 1%	0 0%
<i>1080</i>	<i>Spalls/Delaminations/ Patch Areas</i>	12	ft	0	12	0	0
<i>1110</i>	<i>Cracking-PSC</i>	35	ft	0	35	0	0
CS2: Longitudinal cracking on web of Bm 2-4S near W abut.							
<i>1080</i>	<i>Spalls/Delaminations/ Patch Areas</i>	5	ft	0	0	5	0
<i>7000</i>	<i>Damage</i>	10	ft	0	0	10	0
CS3: HLH's on Bms 3 and 4S of Span 5W and Bms 4S of span 2W.							
826	Beam End Deterioration	60	(EA)	15 25%	20 33%	25 42%	0 0%
<i>1080</i>	<i>Spalls/Delaminations/ Patch Areas</i>	10	(EA)	0	10	0	0
<i>1110</i>	<i>Cracking-PSC</i>	10	(EA)	0	10	0	0
CS2: Cracking/Delam near sole plates.							
<i>1080</i>	<i>Spalls/Delaminations/ Patch Areas</i>	25	(EA)	0	0	25	0
CS3: STS over piers at bearings.							
XXX	Prestressed Concrete Fascia/Exterior Girder/Beam	768	ft	752 98%	8 1%	8 1%	0 0%
<i>1080</i>	<i>Spalls/Delaminations/ Patch Areas</i>	8	ft	0	8	0	0
<i>1080</i>	<i>Spalls/Delaminations/ Patch Areas</i>	3	ft	0	0	3	0
<i>7000</i>	<i>Damage</i>	5	ft	0	0	5	0
CS3: HLH's on Bm 5S of Span 5W and 2W.							
826	Beam End Deterioration	24	(EA)	4 16%	10 42%	10 42%	0 0%
<i>1080</i>	<i>Spalls/Delaminations/ Patch Areas</i>	5	(EA)	0	5	0	0
<i>1110</i>	<i>Cracking-PSC</i>	5	(EA)	0	5	0	0
CS2: Cracking/delam near sole plates.							
<i>1080</i>	<i>Spalls/Delaminations/ Patch Areas</i>	10	(EA)	0	0	10	0
CS3: STS over piers at bearings.							
Notes:							
	NBE						
	ADE						
<i>Italic</i>	Defect						

Figure 4-5. An implementation of the updated MI safety inspection report format

5 EVALUATION OF STAINING TECHNIQUES

5.1 URANYL ACETATE TESTING

To evaluate the performance of uranyl acetate as an effective reagent in identifying ASR, a series of testing was conducted using reactive fine and coarse aggregates, as well as mortar bars and concrete prisms prepared with reactive aggregate. These specimens were subjected to various exposure conditions to accelerate, retard, or arrest the development of ASR and to contaminate specimens for evaluating possible impacts on the characteristic yellowish-green color.

5.1.1 Performance Evaluation Using Reactive Aggregate

The specimen labels, exposure conditions, and exposure duration for Spratt coarse aggregate are listed in Table 5-1. Table 5-2 lists the specimen labels, exposure conditions, and exposure duration for Arcosa sand, the fine aggregate. Control specimens were evaluated using uranyl acetate after being oven dried at 176° F for the durations listed in the tables. These specimens are labeled as “Oven Dry @ 176,” as shown in the tables. The evaluation procedures followed ASTM C856-14 (2014). However, the standard procedure was slightly modified by keeping the aggregate soaked in uranyl acetate for 30 minutes, as proposed by Igarashi et al. (2016). Specimens were inspected under daylight prior to prescreening under short-wave UV light to identify natural fluorescence. Subsequent observations were made immediately after the uranyl acetate treatment and continued for 72 hours. A summary of findings is presented in this section.

Table 5-1. Exposure Conditions and Duration for Coarse Aggregate (Spratt)

Specimen label (a)	Exposure condition (b)	Exposure duration (days) (c)
Oven Dry @ 176	Oven dried at 176° F	21
1N-NaOH @ 176	Soaked in 1N NaOH solution at 176° F	21
1N-NaOH @ 73	Soaked in 1N NaOH solution at 73° F	21
3% NaCl @ 176	Soaked in 3% NaCl solution at 176° F	21
3% NaCl @ 73	Soaked in 3% NaCl solution at 73° F	21

Table 5-2. Exposure Conditions and Duration for Fine Aggregate (Arcosa Sand)

Specimen label (a)	Exposure condition (b)	Exposure duration (days) (c)
Oven Dry @ 176	Oven dried at 176° F	56
1N-NaOH @ 176	Soaked in 1N NaOH solution at 176° F	63
1N-NaOH @ 73	Soaked in 1N NaOH solution at 73° F	63
3% NaCl @ 176	Soaked in 3% NaCl solution at 176° F	56
3% NaCl @ 73	Soaked in 3% NaCl solution at 73° F	56

Spratt aggregate is a siliceous limestone and has been used as a reference to calibrate ASR test methods (Hooton et al. 2013, Gautam and Panesar 2017, Strack et al. 2020). XRD analysis of Spratt confirmed the presence of calcite with minor amounts of dolomite and quartz. Spratt aggregate exposed to various conditions listed in Table 5-1 were inspected under daylight, prescreened, soaked in uranyl acetate solution for 30 minutes, rinsed with distilled water, and observed several times under UV light for 1 hour. The major observations are summarized in Table 5-3 and Table 5-4. Only the aggregate exposed to 1N-NaOH at 176° F produced the yellowish-green fluorescence indicating ASR. The aggregate exposed to 3% NaCl at 176° F had a couple of very small green color patches but did not produce distinct results compared to all the other aggregates. As shown in Table 5-4, continued observation showed the stability of the characteristic yellowish-green fluorescence and the appearance of a bluish-green fluorescence, the latter being the color of dry uranyl acetate. Since the surface drying rate varies based on the ambient conditions, the uranyl acetate fluorescence can appear much earlier than an hour providing misleading indicators to novice technicians. Based on our experience, observing fluorescence immediately after uranyl acetate treatment, as explained in ASTM C856-14 (2014), will better indicate the presence of ASR.

Table 5-3. Observation of Coarse Aggregate (Spratt) Exposed to Various Conditions


























Test condition	Oven Dry @ 176	1N-NaOH @ 176	1N-NaOH @ 73	3% NaCl @ 176	3% NaCl @ 73
Daylight observation prior to uranyl acetate treatment					
Observation under UV light prior to uranyl acetate treatment (prescreening)					
Observation under UV light immediately after uranyl acetate treatment					

Table 5-4. Observation of UA Treated Coarse Aggregate (Spratt) Against Drying Time

Specimen label	Immediately	5 min.	15 min.	30 min	60 min.
Oven Dry @ 176					
1N-NaOH @ 176					

The elements in Arcosa sand were documented through a literature review. Mineralogically, the Arcosa sand aggregate is dominated by quartz (about 80%) with some rock fragments (i.e. Basalt, Sandstone, Limestone, Chert, Flint, Phyllite, Granite), and some Feldspar that does not have any natural fluorescence. Arcosa sand exposed to various conditions listed in Table 5-2 was inspected under daylight, prescreened, soaked in uranyl acetate solution for 30 minutes, rinsed with distilled water, and observed several times under UV light for up to 72 hours. As shown in Figure 5-1c, yellowish-green fluorescence was observed, an indication of the presence of ASR after exposing the aggregates to 1N NaOH at 176° F for 63 days. Figure 5-2 shows the possibility of fine aggregate developing ASR at room temperature with high alkali exposure. As shown in Figure 5-3, the exposure to 3% NaCl at 176° F for 56 days did not promote ASR.

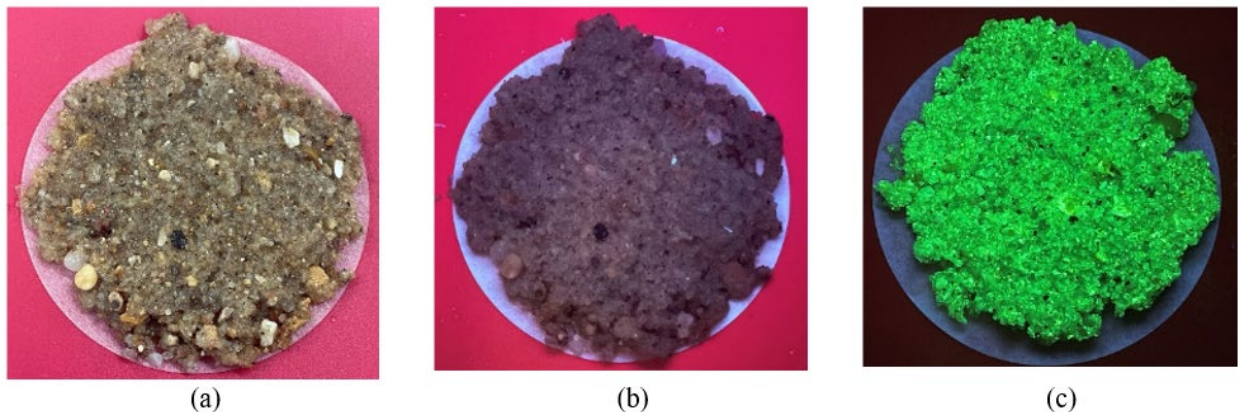


Figure 5-1. Observation of Arcosa sand exposed to 1N NaOH at 176° F for 63 days (a) under daylight, (b) prescreening, and (c) under UV light immediately after uranyl acetate treatment

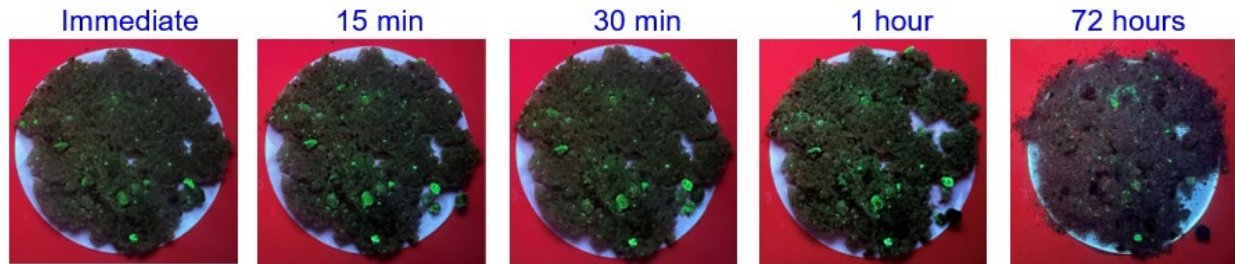


Figure 5-2. Observation of Arcosa sand exposed to 1N NaOH at 73° F for 63 days

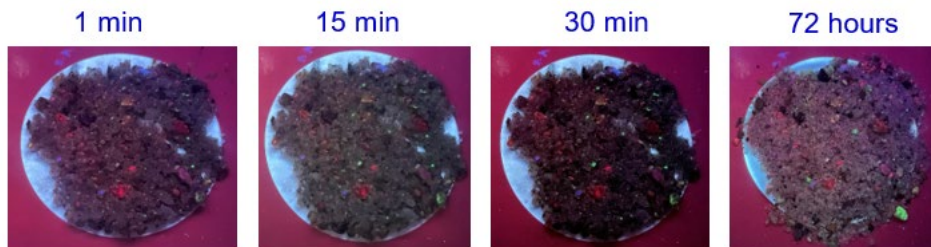


Figure 5-3. Observation of Arcosa sand exposed to 3% NaCl at 176° F for 56 days

5.1.2 Performance Evaluation Using Mortar Bars

The preparation of 1 × 1 × 11.25 in. mortar bars with Arcosa sand and the evaluation of expansion due to ASR are described in Section 7.2. The mortar bars exposed to 1N NaOH at 176° F exceeded the expansion threshold of 0.1% in 12 days. An average expansion of 0.97% was recorded after maintaining the exposure condition for 238 days. These specimens were dry cut in the transverse direction to prepare ½ in. thick slices. The newly exposed surfaces were cleaned by blowing compressed air and observed under daylight. As shown in Figure 5-4a, several cracks in a large aggregate (highlighted with red lines) and a void due to a deteriorated aggregate were observed. Fluorescence was not observed during prescreening (Figure 5-4b). The specimen was soaked in uranyl acetate solution for 30 minutes, rinsed with distilled water, and observed several times under UV light for up to 1 hour. The observations are documented in Figure 5-4c to f. As shown in Figure 5-4c, similar to the observation state by Natesaiyer and Hover (1988), a yellowish-green fluorescence was observed in reaction rims and cracks in the aggregates and the paste.

The 1 × 1 × 11.25 in. mortar bars with Arcosa sand and 0.35 w/c were immersed in 1N NaOH, 3% NaCl, and 0.1N NaOH solutions. The mortar bars exposed to 0.1N NaOH had 1.25% Na₂O_{eq.}. The mortar bars exposed to the other two conditions had 0.51% Na₂O_{eq.}. The exposure temperature was maintained at 104° F for 163 days, 140° F for 26 days, and 176° F for 49 days. The expansions of the mortar bars exposed to 1N NaOH, 3% NaCl, and 0.1N NaOH were 0.282%,

0.046%, and 0.010%, respectively. Interestingly, the mortar bars exposed to 3% NaCl and elevated temperatures for 238 days developed ASR, as shown in Figure 5-5.

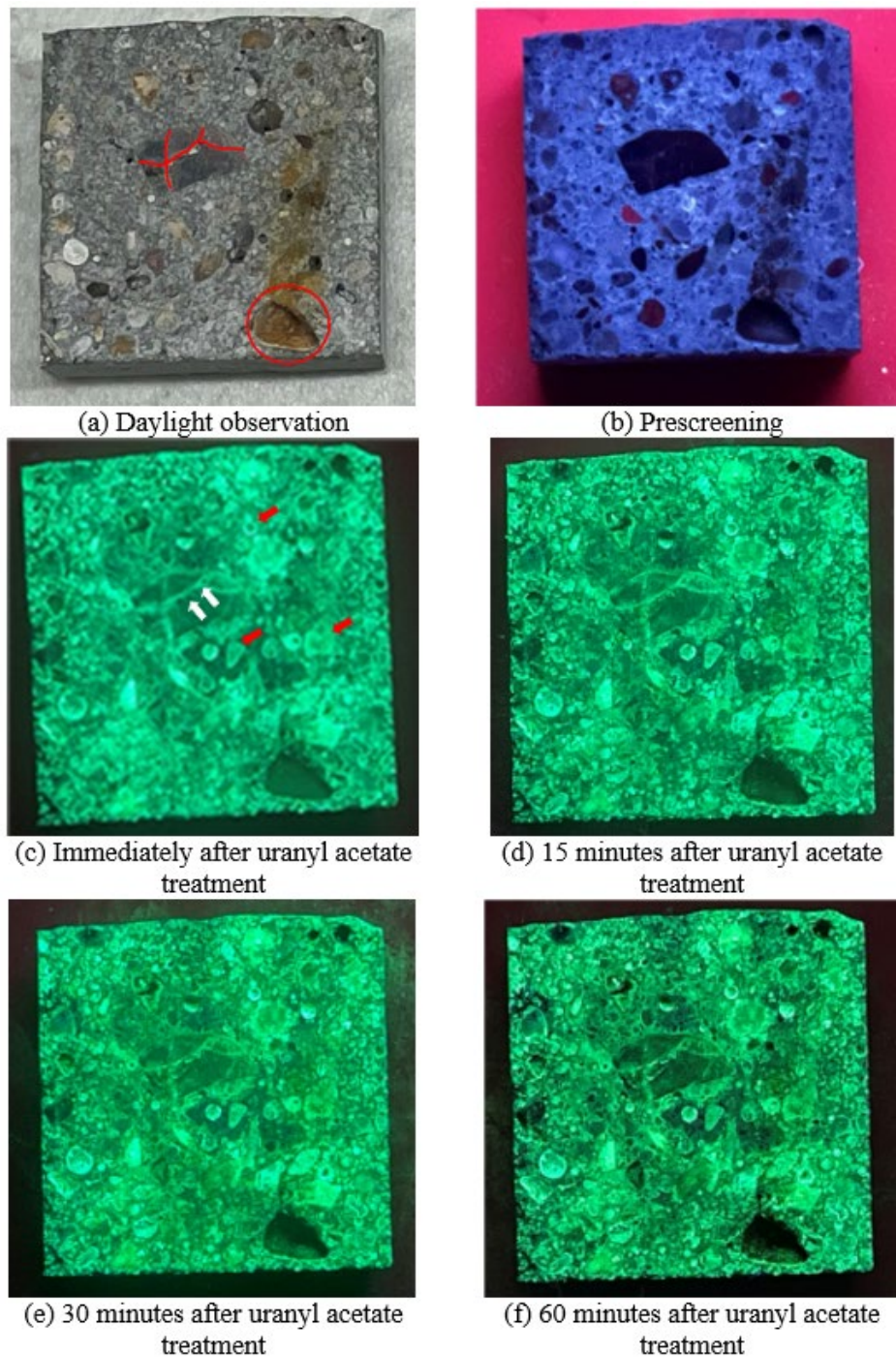


Figure 5-4. Observation of mortar bars with Arcosa sand exposed to 1N NaOH at 176° F (a) under daylight - cracks in an aggregate are highlighted in red and a void in the surface is circled, (b) prescreening (c) immediately after uranyl acetate treatment – red arrows show reaction rims and white arrows show the fluorescence in the cracks, (d) 15-minute observation, (e) 30-minute observation, and (f) 60-minute observation after the uranyl acetate treatment.

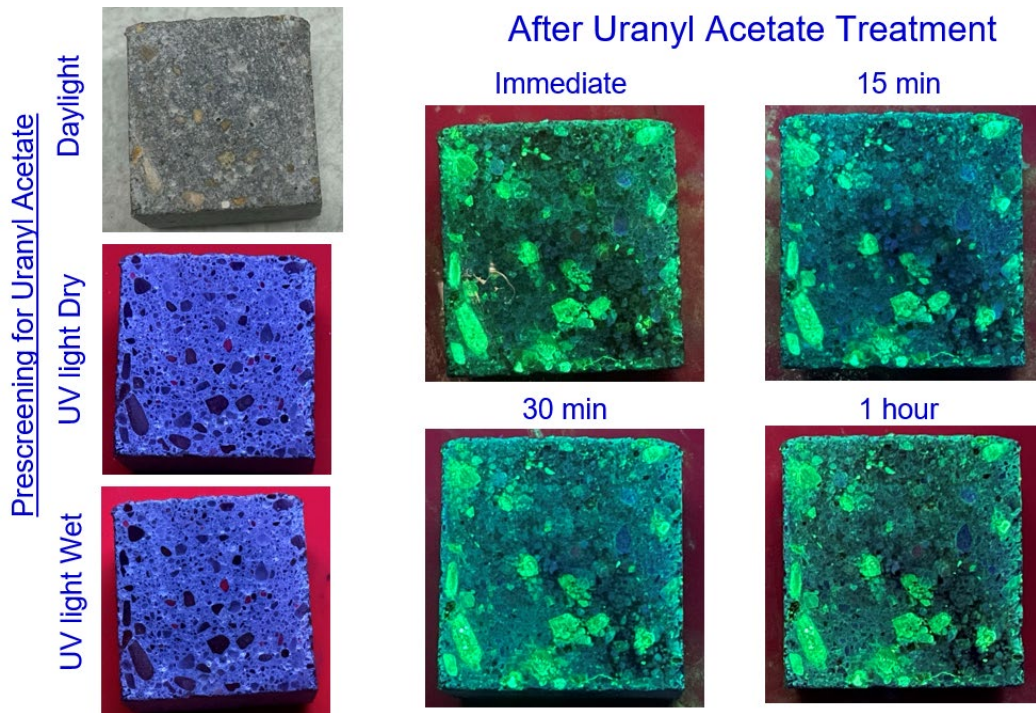


Figure 5-5. Yellowish-green fluorescence observed on mortar bars exposed to 3% NaCl and elevated temperatures for 238 days

5.1.3 Performance Evaluation Using Concrete Prisms

The $3 \times 3 \times 11.25$ in. concrete prisms fabricated using Arcosa sand and Spratt coarse aggregate were exposed to 1N NaOH at 176° F for 218 days. The recorded expansion at the end of the 218-day exposure was 0.95%. One of the prisms was dry cut in the transverse direction to make thin slices and cleaned by blowing compressed air. One of the slices was soaked in uranyl acetate solution for 30 minutes, rinsed with distilled water, and observed several times under UV light for up to 1 hour. The observations are shown in Figure 5-6. Several cracks in aggregates and paste closer to the periphery were observed under daylight (Figure 5-6a). As depicted in Figure 5-6b, natural fluorescence was not observed during prescreening. The observations from immediately after treatment and up to 1 hour under the UV light are shown in Figure 5-6c to f. As shown in Figure 5-6c, yellowish-green fluorescence is observed in the reaction rims, as well as the cracks in the aggregate and the cement paste.

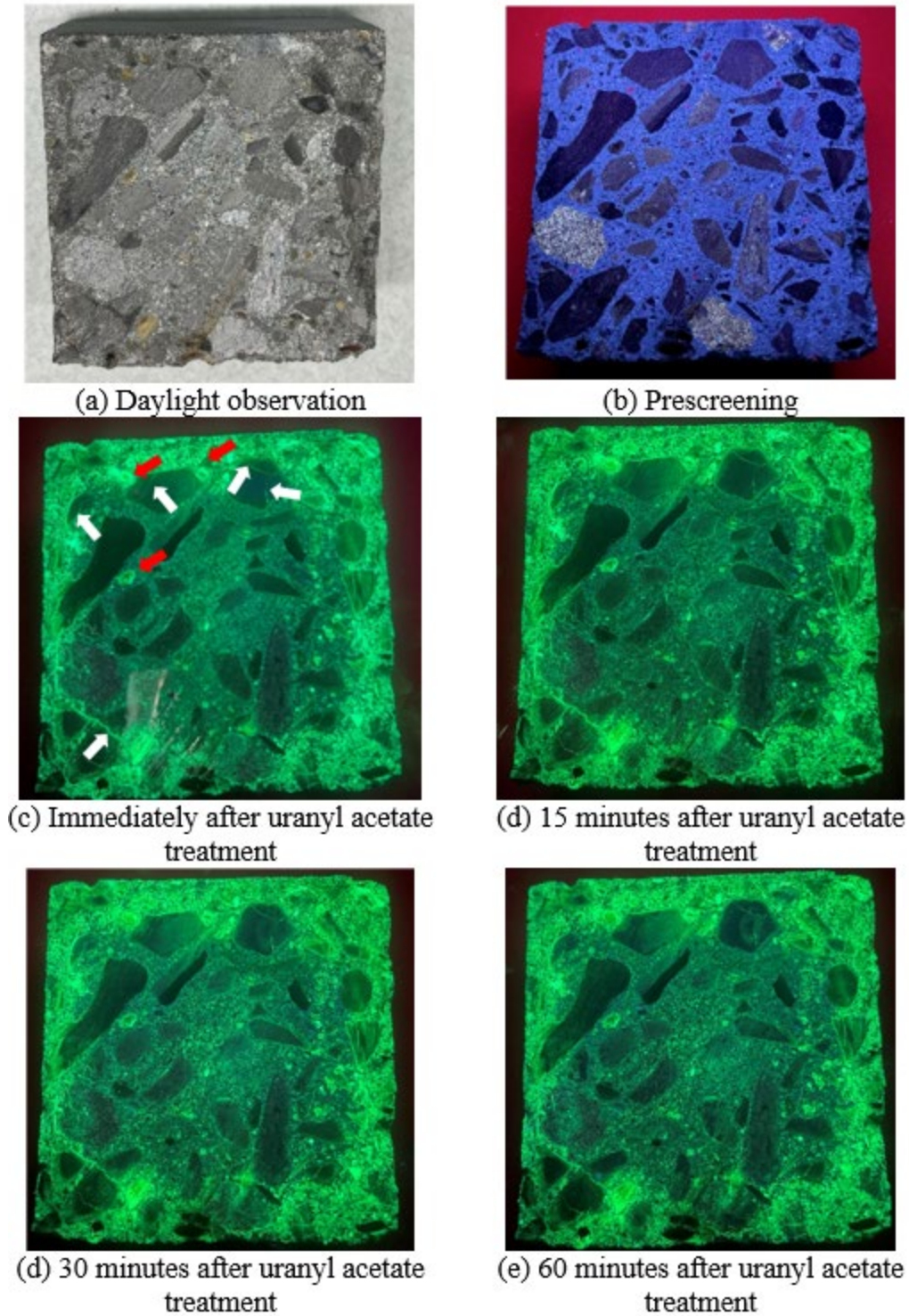


Figure 5-6. Observation of $3 \times 3 \times 11.25$ in. concrete prisms with Arcosa sand and Spratt coarse aggregate exposed to 1N NaOH at 176° F (a) under daylight, (b) prescreening, (c) immediately after uranyl acetate treatment – red arrows show the fluorescence in reaction rims and white arrows show the fluorescence in aggregate cracks, (d) 15-minute observation, (e) 30-minute observation, and (f) 60-minute observation after uranyl acetate treatment.

5.2 SODIUM COBALTINITRIDE/ RHODAMINE B TESTING

The previous section described the effectiveness of uranyl acetate as a reagent for identifying ASR. However, the detection of nonexpansive gels from expansive ones is not possible with this method unless the cracking intensities are correlated. Since the sodium cobaltinitride/rhodamine B combination allows for identifying nonexpansive gels from expansive ones, a series of testing was conducted using similar specimens as used for the evaluation of uranyl acetate performance. The commercial product, ASR Detect®, with two reagents was used in this study.

Among these two reagents, sodium cobaltinitrite is a well-known product used in analytical chemistry to determine K^+ content in a solution. Since the chemical reaction between the dissolved sodium cobaltinitrite with potassium forms a yellowish precipitate, the yellow stain highlights the areas with ASR gels rich in K^+ . The degree of reactivity can be diagnosed based on the extent of the yellow stain. Rhodamine B, typically referred to as the “pink” or “red” solution, allows for identifying the intensity of Ca^{2+} in nonexpansive gels when the color changes from orange to light purple-red.

Reactive fine and coarse aggregates and the mortar bars prepared with reactive aggregates were used for the evaluation of these two reagents. These specimens were subjected to various exposure conditions to accelerate, retard, or arrest the development of ASR and to contaminate specimen surfaces for evaluating possible impacts on color signatures.

5.2.1 Performance Evaluation Using Reactive Aggregates

The specimen labels, exposure conditions, and exposure duration for Spratt (coarse aggregate) and Arcosa sand (fine aggregate) are listed in Table 5-1 and Table 5-2, respectively. At the end of the exposure durations of coarse and fine aggregates, the specimens were treated with yellow solution (YS) for 15 minutes, rinsed with distilled water, and observed several times under daylight for 30 minutes. Then, they were treated with red solution (RS) for 15 minutes, rinsed with distilled water, and observed several times under daylight for 30 minutes. The coarse aggregate used for this evaluation was exposed to three different conditions (dried at 176° F, soaked in 1N NaOH at 176° F, and soaked in 3% NaCl at 176° F). The results are shown in Figure 5-7. Yellow stain is not visible on any of them even though the presence of ASR on the aggregate exposed to 1N NaOH at 176° F was confirmed through uranyl acetate testing. The absence of K^+ ions on these aggregates is the primary reason for this observation. The red solution is visible on all the aggregates; the

contrast and intensity is the greatest on the aggregate exposed to 3% NaCl at 176° F. This observation highlights the potential for misinterpretation of results in the presence of NaCl.

The fine aggregate used for this evaluation was exposed to three different conditions (dried at 176° F, soaked in 1N NaOH at 176° F, and soaked in 3% NaCl at 176° F). The first row in Figure 5-8 shows the observation of uranyl acetate treated samples under UV light. As seen in the figure, the sample exposed to 1N NaOH at 176° F developed a detectable level of ASR products. However, when treated with the ASR Detect® solutions, the expected unique color signatures were not observed due to the lack of K^+ and Ca^{+2} ions.



Figure 5-7. Observation of coarse aggregate (Spratt) stored under various exposure conditions and treated with ASR Detect®

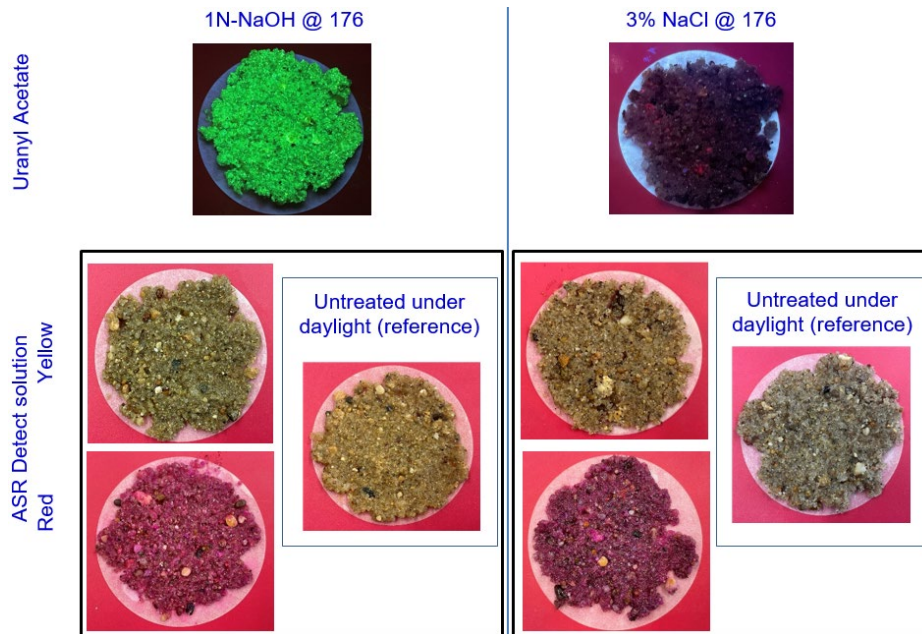


Figure 5-8. Observation of fine aggregate (Arcosa Sand) stored under various exposure conditions and treated with uranyl acetate and ASR Detect®

5.2.2 Performance Evaluation Using Mortar Bars

A $1 \times 1 \times 11.25$ in. mortar bar with Chert aggregate was subjected to 1N NaOH at 176° F. The 14-day expansion was 0.8%. After 14 days of exposure, the specimen was removed and stored under laboratory conditions for about a year. This specimen was sawcut and used to evaluate uranyl acetate and ASR Detect® staining techniques. As shown in Figure 5-9, specimens 1 and 2 share the same sawcut and indicate identical deterioration patterns. The presence of ASR in specimen 1 was evaluated using uranyl acetate, and the change in color intensity was observed for up to 45 minutes. As shown in the 2nd row of Figure 5-9, the presence of ASR gel around fine aggregate is clearly visible during the first five minutes. With time, uranyl acetate color precipitates and masks the color intensities around the aggregate, making the ASR products less visible. Specimen 2 was treated with the yellow stain. As shown in the 3rd row of Figure 5-9, yellow stain was observed, but the intensity reduced drastically within 10 minutes. The color intensity of the yellow stain immediately after the treatment was not as high as what is shown in literature, possibly due to the lack of K^+ ions in the treated surface. Following 10 minutes of observation, the same surface was treated with the red solution and observed under daylight for more than 30 minutes. As shown in the figure, using distinct color observations to identify the

presence of non-expansive ASR is a challenge; this is primarily due to the lack of contrast in color, as well as a scarcity of adequate guidelines and examples in literature.

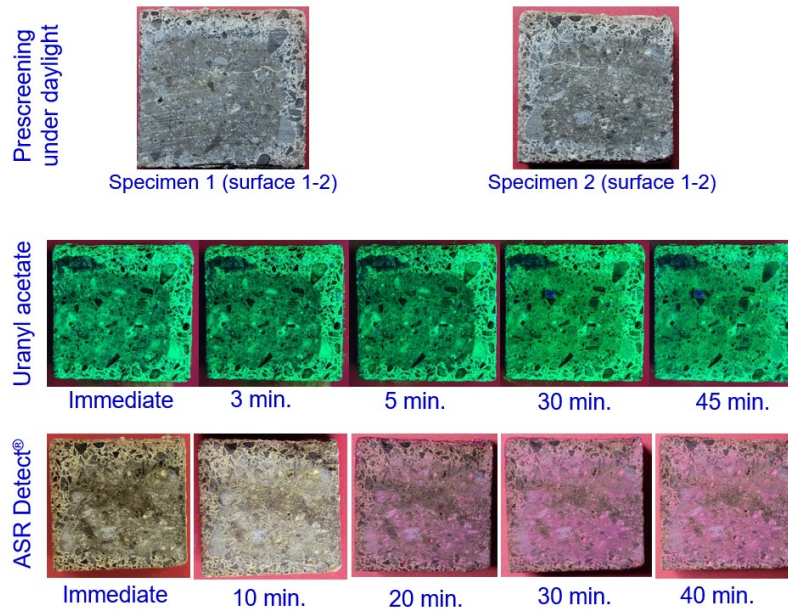


Figure 5-9. Observation of mortar bars prepared with chert aggregate, stored under various exposure conditions, and treated with uranyl acetate and ASR Detect®

5.3 SUMMARY

The capabilities and limitations of uranyl acetate to identify ASR was evaluated using specimens prepared with the following: (i) reactive fine and coarse aggregates, (ii) mortar bars consisting of reactive fine aggregate, and (iii) concrete prisms consisting of reactive coarse and fine aggregates exposed to different exposure conditions. The ASTM C856-14 (2014) procedure was modified by adopting the recommendations made by Igarashi et al. (2016). Instead of wetting the specimens using a squeeze bottle, the specimens were immersed in a uranyl acetate solution for 30 minutes to observe the saturation in fluorescence. Some literature recommended giving adequate time after treatment to dry the specimen. However, the laboratory analysis showed that the fluorescence intensity of uranyl ions increases as the specimen dries, which may lead to misinterpreting the observations. The color signatures developed on reactive aggregates were used to evaluate the observations made on the mortar bars and concrete prisms.

The results are highly vulnerable to personal judgement; thus, an experienced person must interpret the data. This can be avoided by adopting image analysis tools to extract the color signatures. However, additional investigations are required to standardize the image analysis procedures, with consistent equipment, exposure conditions, and image quality.

Uranyl acetate is the most reliable field testing method available to screen for ASR. One of the major challenges of implementing this method in the field is the interference of the ambient light while observing the unique fluorescent signatures using a UV light. The current practice for minimizing the ambient light interference is to use a sealed metal box with a UV light and an opening to view the treated surface. Another common approach is to use a dark cloth to cover the operator's upper body and the treated area. The implementation of these methods in the field is risky and inconvenient, and could lead to misinterpretation of the results. Therefore, additional research is needed to develop new tools and techniques to screen for ASR under field conditions.

6 GUIDELINES FOR LOAD RATING OF DISTRESSED PSC BOX- AND I-BEAMS

6.1 OVERVIEW

This chapter presents guidelines for incorporating prestressed concrete (PSC) box- and I-beam deteriorations and distresses during flexural rating of beams. These guidelines were developed using the information collected through a comprehensive review of literature; inspection of a selected number of PSC I-beam bridges (documented in Chapter 3); the measurement of crack depths on two fascia beams (documented in Section 3.5.3); and the past experience of the team documented in Attanayake and Aktan (2015), Attanayake and Aktan (2011), Aktan et al. (2009), and Aktan et al. (2005). The guidelines are provided for (1) the estimation of concrete and prestressing steel properties, (2) the calculation of beam section properties and the number of effective prestressing strands, and (3) the possible implementations of updated material properties, cross-section properties, and prestressing parameters in AASHTOWare BrR.

6.2 RECOMMENDED GUIDELINES

6.2.1 Concrete Material Properties

According to the data presented in Section 2.7, the compressive strength of concrete in decommissioned prestressed beams without ASR or similar deterioration mechanisms is greater than the design strength. The measured compressive strength of such members was at least 20% to more than 50% greater than the design strength. Even though the compressive strength of concrete is not greatly affected due to ASR, the lowest values reported in literature show a maximum reduction of about 20% with an expansion of 0.1% (ISE 1992), which is considered to be a very high degree of expansion. Since ASR was limited to fine aggregates in the inspected bridges and the damage levels are not correlated to the distresses observed in Michigan bridge beams, a maximum compressive strength reduction of 20% is recommended when a high level of expansion due to ASR is suspected. Since bridge inspectors noted “possible ASR” in the comments when they observed longitudinal and/or map cracking on fascia beams, a set of pictures and instructions needs to be provided to help inspectors identify distress types and the possible causes. Severe box-beam cracking was documented due to freeze-thaw damage. The freeze-thaw damaged concrete shall be excluded from the section capacity calculation.

The concrete modulus of elasticity and tensile strength (splitting tensile strength and modulus of rupture) decrease with the increase in concrete expansion due to ASR. Table 6-1 presents the reduction in concrete modulus of elasticity and tensile strength against the 28-day values. The reduction in concrete modulus of elasticity is based on the data in ISE (1992), Kawabata et al. (2017), Martin et al. (2017), and Abd-Elssamad et al. (2020). The reduction in concrete tensile strength is based on the data in ISE (1992) and Sanchez (2014).

Table 6-1. Reduction in Concrete Modulus of Elasticity and Tensile Strength Due to ASR

Expansion level (%)	Reduction in compressive strength (%)	Reduction in modulus of elasticity (%)	Reduction in tensile strength (%)
$0.00 < \epsilon \leq 0.01$	0-5	0 – 3	0 - 6
$0.01 < \epsilon \leq 0.03$	0-5	3 – 10	6 - 22
$0.03 < \epsilon \leq 0.04$	0-5	10 – 13	22 - 29
$0.04 < \epsilon \leq 0.05$	0-5	13 – 15	29 - 38
$0.05 < \epsilon \leq 0.07$	5-10	15 – 21	38 - 43
$0.07 < \epsilon \leq 0.10$	10-20	21 – 28	43 - 47
$0.10 < \epsilon \leq 0.30$	20-30	28 – 56	47 - 61
$0.30 < \epsilon \leq 0.50$	30-40	56 – 67	> 61
$0.50 < \epsilon \leq 1.00$	> 40	67 – 74	> 61

6.2.2 Effective Concrete Section Properties

When calculating the concrete section properties, one should only consider the effective concrete cross-section after eliminating the concrete area subjected to spalls and delamination. In the presence of delamination, one must remove all the delaminated concrete to determine the depth of concrete deterioration. For concrete with suspected regions of unsound concrete, the area of unsound concrete must be located and eliminated from the section property calculation.

In this study, a Mathcad sheet (*Load Rating of PSC Box Beams - LFR and LRFR*) was prepared to calculate the reduced cross-section properties of distressed PSC box-beams. Spalls are typically observed along the bottom flange edges. Figure 6-1 defines necessary dimensions (L_1 , L_2 , R_1 , and R_2) that can be recorded during scoping inspections and used in the Mathcad sheet to calculate cross-section properties.

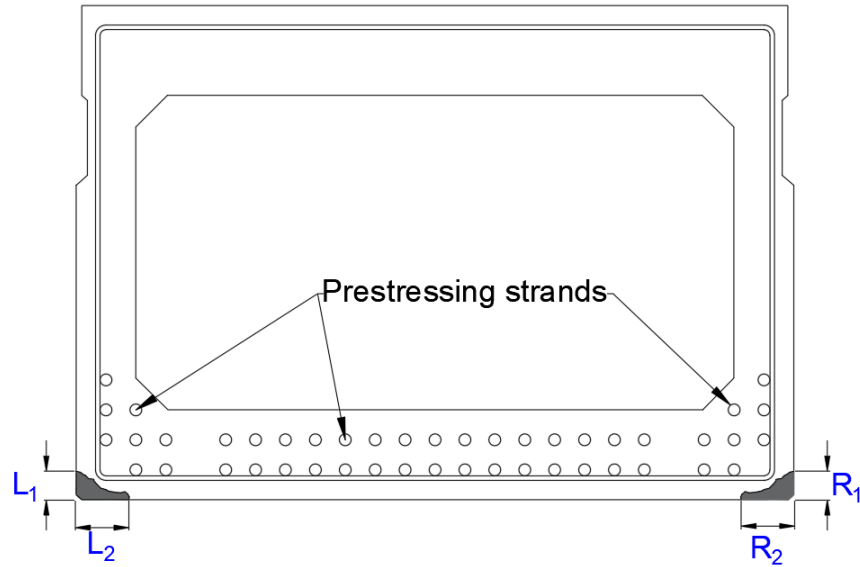


Figure 6-1. Measurements to define bottom flange edge spalls

Since spalls due to causes other than high-load-hits were not frequently reported in I-beams, the Mathcad sheet only includes formulations to evaluate box-beam section properties and rating factors.

6.2.3 Prestressing Steel Material Properties

Since the distressed strands are excluded from load rating calculations, the design strength and modulus values need to be considered for load rating.

6.2.4 Effective Number of Prestressing Strands

The guidelines to determine the number of effective prestressing strands in a section is presented. The redevelopment of severed strands depends on the concrete quality surrounding the damaged area.

6.2.4.1 Guidelines for Estimating Strand Loss in PSC Box-Beams

The number of ineffective strands in a cross-section is estimated based on the presence of (1) longitudinal, map, and random cracks and (2) other conditions such as spalls, delamination, exposed strands, corroded/broken strands, exposed stirrups, and wet/stained areas. Table 6-2 and Figure 6-2 detail the necessary guidelines.

Table 6-2. Guidelines for Excluding Ineffective Strands Due to Cracking in Box-Beams



Case	Location and/or Nature of crack(s)	Other observations	Action(s)
1	<p>Longitudinal crack(s) closer to the middle of beam bottom flange. No spalls.</p> 	<p>With or without rust stains or other discoloration of the concrete adjacent to the cracks.</p>	<p>Exclude strands from all rows adjacent to the cracks. (See Figure 6-2 Case #1).</p>
2	<p>Longitudinal crack(s) at the bottom flange and closer to the webs, or at the web and closer to the bottom flange. Cracks are more or less parallel to the edges. No spalls.</p> 	<p>With or without rust stains or other discoloration of the concrete adjacent to the cracks.</p>	<p>Exclude strands from all rows adjacent to the cracks. (See Figure 6-2 Case #2).</p>

Table 6-2. Guidelines for Excluding Ineffective Strands Due to Cracking in Box-Beams (Cont.)




Case	Location and/or Nature of crack(s)	Other observations	Action(s)
3	<p>Longitudinal crack(s) located towards the bottom edge of the beam bottom flange. Cracks are not parallel to the edge. No spalls.</p> 	<p>With or without rust stains or other discoloration of the concrete adjacent to the cracks.</p>	<p>Exclude strands from all rows adjacent to the cracks and the ones intersecting the cracks. Figure 6-2 does NOT include this case since it is difficult to show a non-parallel crack on a 2D diagram.</p>
4	<p>Two or more longitudinal cracks observed crossing or meeting. No spalls.</p> 	<p>With or without rust stains or other discoloration of the concrete adjacent to the cracks.</p>	<p>Exclude strands from all rows located within the cracked zone and one strand from all rows of strands located adjacent to the perimeter of the cracked zone. (See Figure 6-2 Case #4).</p>

Table 6-2. Guidelines for Excluding Ineffective Strands Due to Cracking in Box-Beams (Cont.)

Case	Location and/or Nature of crack(s)	Other observations	Action(s)
5	Map cracks in the bottom flange and web. (An image to be added)	With or without rust stains or other discoloration of the concrete adjacent to the cracks	Include all strands present at the section for capacity calculation. (See Figure 6-2 Case #5).
6	Random cracks at beam soffit. 	With or without rust stains or other discoloration of the concrete adjacent to the cracks	Exclude all the strands from all rows located within and adjacent to the cracked zone. Typically, freeze-thaw damage results in such cracking. If it is confirmed that the deterioration is due to free-thaw actions, strands can be in good condition. However, beam webs could also be damaged due to freeze-thaw making it unsafe to keep the structure open to traffic. Freeze-thaw damage was the primary reason for replacing the Brady Street over the lower branch of the Rouge River bridge in March 2020 after being in service only for 26 years. (See Figure 6-2 Case #6).

Note (for cases 1 – 4):

- If the longitudinal crack(s) extends throughout the beam span, with or without rust stains or other discoloration of the concrete adjacent to the cracks, disregard the total length of strands.
- If the longitudinal crack(s) is shorter than the beam length and the region beyond the crack has sound concrete, disregard the length of the strand equivalent to the length of the crack plus a development length (to either side of the crack). Refer AASHTO LRFD (2017) Section 5.11.4 to calculate the prestressing strand development length.

As shown in Figure 6-2, a 48 × 33 in. box-beam section is selected as an example to illustrate the number of strands to be excluded from capacity calculations. The numbers in the figure represent the distress cases listed in Table 6-2.

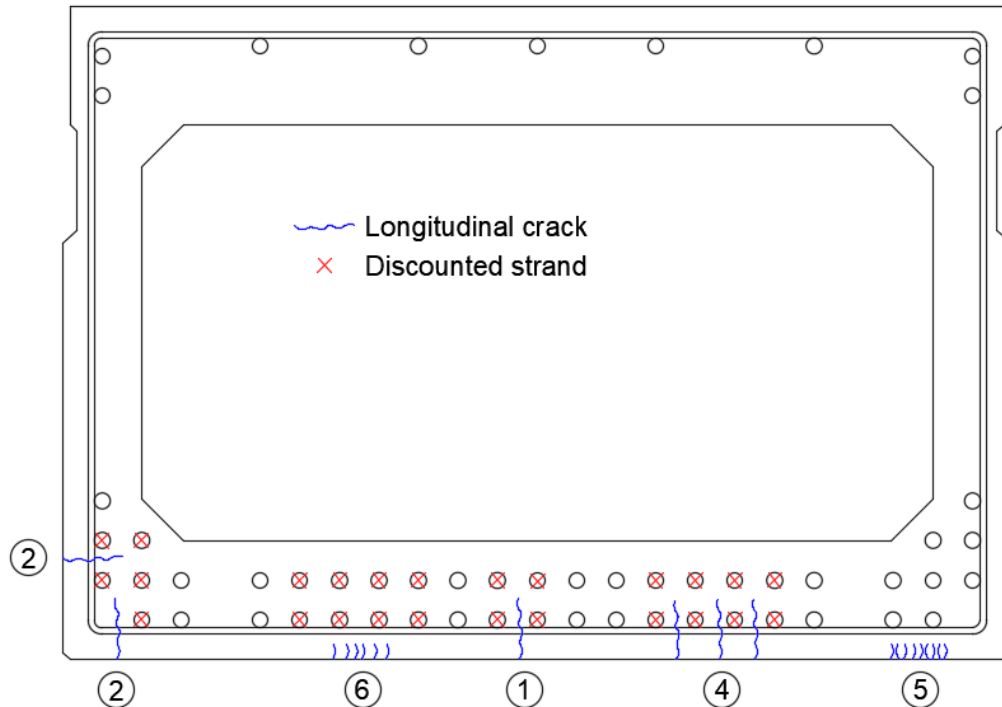


Figure 6-2. Guidelines for excluding ineffective strands in the presence of longitudinal, map, and random cracks in box-beams (Case #3 is not shown)

Table 6-3 lists 9 additional cases covering all distress types observed in PSC box-beams and the guidelines to determine the number of ineffective prestressing strands in a selected cross-section. The numbers in Figure 6-3 represent the distress cases listed in Table 6-3. Consequently, a 48 × 33 in. box-beam section is selected to illustrate the number of strands to be excluded from capacity calculations.

Table 6-3. Guidelines for Excluding Ineffective Strands from Distressed Box-Beams


Case	Nature of deterioration	Observations	Action(s)
1	Concrete spall/Delamination	<p>No exposed stirrups or strands. Sound concrete in the vicinity of the spall.</p> 	<p>Include all strands present at the section for capacity calculation.</p> <p>(See Figure 6-3a case #1).</p>
2	Spall/Delamination	<p>No exposed stirrups or strands. Unsound concrete in the vicinity of the spall.</p> <p>(An image to be added).</p>	<p>Remove all delaminated concrete to determine the depth of concrete deterioration. The removal of deteriorated concrete might expose prestressing strands and provide necessary information to decide on the number of strands to be excluded from capacity calculation.</p> <p>If strands are not visible, exclude strands adjacent to the affected area from capacity calculation.</p> <p>(see Figure 6-3b case #2).</p>

Table 6-3. Guidelines for Excluding Ineffective Strands from Distressed Box-Beams (Cont.)



3	Exposed strand(s) with spalls.	<p>Sound concrete in the vicinity of the spall.</p> 	<p>Include all strands present at the section for capacity calculation.</p> <p>(See Figure 6-3a case #3).</p>
4	Exposed strand(s) with spalls.	<p>Unsound concrete in the vicinity of the spall.</p> <p>(An image to be added.)</p>	<p>Remove unsound concrete to estimate the depth of degradation. Include all strands present at the section for capacity calculation unless the conditions show otherwise.</p> <p>(See Figure 6-3b case #4).</p>
5	Exposed stirrups.	<p>Sound concrete surrounding the exposed stirrups.</p> 	<p>Exclude strands located in the lower row directly above the exposed stirrups.</p> <p>(See Figure 6-3a case #5).</p>

Table 6-3. Guidelines for Excluding Ineffective Strands from Distressed Box-Beams (Cont.)





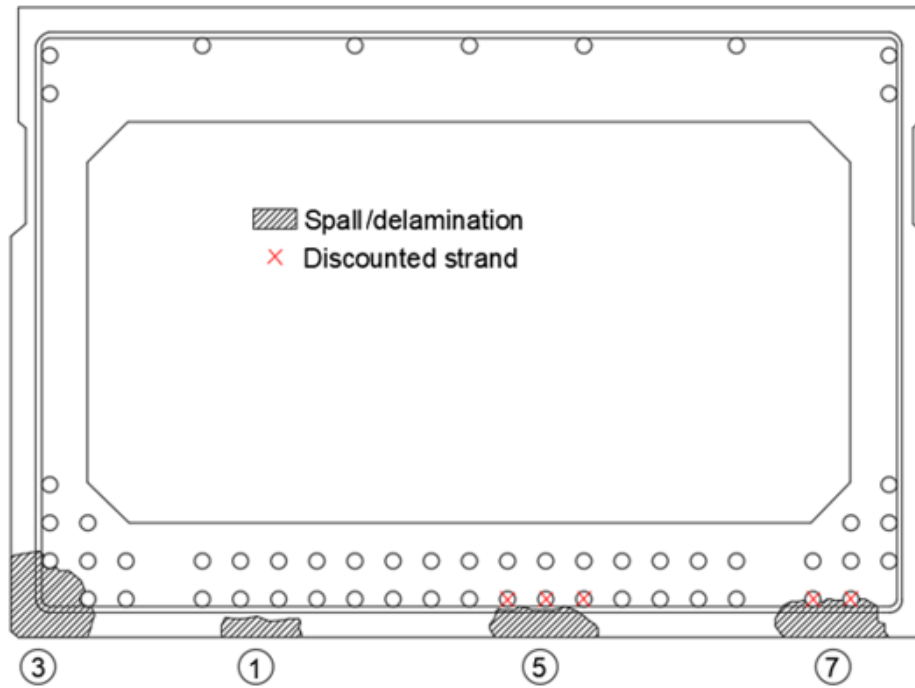
<p>6</p>	<p>Exposed stirrups.</p>	<p>Unsound concrete surrounding the exposed reinforcement stirrups.</p> 	<p>Exclude strands in all rows located above the area of unsound concrete.</p> <p>(See Figure 6-3b case #6).</p>
<p>7</p>	<p>Corroded/ Broken strand(s) with spalls.</p>	<p>Sound concrete in the vicinity of the corroded/broken strands.</p> 	<p>Exclude corroded/broken strand(s) from capacity calculation.</p> <p>(See Figure 6-3a case #7).</p>

Table 6-3. Guidelines for Excluding Ineffective Strands from Distressed Box-Beams (Cont.)

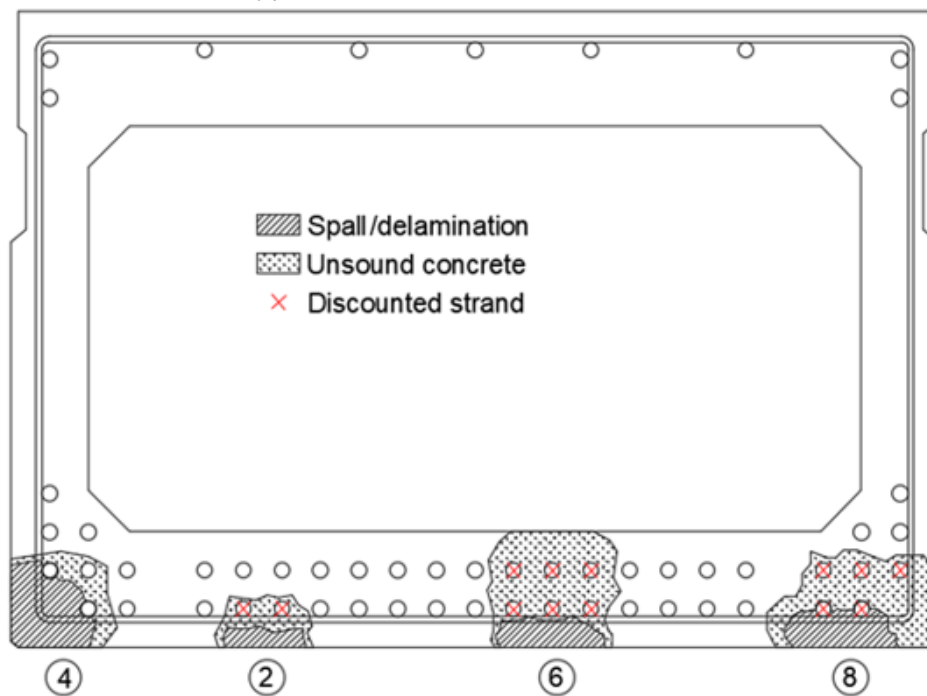
<p>8</p>	<p>Corroded/ Broken strand(s) with spalls.</p>	<p>Unsound concrete in the vicinity of the corroded/broken strands.</p> 	<p>Exclude exposed/broken strand(s) and all strands located in rows above and immediately adjacent to the area with unsound concrete from capacity calculation.</p> <p>(See Figure 6-3b case #8).</p>
<p>9</p>	<p>Wet or stained areas at the soffit or edges of beams</p>	<p>Sound concrete within the wet or stained area.</p> 	<p>Do not exclude strands from capacity calculation.</p>

Note:

- *If the corroded/broken strand(s) extends throughout the span, with or without rust stains or other discoloration of the concrete adjacent to the damaged region, exclude the total length of strands.*
- *If the corroded/broken strand(s) extends for a length much shorter than the beam span and the region extending away from the damaged area has sound concrete, disregard the length of the strand in the damage region plus a development length (to either side of the damage region). Refer AASHTO LRFD (2017) Section 5.11.4 to calculate the prestressing strand development length.*



(a) Deteriorations with sound concrete



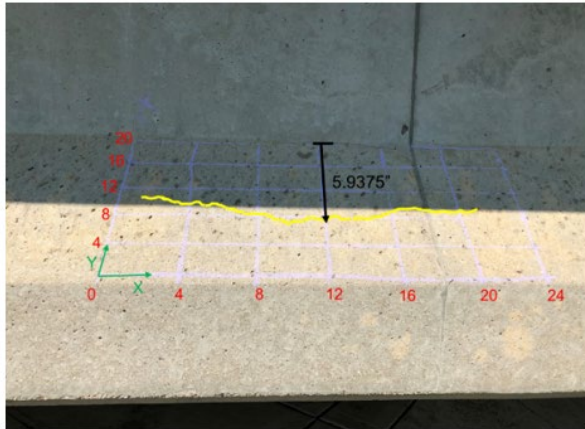
(b) Deteriorations with unsound concrete

Figure 6-3. Guidelines for determining the deteriorated concrete area and prestressing strands in box-beams
 (The distresses are shown for a MI 48 × 33 in. box-beam section.)

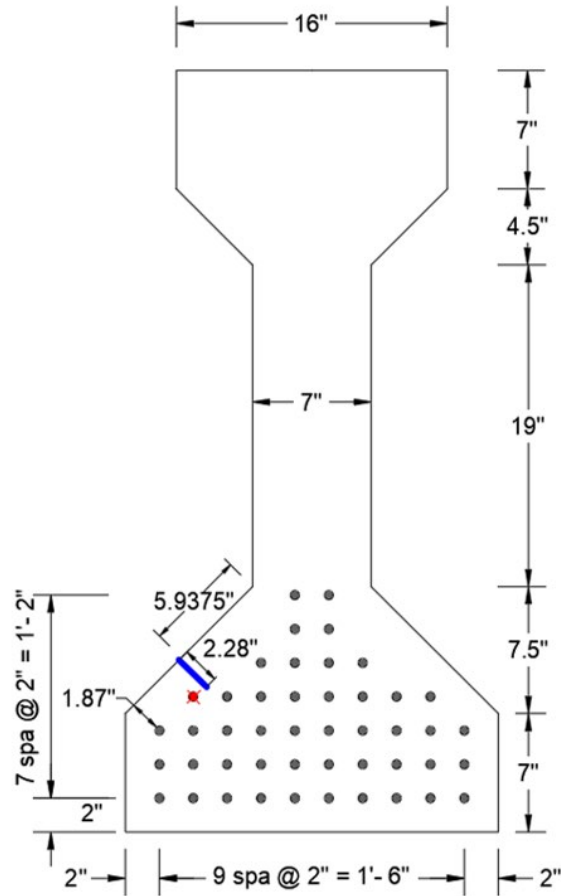
6.2.4.2 Guidelines for Estimating Strand Loss in PSC I-beams

Longitudinal and map cracks were predominantly observed in I-beams. As discussed in Chapter 3, field inspection and ASR testing showed that the map cracks were not deep enough to impact prestressing strand durability and bond. The longitudinal cracks that were documented in the fascia beam bottom flange and located within the span were developed due to a combined action of exposure to environmental elements, the presence of map cracks, and the stresses due to prestressing. Unfortunately, none of the previous studies documented in literature evaluated the depth of such cracks within in-service PSC beams. The limited evaluation of crack depths documented in Section 3.5.3 shows that 0.01 to 0.016 in. wide cracks can be as deep as 2.32 in. Yet, the impact of such cracks on strand durability and bond integrity depends on the location of the crack and strand layout, as shown with the following two examples.

Figure 6-4 shows a longitudinal crack on the inclined surface of the bottom flange of the southern exterior beam of the bridge (S.N. 424) that carries Lincoln Road over I-75 southbound. The crack is assumed to be perpendicular to the inclined surface of the beam bottom flange. As shown in Figure 6-4a, the position of the crack varies over the inclined surface. According to the data presented in Section 3.5.3, the maximum estimated crack depth was 2.28 in. at $x = 12$ inches. At the maximum crack depth location, the distance to the crack from the web-bottom flange interface was 5.9375 in. (see Figure 6-4a). As shown in Figure 6-4b, this 2.28 in. deep crack is in close proximity to a strand. Hence, the presence of this 2.28 in. deep crack requires the strand marked in red to be excluded from the load capacity calculation.



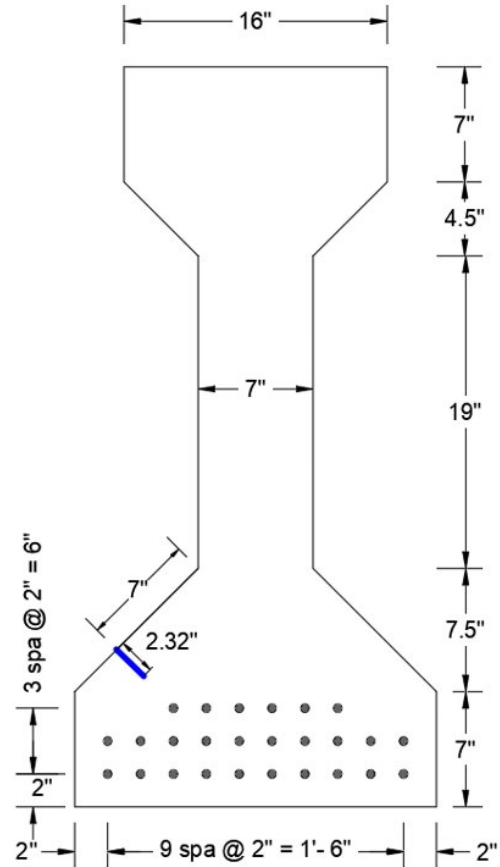
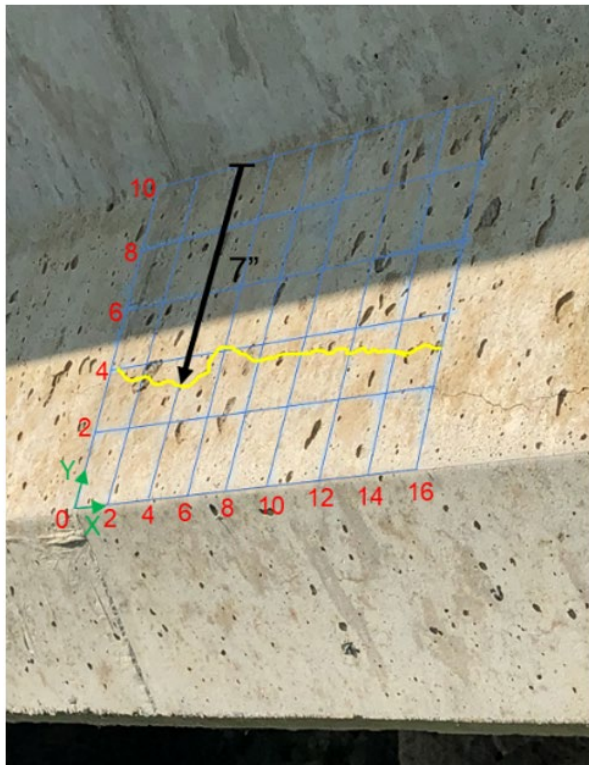
(a) Position of the longitudinal crack on the inclined surface



(b) Presence of the longitudinal crack within the beam cross-section

Figure 6-4. Estimating the loss of strands in a distressed PSC I-beam of S.N. 424 bridge

Figure 6-5 shows the longitudinal crack in the inclined surface of the bottom flange of the I-beam in the bridge (S.N. 2618) that carries M-57 over the Flint River. As shown in Figure 6-5a, the position of the crack varies over the inclined surface. According to the data presented in Section 3.5.3, the maximum estimated crack depth was 2.32 in. at $x = 4$ inches. At the maximum crack depth location, the distance to the crack from the web-bottom flange interface was 7 in. (see Figure 6-5a). As shown in Figure 6-5b, this 2.32 in. deep crack is not in close proximity to a strand. Hence, none of the strands are excluded from the load capacity calculation.



(a) Position of the longitudinal crack on the inclined surface (b) Presence of the longitudinal crack within the beam cross-section

Figure 6-5. Estimating the loss of strands in a distressed PSC I-beam of S.N. 2618 bridge

As shown with the above two examples, the impact of longitudinal cracks on strand durability and bond integrity depends on the locations of the cracks and strand layout. As a rule of thumb, it is recommended to use a 2.5 in. depth for cracks that are narrower than 0.016 in. To develop more rational guidelines, a crack width vs. depth relationship needs to be developed for the typical bridge beams. Another option is to train MDOT engineers to implement the crack depth evaluation procedures described in Section 3.5 of this report.

6.3 IMPLEMENTATION OF THE RECOMMENDED GUIDELINES IN AASHTOWARE BrR

6.3.1 Defining Concrete Material Properties in AASHTOWare BrR

Users must identify relevant values for concrete modulus of elasticity and modulus of rupture based on the recommendations given in Section 6.2.1. Subsequently, they shall input the selected values using the dialog box shown in Figure 6-6.

The dialog box titled "Bridge Materials - Concrete" contains the following fields and values:

Property	Value	Unit
Name		
Description		
Compressive strength at 28 days (f'_c)		ksi
Initial compressive strength (f'_{ci})		ksi
Coefficient of thermal expansion	0.0000060000	1/F
Density (for dead loads)		kcf
Density (for modulus of elasticity)		kcf
Std Modulus of elasticity (E_c)		ksi
LRFD Modulus of elasticity (E_c)		ksi
Std Initial modulus of elasticity		ksi
LRFD Initial modulus of elasticity		ksi
Poisson's ratio	0.200	
Composition of concrete	Normal	
Modulus of rupture		ksi
Shear factor	1.000	
Splitting tensile strength (f_{ct})		ksi

Buttons at the bottom: Copy To Library..., Copy from Library..., OK (highlighted), Apply, Cancel

Figure 6-6. AASHTOWare BrR dialog box for defining material properties

6.3.2 Defining Beam Cross-Section Properties in AASHTOWare BrR

Users should define section properties using the dialog box shown in Figure 6-7. For box-beams, they will use the values from the Mathcad sheet (*Load Rating of PSC Box Beams - LFR and LRF*).

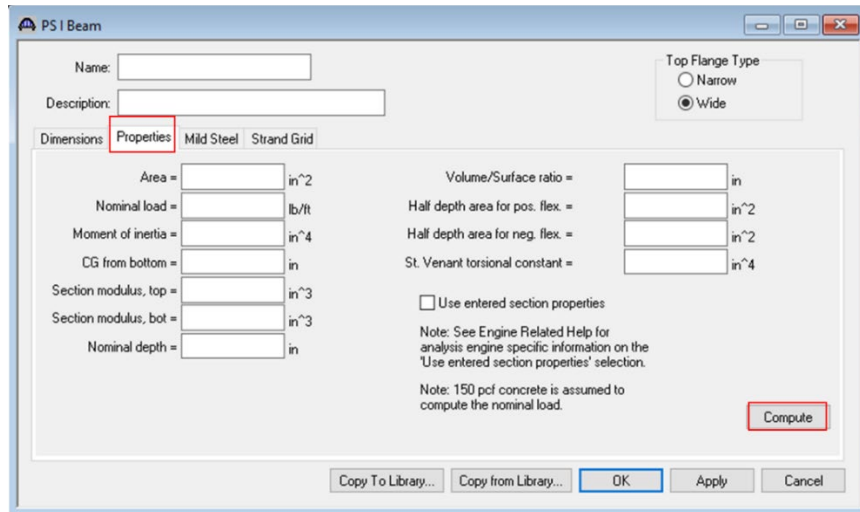


Figure 6-7. AASHTOWare BrR dialog box for defining section properties

6.3.3 Defining Prestressing Strand Layout in AASHTOWare BrR

Users should follow the recommended guidelines given in Section 6.2.4.1 and 6.2.4.2 to estimate the effective number of prestressing strands for the listed distress cases. They will then update the prestressing strand layout parameters in Figure 6-8 or use the output from the Mathcad sheet (*Load Rating of PSC Box Beams - LFR and LFRF*) to define the parameters in Figure 6-9.

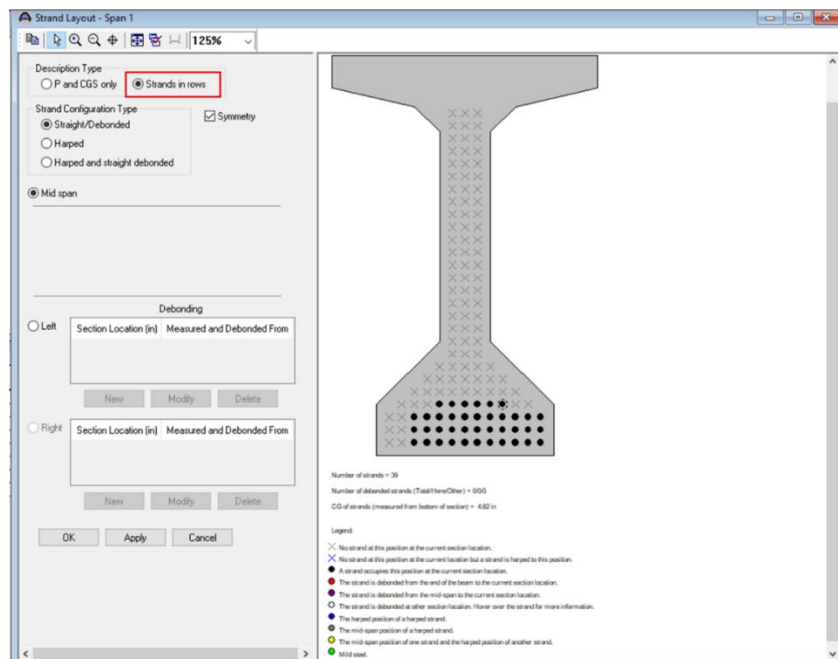


Figure 6-8. AASHTOWare BrR dialog box for defining strands in rows

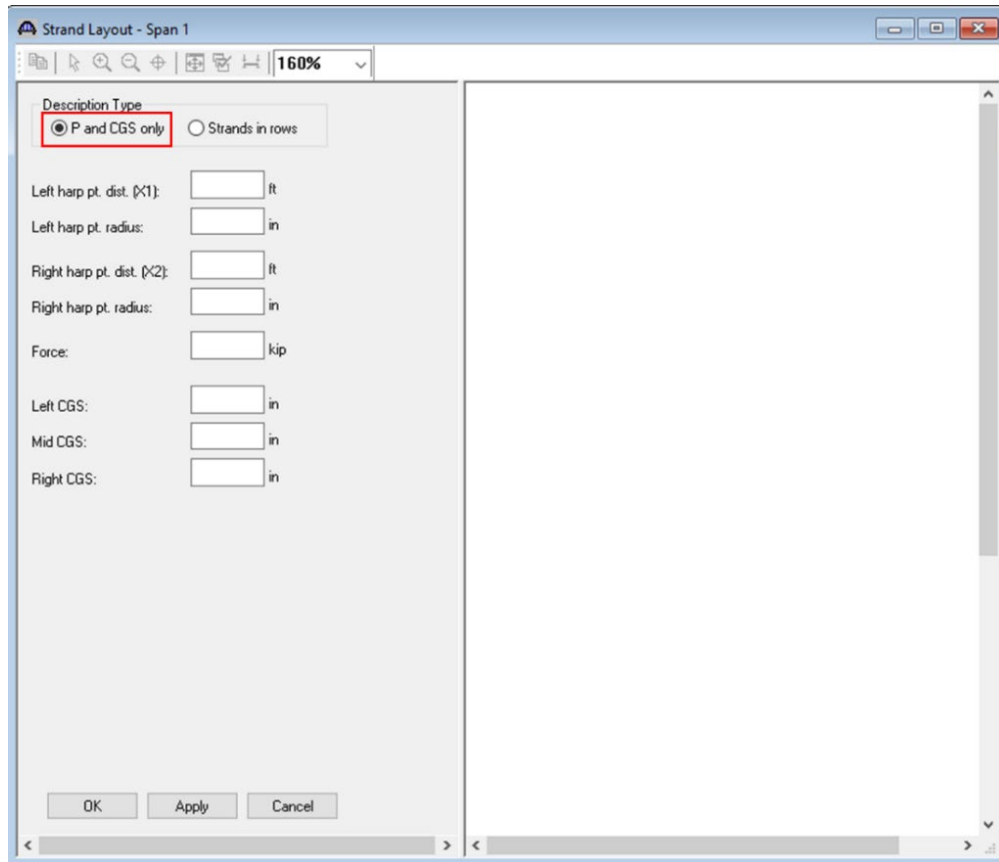


Figure 6-9. AASHTOWare BrR dialog box for defining prestressing force and the center of gravity

7 PERFORMANCE EVALUATION OF CONCRETE PROTECTIVE SYSTEMS

7.1 OVERVIEW

The experimental program conducted in this study had two objectives: (1) preparation of mortar and concrete specimens with confirmed ASR for the evaluation of staining techniques used for the field evaluation of ASR in concrete and (2) performance evaluation of surface coatings and sealants to control concrete internal moisture (internal relative humidity – IRH).

7.2 IMPACT OF MIX DESIGN AND EXPOSURE ON MORTAR AND CONCRETE EXPANSION

The impact of mix designs and exposure conditions on the rate of alkali-silica reactivity in the mortar and concrete specimens was evaluated. Once the expansion thresholds were exceeded, the specimens were used to evaluate the effectiveness of the staining techniques for screening ASR in concrete. In the meantime, the results were used to select a mix design for the slab specimens to evaluate the curing conditions (before and after the application of concrete protective systems) and the effectiveness of sealants and coatings to control IRH.

7.2.1 Accelerated Mortar Bar Test

The primary objective of this test is to evaluate the reactivity levels of fine aggregate (Arcosa sand) under various exposure conditions by measuring the mortar bar expansion. Two different water-cement (w/c) ratios were used. As learned from the fabricator survey, a w/c ratio of 0.35 is typical for PSC bridge beams. The w/c of 0.47 was used to prepare standard specimens conforming to ASTM C1260 (2021). The equivalent alkalinity content ($\text{Na}_2\text{O}_{\text{eq}}$) of Type I cement used in the mixes was 0.51%. To evaluate the impact of increased alkalinity level, two other mortar mixes with the same w/c were developed by adding NaOH into the mix resulting in an $\text{Na}_2\text{O}_{\text{eq}}$ of 1.25%. The design of four mortar mixes is given in Table 7-1. After fabrication and curing of the specimens for 1 day as per the ASTM C1260 (2021) standard, a group of three specimens was subjected to different exposure conditions. Table 7-2 lists the exposure conditions and the assigned labels for the specimens. For example, row 1 of Table 7-2 shows that three mortar bars were fabricated with Mix 1 and exposed to 1N NaOH at 176° F. The label assigned for this set of specimens is MB-0.35/0.51-1N NaOH-176-*

where,

MB: Mortar bar

0.35: w/c ratio

0.51: Na₂O_{eq} in %

1N NaOH: Exposure medium

176: Exposure temperature in ° F

* : Specimen labels as A, B, and C.

Since the ASTM C1293 (2020) recommends maintaining prisms at 101° F (38° C) for a one-year duration to evaluate ASR susceptibility, 101° F was selected as a lower bound to evaluate the reactivity levels of fine aggregate. Literature indicates concrete expansion under a high concentration of NaCl; however, looking at possible exposure of PSC beams to NaCl and possible impacts on the results of staining techniques, a set of specimens prepared with Mix 1 were exposed to 3% NaCl at 101° F.

Table 7-1. The Design of Mortar Mixes for Three Specimens - Phase 1 Testing

Mix composition	Mix 1	Mix 2	Mix 3	Mix 4
Water-cementitious material ratio	0.35	0.35	0.47	0.47
Fine aggregate (SSD ³) (lb) (Arcosa sand)	0.97	0.97	0.97	0.97
Type I cement (lb)	2.18	2.18	2.18	2.18
Deionized (DI) water (lb)	0.34	0.34	0.46	0.46
Added sodium hydroxide (lb)	NA ¹	0.01	NA	0.01
Equivalent alkalinity (%)	0.51²	1.25	0.51	1.25

¹ - Not applicable

² - From cement itself

³ - Saturated surface dry

Table 7-2. Exposure Conditions and Labels for Mortar Bars

Mortar mix (a)	No. of specimens (b)	Exposure medium (c)	Exposure temperature (° F) (d)	Specimen label (e)
Mix 1	3	1 N NaOH	176	MB-0.35/0.51-1N NaOH-176-*
Mix 1	3	1N NaOH	101	MB-0.35/0.51-1N NaOH-101-*
Mix 1	3	3% NaCl	101	MB-0.35/0.51-3% NaCl-101-*
Mix 2	3	0.1N NaOH	101	MB-0.35/1.25-0.1N NaOH-101-*
Mix 3	3	1 N NaOH	101	MB-0.47/0.51-1N NaOH-101-*
Mix 4	3	0.1N NaOH	101	MB-0.47/1.25-0.1N NaOH-101-*

The initial expansion readings of all the mortar bars were recorded at room temperature after demoulding. The zero readings and the subsequent expansion measurements were recorded at respective exposure temperatures as per the ASTM C1260 (2021) procedures.

7.2.1.1 Results and Discussion

Figure 7-1 shows the expansion results of mortar bars in 1N NaOH at 176° F. These mortar bars pass the predetermined expansion threshold of 0.1% in less than 14 days of exposure, indicating the moderate reactivity of Arcosa sand (ASTM C1778 2020).

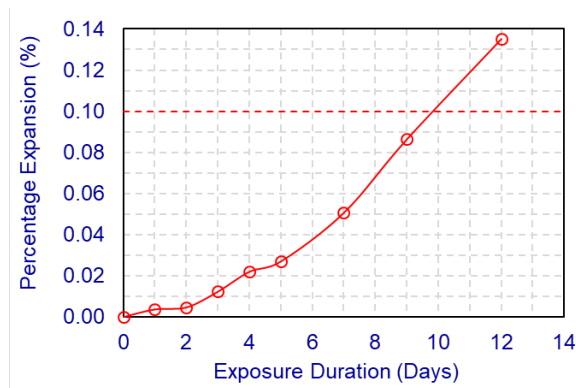


Figure 7-1. Expansion of mortar bars with 0.35 w/c in 1N NaOH at 176° F (MB-0.35/0.51-1N NaOH-176)

As shown in Figure 7-2, mortar bars fabricated using the 0.35 w/c mix (with and without added NaOH) were initially exposed to 1N NaOH, 3% NaCl, and 0.1N NaOH at 101° F for 89 days. At the end of initial exposure, mortar bars immersed in 1N NaOH and 3% NaCl reached an average expansion of 0.025%, while mortar bars exposed to 0.1N NaOH achieved an average expansion of 0.029%. Following 89 days, the exposure temperature of mortar bars B and C in each exposure medium increased to 120° F and 140° F, respectively. The temperature of mortar bar A was continued at 101° F. Only the mortar bars exposed to 1N NaOH at 120° F and 140° F passed the 0.1% expansion limit at 14 days after increasing the temperature. Mortar bars exposed to 101° F did not have a measurable increase in expansion beyond what was recorded at 89 days. The mortar bars exposed to 3% NaCl and 0.1N NaOH at 120° F and 140° F had a noticeable expansion within 14 days.

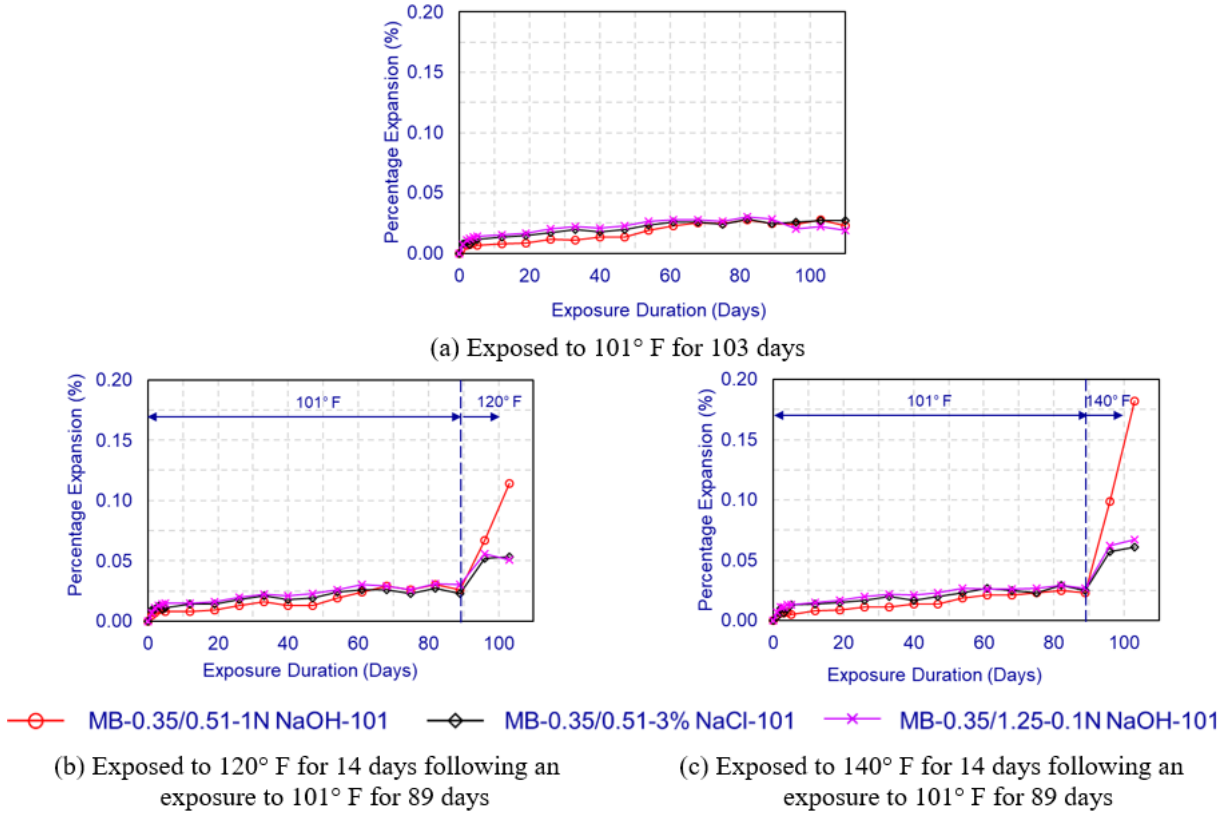


Figure 7-2. Expansion of mortar bars with 0.35 w/c under different exposure conditions

The expansion results of mortar bars fabricated with 0.47 and 0.35 w/c ratios are shown in Figure 7-3. The mortar bars exposed to 1N NaOH at 101° F have an $\text{Na}_2\text{O}_{\text{eq}}$ of 0.51%, while the mortar bars exposed to 0.1N NaOH at 101° F have an $\text{Na}_2\text{O}_{\text{eq}}$ of 1.25%. Interestingly, the mortar bars with 0.47 w/c and an $\text{Na}_2\text{O}_{\text{eq}}$ of 0.51% started expanding at a higher rate after 60 days when exposed to 1N NaOH at 101° F. Mortar bars with 0.35 w/c did not expand when exposed to 101° F irrespective of the $\text{Na}_2\text{O}_{\text{eq}}$ content and the exposure medium. Also, the mortar bars with 0.47 w/c and an $\text{Na}_2\text{O}_{\text{eq}}$ of 1.25% did not expand when exposed to 0.1N NaOH at 101° F even with a greater $\text{Na}_2\text{O}_{\text{eq}}$ content. The results indicate that a high concentration exposure medium (i.e. 1N NaOH) and higher w/c ratio (i.e. 0.47) are required to yield a greater expansion due to ASR at 101° F.

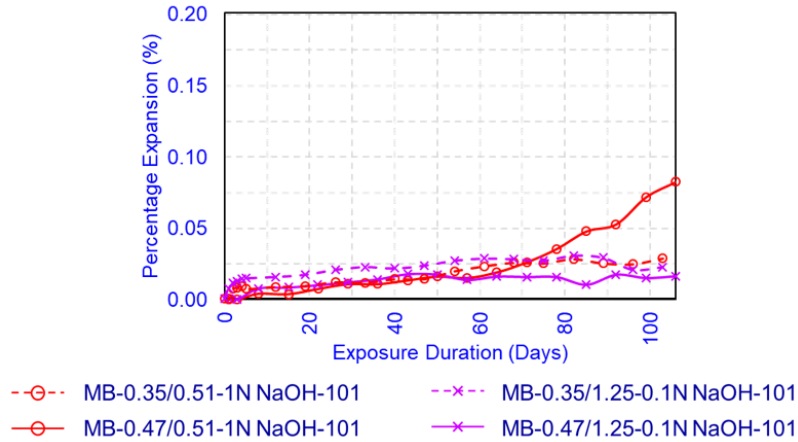


Figure 7-3. Expansion of mortar bars with 0.47 and 0.35 w/c under different exposure conditions

Considering the lower w/c ratios used in PSC beams and the penetrating sealant performance differences with respect to w/c ratios, the 0.35 w/c ratio was selected for preparing concrete slabs to evaluate sealant and coating performance. As a favorable exposure condition to develop ASR in concrete with a 0.35 w/c, 1N NaOH with temperature greater than 120° F was selected. Since 0.1N NaOH also shows a certain degree of expansion in mortar bars with 0.35 w/c at or above 120° F, 0.1N NaOH was selected as an alternative exposure medium. At the end of the expansion testing, these specimens were used to evaluate the performance of staining techniques.

7.2.2 Expansion of Concrete Prisms and Slabs

The objective of testing is to identify the exposure conditions that promote ASR in concrete slabs prepared with the selected mixes. As shown in Table 7-3, the concrete mixes included Spratt and Arcosa sand as coarse and fine aggregates. Since a high alkaline cement with 0.96% $\text{Na}_2\text{O}_{\text{eq}}$ was used as the binder, the $\text{Na}_2\text{O}_{\text{eq}}$ of Mix 1 is 0.96%. With the added NaOH, the $\text{Na}_2\text{O}_{\text{eq}}$ of Mix 2 is 1.25%. Slabs were not used as the standard specimens for ASR testing; thus, two prisms were fabricated with the Mix 1 concrete and exposed to conditions similar to the slabs fabricated with the same concrete. A total of six slabs ($12 \times 12 \times 5.5$ in.) and two prisms ($3 \times 3 \times 11.25$ in.) were fabricated. This included 4 slabs from Mix 1 and 2 slabs from Mix 2. The sides of the slabs were coated with epoxy paint to promote one-dimensional moisture transfer.

Slabs were instrumented with four Demec gauge studs, two vibrating wire (VW) gauges, and a thermocouple, as shown in Figure 7-4. The VW gauges were placed at a depth of 2.375 in. from the top surface and in-line with two stud lines, 1-2 and 3-4. The studs were used to measure

the near surface expansion. The VW gauge readings were used to evaluate the depth of influence of the expansion due to ASR and the temperature at that depth. Thermocouples improved the redundancy of the temperature measurements since the temperature is used as one of the primary parameters for evaluating slab expansion. Six cylinders from each mix were fabricated to measure compressive strengths at 7 and 28 days.

Table 7-3. Concrete Mix for Slabs and Prisms (per yd³)

Mix composition	Mix 1	Mix 2
Coarse aggregate (SSD ¹) (lb) Spratt aggregate	1730	1730
Fine aggregate (SSD) (lb) Arcosa sand	1388	1388
Type I cement (lb)	705	705
Air entraining admixture (fl oz)	2.5	2.5
Water reducing admixture (fl oz)	70.5	70.5
Water (lbs)	247	247
Water-cementitious material ratio	0.35	0.35
Added sodium hydroxide (lb)	NA ²	3.24
Equivalent alkalinity (%)	0.96³	1.25

¹. Saturated surface dry

². Not applicable

³. From cement

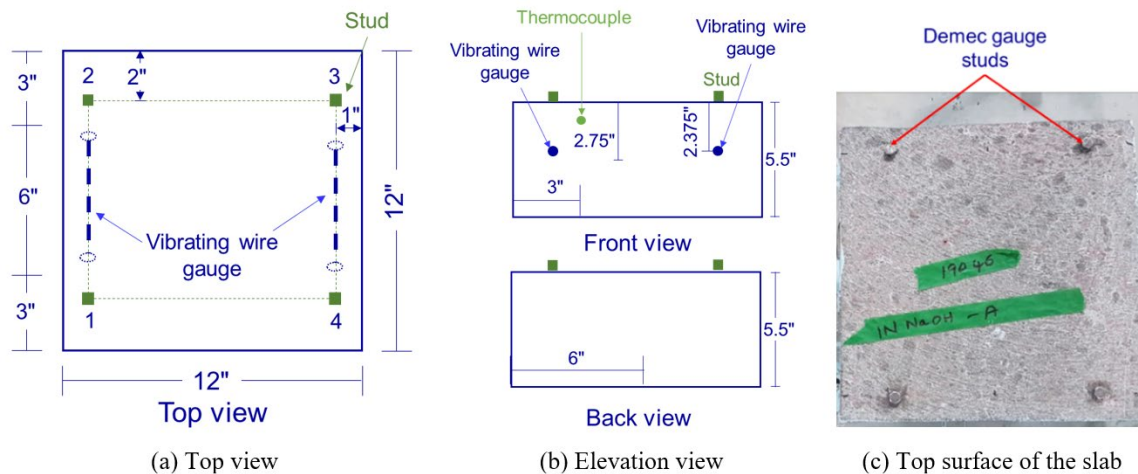


Figure 7-4. Instrumented slab for the evaluation of concrete expansion

After fabrication and curing specimens for 28 days, two prisms of Mix 1 were exposed to 1N NaOH at 176° F following ASTM C1260 (2021) to determine the rate of expansion and the reactivity level of the combined coarse and fine aggregates. Two slabs were ponded with NaOH and initially exposed to 120° F to evaluate the impact of exposure conditions and the concrete mix on slab expansion rates. Table 7-4 lists the exposure conditions and the assigned labels for the

specimens. For example, the prisms fabricated with Mix 1 and exposed to 1N NaOH at 176° F were labelled as P1-CP-0.96-1N NaOH-176-*. Similarly, the slabs fabricated with Mix 1 and exposed to 1N NaOH at 120° F were labelled as P1-CS-0.96-1N NaOH-120-*

where,

P1: Phase 1

CP: Concrete prisms

CS: Concrete slabs

0.96: Na₂O_{eq} in %

1N NaOH: Exposure medium

176: Exposure temperature in ° F

* : Specimen labels as A, B, and C.

This set of expansion testing was considered as Phase I since this provides preliminary data for developing the mixes and curing conditions for the evaluation of concrete protective systems. The initial and zero expansion readings of the prisms were recorded following ASTM C1293 (2020) and ASTM C1260 (2021) procedures, respectively. The subsequent expansion measurements were recorded periodically at 7 days as per ASTM C1260 (2021). The zero reading and expansion measurements of slabs were recorded at room temperature.

Table 7-4. Experimental Program for Concrete Specimens Investigated During Phase 1

Concrete mix (a)	No. of specimen (b)	Exposure medium (c)	Exposure temperature (° F) (d)	Specimen label (e)
Mix 1	2	1 N NaOH	176	P1-CP-0.96-1N NaOH-176-*
Mix 1	2	1 N NaOH	120	P1-CS-0.96-1N NaOH-120-*
Mix 1	2	0.1N NaOH	120	P1-CS-0.96-0.1N NaOH-120-*
Mix 2	2	0.1N NaOH	120	P1-CS-1.25-0.1N NaOH-120-*

7.2.2.1 Results and Discussion

Table 7-5 presents fresh and hardened concrete properties. The recorded air content of concrete mixes is lower than the MDOT limit of 5.5% listed in the special provision for quality control and acceptance of structural precast concrete (12SP-708C-02). However, air content is not a vital parameter in this study since these specimens were not subjected to freeze-thaw cycles. An air entraining admixture was used in the mixes to maintain workability.

Table 7-5. Fresh and Hardened Concrete Properties - Phase 1

Property (a)	Mix 1 (b)	Mix 2 (c)
Temperature (° F)	72	72
Slump (in.)	5	4
Unit weight (lb/ft ³)	149.6	147.6
Air content (%)	2.8	4.2
7-day compressive strength (psi)	6520	6290
28-day compressive strength (psi)	7840	7450

Figure 7-5 shows the percentage expansion of concrete prisms exposed to 1N NaOH at 176° F. These prisms exceeded the 0.1% threshold in 23 days of exposure. Surface cracks with a maximum width of 0.004 in. were documented after 30 days of exposure (Figure 7-6). Moreover, the expansion was measured periodically for 317 days. These prisms expanded and reached a plateau of 1.86% in 303 days. As a result, the maximum crack width measured at the end of testing was 0.035 in.

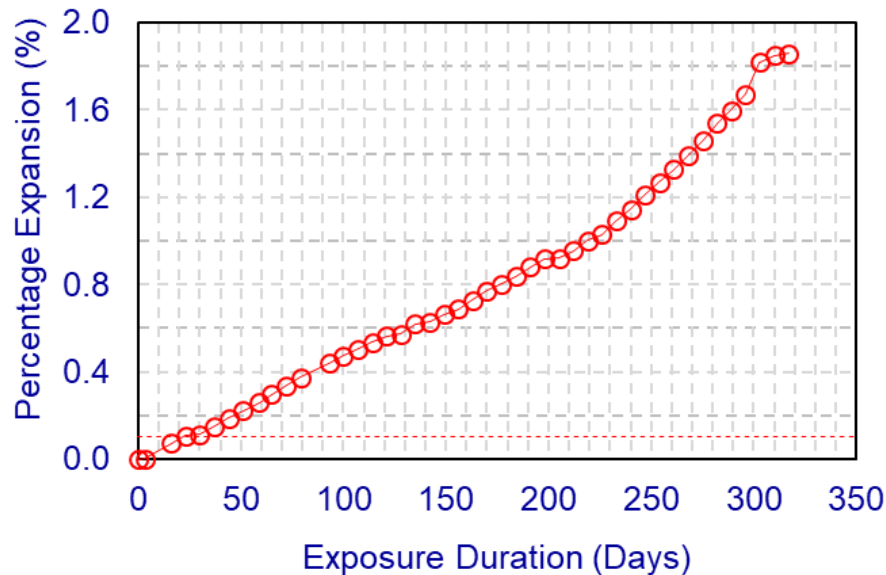
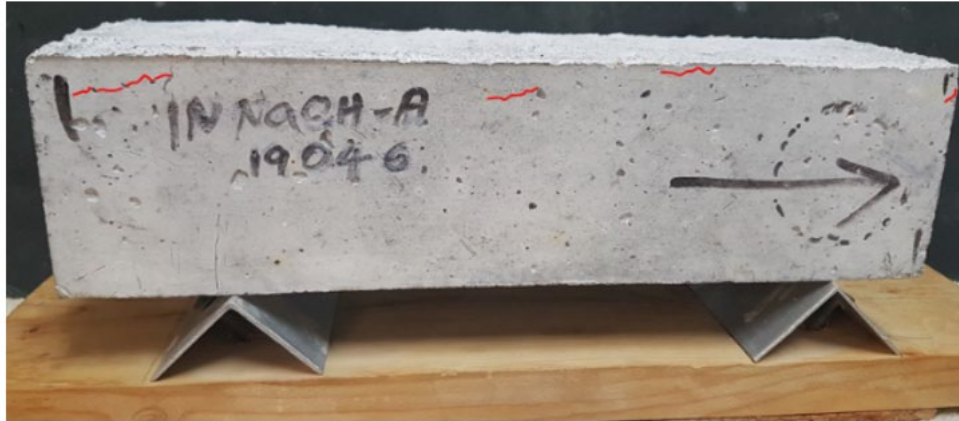


Figure 7-5. Expansion of concrete prisms with 0.35 w/c exposed to 1N NaOH at 176° F (P1-CP-0.96-1N NaOH-176)



(a) Concrete prisms with 0.35 w/c exposed to 1N NaOH at 176° F (The red lines indicate cracks)



(b) A close-up view showing a 0.004 in. wide crack

Figure 7-6. Cracking observed on a concrete prism with 0.35 w/c after exposing it to 1N NaOH at 176° F (P1-CP-0.96-1N NaOH-176)

Figure 7-7 shows slab expansion under various exposure conditions. These six slabs were exposed to 120° F for 21 days. Since the slabs did not expand under 120° F, the temperature was increased to 140° F. Following 35 days of exposure to 140° F, the temperature was increased to 176° F. As shown in Figure 7-7, irrespective of the $\text{Na}_2\text{O}_{\text{eq}}$ and the concentration of NaOH, the rate of expansion increases with the exposure temperature. The slabs with an $\text{Na}_2\text{O}_{\text{eq}}$ of 0.96% expanded to 0.061% and 0.053% when exposed to 1N NaOH and 0.1N NaOH for 77 days, respectively. The slabs with an $\text{Na}_2\text{O}_{\text{eq}}$ of 1.25% reached an average expansion of 0.075%. The results show that the $\text{Na}_2\text{O}_{\text{eq}}$ in the concrete mix, the Na^+ concentration in the exposure medium, and the exposure temperature are the critical factors to control concrete expansion due to ASR.

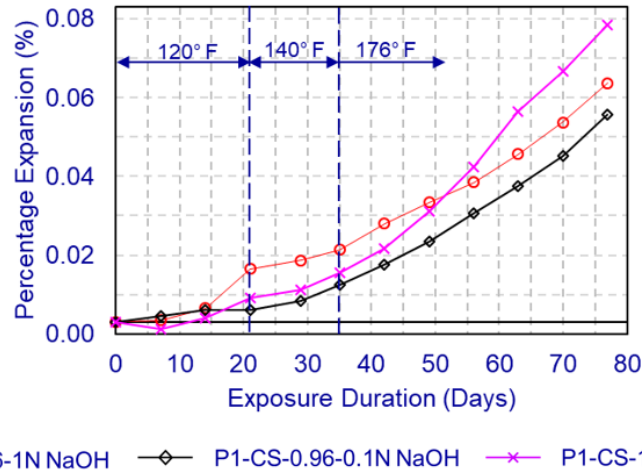


Figure 7-7. Expansion of concrete slabs with 0.35 w/c exposed to 1N and 0.1N NaOH solutions

Figure 7-8 shows the variation of slab temperature. Thermocouples recorded the temperature at 1 in. below the top surface. VW gauges recorded the temperature and strain at 2.375 in. from the top surface. Even though the operating temperature range of VW gauges is -4° F to 176° F, the maximum recorded temperature was limited to 167° F. Since the VW gauges and the thermocouples recorded similar temperatures around 140° F, thermocouple readings were used to establish the VW gauge temperature profile which is required to calculate concrete strain during the exposure to high temperatures with 1N NaOH ponding. As shown in Figure 7-8, concrete at the depth of VW gauges contracted continuously under high temperature even though the top surface expanded due to ponding with 1N NaOH. This difference in inter-layer expansion is beneficial to develop surface cracks with an adequate duration of exposure to evaluate the performance of coatings. The findings support using an $\text{Na}_2\text{O}_{\text{eq}}$ of 1.25% in concrete mixes that will be used for evaluating coating performance and exposing these slabs to 1N NaOH at 176° F to accelerate the expansion.

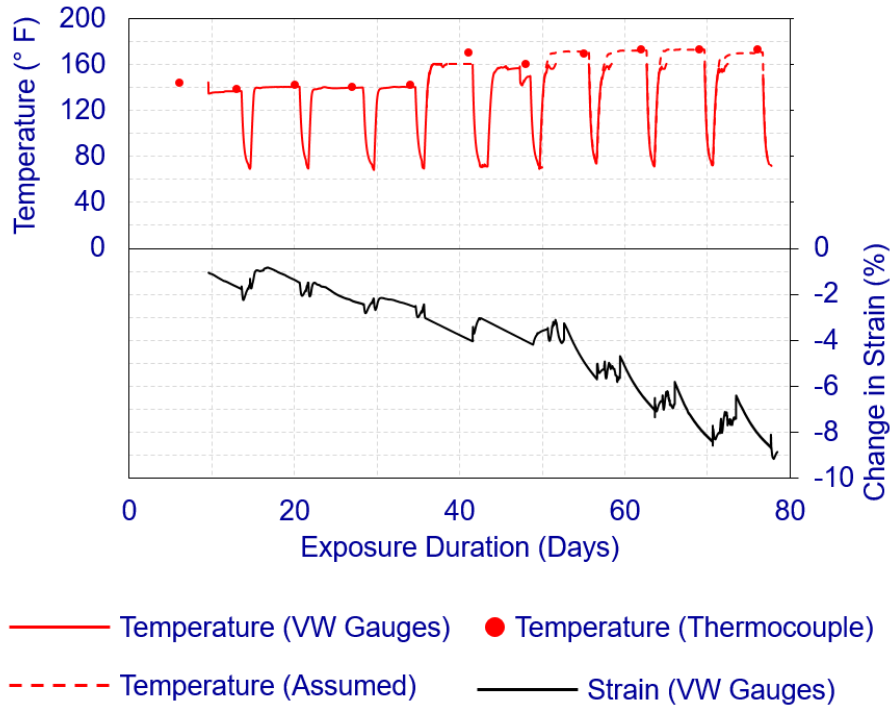


Figure 7-8. Temperature and strain variation against the exposure duration

7.3 PERFORMANCE OF CONCRETE PROTECTIVE SYSTEMS

Due to Covid-19 related challenges securing Spratt aggregate was a challenge. Hence, Moose Lake aggregate was selected as the coarse aggregate. This required re-evaluating the expansion characteristics of concrete mixes to decide on the slab exposure condition and duration to develop at least 0.04% expansion due to ASR before the application of the protective systems.

Two concrete mixes were developed using an $\text{Na}_2\text{O}_{\text{eq}}$ of 0.96 and 1.25%. These mixes included Moose Lake aggregates and Arcosa sand as coarse and fine aggregates (Table 7-6). A total of fifteen $3 \times 3 \times 11.25$ in. prisms and fifteen $12 \times 12 \times 5.5$ in. slabs were fabricated. Six prisms and two slabs were fabricated from Mix 1 and the rest of the specimens were fabricated from Mix 2. As shown in Figure 7-9, four Demec gauge studs were installed at each corner of the specimen with a spacing of 2 in. from adjacent sides. Moreover, on the 8th day after fabrication, two RH probes were installed at 1.00 in. and 2.75 in. from the top surface. In addition, thermocouples were installed at 1.00 in. below the top surface.

Table 7-6. Concrete Mix Design for Protective System Performance Evaluation (per yd³)

Mix composition	Mix 1	Mix 2
Coarse aggregate (SSD ¹) (lb) Moose lake aggregate	1600	1600
Fine aggregate (SSD) (lb) Arcosa sand	1455	1455
Type I cement (lb)	705	705
Air entraining admixture (fl oz)	2.1	2.5
Water reducing admixture (fl oz)	141.0	70.5
Water (lbs)	247	247
Water-cementitious material ratio	0.35	0.35
Added sodium hydroxide (lb)	NA ²	6.73
Equivalent alkalinity (%)	0.96 ³	1.25

- ¹. Saturated surface dry
- ². Not applicable
- ³. From cement itself

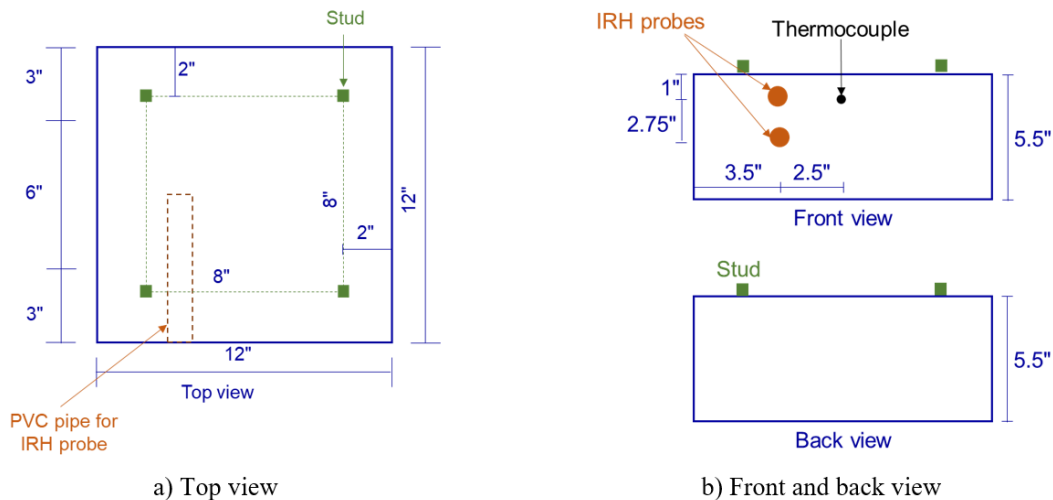


Figure 7-9. Instrumentation for concrete protective system performance evaluation

7.3.1 Reactivity Level of Aggregates

Six prisms and two slabs of Mix 1 were used to evaluate the reactivity level of the aggregate. As shown in Table 7-7, a group of three concrete prisms was exposed to 1N NaOH at 176° F after 1 day of wet curing following ASTM C1260 (2021) to determine the reactivity level of the combined coarse and fine aggregate and the level of expansion that can be achieved under aggressive conditions. The initial and zero expansion readings of the prisms were recorded conforming to ASTM C1260 (2021). The subsequent expansion measurements were recorded periodically at 7 days conforming to ASTM C1260 (2021).

Table 7-7. Exposure Conditions and Specimens for Expansion Evaluation

Concrete mix (a)	No. of specimen (b)	Wet curing duration (days) (c)	Exposure medium (c)	Exposure temperature (° F) (d)	Temperature at the time of measurement (° F) (f)	Specimen label (g)
Mix 1	3	1	1 N NaOH	176	176	P2-CP-0.96-1N NaOH-176-01
Mix 1	3	7	1 N NaOH	176	73	P2-CP-0.96-1N NaOH-176-07
Mix 1	2	7	1 N NaOH	176	73	P2-CS-0.96-1N NaOH-176-07

The remaining three prisms were wet cured for 7 days along with the slab specimens. Initial and zero expansion readings of these concrete prisms were recorded as per the ASTM C1293 (2020). The zero reading and the succeeding expansion measurements of slabs were recorded at room temperature. Table 7-7 lists the exposure conditions and the assigned labels for the specimens. For example, row 1 of Table 7-7 shows the three prisms fabricated with Mix 1 and exposed to 1N NaOH at 176° F. The P2 in the label represent the 2nd phase of experimental studies.

7.3.2 Influence of Curing Conditions

Following 28 days of wet curing durations, nine prisms of Mix 2 were divided into groups of three specimens and exposed to different exposure mediums at 176° F, as listed in Table 7-8. The initial, zero, and successive expansion readings were recorded at room temperature following ASTM C1293 (2020) procedures. The subsequent expansion measurements for both prisms and slabs were recorded periodically at 7 days.

Table 7-8. Evaluation of Exposure Conditions on Concrete Prism Expansion

Concrete mix (a)	No. of specimen (b)	Exposure medium (c)	Specimen label (g)
Mix 2	3	1 N NaOH	P2-CP-1.25-1N NaOH-176-28
Mix 2	3	100% RH	P2-CP-1.25-100% RH-176-28
Mix 2	3	Lime saturated water	P2-CP-1.25-LS -176-28

7.3.3 Evaluation of Protective Systems

Following 28 days of wet curing, the top surfaces of thirteen slabs prepared with Mix 2 were exposed to 1N NaOH at 176° F until they reached the prescribed expansion limit of 0.04%. After reaching the expansion limits, slabs were removed from the curing chamber and allowed to dry for 3 days. Following the drying period, the top surface was sandblasted conforming to MDOT's special provisions for silane treatment of bridge concrete (20TM710(A290)) (MDOT 2021c) and

concrete surface coatings (20RC710(A285)). Four types of protective systems were considered: (i) penetrating sealant, (ii) coating, (iii) penetrating sealant and coating, and (iv) lithium nitrate and coating. A pair of specimens was treated with each treatment scheme conforming to the manufacturer's guidelines. A slab was left untreated as a reference. Even though breathable sealants and coatings were used, these materials do not provide 100% breathability. When the concrete surface heats up, moisture is drawn towards the heated surface. This will allow moisture accumulation beneath the sealants and coatings. Hence, lithium nitrate was used as a primer for coatings to control possible development of ASR underneath the coating.

Specimen label, primer, coating types, theoretical coverage of each layer, the number of specimens, and recommended application methods are listed in Table 7-9. For example, two slabs mentioned in the fourth row were labeled as P-1 + C-1. As listed in columns b, c, and d of Table 7-9, these slabs were treated with one coat of Benjamin Moore Ultra Spec[®] Interior/Exterior Acrylic High-Build Masonry Primer 609 following two coats of Benjamin Moore Ultra Spec[®] Masonry Elastomeric Waterproofing Coating Flat 0359. The recommended coverage from one gallon of primer is 350 to 400 ft², while one gallon of coating is for 80 to 100 ft². As shown in column f of Table 7-9, the coating can be applied using a brush, roller, power roller, or airless spray with 2500 to 3000 psi pressure. The bolded text in column f of Table 7-9 shows the methods used to apply the primer and coating during this experimental work.

Table 7-9. Concrete Protective Systems

Specimen label (a)	Primer (b)	1 st coat (c)	2 nd coat (d)	Number of specimens treated (e)	Application methods (f)
Reference	NA ¹	NA	NA	1	NA
PS-1	NA	SIL-ACT [®] ATS-200 (150 - 400) ²	NA	2	Spray Brush Roller
PS-2	NA	Protectosil [®] BH-N (125 - 350)	NA	2	Spray (15 to 25 psi) Brush Roller (1 in. nap)
P-1 + C-1	Benjamin Moore Ultra Spec [®] Interior/Exterior Acrylic High- Build Masonry Primer 609 (350 - 400)	Benjamin Moore Ultra Spec [®] Masonry Elastomeric Waterproofing Coating Flat 0359 ³ (80 - 100)	Benjamin Moore Ultra Spec [®] Masonry Elastomeric Waterproofing Coating Flat 0359 (80 - 100)	2	Airless spray (2500 to 3000 psi) Brush Roller
P-2 + C-2	Si-Primer (203.73)	Si-Rex 03 (325.97)	Si-Rex 03 (325.97)	2	Spray Brush Roller
PS-1 + C-1	SIL-ACT [®] ATS-200 (150 - 400)	Benjamin Moore Ultra Spec [®] Masonry Elastomeric Waterproofing Coating Flat 0359 (80-100)	Benjamin Moore Ultra Spec [®] Masonry Elastomeric Waterproofing Coating Flat 0359 (80 - 100)	2	Spray Brush Roller
LN + C-1	30% Lithium nitrate (LiNO ₃) (150 - 400)	Benjamin Moore Ultra Spec [®] Masonry Elastomeric Waterproofing Coating Flat 0359 (80 - 100)	Benjamin Moore Ultra Spec [®] Masonry Elastomeric Waterproofing Coating Flat 0359 (80 - 100)	2	Spray Brush Roller

¹ - Not applicable

² - Coverage rate in ft²/gal as per technical data sheets

³ - MDOT has approved Benjamin Moore Super Spec[®] Masonry 100% Acrylic Elastomeric Coating Flat 056. However, personal communication with the product supplier confirmed that this product was replaced with Benjamin Moore Ultra Spec[®] Masonry Elastomeric Waterproofing Coating Flat 0359. According to the information in technical datasheets, both coatings have similar performance.

Following treatments, all thirteen slabs were partially submerged in a water tank for 30 days, allowing them to absorb moisture from the bottom surface. Once saturated, the slabs were removed from the water tank, and the bottom surface was sealed with plastic to prevent moisture loss. As depicted in Figure 7-10, the sides and the bottom surface of the slabs were insulated using foams and reflective insulations to promote heating only the top surface when the specimens were placed under infrared light. This was to promote moisture evaporation from the top surface (treated surface) promoting one-dimensional moisture transfer. Two small $\frac{1}{4}$ in. diameter vinyl pipes were installed with one end open at the bottom of the slabs (i) to avoid the possibility of developing a negative pressure and (ii) for future use to inject water and saturate the slabs from the bottom. Visual inspection on coatings was performed before the specimens were exposed to 120° F at 25% RH. Following 16, 32, and 73 days of exposure, treated surfaces were visually inspected.



Figure 7-10. Insulated treated slab before exposure to 120° F at 25% RH

A custom-designed Arduino system with compatible temperature/humidity sensors was used to monitor the variation of IRH and the temperature inside the concrete slabs after applying the selected treatment methods. These sensors were waterproofed to prevent possible electrical shortages due to condensation on the surface.

7.3.4 Results and Discussion

7.3.4.1 Reactivity Level of the Aggregate

Figure 7-11 shows the expansion of prisms fabricated using Mix 1 and exposed to 1N NaOH at 176° F. The expansion increases with the exposure duration. The prisms exposed to 1N NaOH following 1 day and 7 days of wet curing duration shows an average expansion of 0.31% and

0.34%, respectively, at 195 and 188 days of exposure. The results do not show a major impact of the wet curing duration. Compared to Moose Lake aggregate, the concrete prisms with Spratt and Arcosa sand, exposed to similar environmental conditions, show a more significant expansion of 0.92% at 198 days of exposure.

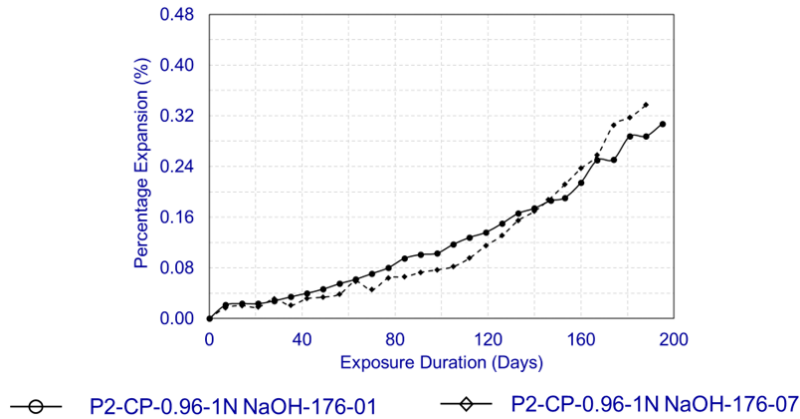


Figure 7-11. Expansion of concrete prisms with $\text{Na}_2\text{O}_{\text{eq}}$ of 0.96% in 1N NaOH at 176° F

Correspondingly, slabs with identical concrete mixes show comparable results. As shown in Figure 7-12, the slabs reached an expansion of 0.067% after exposing to 1N NaOH at 176° F for 189 days. At the end of 84 days of identical exposure, the slabs fabricated with Spratt aggregate exceeded 0.061% expansion, while the slabs with Moose Lake aggregate took 126 days to reach this expansion limit. Hence, it can be concluded that the reactivity level of Moose Lake aggregate used in Phase 2 is lower than the Spratt used in Phase 1.

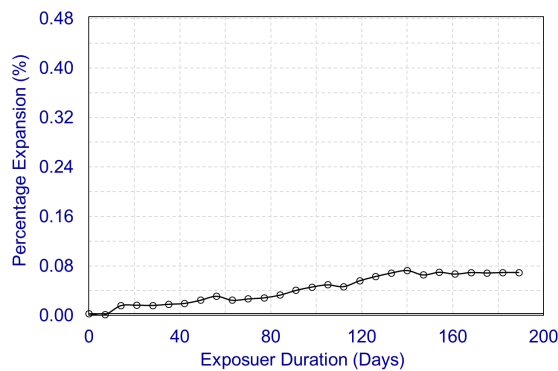


Figure 7-12. Expansion of concrete slabs with $\text{Na}_2\text{O}_{\text{eq}}$ of 0.96% in 1N NaOH at 176° F (P2-CS-0.96-1N NaOH-176-07)

7.3.4.2 Performance of Protective Systems

Figure 7-13 shows the expansion of slab specimens exposed to 1N NaOH at 176° F. As shown in the figure, these slabs achieved an average expansion of 0.04% after 56 days of exposure to 1N NaOH solution at 176° F.

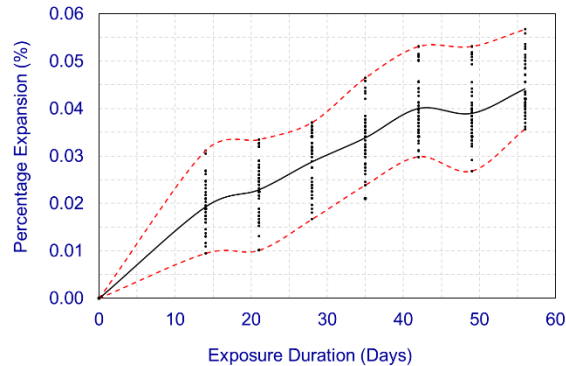


Figure 7-13. Expansion of slabs with 0.35 w/c exposed to 1N NaOH at 176° F

Note: Red dashed lines represent the upper and lower bounds of recorded readings. The black line represents the average.

Figure 7-14 shows the top surface of a slab before and after sandblasting. Cavities and exposed coarse aggregate were noted during the post-sandblasting inspection. Similar cavities were observed in PSC beams during bridge inspection; thus, no additional surface preparation was performed before applying the selected treatment methods.

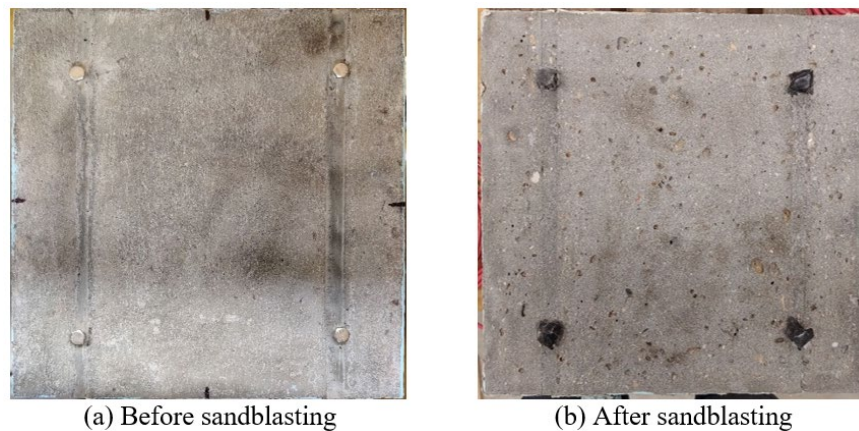


Figure 7-14. Top surface of a slab before and after sandblasting

As depicted in Figure 7-15, the IRH at the beginning and end of the saturation period varies from slab to slab. The differential breathability properties among the candidate treatment methods might influence the absorption-desorption properties; thus, they affect the final IRH of the slabs.

Therefore, the IRH values were normalized and compared to evaluate the performance of each treatment method. Each recorded IRH value was normalized using the maximum recorded IRH of the particular slab. Figure 7-16 and Figure 7-17 present the variation of normalized IRH of sealant and coating applied slabs, respectively. As per the computed results in Figure 7-16, both penetrating sealants performed better than the control specimen. Similar results were reported by Pfeifer and Scali (1981). Both sealants performed equally well since both are 100% alkyltrialkoxysilanes. As listed in Table 7-10, Protectosil® BH-N performed slightly better than SIL-ACT® ATS-200 with 27% and 25.67% reductions in IRH, respectively.

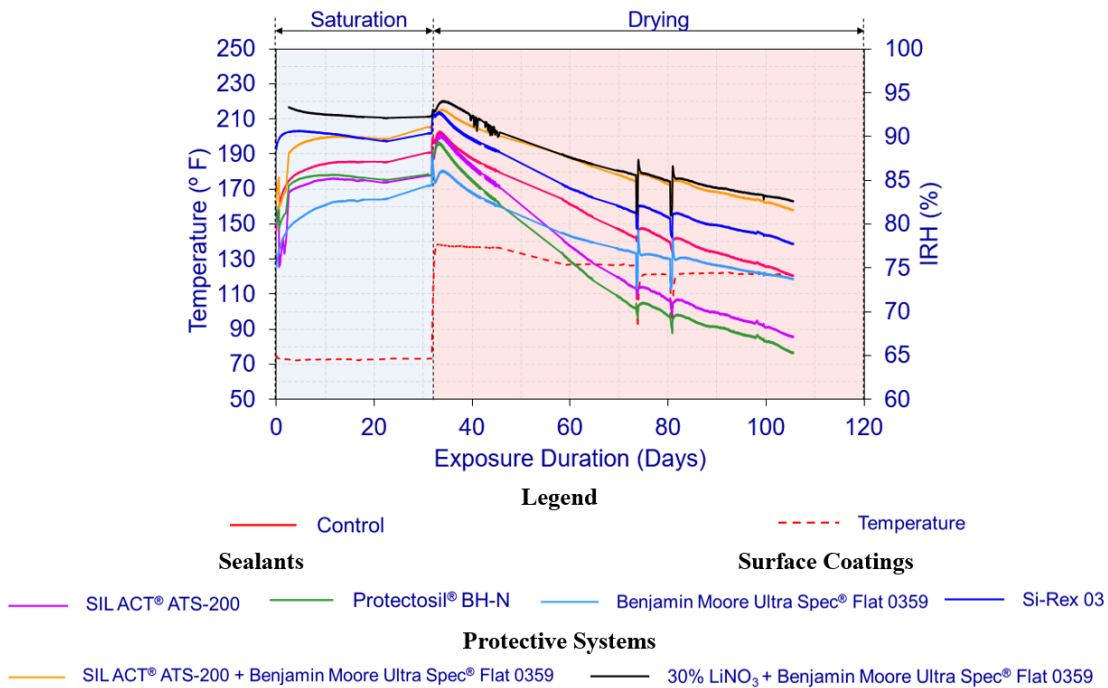


Figure 7-15. Variation of slab temperature and IRH against the exposure duration

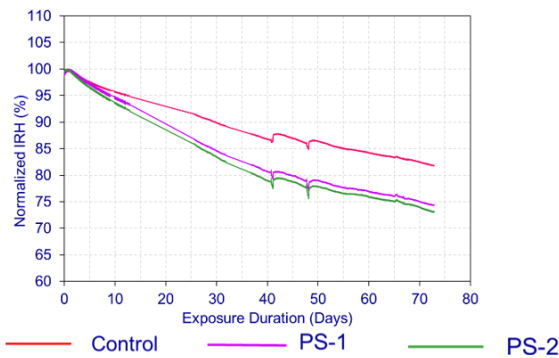


Figure 7-16. Variation of IRH in the sealant applied slabs against drying time

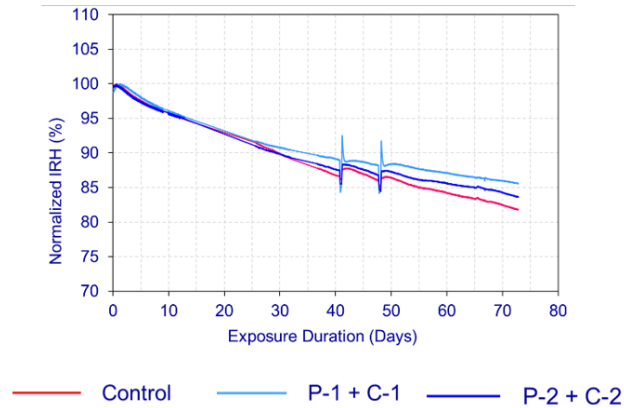


Figure 7-17. Variation of IRH in the coated slabs against drying time

Table 7-10. Concrete Protective System Performance at the End of 73-Day Exposure to 120° F at 25% RH

Specimen label (a)	Protective system (b)	Reduction of IRH (%) (c)
Reference	None	18.19
PS-1	SIL-ACT® ATS-200	25.67
PS-2	Protectosil® BH-N	27.00
P-1 + C-1	Benjamin Moore Ultra Spec® Masonry Elastomeric Waterproofing Coating Flat 0359 with the recommended primer	14.43
P-2 + C-2	Si-Rex 03 with Si-Primer	16.35
PS-1 + C-1	Benjamin Moore Ultra Spec® Masonry Elastomeric Waterproofing Coating Flat 0359 with SIL-ACT® ATS-200 as the primer	16.52
LN + C-1	30% LiNO ₃ pretreated slabs with Benjamin Moore Ultra Spec® Masonry Elastomeric Waterproofing Coating Flat 0359 and recommended primer	12.17

As shown in Figure 7-17 and Table 7-10, Si-Rex 03 with Si-Primer performed better than Benjamin Moore Ultra Spec® Masonry Elastomeric Waterproofing Coating Flat 0359 with the recommended primer. The reduction of IRH is 16.35% and 14.43% respectively. However, both drying rates are lower than the reference of 18.19%.

The performance of the multi-coating systems is presented in Figure 7-18. Replacing the primer of the elastomeric acrylic coating with a 100% alkyltrialkoxysilane improves the water vapor transmission capacity. Yet, the performance of Si-Rex 03 with Si-Primer and Benjamin Moore Ultra Spec® Masonry Elastomeric Waterproofing Coating Flat 0359 SIL-ACT® ATS-200 as the primer is similar: 16.35% and 16.52% respectively. Using 30% LiNO₃ as a pretreatment reduced the water vapor transmission capacity to 12.17%.

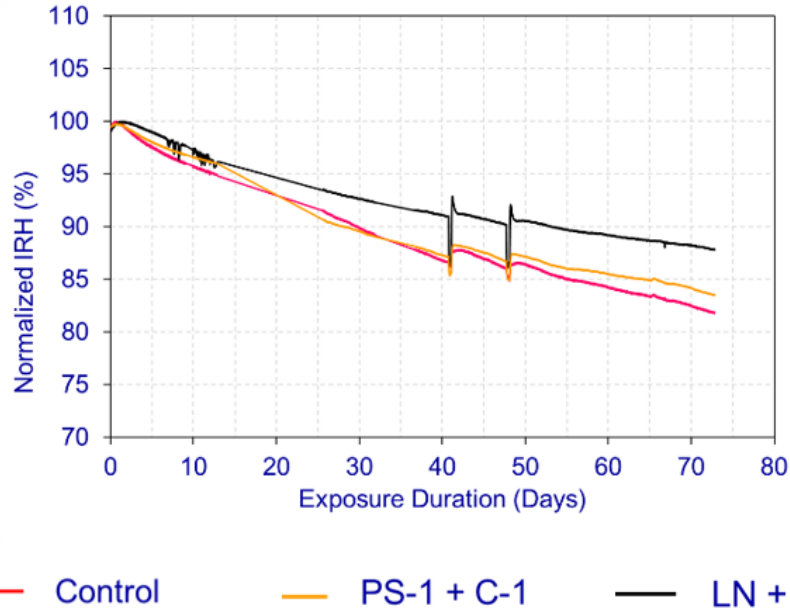
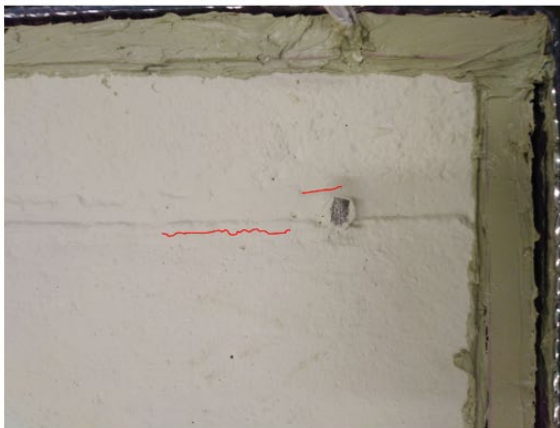


Figure 7-18. Variation of IRH in the slabs with multi-coating systems against drying time

Post-treatment inspection identified several cracks in the silicon resin layer of P-2 + C-2 slabs at locations where the coating thickness was greater than the limit specified by the manufacturer due to surface irregularities (Figure 7-19). Certain cracks propagated after 16 days of exposure. These observations indicate that the silicon resin layer is sensitive to the layer thickness, and special attention is required during the application to maintain the proper layer thickness. The surface condition of all slabs was recorded in Table 7-11.



(a) Initial cracks in Si-Rex 03 applied slabs before exposed to 120° F. Red color line represents the cracks in the coating.



(b) Cracks in Si-Rex 03 applied slabs after 16 days of exposure to 120° F. Red color line represents the cracks in the coating.

Figure 7-19. Cracking in Si-Rex 03 coating

Table 7-11. Coating Conditions Recorded Through Visual Inspection

Specimen label (a)	Protective system (b)	Observation of 1 st layer (c)	Observation of 2 nd layer (d)
Reference	None	NA ¹	NA
PS-1	SIL-ACT [®] ATS-200	NA	NA
PS-2	Protectosil [®] BH-N	NA	NA
P-1 + C-1	Benjamin Moore Ultra Spec [®] Masonry Elastomeric Waterproofing Coating Flat 0359 with recommended primer	No damage was observed in the coating.	No damage was observed in the coating.
P-2 + C-2	Si-Rex 03 with Si-Primer	The coating had cracking when the layer is thicker than specified.	The coating cracked when the layer thickness is greater than specified (Figure 7-19a and b). A thin layer was applied over the painted surface to bridge the cracks and seal the surface as per the manufacturer's recommendations.
PS-1 + C-1	Benjamin Moore Ultra Spec [®] Masonry Elastomeric Waterproofing Coating Flat 0359 with SIL-ACT [®] ATS-200 as the primer	No damage was observed in the coating.	No damage was observed in the coating.
LN + C-1	30% LiNO ₃ pretreated slabs with Benjamin Moore Ultra Spec [®] Masonry Elastomeric Waterproofing Coating Flat 0359 and recommended primer	The first layer of the coating peeled off. There was no adequate bond between the LiNO ₃ pretreated surface and the paint. The entire first layer was removed and the top surface was sandblasted. A layer of Benjamin Moore Ultra Spec [®] Interior/Exterior Acrylic High-Build Masonry Primer 609 was applied over the LiNO ₃ applied top surface before applying the 1 st layer of coating. Later inspection shows that applying primer increased the bond between the coating and the concrete surface. No damage was observed in the reapplied coating layer.	No damage was observed in the coating.

¹ - Not applicable. Visual inspection was not performed in these slabs.

7.4 COST ESTIMATION

According to the rates published in the MDOT Bridge Scoping Cost Estimate Worksheet (MDOT 2022b) as of February 9, 2022, the application cost of elastomeric concrete surface coatings and penetrating sealants, including surface preparation, is 32.00 USD/yd² and 7.00 USD/ ft², respectively. Since the rates are provided as lump sums, it is not possible to identify the costs for surface preparation and application as two items. Therefore, the comparison is made solely based on the material costs as of September 2021. The costs for penetrating sealants, coatings, and multi-layer coating systems are documented in Table 7-12, Table 7-13, and Table 7-14, respectively. For example, the total material cost for Benjamin Moore Ultra Spec[®] Masonry Elastomeric Waterproofing Coating Flat 0359 with the recommended primer is given in the 1st two rows of Table 7-13. The average area covered by a gallon of coating and the primer are 375 and 90 ft², respectively. Since the unit price of the primer and coating is \$32 and \$43, respectively, the total cost for the application of two coats is \$1042 per 1000 ft². According to the material costs, the application of Si-Rex 03 with Si-Primer to cover a 1000 ft² area is about 50% cheaper than the application of Benjamin Moore Ultra Spec[®] Masonry Elastomeric Waterproofing Coating Flat 0359 with the recommended primer. Also, the application of Si-Rex 03 with Si-Primer to cover a 1000 ft² area is about 50% cheaper than the application of Benjamin Moore Ultra Spec[®] Masonry Elastomeric Waterproofing Coating Flat 0359 with SIL-ACT[®] ATS-200 as the primer.

Table 7-12. Cost of Penetrating Sealants

Product (a)	Coverage (ft²/gal) (b)	Unit price as of September 2021 (USD/gal) (c)	Cost per 1000 ft² (USD) (d)
SIL-ACT [®] ATS-200	150 – 400 (average 275)	28.00	$28 \times (1000 / 275) = 102$
Protectosil [®] BH-N	100 – 350 (average 225)	40.00	$40 \times (1000 / 225) = 178$

Table 7-13. Cost of Surface Coatings

Product (a)	Coverage (ft ² /gal) (b)	Unit price as of September 2021 (USD/gal) (c)	Item cost per 1000 ft ² (USD) (d)	Total cost per 1000 ft ² (USD) (e)
Benjamin Moore Ultra Spec[®] Masonry Elastomeric Waterproofing Coating Flat 0359 with the recommended primer				
Primer	350 - 400 (average 375)	32.00	$32 \times (1000 / 375) = 86$	86 + 956 = 1042
Coating (2 layers)	80 - 100 (average 90)	43.00	$43 \times 2 \times (1000 / 90) = 956$	
Si-Rex 03 with Si-Primer				
Primer	203.73	32.00	$32 \times (1000 / 203.73) = 157$	157 + 385 = 542
Coating (2 layers)	325.97	63.00	$63 \times 2 \times (1000 / 325.97) = 385$	

Table 7-14. Cost of Multi-Layer Coating Systems

Product (a)	Coverage (ft ² /gal) (b)	Unit price as of September 2021 (USD/gal) (c)	Item cost per 1000 ft ² (USD) (d)	Total cost per 1000 ft ² (USD) (e)
Benjamin Moore Ultra Spec[®] Masonry Elastomeric Waterproofing Coating Flat 0359 with SIL-ACT[®] ATS-200 as the primer				
SIL-ACT [®] ATS-200	150 – 400 (average 275)	28.00	$28 \times (1000 / 275) = 102$	102 + 956 = 1058
Coating (2 layers)	80 - 100 (average 90)	43.00	$43 \times 2 \times (1000 / 90) = 956$	
30% LiNO₃ pretreatment with Benjamin Moore Ultra Spec[®] Masonry Elastomeric Waterproofing Coating Flat 0359 and the recommended primer				
30% LiNO ₃	150 – 400 (average 275)	789.25	$789.25 \times (1000 / 275) = 2870$	2870 + 86 + 956 = 3912
Primer	350 - 400 (average 375)	32.00	$32 \times (1000 / 375) = 86$	
Coating (2 layers)	80 - 100 (average 90)	43.00	$43 \times 2 \times (1000 / 90) = 956$	

7.5 SUMMARY

An extensive experimental study was conducted to evaluate staining techniques commonly used for screening ASR in concrete. The specimens prepared to evaluate aggregate reactivity levels were used for this purpose. In addition, the results from mortar and concrete expansion study were used to develop guidelines for the preparation and curing of concrete slabs to evaluate the performance of concrete protective systems. The reduction in internal relative humidity (IRH) was used as the performance parameter for evaluating the performance of sealants and coatings.

Finally, the performance of penetrating sealants, concrete surface coatings, and a combination thereof for controlling IRH was evaluated. The following observations are documented from the experimental results:

1. The Protectosil® BH-N performed slightly better than the SIL-ACT® ATS-200 even though both are 100% alkyltrialkoxysilanes.
2. The Si-Rex 03 with Si-Primer performed better than the Ultra Spec® Masonry Elastomeric Waterproofing Coating Flat 0359 with the recommended primer. However, Si-Rex 03 is more sensitive to coating thickness, and special attention is required during the application to prevent cracking. It is recommended to adhere to the manufacturer's guidelines and evaluate the use of a sprayer to control the coating thickness.
3. The application of SIL-ACT® ATS-200 as the primer for Ultra Spec® Masonry Elastomeric Waterproofing Coating Flat 0359 enhanced the concrete drying rate. However, this combined system had similar performance with the Si-Rex 03 with Si-Primer. Since SIL-ACT® ATS-200 and Si-Primer are silanes, using them as the primer provides a multi-layer protection to concrete.
4. Applying 30% LiNO₃ as a pretreatment for Ultra Spec® Masonry Elastomeric Waterproofing Coating Flat 0359 lowers the water vapor permeance compared to the other multi-layer concrete protective systems.

The selection of a suitable concrete protection method should be determined based on the degree of concrete deterioration and the life-cycle performance, including the cost. It is recommended to evaluate the long-term and life-cycle performance of Si-Rex 03 with Si-Primer and the Ultra Spec® Masonry Elastomeric Waterproofing Coating Flat 0359 with SIL-ACT® ATS-200 as the primer. The material costs of these two systems have a significant difference. Si-Rex 03 with Si-Primer costs \$542 per 1000 ft², whereas the Ultra Spec® Masonry Elastomeric Waterproofing Coating Flat 0359 with SIL-ACT® ATS-200 as the primer costs \$1058 to cover the same area.

Considering the available guidelines, 100% silane sealants can be applied to protect components with surface crack widths less than 0.002 in. However, when a surface is exposed directly to a source of moisture, such as the outside and bottom surfaces of a fascia beam, it is recommended to use Si-Rex 03 with Si-Primer or the Ultra Spec® Masonry Elastomeric Waterproofing Coating Flat 0359 with SIL-ACT® ATS-200 as the primer to protect the surface as

long as there are no active cracks that are wider than the crack bridging limits specified in the manufacturer's technical data sheets. It is recommended to use the above-stated coating systems at the fabrication yard on new fascia beams to protect all the surfaces, except the top. For the fascia beams on in-service bridges, all the exposed surfaces need to be protected using any of the above coating systems. The application of coatings on the inside surface is recommended since the moisture is drawn towards the outside surface as it warms up when exposed to sunlight while the moisture enters through other surfaces.

When the existing cracks are wider than the tolerable limits of coatings defined as the crack bridging ability, the cracks need to be repaired before the application of coatings. Additional research needs to be conducted to evaluate the crack bridging ability and the durability (adhesion, weathering against UV, cohesion, freeze-thaw resistance, and color retention) of the recommended coatings to define service life of such systems/products.

8 SUMMARY, CONCLUSIONS, AND RECOMMENDATIONS

8.1 SUMMARY

The Michigan Department of Transportation (MDOT) suspected that the mild to significant concrete deterioration observed on many prestressed concrete (PSC) beam bridges constructed in the 1970's and 1980's was due to alkali-aggregate reactivity (AAR) and other material compatibility issues. Map and longitudinal cracking are reported on PSC beams due to chemical reactions and/or physical mechanisms that result in volume expansion of concrete components. Concrete volume expansion and cracking are reported in beams with delayed ettringite formation (DEF) and AAR when subjected to moisture. In Michigan, the deterioration is further aggravated due to freeze-thaw exposure. This project was initiated to determine the status of the Michigan Department of Transportation (MDOT) bridge inventory with regards to the concrete deterioration of PSC beams, to develop inspection guidelines, to evaluate alkali-silica reaction (ASR) screening test methods for field application, to create capacity calculation and load rating guidelines of PSC beams with varying stages of concrete deterioration, and to offer rehabilitation options. This project was organized into six tasks to accomplish the objectives.

8.2 CONCLUSIONS AND RECOMMENDATIONS

8.2.1 Concrete Deterioration in PSC Beams

The records of 1136 PSC I-beam bridges were reviewed, and 136 bridges were identified as having material related distress in the beams. This represents about 12% of the I-beam bridge population. An ArcGIS file was submitted with the final report showing the geospatial distribution of the bridges. Interestingly, all the bridges are located in Michigan's lower peninsula with a majority in the University region. Inventory analysis, condition assessment of a selected number of bridges, and screening for ASR revealed a minor level of ASR in fine aggregate. The concrete deterioration was observed over the bottom flange top surface of fascia beams that were exposed to direct sunlight. Since the level of ASR was not adequate to develop longitudinal cracking at the top surface, it can be concluded that the deteriorations are due to the combined effect of several mechanisms including freeze-thaw. The depth of ASR damaged concrete was limited to the near surface area. The maximum longitudinal crack depth of 2.32 in. was measured for crack widths not greater than 0.016 in.

In addition to the I-beam bridges, the causes of deterioration in a box-beam bridge were investigated. Several bridge beams had severe random cracking at the ends, webs, and the soffits. Investigations revealed the presence of delayed ettringite formation (DEF) at beam ends. However, the severe cracking at the webs and soffit was attributed to freeze-thaw damage since the beam concrete only had 2 to 3% of air. Appendix D presents the condition of the box-beam bridge superstructure, along with beam ends and webs, to understand the significance of the freeze-thaw damage. This observation highlights the need for identifying other box-beam bridges with random (or spider web) cracking at the beam soffit to decide on the need for further assessment of such bridges to confirm beam end and web integrity.

8.2.2 Inspection Guidelines

The current inspection procedures, data recording formats, and condition state definitions were reviewed. The current process does not explicitly document the condition of fascia beams. Fascia beams of twelve percent (12%) of I-beam bridges showed material related distress that develops into longitudinal cracking. Even though the longitudinal cracking was significant, its significance is not highlighted with the current data-recording format because the crack length is expressed as a fraction of the total beam length. Therefore, a separate agency developed element (ADE) was defined, and an implementation example is provided in the report. Also, the current inspection guidelines are not granular enough to identify the type of cracks in PSC beams. This is a major drawback to identify the causes of cracking and its significance. Therefore, a set of images is included in the report that can be used to define the crack types for bridge inspectors. If these images are digitally linked to the inspection templates, the inspectors can select the images representing the type of cracks that they observe instead of documenting their observations as comments. This process can be programmed to provide a specific code in the database to avoid the inconsistencies observed in the inspector comments. Furthermore, such a process will provide consistent and reliable data to use with advanced data analytics tools as needed.

8.2.3 Staining Techniques for Detecting ASR Under Field Conditions

Only uranyl acetate and sodium cobaltinitrite/rhodamine B combination have shown the ability to highlight ASR gel in distinct colors. The application of uranyl acetate to identify ASR gel is well documented. The sodium cobaltinitrite/rhodamine B combined method is capable of identifying

ASR gels with K^+ and Ca^{2+} . This technique is not suitable for detecting Na^+ rich ASR gels since sodium cobaltinitrite is a well-known product used in analytical chemistry to determine the K^+ content of a solution. The strengths and challenges of implementing these staining techniques were evaluated, and the findings indicate that uranyl acetate is the only method available so far to be confidently implemented under field and laboratory conditions.

8.2.4 Load Rating Guidelines

Even though 12% of I-beam bridges have fascia beam distress, the primary concern is the longitudinal cracking at the top of the bottom flange getting exposed directly to the environmental elements. The guidelines are to exclude the strands adjacent to the cracks during capacity calculations. However, the number of ineffective strands depends on the depth of crack and the strand layout at the specific section. As a rule of thumb, it is recommended to use 2.5 in. as the depth of cracks when the crack width is not wider than 0.016 in. Two examples are presented in this report to highlight the process. For box-beams, detailed guidelines are provided to determine the area of deteriorated concrete and the number of ineffective strands. A Mathcad calculation sheet is provided to calculate input parameters of AASHTOWare BrR for load rating of distressed box beams. The sheet can be used as a stand-alone tool to perform load rating of box-beams. A user manual is provided in Appendix E.

8.2.5 Concrete Protective Systems

Since one of the primary factors that contributes to concrete deterioration is moisture, the protective systems for PSC beams should allow for breathability of concrete while preventing moisture intrusion. The performance of four types of concrete protective systems were evaluated using breathability as the performance parameter and the internal relative humidity (IRH) as the measure. The protective systems included (i) penetrating sealants, (ii) coatings, (iii) penetrating sealant and coating, and (iv) lithium nitrate and coating. Even though breathable sealants and coatings were used, these materials might not be 100% breathable. When the outside concrete surface of fascia beams heats up with solar exposure, moisture is drawn towards the heated surface. This allows for moisture accumulation beneath the sealants and coatings. Hence, lithium nitrate was used as a primer for coatings to control the possible development of ASR underneath the

coating. A cost estimate was prepared using the prices as of 09/2021. The following conclusions were developed from the experimental results and cost estimates:

1. The MDOT product qualification process requires evaluating penetrating sealant performance using a Grade D structural concrete mix with a 0.45 water-cementitious material ratio (w/c). The product evaluation methods listed in the current MDOT specifications need to be revised to reflect the concrete mixes used in PSC bridge beams, curing methods, and the concrete age at the time of sealant application. It is recommended to review and evaluate the Alberta Transportation specifications for Type 1c sealers, which are recommended for precast concrete, to develop MDOT specifications for the selection of sealers for PSC bridge beams.
2. Literature documents the application of coatings on PSC beams as early as the 4th calendar day, counted from the day of casting, if short term crack growth has subsided and the crack width is less than 0.007 in. Also, Si-Rex03 has been applied on PSC beams within 24 hours of concrete placement. These records highlight the possibility of applying coatings at the fabrication yard to protect beams and the need for maintaining a close working relationship with the product manufacturers to develop application guidelines.
3. The Protectosil[®] BH-N had slightly better breathability than the SIL-ACT[®] ATS-200. However, the cost of Protectosil[®] BH-N and SIL-ACT[®] ATS-200 as of 09/2021 was \$178 and \$102 per 1000 ft², respectively, meaning the former is more expensive.
4. The Si-Rex 03 with Si-Primer and the Ultra Spec[®] Masonry Elastomeric Waterproofing Coating Flat 0359 with SIL-ACT[®] ATS-200 as the primer have comparable performance. Si-Rex 03 is more sensitive to coating thickness, and special attention is required during the application to prevent cracking. It is recommended to adhere to the manufacturer's guidelines and evaluate the use of a sprayer to control the coating thickness. As of 09/2021, the cost of Si-Rex 03 with Si-Primer was \$542 per 1000 ft², whereas the Ultra Spec[®] Masonry Elastomeric Waterproofing Coating Flat 0359 with SIL-ACT[®] ATS-200 as the primer was \$1058 to cover the same area.
5. Applying 30% LiNO₃ as a pretreatment for Ultra Spec[®] Masonry Elastomeric Waterproofing Coating Flat 0359 lowers the water vapor permeance compared to the other multi-layer concrete protective systems. Also, the cost of this protective system as of 09/2021 was \$3,912 per 1000 ft².

6. The effective service life of penetrating sealants, coatings, and protective systems ranges from 6 to 10 years, 11 to 15 years, and 16 to 20 years, respectively. However, the effectiveness of these applications depends on the quality of the substrate, application parameters, and the specific product selected for the components. Since the data for service-life estimations are collected over regular concrete mixes, additional studies need to be conducted using concrete mixes and curing methods used for PSC bridge beams as well as the concrete age at the application of sealants and coatings. Also, the manufacturers of the qualified products need to be consulted to gather additional test data to assess the performance.
7. The lower upper limit of the crack bridging ability of coatings in the qualified products list is 0.004 in. Considering the challenges for effectively sealing cracks that are narrower than 0.004 in. through epoxy injection and the capabilities of coatings to bridge the cracks that are 0.004 in. or wider, it is recommended to use concrete protective systems on PSC beams when the crack width is less than 0.004 in.
8. It is recommended to adopt the sealant and coating evaluation method implemented in this study to assess the system performance since it considers the substrate, substrate preparation, application, curing, and the type of sealants and coatings as system parameters.

8.3 RECOMMENDATIONS FOR FURTHER RESEARCH

The following recommendations are provided for further research:

1. About 12% of the MDOT I-beam bridge inventory has map and/or longitudinal cracking on fascia beams, which is an indication of concrete deterioration. The location of these bridges is provided in the ArcGIS file submitted with this report. It is recommended to collect specimens during repair and replacement activities to identify the causes of concrete deterioration to validate the findings of this study.
2. Uranyl acetate is the most reliable field testing method available to screen for ASR. One of the major challenges of implementing this method in the field is the interference of the ambient light while observing the unique fluorescent signatures using a UV light. The current practice for minimizing the ambient light interference is to use a sealed metal box with a UV light and an opening to view the treated surface. Another common approach is to use a dark cloth to cover the operator's upper body and the treated area. The implementation of these

methods in the field is risky and inconvenient, and could lead to misinterpretation of the results. Therefore, it is recommended to develop a remote-controlled digital imaging system to alleviate the field implementation challenges.

3. It is recommended to follow the procedure demonstrated in this report to develop crack depth vs. crack width relationships for PSC beams to use as a decision-support tool for determining the number of ineffective strands in a section for load rating.
4. It is recommended to evaluate the crack bridging ability and long-term performance of Si-Rex 03 with Si-Primer and the Ultra Spec[®] Masonry Elastomeric Waterproofing Coating Flat 0359 with SIL-ACT[®] ATS-200 as the primer to define the service life of such systems/products and determine the reapplication time.

9 REFERENCES

1. AASHTO BEIGM. (2010). *AASHTO Bridge Element Inspection Guide Manual (BEIGM)*, 1st Ed., American Association of State Highway and Transportation Officials, 444 North Capitol Street NW, Suite 249, Washington, D.C. 20001.
2. AASHTO MBE. (2018). *The Manual for Bridge Evaluation (MBE)*, 3rd Ed., American Association of State Highway and Transportation Officials, 444 North Capitol Street NW, Suite 249, Washington, D.C. 20001.
3. AASHTO MBEI. (2014). *Manual for Bridge Element Inspection – 2015 Interim*, American Association of State Highway and Transportation Officials, 444 North Capitol Street, NW Suite 249, Washington, D.C. 20001.
4. AASHTO MBEI. (2019). *Manual for Bridge Element Inspection (MBEI)*, 2nd Ed., American Association of State Highway and Transportation Officials, 444 North Capitol Street NW, Suite 249, Washington, D.C. 20001.
5. AASHTO SSHB. (2002). *Standard Specifications for Highway Bridges*, 17th Ed., American Association of State Highway and Transportation Officials, 444 North Capitol Street NW, Suite 249, Washington, D.C. 20001.
6. AASHTO. (2017). *AASHTO LRFD Bridge Design Specifications*, 8th Ed., American Association of State Highway and Transportation Officials, 444 North Capitol Street NW, Suite 249, Washington, D.C. 20001.
7. AASHTOWARE. (2018). “AASHTOWARE Bridge Rating.” <<https://www.aashtoware.org/wp-content/uploads/2018/03/Bridge-Rating-Product-Brochure-FY-2019-11022018.pdf>>. (Accessed on: 7-28-2021 at 1:24 pm).
8. Abd-Elssamd, A., Ma, Z. J., Le Pape, Y., Hayes, N. W., and Guimaraes, M. (2020). “Effect of Alkali-Silica Reaction Expansion Rate and Confinement on Concrete Degradation.” *ACI Materials Journal*, 117 (1), pp. 265 - 277.
9. ACI. (2014). *Guide to Material Selection for Concrete Repair*, Report No. ACI 546.3R-14, American Concrete Institute (ACI), 38800 Country Club Drive, Farmington Hills, Detroit, Michigan 48331.
10. ACS. (2021). “MIRA A1040 Operation Manual.” *A1040 MIRA*, <<https://acs-international.com/product/a1040-mira/>> (Last accessed: July 4, 2021).

11. Ahmed, T., Burley, E., Rigden, S., and Abu-Tair, A. I. (2003). "The Effect of Alkali Reactivity on the Mechanical Properties of Concrete." *Construction and Building Materials*, 17(2), pp. 123 - 144.
12. Ahrland, S., Grenthe, I., and Noren, B. (1960a). "The ion Exchange Properties of Silica Gel-I- The Sorption of Na⁺, Ca²⁺, Ba²⁺, UO₂²⁺, Gd³⁺, Zr(IV), Nb, U(IV), and Pu(IV)." *Acta Chemical Scandinavica*, 14, pp. 1059 – 1076.
13. Ahrland, S., Grenthe, I., and Noren, B. (1960b). "The ion Exchange Properties of Silica Gel-II- Separation of Plutonium and Fission Products from Irradiated Uranium." *Acta Chemical Scandinavica*, 14, pp. 1077 – 1090.
14. Aktan, H. M., Fu, G., Dekelbab, W., and Attanayake, U. (2003). *Investigate Causes and Develop Methods to Minimize Early-Age Deck Cracking on Michigan Bridge Decks*, Report No. RC-1437, Michigan Department of Transportation, Construction and Technology Division, PO Box 30049, Lansing, Michigan 48909.
15. Aktan, H., Ahlborn, T., Attanayake, U., and Gilbertson, C. G. (2005). *Condition Assessment and Methods of Abatement of Prestressed Concrete Box-Beam Deterioration – Phase I*, Report No. RC-1470, Michigan Department of Transportation, Construction and Technology Division, PO Box 30049, Lansing, Michigan 48909.
16. Aktan, H., Ahlborn, T., Koyuncu, Y., Rutyna, J., and Kasper, J. (2002). *Causes and Cures for Prestressed Concrete I-Beam End Deterioration*, Report No. 1412, Michigan Department of Transportation, Construction and Technology Division, PO Box 30049, Lansing, Michigan 48909.
17. Aktan, H., Attanayake, U., Ulku, E., Ahlborn, T., and Deshpande, Y. (2009). *Condition Assessment and Methods of Abatement of Prestressed Concrete Box-Beam Deterioration: Phase II – Volume I*, Report No. RC-1527, Michigan Department of Transportation, Construction and Technology Division, PO Box 30049, Lansing, Michigan 48909.
18. ALDOT. (2015). *ALDOT-367 Production and Inspection of Precast Non- Prestressed and Prestressed Concrete*, Alabama Department of Transportation, 1409 Coliseum Blvd #2060, Montgomery, Alabama 36130.
19. Alfaiakawi, A., Roberts-Wollmann, C. L., Hebdon, M., and Koutromanos, I. (2020). *Experimental and Analytical Evaluation of Residual Capacity of Corrosion-Damaged*

- Prestressed Concrete Bridge Girders*, Report No. FHWA/VTRC 21-R6, Virginia Transportation Research Council, Charlottesville, Virginia 22903.
20. Almusallam, A. A., Khan, F. M., Dulaijan, S. U., and Al-Amoudi, O. S. B. (2003). “Effectiveness of Surface Coatings in Improving Concrete Durability.” *Cement and Concrete Composite*, 25, pp. 473 – 481.
 21. Amunugama, A. R. M. H. B. and Attanayake, U. (2021). “Element Level Bridge Inspection in the U.S.—Challenges for Assessing Specific Distress Type, Location and Progression.” In: *Dissanayake, R., Mendis, P., Weerasekera, K., De Silva, S., Fernando, S. (Eds) ICSECM 2019. Lecture Notes in Civil Engineering*, Vol 94. Springer, Singapore. <https://doi.org/10.1007/978-981-15-7222-7_1>.
 22. AT. (2000a). *BT001 - Test Procedure for Measuring the Vapor Transmission, Waterproofing and Hiding Power of Concrete Sealers*, Alberta Transportation, Alberta, Canada. <http://www.transportation.alberta.ca/Content/docType254/Production/BT001_JULY2000.pdf> (Last accessed: April 10, 2020)
 23. AT. (2000b). *BT010 - Test Procedure for Casting and Storing Concrete Test Specimens for Use in Approval Testing of Sealers*, Alberta Transportation, Alberta, Canada. <http://www.transportation.alberta.ca/Content/docType254/Production/BT010_JULY2000.pdf> (Last accessed: April 10, 2020)
 24. AT. (2008). *Best Practice Guidelines for Selecting Concrete Bridge Deck Sealers*, Alberta Transportation, Alberta, Canada. <<http://www.transportation.alberta.ca/Content/docType253/Production/BrSealerGdln.pdf>> (Last accessed: April 10, 2020)
 25. AT. (2010). *B388 – Specification for Concrete Sealers*, Alberta Transportation, Alberta, Canada. <<http://www.transportation.alberta.ca/Content/docType253/Production/B388APRIL2010.pdf>> (Last accessed: April 10, 2020)
 26. AT. (2020). *Approved Product List for Bridge Concrete Sealers*, Alberta Transportation, Alberta, Canada. <<http://www.transportation.alberta.ca/PlanningTools/GMS/ProductList/BridgeConcreteSealerList.pdf>> (Last accessed: April 10, 2020)
 27. Attanayake, U. and Aktan, H. (2011). “Capacity Evaluation of a Severely Distressed and Deteriorated 50-Year-Old Box Beam with Limited Data.” *Journal of Performance of Constructed Facilities*, 25(4), pp. 299 - 308.

28. Attanayake, U. and Mazumder, A. F. (2021). "A Performance-Based Approach for Deciding the Age of New Concrete for Thin Epoxy Overlay Application." *Transportation Research Record*, 2675(10), pp. 1055 - 1068.
29. Attanayake, U. B., and Aktan, H. (2015). "The First Generation ABC System, Evolving Design, and Half a Century Performance– Michigan Side-by-Side Box-Beam Bridge." *ASCE Journal of Performance of Constructed Facilities*, 29 (3).
30. Attanayake, U., Dissanayake, A., Mayer, K., and Wiggenhauser, H. "SAFT Analysis and Phase Evaluation Procedures Using Ultrasonic Shear Wave Imaging Device (MIRA) Data." *Proc., 97th TRB Annual Meeting, No. 18-03720*, Washington D.C. 20001, January 07-11, 2018.
31. Baehaki, Andi, M., and Yohanes, G. R. (2019). "Experimental Study of Crack Depth Measurement of Concrete with Ultrasonic Pulse Velocity (UPV)." *IOP Conference Series: Materials Science and Engineering*, 673(2019) 012047.
32. Bartell, E. F., and Fu, Y. (1929). "Adsorption from the Aqueous Solution by Silica." *The Journal of Physical Chemistry*, 33, pp. 676 – 687.
33. Batic, O., Giaccio, G., and Zerbino, R. (2004). "On the Effect of ASR Cracking on the Mechanical Behavior of Concrete in Tension and Compression." *Proceedings of the 12th International Conference on Alkali-Aggregate Reaction in Concrete*, October 15-19 2004, Beijing International Convention Center, Beijing, China, pp. 1136-1141.
34. Ben Haha, M. (2006). *Mechanical Effects of Alkali-Silica Reaction in Concrete Studied by SEM-Image Analysis*, PhD. Dissertation, EPFL, Rte Cantonale, 1015 Lausanne, Switzerland.
35. Bérubé, M-A., Smaoui, N., Fournier, B., Bissonnette, B., and Durand, B. (2005). "Evaluation of the Expansion attained to Date by Concrete affected by Alkali–Silica Reaction. Part III: Application to existing structures." *Canadian Journal in Civil Engineering*, 32, pp. 463 - 479.
36. Blight, G. E. and Alexander, M. G. (2010). *Alkali-Aggregate Reaction and Structural Damage to Concrete*, 1st Ed., CRC Press/Balkema, P.O. Box 447, 2300 AK Leiden, The Netherlands.
37. British Standards Institute (BSI). (1997). *BS 1881-203: Testing Concrete - Part 203: Recommendations for Measurement of Velocity of Ultrasonic Pulses in Concrete*, BSI, 389 Chiswick High Road, London, W4 4AL, UK.

38. Buford, A. R. (2013). *In Situ Monitoring of Alkali-Silica Reaction (ASR) Affected Concrete: A Study on Crack Indexing and Damage Rating Index to Assess the Severity of ASR and to Monitor ASR Progression*, Nuclear Regulatory Commission, Washington, D.C. 20555.
39. Bungey, J. H., Millard, S. G., and Grantham, M. G. (2006). "Chapter 3 – Ultrasonic pulse velocity methods." In *Testing of Concrete*, 4th Ed., Taylor and Francis, 2 Park Square, Milton Park, Abingdon, Oxon OX14 4RN, UK, pp. 51 - 81.
40. Caltrans. (2017). *Caltrans Bridge Element Inspection Manual*, California Department of Transportation, 1120 N Street, Sacramento, California 95814.
41. CSA International. (2000). *A864-00: Guide to the Evaluation and Management of Concrete Structures Affected by Alkali-Aggregate Reaction*, CSA International, Consolidated Mailing List, 178 Rexdale BLVD, Toronto on M9W 1R3, Canada.
42. Delucchi, M. and Cerisola, G. (2005). "Influence of Thickness on Mechanical Properties and Crack-Bridging Ability of Coatings for Concrete." *Progress in Organic Coatings*, 54, pp. 305 – 309.
43. Delucchi, M., Barbucci, A., and Cerisola, G. (2004). "Crack-Bridging Ability of Organic Coatings for Concrete: Influence of the Method of Concrete Cracking, Thickness and Nature of The Coating." *Progress in Organic Coatings*, 49, pp. 336 – 341.
44. Delucchi, M., Barbucci, A., Temtchenko, T., Poggio, T., and Cerisola, G. (2002). "Study of the Crack-Bridging Ability of Organic Coatings for Concrete: Analysis of the Mechanical Behaviour of Unsupported and Supported Films." *Progress in Organic Coatings*, 44, pp. 261 – 269.
45. Diamanti, M. V., Brenna, A., Bolzoni, F., Berra, M., Pastore, T., and Ormellese, M. (2013). "Effect of Polymer Modified Cementitious Coatings on Water and Chloride Permeability in Concrete." *Construction and Building Materials*, 49, pp. 720 – 728.
46. Diamond, S. (1996). "Delayed Ettringite Formation- Processes and Problems." *Cement and Concrete Composites*, 18, pp. 205 – 215.
47. DOT&PF. (2020). *Standard Specifications for Highway Construction*, Alaska Department of Transportation and Public Facilities, P.O. Box 112500, Juneau, AK 99811, pp. 178 – 180.
48. Durand, B. (1995). "Review of repair methods used at Hydro-Quebec to inhibit alkali-aggregate reactions in concrete structures". Proceedings of the *USCOLD Second*

International Conference on Alkali-Aggregate Reactions in Hydroelectric Plants and Dams, 22-27 Oct 1995, Chattanooga, Tennessee, pp. 289- 310.

49. Esposito, R., Anaç, C., Hendriks, M. A. N., and Çopuroğlu, O. (2016). “Influence of the Alkali-Silica Reaction on the Mechanical Degradation of Concrete.” *Journal of Materials in Civil Engineering*, 28(6), pp. 04016007.
50. Fan, S. and Hanson, J. (1998). “Effect of Alkali Silica Reaction Expansion and Cracking on Structural Behavior of Reinforced Concrete Beams.” *ACI Structural Journal*, 95(5), pp. 488 - 495.
51. Federal Register (FR). (2004). “National Bridge Inspection Standards.” *Federal register—rules and regulations*, 69(239), pp. 74419 – 74439.
52. Fournier, B. and Bérubé, M. A. (2000). “Alkali-Aggregate Reaction in Concrete: A Review of Basic Concepts and Engineering Implications.” *Canadian Journal of Civil Engineering*, 27(2), pp. 167 - 191.
53. Franzoni, E., Varum, H., Natali, M. E., Bignozzi, M. C., Melo, J., Rocha, L., and Pereira, E., (2014). “Improvement of Historic Reinforced Concrete/Mortars by Impregnation and Electrochemical Method.” *Cement and Concrete Composites*, 49, pp. 50 – 58.
54. Frosch, R. J., Williams, C. S., Molley, R. T., and Whelchel, R. T. (2020a). *Concrete Box Beam Risk Assessment and Mitigation: Volume 1—Evolution and Performance*, Report No. FHWA/IN/JTRP-2019/06, Indiana Department of Transportation State Office Building 100 North Senate Avenue Indianapolis, Indiana 46204.
55. Frosch, R. J., Williams, C. S., Molley, R. T., and Whelchel, R. T. (2020b). *Concrete Box Beam Risk Assessment and Mitigation: Volume 2—Evaluation and Structural Behavior*, Report No: FHWA/IN/JTRP-2020/07, Indiana Department of Transportation State Office Building 100 North Senate Avenue Indianapolis, Indiana 46204.
56. Frýbort, A., Štulířová, J, and Grošek, J. (2020). “Complementary Analyses of Concrete Characteristics Performed on Cores Taken from Concrete Pavements.” *Proc., 4th International Scientific Conference Structural and Physical Aspects of Construction Engineering*, EDP Sciences - Web of Conferences, Les Ulis Cedex A, France.
57. Gautam, B. (2016). *Effect of Multiaxial Stresses on Alkali-Silica Reaction Damage of Concrete*, PhD. Dissertation, Department of Civil Engineering, University of Toronto, Canada.

58. Gautam, B. P. and Panesar, D. K. (2017). "The Effect of Elevated Conditioning Temperature on the ASR Expansion, Cracking and Properties of Reactive Spratt Aggregate Concrete." *Construction and Building Materials*, 140, pp. 310 - 320.
59. Gautam, B., Panesar, D., Sheikh, S., and Vecchio, F. (2017). "Effect of multiaxial stresses on alkali-silica reaction damage of concrete." *ACI Materials Journal*, 114(4), pp. 595 - 604.
60. Giaccio, G., Zerbino, R., Ponce, J., and Batic, O. (2008). "Mechanical Behavior of Concretes Damaged by Alkali-Silica Reaction." *Cement and Concrete Research*, 38(7), pp. 993 - 1004.
61. Giannini, E., and Folliard, K. (2012) "Stiffness Damage and Mechanical Testing of Core Specimens for the Evaluation of Structures Affected by ASR." *Proc., 14th International Conference on Alkali-Aggregate Reaction in Concrete*, ICAAR, Austin, Texas.
62. Godart et al. (1992). "Diagnosis and Monitoring of Concrete Bridges Damaged by A.A.R. in Northern France." *Proc., 9th International Conference on Alkali-Aggregate Reaction in Concrete*, ICAAR, Westminster, London, UK.
63. Guthrie, G. D. and Carey. J. W. (1997). "A Simple Environmentally Friendly, and Chemically Specific Method for the Identification and evaluation of the Alkali-Silica Reaction." *Cement and Concrete Research*, 27(9), pp. 1407 – 1417.
64. Guthrie, G. D. and Carey. J. W. (1998). *Geochemical Methods for the Identification of ASR Gel*, Report No: LA-UR-98-3570, Geology and Geochemistry Group, Mail Stop D462, Los Alamos National Laboratory, Los Alamos, New Mexico 87545.
65. Guthrie, G. D. and Carey. J. W. (1999). "Geochemical Method for Identifying Alkali-Silica-Reaction Gel." *Transportation Research Records*, 1668, pp. 68 – 71.
66. Hafçı, A. (2013). *Effect of Alkali-Silica Reaction Expansion on Mechanical Properties of Concrete*, Master's thesis, Middle East Technical University, Ankara, Turkey.
67. Hagen, M. G. (1995). *Field Performance of Penetrating Sealers for Concrete Bridge Decks*, Minnesota Department of Transportation, 395 John Ireland Boulevard, St. Paul, Minnesota 55155.
68. Hall, C., Barnes, P., Billimore, A. D., Jupe, A. C., and Turrillas, X. (1996). "Thermal Decomposition of Ettringite $\text{Ca}_6[\text{Al}(\text{OH})_6]_2(\text{SO}_4)_3 \cdot 26\text{H}_2\text{O}$." *Journal of Chemistry Society, Faraday Transactions*, 92.
69. Harries, K. A. (2006). *Full-scale Testing Program on De-Commissioned Beams from the Lake View Drive Bridge*, Report No. FHWA-PA-2006-008-EMG001, The Pennsylvania

Department of Transportation, Bureau of Planning and Research 400 North Street, 6th Floor East Harrisburg, Pennsylvania 17120.

70. Harries, K. A. and Miller, R. (2012). *Guide to Recommend Practice for the Repair of Impact-Damaged Prestressed Concrete Bridge Girders*, Transportation Research Board, National Academy of Sciences, 2101 Constitution Avenue, N.W. Washington, D.C. 20418.
71. Harries, K. A., Kasan, J., and Aktas, J. (2009). *Repair Method for Prestressed Girder Bridges*, Report No. FHWA-PA-2009-008-PIT 006, The Pennsylvania Department of Transportation, Bureau of Planning and Research, 400 North Street, 6th Floor East Harrisburg, Pennsylvania 17120.
72. Hartle, R. A., Ryan, T. W., Eric Mann, E., Danovich, L. J., Sosko, W. B., and Bouscher, J. W. (2002). *Bridge Inspector's Reference Manual*, Report No. FHWA NHI 03-001, Federal Highway Administration, Turner-Fairbank Highway Research Center, 6300 Georgetown Pike, McLean, Virginia 22101.
73. Hayes, N. W. (2020). *Effect of Alkali-Silica Reaction on Confined Reinforced Concrete*, PhD. Dissertation, University of Tennessee, Knoxville, Tennessee 37996.
74. Helmerich, R., Mielentz, F., Milmann, B., Adam, L., Villalobos, S., Guimaraes, M., and Wiggenghauser, H. (2015). "Detection of Cracks Perpendicular to the Surface Using Acoustic Methods." *Proc., International Symposium Non-Destructive Testing in Civil Engineering (NDT-CE)*, Berlin, Germany.
75. Helmuth, R. (1993). *Alkali-Silica Reactivity: An Overview of Research*, Report No. SHRP-C-342, Strategic Highway Research Program, 2101 Constitution Avenue N.W., Washington, D.C. 20418.
76. Hooton, R. D., Rogers, C., MacDonald, C. A., and Ramlochan, T. (2013). "Twenty-Year Field Evaluation of Alkali-Silica Reaction Mitigation." *ACI Material Journal*, 110(5), pp. 539 – 548.
77. Hou, P., Cheng, X., Qian, J., and Shah, S. P. (2014). "Effects and Mechanisms of Surface Treatment of Hardened Cement-Based Materials with Colloidal NanoSiO₂ and its Precursor." *Construction and Building Materials*, 53, pp. 66 – 73.
78. ICC (2018). *2018 International Building Code* ® (IBC), International Code Council, 500 New Jersey Avenue, NW, 6th Floor, Washington, D.C. 20001.

79. IDOT (2020). *Manual for Fabrication of Precast Prestressed Concrete Products*, Illinois Department of Transportation, Bureau of Materials and Physical Research, 126 E Ash St, Springfield, Illinois 62704.
80. IDOT. (2004). *Guidelines for Estimating Strand Loss in Precast Prestressed Concrete (PPC) Deck Beam Bridges*, Illinois Department of Transportation (IDOT), Hanley Building, 2300 S. Dirksen Parkway, Springfield, Illinois 62764.
81. Igarashi, G., Yamada, K., Xu, Y., Wong, H., Hirono, S., and Ogawa, S. (2016). "Image Analysis of Alkali-Aggregate Gel in Concrete Prism Test with Alkali-Wrapping." *Proc., 15th International Conference on Alkali-Aggregate Reaction in Concrete*, ICAAR, Sao Paulo, Brazil.
82. INDOT (2013). *Inspection & Sampling Procedure for Prestressed Structural Members Manual*, Indiana Department of Transportation, 100 N Senate Ave, Indianapolis, Indiana 46204.
83. ISE (1992). *Structural Effects of Alkali-Silica Reaction- Technical Guidance on the Appraisal of Existing Structures*, Institution of Structural Engineers, IStructE Ltd., 11 Upper Belgrave Street, London, SW1X 8BH, UK.
84. Jia, L., Shi, C., Pan, X., Zhang, J., and Wu, L. (2016). "Effects of Inorganic Surface Treatment on Water Permeability of Cement-Based Materials." *Cement and Concrete Composite*, 64, pp. 85 – 92.
85. Jones, A., and Clark, L. (1996). "The Effects of Restraint on ASR Expansion of Reinforced Concrete." *Magazine of Concrete Research*, 48(174), pp. 1-13.
86. Kalyan, T. and Kishen, C. J. M. (2014). "Experimental Evaluation of Cracks in Concrete by Ultrasonic Pulse Velocity." *Proc., Asia Pacific Conference on Non-Destructive Testing (14th APCNDT)*, Mumbai, India.
87. Kasan, J. L. and Harries, K. A. (2011). "Redevelopment of Prestressing Force in Severed Prestressed Strands." *Journal of Bridge Engineering*, 16(3), pp. 431 - 437.
88. Kasan, J. L. and Harries, K. A. (2013). "Analysis of Eccentrically Loaded Adjacent Box Girders." *Journal of Bridge Engineering*, 18(1), pp. 15 - 25.
89. Kawabata, Y., Seignol, J.-F., Martin, R.-P., and Toutlemonde, F. (2017). "Macroscopic Chemo-Mechanical Modeling of Alkali-Silica Reaction of Concrete under Stresses." *Construction and Building Materials*, 137, pp. 234 - 245.

90. Kim, Y. J. (2006). *Strengthening Concrete Structures with Prestressed CFRP Sheets: Laboratory and Numerical Investigations to Field Application*, PhD. Dissertation, Queen's University Kingston, Ontario, Canada.
91. Kim, Y. J., Green, M. F., and Wight, R. G. (2008). "Live Load Distributions on an Impact-Damaged Prestressed Concrete Girder Bridge Repaired Using Prestressed CFRP Sheets." *Journal of Bridge Engineering*, 13(2), pp. 202 - 210.
92. Kolthoff, I. M. and Stenger, V. A. (1931). "The Adsorption of Cations from Ammonical Solution by Silica Gel." *The Journal of Physical Chemistry*, 36, pp. 2113 – 2126.
93. Kolthoff, I. M. and Stenger, V. A. (1933a). "The Adsorption of Alkali Hydroxides by Silica Gel in the Presence of Ammonia and Ammonium Salts." *The Journal of Physical Chemistry*, 38, pp. 249 – 258.
94. Kolthoff, I. M. and Stenger, V. A. (1933b). "The Adsorption of Calcium and Copper from Ammonical Medium by Silica Gel." *The Journal of Physical Chemistry*, 38, pp. 475 – 486.
95. Kongshaug, S. S., Oseland, O., Kanstad, T., Hendriks, M. A. N., Rodum, E., and Markeset, G. (2020). "Experimental investigation of ASR-affected concrete – The influence of uniaxial loading on the evolution of mechanical properties, expansion and damage indices." *Construction and Building Materials*, 245, pp. 118384.
96. Kosmatka, S. H. and Wilson, M. L. (2011). *Design and Control of Concrete Mixtures*, 15th Ed., Portland Cement Association, 5420 Old Orchard Road, Skokie, Illinois 60077.
97. Kriha, B. (2016), *Aesthetic Coatings for Concrete Bridge Components*, Master Theses, The University of Wisconsin, Milwaukee, Wisconsin 53211.
98. Kuzel, H. –J. (1996). "Initial Hydration Reactions and Mechanisms of Delayed Ettringite Formation in Portland Cement." *Cement and Concrete Composites*, 18, pp. 195 – 203.
99. Lee, Y. H. and Oh, T. (2016). "The Measurement of P-, S-, and R-Wave Velocities to Evaluate the Condition of Reinforced and Prestressed Concrete Slabs." *Advances in Materials Science and Engineering*, 2016(6), pp. 1 - 14.
100. Leemann, A. and Griffa, M. (2013). *Diagnosis of Alkali-Aggregate Reaction in Dams*, SFOE-Project No. SI/500863-01, Swiss Federal Office of Energy (SFOE), 3003 Bern, Switzerland.

101. Mak, J., Vessalas, K., and Thomas, P. (2012). "Evaluation of Factors Pertaining to Delayed Ettringite Formation in Steam Cured Precast Concrete Members." *Proc., The New Zealand Concrete Industry*, Claudelands, Hamilton, New Zealand.
102. Martin, R.-P., Sanchez, L., Fournier, B., and Toutlemonde, F. (2017). "Evaluation of different techniques for the diagnosis & prognosis of internal swelling reaction (ISR) mechanisms in concrete." *Construction and Building Materials*, 156, pp. 956 - 964.
103. Mayans, K., F. D. and Garcia, B., and Miguel, J. (2014). *Analysis of a Damaged and Repaired Prestressed Concrete Bridge Girder by Vehicle Impact and Effectiveness of Repair Procedure*, Thesis, Barcelona School of Civil Engineering, Barcelona, Spain.
104. Mayer, K., Chinta, P. K., Langenberg, K. J., and Krause, M. (2012). "Ultrasonic Imaging of Defects in Known Anisotropic and Inhomogeneous Structures with Fast Synthetic Aperture Methods." *Proc., 18th World Conference on Nondestructive Testing*, Durban, South Africa.
105. Mayer, K., Langenberg, K. J., Krause, M., Milmann, B., and Mielentz, F. (2008). "Characterization of Reflector Types by Phase-Sensitive Ultrasonic Data Processing and Imaging." *Journal of Nondestructive Evaluation*, 27, pp. 35 - 45.
106. MDOT BAG. (2009). *MDOT Bridge Analysis Guide (BAG) 2005 Edition with 2009 Interim Update*, Michigan Department of Transportation, 425 W. Ottawa St., Lansing, Michigan 48909.
107. MDOT. (2018b). *Materials Source Guide*, October 2018 Ed., Michigan Department of Transportation, 425 W. Ottawa St., Lansing, Michigan 48909.
108. MDOT. (2019a). *Materials Source Guide*, October 2019 Ed., Michigan Department of Transportation, 425 W. Ottawa St., Lansing, Michigan 48909.
109. MDOT. (2019c). *Materials Quality Assurance Procedures Manual*, October 2019 Ed., Michigan Department of Transportation, 425 W. Ottawa St., Lansing, Michigan 48909.
110. MDOT. (2020). *Materials Source Guide*, October 2020 Ed., Michigan Department of Transportation, 425 W. Ottawa St., Lansing, Michigan 48909.
111. MDOT. (2021a). *Structural Fabrication Quality Manual*, Structural Fabrication Unit, Bureau of Bridges and Structures, Michigan Department of Transportation, 425 W. Ottawa St., P.O. Box 30050, Lansing, MI 48933, pp.96 – 118.
112. MDOT. (2022a). "Construction Manual." <https://mdotwiki.state.mi.us/construction/index.php/Main_Page> (Last accesses: January 12, 2022)

113. MDOT. (2022b). *Bridge Repair Cost Estimate Worksheet- Key: Unit Cost Assumptions*, Michigan Department of Transportation, 425 W. Ottawa St., P.O. Box 30050, Lansing, Michigan 48933.
114. Medeiros, M. H. F. and Helene, P. (2009). "Surface Treatment of Reinforced Concrete in Marine Environment: Influence on Chloride Diffusion Coefficient and Capillary Water Absorption." *Construction and Building Materials*, 23, pp. 1476 – 1484.
115. Memberg, L. S., Klingner, R. E., and Fowler, T. J. (2002). *Bridges with Premature Concrete Deterioration: Damage Indices, Strand-Pullout Tests, and Field Observations*, Report No. FHWA/TX-03/0-1857-4, Center for Transportation Research, The University of Texas, 3208 Red River, Suite 200, Austin, Texas 78705.
116. MiBEIM. (2017). *Michigan Bridge Element Inspection Manual (MiBEIM)*, Michigan Department of Transportation, 425 W. Ottawa St., Lansing, Michigan 48909.
117. Miki, T., Miyagawa, Y., and Mastutani, K. (2013). "Observation for Internal Cracks of Concrete Affected by Alkali-Silica Reaction and Its Compressive Failure Behavior." *Proc., 3rd International Conference on Sustainable Construction Materials and Technologies (SCMT3)*, Kyoto Research Park, Kyoto, Japan.
118. Mostafa. K. and Sanders. D. (2018). *Improving the Long-term Performance of Concrete Bridge Decks Using Deck and Crack Sealers*, Report No. CCEER 18-02, University Transportation Center, Reno, Nevada 89557.
119. Multon, S., Seignol, J.-F., and Toutlemonde, F. (2005). "Structural Behavior of Concrete Beams Affected by Alkali-Silica Reaction." *Materials Journal*, 102(2), pp. 67 - 76.
120. Muynck. W. D., Cox, K., Belie, N. D., and Verstraete, W. (2008). "Bacterial Carbonate Precipitation as an Alternative Surface Treatment for Concrete." *Construction and Building Materials*, 22 (5), pp. 875 – 885.
121. Na, O., Xi, Y., Ou, E., and Saouma, V. E. (2016). "The Effects of Alkali-Silica Reaction on the Mechanical Properties of Concretes with Three Different Types of Reactive Aggregate." *Structural Concrete*, 17(1), pp. 74 - 83.
122. Naito, C., Jones, L., and Hodgson, I. (2011). "Development of Flexural Strength Rating Procedures for Adjacent Prestressed Concrete Box Girder Bridges." *Journal of Bridge Engineering*, 16(5), pp. 662 - 670.

123. Naito, C., Sause, R., Hodgson, I., Pessiki, S., and Macioce, T. (2010). "Forensic Examination of a Noncomposite Adjacent Precast Prestressed Concrete Box Beam Bridge." *Journal of Bridge Engineering*, 15(4), pp. 408 - 418.
124. Natesaiyer, K. and Hover, K. C. (1988). "Insitu Identification of ASR Products in Concrete." *Cement and Concrete Research*, 18, pp. 455 – 463.
125. Natesaiyer, K. and Hover, K. C. (1989). "Further Study of An In-situ Identification Method for Alkali-Silica Reaction Products in Concrete." *Cement and Concrete Research*, 19, pp. 770 – 778.
126. Newton, B. (2010). "AASHTO Guide Manual for Bridge Element Inspection." <<http://sp.bridges.transportation.org/Documents/2010%20SCOB%20presentations/AASHTO%20Guide%20Manual%20for%20Bridge%20Element%20Inspection%20-%20Barton%20Newton.pdf>> (Last accessed: November 2, 2021)
127. Nguyen, T., Yu, Y., Li, J., and Gowripalan, N. (2019). "Evaluation of elastic modulus reduction due to ASR." *Concrete in Australia*, 45(2), pp. 47 - 52.
128. Nixon, R. (2002). "Coating Selection and Important Properties of Coatings for Concrete." *Journal of Protective Coatings and Linings*.
129. NJDOT. (2015). *Bridge Element Inspection Manual*, New Jersey Department of Transportation, P.O. Box 600, Trenton, New Jersey 08625.
130. ODOT. (2019). *Construction and Material Specifications*, Ohio Department of Transportation, Office of Contracts, P.O. Box 899, Columbus, Ohio 43216, pp. 372 – 373.
131. Patrick, W. A. and Barclay, E. H. (1925). "The Behavior of Silica Gel towards Certain Alkalies and Salts in Aqueous Solution." *The Journal of Physical Chemistry*, 29, pp. 1400-1405.
132. PCI. (2016). *Manual for the Evaluation and Repair of Precast, Prestressed Concrete Bridge Products Including: Imperfections or Damage Occurring During Production, Handling, Transportation, and Erection*, Report No. MNL-137-06, 1st Ed., Precast/Prestressed Concrete Institute (PCI), 8770 W Bryn Mawr Ave Suite 1150, Chicago, Illinois 60631.
133. PennDOT. (2010). *PUB 238 (3-10): Bridge Safety Inspection Manual*, 2nd Ed. Pennsylvania Department of Transportation, 400 North Street, 6th Floor East Harrisburg, Pennsylvania 17120.

134. Peterson, K. (1999). "Concrete Microscopy Library- Fluorescent Microscopy." <<http://publish.illinois.edu/concretemicroscopylibrary/fluorescent-microscopy/>> (Last accessed: January 17, 2022).
135. Pfeifer, D. W. and Scali, M. J. (1981). *Concrete Sealers for Protection of Bridge Structures*, NCHRP Report No. 244, Transportation Research Board, National Academy of Sciences 2101 Constitution Avenue, N.W. Washington, D.C. 20418.
136. Pigino, B., Leemann, A., Franzoni, E., and Lura, P. (2012). "Ethyl Silicate for Surface Treatment of Concrete-Part II: Characteristics and Performance." *Cement and Concrete Composite*, 34, pp. 314 – 321.
137. Pincheira, J. A. and Dorshorst, M. A. (2005). *Evaluation of Concrete Deck and crack Sealer*, Report No: WHRP 06-09, Wisconsin Department of Transportation 4802 Sheboygan Avenue Madison Wisconsin 73707.
138. Pinto, R., Medeiros, A., Padaratz, I. J., and Andradfe, P. B. (2010). "Use of Ultrasound to Estimate Depth of Surface Opening Cracks in Concrete Structures." *E-Journal of Nondestructive Testing (NDT)*.
139. Poole, A. B., McLachlan, A., and Ellis, D. J. (1988). "A Simple Staining Technique for the Identification of Alkali-Silica Gel in Concrete and Aggregate." *Cement and Concrete Research*, 18(1), pp. 116 – 120.
140. Popovics, J. S. and Abraham, O. (2010). "Chapter 20 - Surface Wave Techniques for Evaluation of Concrete Structures." In *Non-destructive Evaluation of Reinforced Concrete Structures*, Volume 2, Woodhead Publishing Series in Civil and Structural Engineering, pp. 441 – 465.
141. Popovics, J. S., Roesler, J. R., Bittner, J., Amirkhanian, A. N., Brand, A. S., Gupta, P., and Flowers, K. (2017). *Ultrasonic Imaging for Concrete Infrastructure Condition Assessment and Quality Assurance*, Report No. FHWA-ICT-17-007, Illinois Department of Transportation (SPR), Bureau of Research, 126 East Ash Street, Springfield, Illinois 62704.
142. Proceq. (2014). *Pundit Lab PL-200 Ultrasonic Pulse Velocity and Pundit PL-200PE Ultrasonic Pulse Echo*, Proceq SA, Ringstrasse 2, 8603 Schwerzenbach, Switzerland
143. Proceq. (2017). *Proceq Pundit Operating Instructions*, Proceq SA, Ringstrasse 2, 8603 Schwerzenbach, Switzerland.

144. Radlinska, A., McCarthy, L. M., Matzke, J., and Nagel, F. (2014). "Synthesis of DOT Use of Beam End Protection for Extending the Life of Bridges." *The International Journal of Concrete Structures and Materials*, 8(3), pp.185–199.
145. Raupach, M. and Buttner, T. (2014). *Concrete Repair to EN 1504 Diagnosis, Design, Principles and Practice*, CRC Press Taylor & Francis Group, 6000 Broken Sound Parkway NW, Suite 300 Boca Raton, Florida 33487.
146. Reed, R. G. (2016). *Measuring Relative Humidity in Concrete Pavements as a Method to Assess ASR Mitigation*, Civil Engineering Undergraduate Honors Theses, University of Arkansas, Fayetteville, Arkansas 72701.
147. Rivard, P. and Saint-Pierre, F. (2009). "Assessing Alkali-Silica Reaction Damage to Concrete with Non-Destructive Methods: from the Lab to the Field." *Construction and Building Materials*, 23(2), pp. 902 - 909.
148. Rivard, P., Fournier, B., and Ballivy, G. (2002). "The Damage Rating Index Method for ASR Affected Concrete - A Critical Review of Petrographic Features of Deterioration and Evaluation Criteria." *Cement, Concrete and Aggregates*, 24, pp. 81 – 91.
149. Rooke, A. (2018). *Guide to Bridge Technology Part 7: Maintenance and Management of Existing Bridges*, Austroads Ltd., Level 9, 287 Elizabeth street, Sydney, NSW 2000, Australia, pp. 117.
150. Sagradyan, A. and Ogura, N. (2021). "Evaluation of influence of prestressing on ASR-damaged concrete using NDT." In *Bridge Maintenance, Safety, Management, Life-Cycle Sustainability and Innovations*, Yokota & Frangopol (eds), 2021 Taylor & Francis Group, London, UK, pp. 2386 – 2392.
151. Sanchez, L. F. M. (2014). *Contribution to the Assessment of Damage in Aging Concrete Infrastructures Affected by Alkali-Aggregate Reaction*, Doctoral Thesis, University of Laval, Quebec, Canada.
152. Sanchez, L. F. M., Fournier, B., Jolin, M., and Duchesne, J. (2015). "Reliable Quantification of AAR Damage through Assessment of the Damage Rating Index (DRI)." *Cement and Concrete Research*, 67, pp. 74 – 92.
153. Sanchez, L. F. M., Fournier, B., Jolin, M., Mitchell, D., and Bastien, J. (2017). "Overall Assessment of Alkali-Aggregate Reaction (AAR) in Concretes Presenting Different

- Strengths and Incorporating a Wide Range of Reactive Aggregate Types and Natures.” *Cement and Concrete Research*, 93, pp. 17 - 31.
154. Sanchez, L., Fournier, B., Jolin, M., Bastien, J., Mitchell, D., and Noel, M. (2016). “Thorough Characterization of Concrete Damage Caused by AAR through the Use of a Multi-Level Approach.” *Proc., 15th International Conference on Alkali-Aggregate Reaction in Concrete*, ICAAR, São Paulo, SP, Brazil.
155. Sanno, C., Maruyama, T., Yamanobe, H., and Torii, K. (2013). “Development of simple method of ASR diagnosis by gel fluorescence method.” *Concrete Engineering Annual Proceedings*, 35(1), pp. 973 - 978.
156. Sargolzhahi, M., Kodjo, S. A., Rivard, P., and Rhazi, J. (2010). “Effectiveness of Nondestructive Testing for the Evaluation of Alkali-Silica Reaction in Concrete.” *Construction and Building Materials*, 24, pp. 1398 – 1403.
157. Sarkar, S. L., Zollinger, D. G., Mukhopandhyay, A. K., Seungwook, L., and Shon, C.-, S. (2004). *Appendix 1 – Handbook for Identification of Alkali-Silica Reactivity in Airfield Pavement*, Texas Transportation Institute, Texas A & M University, College Station, Texas 77840.
158. Screening Eagle Technologies. (2021). “Screening Eagle Acquires Ultrasound Imaging Software Solution.” Screening Eagle.” <<https://www.screeningeagle.com/en/about-us/news/2307>> (Last accessed: July 31, 2021).
159. Shrimmer, F. (2015). “The Damage Rating Index: Assessing the Severity of Alkali Aggregate Reaction in Concrete Dams.” *Proc., of the United States Society on Dams (USSD) Annual Conference*, Louisville, Kentucky.
160. Shrimmer, F. (2019). “Use of the Damage Rating Index as Input for Service Life Prediction in Alkali-Silica Reaction Affected Concrete.” *Advances in Cement Analysis and Concrete Petrography*, ASTM STP1613, D. Cong and D. Broton, Eds., ASTM International, West Conshohocken, Pennsylvania 19428, pp. 89 – 104.
161. Sims, I. and Nixon, P. (2003). “RILEM Recommended Test Method AAR-0: Detection of Alkali-Reactivity Potential in Concrete – Outline Guide to the use of RILEM Methods in Assessments of Aggregates for Potential Alkali-Reactivity.” *Materials and Structures*, 36, pp. 472 - 479.

162. Smaoui, N., Bérubé, M.-A., Fournier, B., Bissonnette, B., and Durand, B. (2004a). "Evaluation of the Expansion Attained to Date by Concrete Affected by Alkali-Silica Reaction. Part I: Experimental Study." *Canadian Journal of Civil Engineering*, 31(5), pp. 826 – 845.
163. Smaoui, N., Fournier, B., Bérubé, M.-A., Bissonnette, B., and Durand, B. (2004b). "Evaluation of the Expansion Attained to Date by Concrete Affected by Alkali-Silica Reaction. Part II: Application to Nonreinforced Concrete Specimens Exposed Outside." *Canadian Journal of Civil Engineering*, 31(6), pp. 997 – 1011.
164. Stark, D. (1991). *Handbook for the Identification of Alkali-Silica Reactivity in Highway Structures*, Report No.: SHRP-C/FR-91-101, Strategic Highway Research Program, 2101 Constitution Ave. NW, Washington, D.C. 20418.
165. Strack, C. M., Barnes, E., Ramsey, M. A., Williams, R. K., Klaus, K. L., and Moser, R. D. (2020). "Impact of Aggregate Mineralogy and Exposure Solution on Alkali-Silica Reaction Product Composition and Structure within Accelerated Test Conditions." *Construction and Building Materials*, 240.
166. Strazhesko, D. N., Strelko, V. B., Belyakov, V. N., and Rubanik, S. C. (1974). "Mechanism of Cation Exchange on Silica Gel." *Journal of Chromatography*, 102, pp. 191 – 195.
167. Swamy, R. and Al-Asali, M. (1988). "Engineering Properties of Concrete affected by Alkali-Silica Reaction." *ACI Materials Journal*, 85(5), pp. 367 – 374.
168. Swamy, R., and Al-Asali, M. (1988). "Expansion of Concrete Due to Alkali Silica Reaction," *ACI Materials Journal*, 85(1), pp. 33-40.
169. Tabatabai, H. and Nabizadeh, A. (2019). *Strength and Serviceability of Damaged Prestressed Girders*. Report No. 0092-17-02, Wisconsin Highway Research Program, Wisconsin Department of Transportation, Research & Library Unit 4822 Madison Yards Way Madison, Wisconsin 53705.
170. TDOT. (2018). *Procedures for Prestressed Concrete Construction (SOP 5-4)*, Division of Materials and Tests, Tennessee Department of Transportation (TDOT), James K. Polk Bldg., Suite 700 505 Deadrick Street Nashville, Tennessee 37243.
171. Tesfamariam, S. and Martín-Pérez, M. (2010). "Chapter 19 – Stress Wave Propagation for Evaluation of Reinforced Concrete Structures." In *Non-destructive Evaluation of Reinforced*

- Concrete Structures*, Volume 2, Woodhead Publishing Series in Civil and Structural Engineering, pp. 417 - 440.
172. The Concrete Society. (2009). *Repair of Concrete Structures with Reference to BS EN 1504*, Technical Report No. 69, Riverside House, 4 Meadows Business Park, Station Approach, Blackwater, Camberley, Surrey CU17 9AB, UK.
 173. Thomas, M. D A, Folliard, K. J., Fournier, B., Rivard, P., and Drimalas, T. (2013b). *Methods for Evaluating and Treating ASR-Affected Structures: Results of Field Application and Demonstration Projects – Volume I: Summary of Findings and Recommendations*, Report No. FHWA-HIF-14-0002, Federal Highway Administration, Office of Pavement Technology, 1200 New Jersey Avenue, Washington, D.C. 20590.
 174. Thomas, M. D A, Folliard, K. J., Fournier, B., Rivard, P., Drimalas, T., and Garber, S. I. (2013c). *Methods for Evaluating and Treating ASR-Affected Structures: Results of Field Application and Demonstration Projects – Volume II: Details of Field Applications and Analysis*, Report No. FHWA-HIF-14-0003, Federal Highway Administration, Office of Pavement Technology, 1200 New Jersey Avenue, Washington, D.C. 20590.
 175. Thomas, M. D. A., Fournier, B., and Folliard, K. J. (2013a). *Alkali-Aggregate Reactivity (AAR) Facts Book*, Report No. FHWA-HIF-13-019, Office of Pavement Technology, Federal Highway Administration, 1200 New Jersey Avenue, Washington, D.C. 20590.
 176. Thomas, M. D. A., Fournier, B., Folliard, K. J., and Resendez, Y. A. (2011). *Alkali-Silica Reactivity Field Identification Handbook*, Office of Pavement Technology Federal Highway Administration 1200 New Jersey Avenue, Washington, D.C. 20590.
 177. Thompson, P. D. and Shepard, R. W. (2000). *AASHTO Commonly-Recognized Bridge Elements, Successful Applications and Lessons Learned*, The handout prepared for the national workshop on Commonly Recognized Measures for Maintenance. <<http://www.pdth.com/images/coreelem.pdf>> (Last accessed: October 20, 2019).
 178. Tosun, K. (2006). "Effect of SO₃ and Fineness on the Rate of Delayed Ettringite Formation in Heat Cured Portland Cement Mortar." *Cement and Concrete Composites*, 28, pp. 761 - 772.
 179. UDOT. (2017). *Bridge Management Manual. Chapter 4 – Load Rating Policies and Procedures*, Utah Department of Transportation, 4501 South 2700 West, PO Box 148410, Salt Lake City, Utah 84114.

180. Van Dam, T. J., Sutter, L. L., Smith, K. D., Wade, M. J., and Peterson, K. R. (2002). *Guidelines for Detection, Analysis, and Treatment of Materials-Related Distress in Concrete Pavements Volume 2: Guidelines Description and Use*, Report No. FHWA-RD-01-164, Federal Highway Administration, Research Technology and Development, 6300 Georgetown Pike, McLean, Virginia 22101.
181. Washer, G., Hammed, M., Brown, H., Fogg, J., Salazar, J., Leshko, B., Conner, R., Koonce, J., Karper, C., and Jansen, P. (2019). *Guidelines to Improve the Quality of Element-Level Bridge Inspection Data*, NCHRP Report No. 259, National Cooperative Highway Research Program, National Academies of Sciences, Engineering, and Medicine, Washington, D.C. 20001.
182. Wehrle, E., Lute, R., Rust, C., Juenger, M. G., and Folliard, K. J. (2010). *The Effect of Coatings and Sealers used to Mitigate Alkali-Silica Reaction and/or Delayed Ettringite Formation in Hardened Concrete*, Report No. TxDOT IAC 12-8XXIA008-1, Texas Department of Transportation, Research and Technology Implementation Office, P.O. Box 5080, Austin, Texas 78705.
183. Wells, D., Palle, S., and Hopwood II, T. (2017). *Proposed Testing of Concrete Sealers*, Report No. KTC-TA-17-04/KHIT2017-6-1F, Kentucky Transportation Center Technical Assistance Report, Lexington, Kentucky 40506.
184. Wells, D., Sudhir, P., Bobby, M. and Theodore, H. (2014). *Sealants, Treatments and Deicing Salt Practices to Limit Bridge Deck Corrosion*, Report No. KTC-14-4/FRT194, Kentucky Transportation Center, Lexington, Kentucky 40506.
185. Wigum, B. J., Pedersen, L. T., Grelk, B., and Lindgård, J. (2006). *State-of-the Art Report: Key Parameters Influencing the Alkali Aggregate Reaction*, PARTNER Report 2.1, European Community - “Competitive and Sustainable Growth” Programme.
186. Williams, M. E. and Choudhuri, D. (2010). “Case Study in the Evaluation and Repair of ASR Deterioration in Concrete Bridge Beams.” *ACI Special Publications*, 277, pp. 143 - 155.
187. Wipf, T. J., Klaiber, F. W., Rhodes, J. D., and Kempers, B. J. (2004). *Repair of Impact Damaged Prestressed Concrete Beams with CFRP. Effective Structural Concrete Repair*, Volume 1 of 3, Iowa DOT Project TR – 428, Iowa Department of Transportation Highway Division and the Iowa Highway Research Board, 800 Lincoln Way, Ames, Iowa 50010.

188. Wong, H. S., Barakat, R., Alhilali, A., Saleh, M., Cheeseman, C. R. (2015). "Hydrophobic Concrete Using Waste Paper Sludge Ash." *Cement and Concrete Research*, 70, pp. 9 - 20.
189. Yaman, I. O., Inci, G., Yeseiller, N., and Aktan, H. M. (2001). "Ultrasonic Pulse Velocity in Concrete Using Direct and Indirect Transmission." *ACI Material Journal*, 98(6), pp. 450 - 457.
190. Yazdani, N. and Montero, M. A. D. L. F. (2016). "Structural Performance of Impact Damaged and Repaired Concrete Bridge Girder using GFRP Rebars." *Innov. Infrastruct. Solut*, pp. 1 - 34.

MDOT Special Provisions

1. MDOT. (2017). *Special Provision for Silane Treatment for Bridge Barriers on Job Number 115752: 12DS710(N030)*, Michigan Department of Transportation, 425 W. Ottawa St., Lansing, Michigan 48909.
2. MDOT. (2018a). *Special Provision for Warranty on Concrete Surface Coating: 12SP-710A-05*, Michigan Department of Transportation, 425 W. Ottawa St., Lansing, Michigan 48909.
3. MDOT. (2018c). *Special Provision for Silane Treatment for Concrete Bridge Surface on Job number 202704:12DS710(N845)*, Michigan Department of Transportation, 425 W. Ottawa St., Lansing, Michigan 48909.
4. MDOT. (2019b). *Silane Treatment for Bridge Barriers and Deck Fascias: 12SM710(A010)*, Michigan Department of Transportation, 425 W. Ottawa St., Lansing, Michigan 48909.
5. MDOT. (2021b). *Special Provision for Concrete Surface Coating: 20RC710(A285)*, Michigan Department of Transportation, 425 W. Ottawa St., Lansing, Michigan 48909.
6. MDOT. (2021c). *Special Provision for Silane Treatment for Bridge Concrete, 20TM710(A290)*, Michigan Department of Transportation, 425 W. Ottawa St., Lansing, Michigan 48909.

ASTM Standards

1. ASTM C1260-21: Standard Test Method for Potential Alkali Reactivity of Aggregates (Mortar-Bar Method)
2. ASTM C1293-20a: Standard Test Method for Length Change of Concrete due to Alkali-Silica Reaction

3. ASTM C157/157M-17: Standard Test Method for Length Change of Hardened Hydraulic-Cement Mortar and Concrete
4. ASTM C1778-22: Standard Guide for Reducing the Risk of Deleterious Alkali-Aggregate Reaction in Concrete
5. ASTM C597-16: Standard Test Method for Pulse Velocity Through Concrete
6. ASTM C856/856M-14 Standard Practice for Petrographic Examination of Hardened Concrete
7. ASTM C856/856M-20: Standard Practice for Petrographic Examination of Hardened Concrete
8. ASTM D2370-16: Standard Test Method for Tensile Properties of Organic Coatings
9. ASTM D412-16: Standard Test Methods for Vulcanized Rubber and Thermoplastic Elastomers—Tension
10. ASTM F2170-19a: Standard Test Method for Determining Relative Humidity in Concrete Floor Slabs Using In-situ Probes.

Technical Data Sheets

1. ChemMasters® (2019). ColorLatic™ Elastomeric Acrylic Coating

Appendix A: Guidelines for estimating prestressing strand loss

Table A-1. Guidelines for strand estimation in PUB 238 (PennDOT 2010)

Observation	Action
Strands adjacent to or intersecting a crack	Strands located adjacent to cracks are assumed to be 100% ineffective
Exposed strand	Cross-sectional area of the exposed strands is reduced by 125% during capacity calculations.
No exposed strands, but signs of internal damages present (such as bottom flange cracking with rust and/or delamination)	Contact Bridge Quality Assurance Division (BQAD) for further instructions.
Significant strand loss (>25%)	Contact BQAD for further instructions.

A.2. Guidelines for Estimating Strand Loss in Precast Prestressed Concrete (PPC) Deck Beam Bridges (2004) of Illinois DOT (IL DOT)

GUIDELINES FOR ESTIMATING STRAND LOSS IN PRECAST PRESTRESSED CONCRETE (PPC) DECK BEAM BRIDGES (February 2004)

Prestressed strands incorporated in PPC Deck Beams shall be disregarded during analysis for load-carrying capacity based on the following observed conditions:

LONGITUDINAL CRACKS

- 1) Cracks observed in the middle area of the beam underside, with or without rust stains or other discoloration of the concrete adjacent to the cracks:
Disregard all strands from all rows of strands that may be located adjacent to the cracks.
- 2) Cracks observed along the edges of the beam underside, with or without rust stains or other discoloration of the concrete adjacent to the cracks:
Disregard at least the strands located adjacent to the edge of the beam in the bottom row of strands. When the crack is extensive in length and its location varies in distance from the beam edge, disregard additional interior strands from all rows of strands that may be intersected by the crack.
- 3) Two longitudinal cracks observed crossing or meeting:
Disregard all strands in all rows of strands located between the cracks and one strand from all rows of strands located adjacent to the outer edge of the cracks.

Note: The intent is to disregard all strands that could intersect the crack and be exposed to air and moisture.

DETERIORATION

- 1) Exposed strands observed with sound concrete adjacent to and above the exposed strands:
Disregard exposed strands only.
- 2) Exposed strands observed with unsound concrete adjacent to and above the exposed strands:
Disregard exposed strands and all strands located in rows above and immediately adjacent to the area of unsound concrete.
- 3) Exposed reinforcement bars observed (#3 or #4 stirrups typically extending less than 1-foot in from the sides of the beam):
Disregard the strands located in the lower row directly above the exposed stirrups. If the concrete is found to be unsound adjacent to the exposed reinforcement bars, disregard all strands in all rows located above the area of unsound concrete.
- 4) Exposed wire mesh or full width reinforcement stirrup bars observed on bottom of beam:
Judge whether or not the wire mesh or reinforcement bars are in contact with the strands.
 - If in contact, disregard all strands in the lower row directly above the exposed wire mesh or stirrups.

Figure A-1. IL DOT's Guidelines for Estimating Strand Loss in Precast Prestressed Concrete (PPC) Deck Beam Bridges

**GUIDELINES FOR ESTIMATING STRAND LOSS IN
PRECAST PRESTRESSED CONCRETE (PPC) DECK BEAM BRIDGES**
(February 2004)

- If not in contact but the concrete adjacent to the exposed wire mesh or stirrups is found to be unsound, disregard all strands located above the area of unsound concrete.
 - If not in contact and concrete adjacent to the exposed wire mesh or stirrups is sound, do not disregard strands during analysis.
- 5) Areas of delaminated concrete observed:
Remove all delaminated concrete to determine the depth of concrete deterioration.
- If reinforcement stirrup bars, wire mesh or strands are exposed, treat as in "1" through "4" above.
 - If no reinforcement, mesh or strands are exposed but there are indications that the exposed concrete is unsound within the affected area, disregard all strands located in the rows of strands above the area.
 - If no reinforcement, mesh or strands are exposed in the affected area and concrete in the area is found to be sound, do not disregard strands in analysis.
- 6) Wet or stained areas observed on bottom or side of beams:
Closely inspect the wet or stained area to determine the soundness of the concrete.
- If close inspection indicates that concrete is unsound or delaminated, treat as in "5" above.
 - If close inspection confirms that the concrete is sound, do not disregard strands in analysis.

Note: Wet and/or rust stained areas should be watch closely. These areas will be the next areas to experience significant deterioration.

Figure A-2. IL DOT's Guidelines for Estimating Strand Loss in Precast Prestressed Concrete (PPC) Deck Beam Bridges (continued)

A1.3. Utah DOT Bridge Management Manual (UDOT 2017)

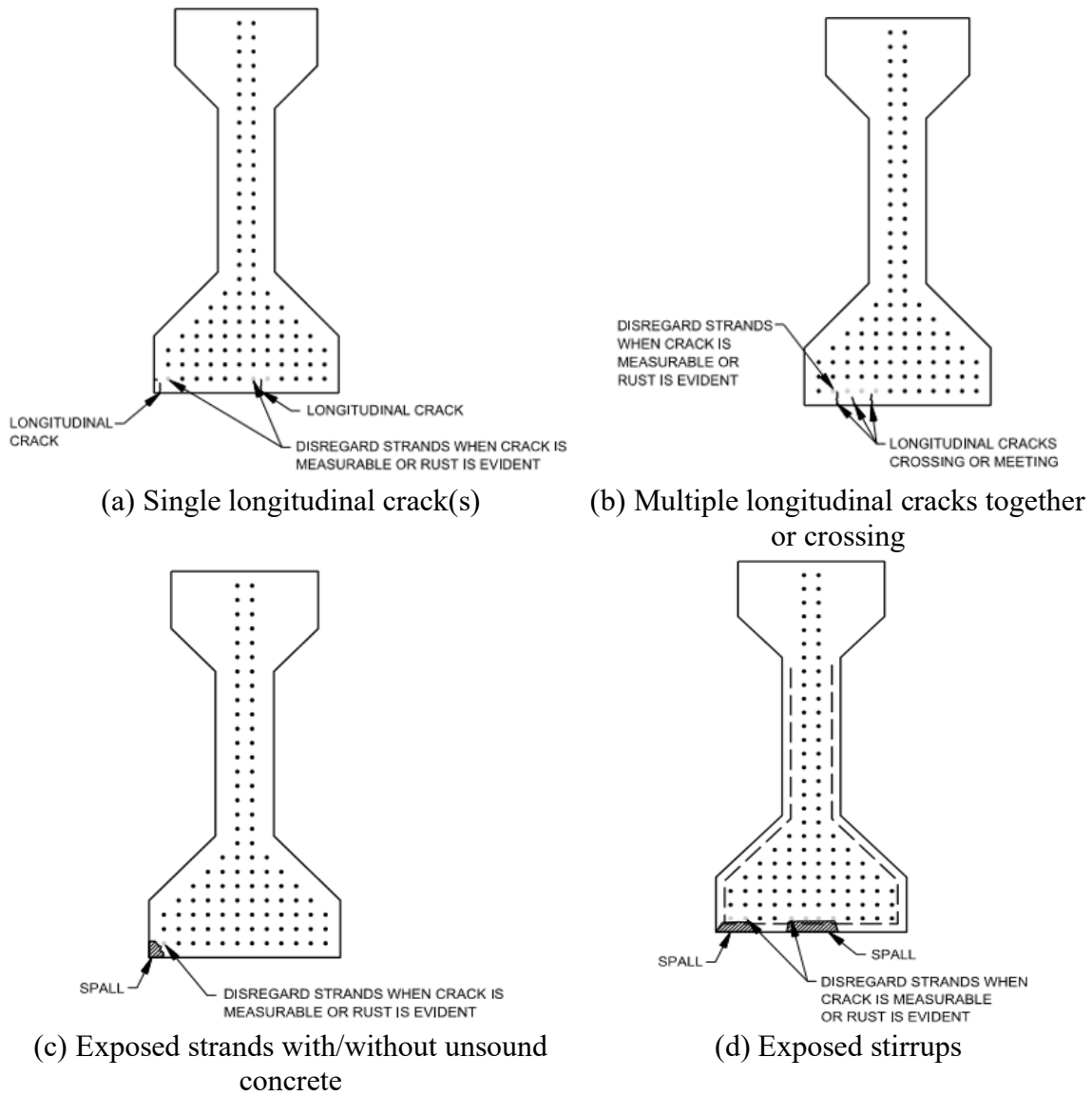


Figure A-3. Prestressing strand disregarding procedure for PC-I girders based on the damages in the cross section (UDOT 2017)

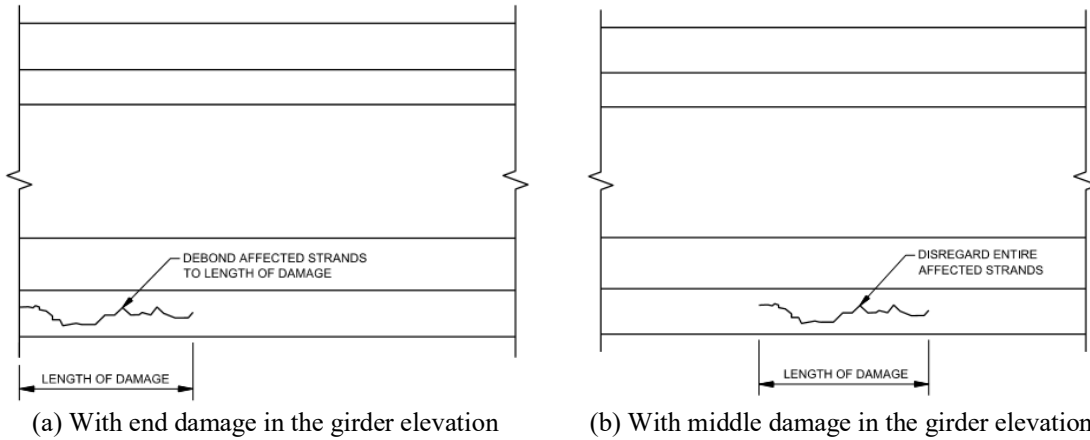


Figure A-4. Prestressing strand disregarding procedure for PC-I girders based on the damages in the span (UDOT 2017)

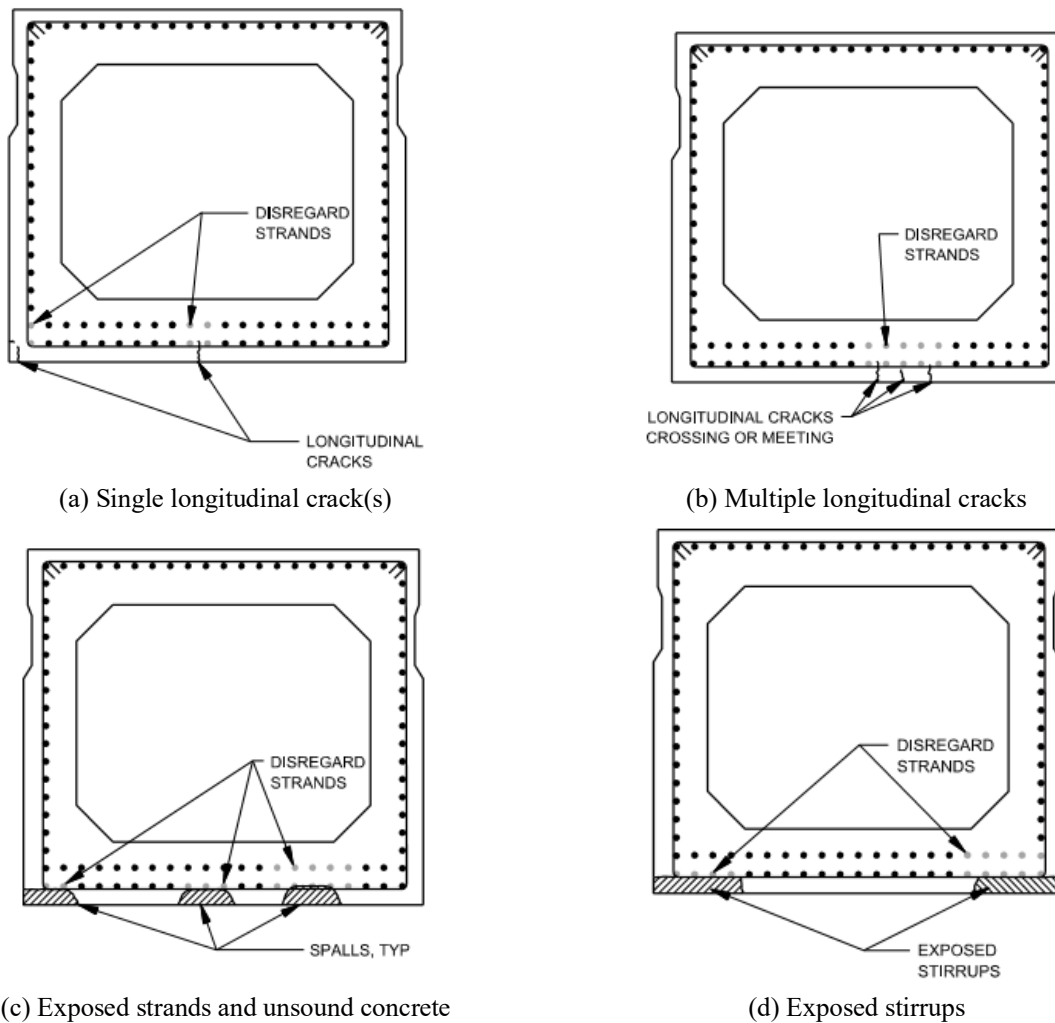


Figure A-5. Prestressing strand disregarding procedure in PC deck girders based on the damages in the cross section (UDOT 2017)

A1.4. Proposed Rating Recommendation for Prestressed Adjacent Box-Girder Bridges with Longitudinal Cracking by Naito et al. (2010)

PennDOT Inspection Methods & Techniques to Determine Non Visible Corrosion of
Prestressing Strands in Concrete Bridge Components

Proposed Rating Recommendations for Prestressed Adjacent Box-Girder Bridges with Longitudinal Cracking

The following guidelines are recommended for the inspection of adjacent prestressed concrete non-composite box-girder bridges. The procedure requires that each beam member be evaluated for the presence of longitudinal cracking, spalled sections, exposed strands, and deteriorated concrete. The damage conditions shall be recorded to scale for each member.

For the purpose of load rating all damage within a region of two development lengths shall be considered to occur at the same section. The computed development length can be used; however, if design information is unavailable the following lengths can be used for typical seven wire strands:

Strand Nominal Diameter [in.]	3/8	7/16	1/2	½ Special
Inspection Window Length [in.]	128	150	170	180

The location of the reduced section strength shall be assumed to occur at the center of the inspection window. The strength reductions shall be based on the presence of longitudinal cracking and deteriorated concrete as noted in the following section.

For Specimens with Longitudinal Cracking

1. The following strand areas shall be reduced to 75% of the original cross-sectional area for capacity calculations:
 - a. Strands on each level directly in line the crack.
 - b. Strands closest to the exterior surface adjacent to and within 3 in. from the longitudinal crack.
2. For beams with longitudinal cracking or corrosion induced spalling, all other strands in the section shall be reduced to 95% of the original cross-sectional area for capacity calculations.

For Specimens with Deteriorated Concrete

(Adopted from "Guidelines for Estimating Strand Loss in Structural Analysis of PPC Deck Beam Bridges" by the Illinois Department of Transportation)

1. For exposed strands observed with sound concrete adjacent to and above the exposed strands, disregard the full strength of the exposed strands for capacity calculations.

Figure A-6. Proposed Rating Recommendation for Prestressed Adjacent Box-Girder Bridges with Longitudinal Cracking by Naito et al. (2010)

2. For exposed strands observed with adjacent unsound concrete, disregard the full strength of the exposed strands and all strands in regions of unsound concrete for capacity calculations.
3. For exposed shear reinforcement bars, disregard the full strength of strands located in the lower row directly above the exposed section of stirrups for capacity calculations. If the concrete is found to be unsound adjacent to the exposed area, disregard the strength of all strands in all rows above the area of unsound concrete in capacity calculations.
4. For area of concrete where delaminations have been observed, remove all delaminated concrete to determine the depth of the concrete deterioration:
 - a. If shear reinforcement bars or strands are exposed, treat as in cases “1” through “3” as shown above.
 - b. If no shear reinforcement bars or strands are exposed but there are indications that the exposed concrete is unsound within the affected area, disregard the strength of all strands located in the rows of strands above the area for capacity calculations.
 - c. If no steel reinforcement is exposed in the affected area and the concrete is deemed as sound, do not disregard the strength of strands in the strength analysis.
5. For wet or stained areas of concrete observed on the bottom or side of beams, closely inspect those areas to determine the soundness of the concrete:
 - a. If close inspection indicates that the concrete is unsound or delaminated, treat as in case “4” above.
 - b. If close inspection confirms that the concrete is sound, do not disregard the strength of strands in the strength analysis.

Figure A-7. Proposed Rating Recommendation for Prestressed Adjacent Box-Girder Bridges with Longitudinal Cracking by Naito et al. (2010) (continued)

A1.5. Modified method to predict the residual flexural capacity in corrosion damaged PC I-girders by Alfailakawi et al. (2020)

- *For Regions of Beams With Longitudinal Cracking:* A given strand's original cross-sectional area should be reduced as follows:
 1. By 40%, for strands directly in line of the crack (Figure 94).
 2. By 20%, for strands within concrete cover distance to the exterior surface adjacent to the longitudinal crack (Figure 94).

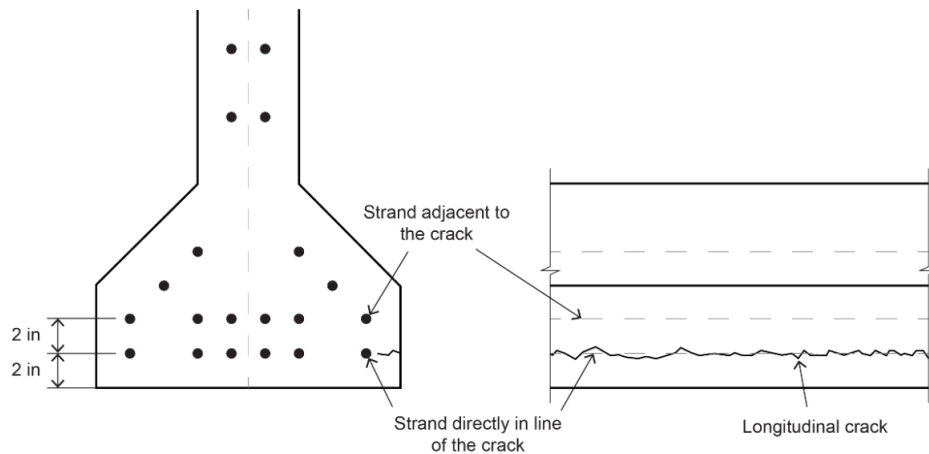


Figure 94. Cross-section and elevation view for I-Beam

- *For Regions of Beams With Delaminations:* All strands in the delaminated area should be reduced to 80% of the original cross-sectional area for capacity calculation. Since most delaminations originate at the layer of strands closest to the surface, it can be assumed that only this layer of strands is within the delaminated area.
- *For Regions of Beams With Spalled Area:* If the spalled section does not include exposed strands, no reduction should be used. If it contains exposed strands, the following should be used:
 1. If the condition of the exposed strands is heavily corroded or cut, disregard the full strength of the exposed strand.
 2. If the condition of the exposed strands is moderate, a reduction of 80% of the original cross-sectional area of the exposed strand shall be considered in the capacity calculation.
- *For Regions of Beams With Patched Area:* A reduction to 10% of the original cross-sectional area is recommended for all the strands in the patched area.

Figure A-8. Proposed modified method by Alfailakawi et al. (2020)

Appendix B: Survey of regional bridge engineers and fabricators

Survey of Regional Bridge Engineers

We are in the process of identifying PC-I and PC box-beams with longitudinal and end cracking similar to what is shown in the following figures. The objective is to identify the bridges with deteriorated girders, potentially due to alkali-aggregate reactivity (AAR) including alkali-silica reactivity (ASR). This survey is conducted as a part of the MDOT-Sponsored Research Project OR19-017: Concrete Deterioration of Prestressed Bridge Beams. Your response to the following questionnaire is greatly appreciated.



a) PC-I girder cracking



b) PC box beam cracking



c) Beam end cracking

1. Do you have bridges with distress similar to what is shown in the above figures? If yes, please list Bridge IDs.

2. If you answered YES to Question 1, are any of those bridges scheduled for replacement of girder, superstructure, or the bridge? If yes, please list Bridge IDs and the scheduled dates.

3. Do you have bridges that have been positively identified as having girder distress due to AAR/ASR? If yes, please list Bridge IDs, facility carried, and feature intersected.

4. Do you have any bridges with repaired girders primarily due to longitudinal cracking and/or confirmed/potential AAR/ASR? If yes, please list Bridge IDs and type of repair.

5. For the purpose of identifying PC girder fabricators, do you have access to construction records of bridges that you have listed above?

6. Please provide any additional comments that may be helpful for achieving the survey/project objectives.

Survey of Fabrication Inspectors

The objectives of the survey are to:

1. document different crack types and their locations observed on PC I, bulb-tee, and box girders during fabrication and bunkering at the plant
2. document girder casting sequence and challenges
3. document exposure conditions during fabrication and curing
4. identify the causes and development stages of girder cracking
5. document distress (cracking) mitigation strategies implemented during and after fabrication, but before shipping
6. document girder repair strategies implemented at the plant to extend the service life of such girders.

This survey is conducted as a part of the MDOT-Sponsored Research Project OR19-017: Concrete Deterioration of Prestressed Bridge Beams. A few example cracks documented at precast plants are shown in the next page as references. Your response to the questionnaire is greatly appreciated.

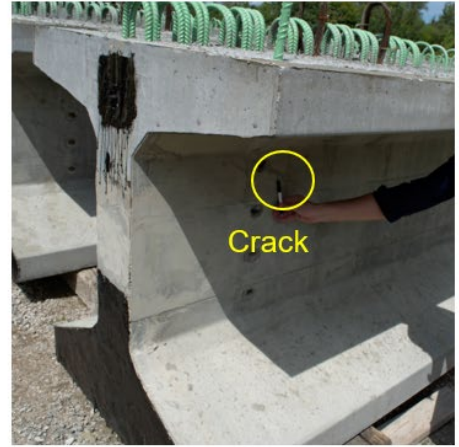
Name, position, contact information, and participant's years of service at this or a related position:

(Note: We will NOT publish or share your contact information. Such information will ONLY be used for contacting you to get additional information or clarifications to the information provided as a response to the survey).

Cracks at girder ends



Cross-section of a bulb-tee girder with harped strands



Isometric view showing a diagonal crack on the web



Close-up views of the diagonal crack

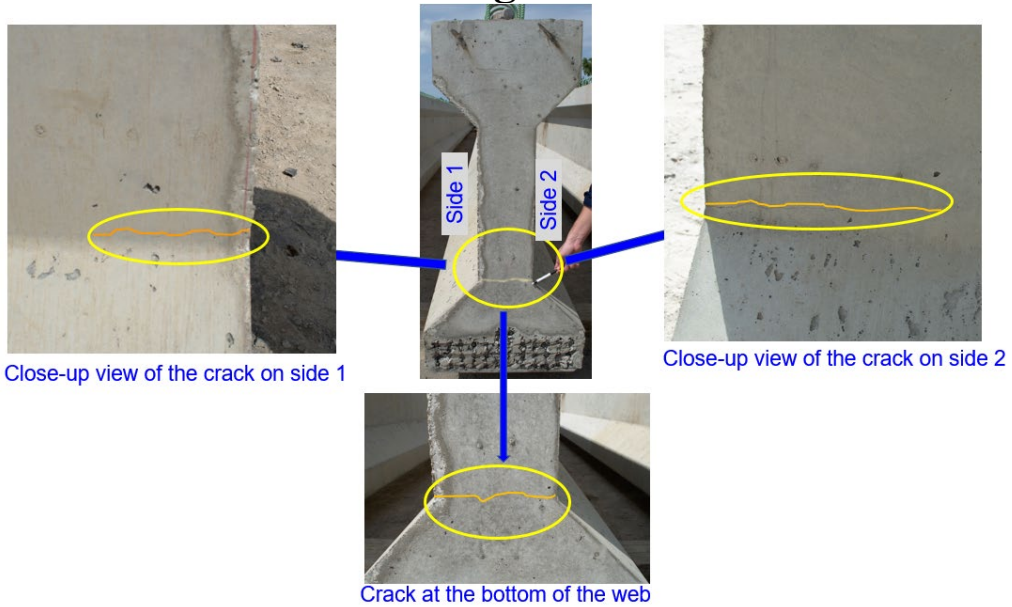


Cross-section of a bulb-tee girder



Close-up views of the crack with efflorescence at the bottom of the web

Cracks at girder ends



Cracks documented on rejected girders sitting at a plant



Bulb-tee section



Longitudinal crack at the top of the web



Map cracking on web

1. Please use a \surd mark to indicate the crack type and location observed on PC girder types listed in the table. Please use ST and SH to indicate the time of cracking. ST – just after stripping; SH – just before shipping

Crack type	PC girder type			Crack location						
	I	Bulb T	Box	Along the girder length		Along the girder height				
				Within 5 ft from the end	Along the length	Top flange	Top of the web	Web	Bottom of the web	Bottom flange
Horizontal /Longitudinal										
Vertical										
Diagonal										
Map										

Additional comments: *(this can include observation of specific cracking, time of cracking, location of cracks, etc.)*

2. Please list the typical repair methods and materials used when

(a) the crack size is < 0.006 in. and located at the end

(b) the crack size is < 0.006 in. and located within the span

(c) the crack size is ≥ 0.006 in. and located at the end

(d) the crack size is ≥ 0.006 in. and located within the span

3. Have you observed any influence of concrete mix ingredients on early age cracking?

If “Yes”, please describe the observations and required corrective actions. Any comparison of mixes used in the 1980s and 1990s with the current mixes is greatly appreciated.

4. Have you observed any influence of fabrication practices on early age cracking?
If “Yes”, please describe the observations and implemented/possible corrective actions.

5. Please sketch and show the typical casting sequence of I and box girders (*you may provide supplemental documents, as needed*)

6. Please sketch and show the typical strand releasing sequence on specific girder types (*you may provide supplemental documents, as needed*).

7. What is the typical range of curing temperatures that you have measured at the plants?

8. Are the girders fabricated under controlled exposure conditions or outdoors?

9. Are the girders stored under controlled exposure conditions or outdoors until they are shipped?

10. What are the typical w/c material ratios used for girder fabrication? Any comparison of mixes used in the 1980s and 1990s with the current mixes is greatly appreciated.

11. Please describe the historical changes that were implemented to mitigate girder cracking at the plants and the observed performance improvements. *If needed, please provide copies of relevant guides/plans/specifications.*

12. Please list any additional comments/observations.

1. Please use a \checkmark mark to indicate the crack type and location observed on PC girder types listed in the table. Please use ST and SH to indicate the time of cracking. ST – just after stripping; SH – just before shipping

Response 1:

Crack type	PC girder type			Crack location						
	I	Bulb T	Box	Along the girder length		Along the girder height				
				Within 5 ft from the end	Along the length	Top flange	Top of the web	Web	Bottom of the web	Bottom flange
Horizontal /Longitudinal		\checkmark		ST/SH					ST/SH	
Vertical		\checkmark		ST						
Diagonal										
Map										

Response 2:

Crack type	PC girder type			Crack location						
	I	Bulb T	Box	Along the girder length		Along the girder height				
				Within 5 ft from the end	Along the length	Top flange	Top of the web	Web	Bottom of the web	Bottom flange
Horizontal /Longitudinal	\checkmark	\checkmark					ST , SH		ST, SH	
Vertical										
Diagonal										
Map										

Response 3:

Crack type	PC girder type			Crack location						
	I	Bulb T	Box	Along the girder length		Along the girder height				
				Within 5 ft from the end	Along the length	Top flange	Top of the web	Web	Bottom of the web	Bottom flange
Horizontal /Longitudinal	ST	ST	ST	ST			ST	ST	ST	
Vertical	ST	ST			ST			ST		ST
Diagonal	ST	ST	ST	ST				ST	ST	
Map										

Response 4:

Crack type	PC girder type			Crack location						
	I	Bulb T	Box	Along the girder length		Along the girder height				
				Within 5 ft from the end	Along the length	Top flange	Top of the web	Web	Bottom of the web	Bottom flange
Horizontal /Longitudinal	√	√					√	√	√	
Vertical		√			√*					
Diagonal	√	√					√	√	√	
Map										

** Vertical along length of larger beams seen before detentioning.*

Response 5:

Crack type	PC girder type			Crack location							
	I	Bulb T	Box	Along the girder length		Along the girder height					
				Within 5 ft from the end	Along the length	Top flange	Top of the web	Web	Bottom of the web	Bottom flange	
Horizontal /Longitudinal	ST/SH	ST/SH	ST/SH	√							
Vertical	ST/SH	ST/SH	ST/SH	√	√	√	√	√			
Diagonal	ST/SH	ST/SH		√							
Map											

2. Please list the typical repair methods and material used when

(a) the crack size is < 0.006 in. and located at the end

Response 1: *N/A*

Response 2: *N/A*

Response 3: *None*

Response 4: *No repair*

Response 5: *As per PCI no repair is necessary for this type of crack size*

(b) the crack size is < 0.006 in. and located within the span

Response 1: *As far as I know we have not had any cracks within the span*

Response 2: *N/A*

Response 3: *None*

Response 4: *No repair*

Response 5: *As per PCI no repair is necessary for this type of crack size*

(c) the crack size is ≥ 0.006 in. and located at the end

Response 1:

Crack injection of qualified product listed in MDOT's Material Source Guide, following MDOT's current Standard Specifications for Construction (speck book), 712.03.U (I have attached a repair plan we've put together for the fabricators to follow).

Response 2: *Epoxy injection*

Response 3: *Crack injection using approved epoxy injection material found on MDOT's QPL (Qualified Products List), or possibly application of a healer sealer.*

QUALIFIED PRODUCTS LIST (QPL)		
Spec. # and Material Name	Product Name	Manufacturers or Suppliers
914.06 Epoxy Resin Adhesive & Temporary Seal (Crack Injection)	Crackbond LR321	Adhesives Technology Corp.
	Crackbond SLV302	Adhesives Technology Corp.
	Akabond 817	Axson, Eaton Rapids, MI (formerly Akemi Corp.)
	Akabond 818	Axson, Eaton Rapids, MI (formerly Akemi Corp.)
	Akabond 819	Axson, Eaton Rapids, MI (formerly Akemi Corp.)
	MasterInject 1380	BASF Construction Chemical, Shakopee, MN
	MBT P&R Concsive 1360	BASF Construction Chemical, Shakopee, MN
	BHS-1617	Blackhawk Sales Co, Inc., Rock Island, IL
	BHS-1618	Blackhawk Sales Co, Inc., Rock Island, IL
	BHS-1619	Blackhawk Sales Co, Inc., Rock Island, IL
	Arndite 8560	Ciba Corporation, East Lansing, MI
	EP-SLV	E-Chem, LLC
	True Grip 150	J. Dedoes, Inc., Milford, MI
	NIP124LV	Epoxy Unlimited, Harrison Twp, MI
	CI 060	Hilti Inc., Columbus, OH
	Dynapoxy EP-450	Pecora Corporation
E Bond 550	Ridgemoor Supply, Kentwood, MI	
Sikadur 35, Hi-Mod LV	Sika Corporation, Lyndhurst, NJ	
Sikadur 52	Sika Corporation, Lyndhurst, NJ	
Pro Poxxy 50 Super LV	Unitex, Kansas City, MO	

Response 4: *Crack injection QPL*

Response 5: *We epoxy inject the beam with Sikadur 52 and 31*

(d) the crack size is ≥ 0.006 in. and located within the span

Response 1:

As far as I know, we have not had any cracks within the span, and if we did we would have it crack injected per 712.03.U of MDOT's spec book.

Response 2: *N/A*

Response 3: *Crack injection using approved epoxy injection material found on MDOT's QPL (Qualified Products List).*

Response 4: *Crack injection QPL*

Response 5: *We epoxy inject the beam with Sikadur 52 and 31*

3. Have you observed any influence of concrete mix ingredients on early age cracking?

If "Yes", please describe the observations and required corrective actions. Any comparison of mixes used in the 1980s and 1990s with the current mixes is greatly appreciated.

Response 1: *No*

Response 2: *No*

Response 3: *No, I have not observed a difference through the years based on mix designs.*

Response 4: *No*

Response 5: *No*

4. Have you observed any influence of fabrication practices on early age cracking?
If “Yes”, please describe the observations and implemented/possible corrective actions.

Response 1: *No*

Response 1: *No*

Response 3:

- *Seems like the more draped strand the higher probability of horizontal cracking in the web of I-beams / bulb-tee beams.*
- *Cracks are also caused by inserts or items like that bolted to the side forms and when the beams cure and shorten cracking is typical extending from that location to the end of the beam if they are fairly close to the end of the beam.*
- *Diagonal cracking from the corners of pavement seats is somewhat common in box beams.*

Response 4: *NR*

Response 5: *No, we have not. As discussed in the office we had tried many ways to avoid cracking in the beams. From adding additional rebar to changing detensioning sequences. Nothing proved successful.*

5. Please sketch and show the typical casting sequence of I and box girders (*you may provide supplemental documents, as needed*)

Response 1:

Typically bottom flange, then web, then top flange

Response 2:

1. *Fabricator starts pouring at the end closes to bunker. And pours the bottom flange all the way down the beam.*
2. *Then the web is poured all the way down. With crew members stinging along the way and as well as external vibrators being used to help consolidate the bottom flange and web.*
3. *A final pass is made to fill the top flange, crew members sting the upper flange and into the web. Crew follows the stingers rough up the surface and place deck clips and safety pins.*

Response 3: *NR*

Response 4:

I-Beam: pour in layers. Depending on the fabricator, 2 or 3 layers

Box Beam: pour bottom layer, add foam voids, add top cage, pour top of beam

Response 5: *NR*

6. Please sketch and show the typical strand releasing sequence on specific girder types (you may provide supplemental documents, as needed).

Response 1:

Detensioning varies with fabricator.

All detensioning is done from the top to bottom

Not sure of Spancrete in Wisconsin, but Peninsula Prestress and Mack-Kalamazoo starts from the outside and works inside.

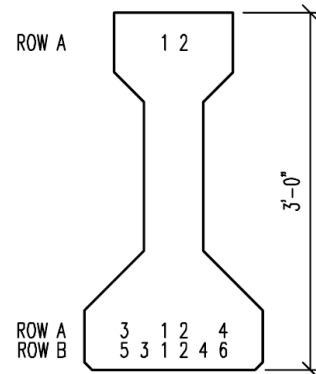
PSI-Decatur starts from the inside and works toward the outside.

Response 2:

The strand release pattern is for a crew member to stand at each beam end and cut the strand from the middle out alternating left to right to equally disperse the tension being released from the strand to the beam.

Response 3:

Typical strand releasing sequence would be the draped strands (or any strands in top flange) first if applicable. Detensioning would then proceed to the uppermost row starting at the middle (from the side) and working side to side symmetrically outward. The same thing would occur with the next row down and continue in the same fashion. Some fabricators may start at the outside of each row and detension working symmetrically inward.



DETENSIONING NOTES

1. ALL DIMENSIONS ARE CASTING DIMENSIONS AND ARE MEASURED ALONG THE SOFFIT AT THE CENTERLINE OF THE BEAM.
2. STRAND DETENSIONING STARTS WITH ROW A THEN B AND SO ON. DETENSION TOTAL ROW IN SEQUENCE BEFORE MOVING TO NEXT ROW.
3. ALL STRANDS ARE PARALLEL.

DETENSIONING DETAIL

Response 4: *Detentioning starts at the top middle and work your way outwards and down*

Response 5: *All of our strand releasing is the same. We begin with the top row and proceed from the outside to inside alternating left to right.*

7. What is the typical range of curing temperatures that you have measured at the plants?

Response 1: *We make sure the concrete temperatures do not exceed 150 degrees F.*

Response 2: *I have observed temperature ranges from 120 to 150 degrees.*

Response 3: *MDOT's maximum curing temperature is 150 degrees Fahrenheit. Typically, from 100 degrees to 140 degrees. I have seen as high as 170 degrees Fahrenheit approximately.*

Response 4: *80 degrees to 140 degrees*

Response 5: *From 90 to 145 degrees*

8. Are the girders fabricated under controlled exposure conditions or outdoors?

Response 1:

All are fabricated outdoors, but PSI-Decatur has beam beds in a building that they are working on closing off to work through the winter.

Response 2:

The 3 places I have been most were poured outside with no cover over the bed.

Response 3: *Typically, the girders are cast outdoors. Some could have a building for cover however the temperature would be basically the same as outside.*

Response 4: *Both*

Response 5: *Outdoors.*

9. Are the girders stored under controlled exposure conditions or outdoors until they are shipped?

Response 1: *All girders, from all fabrication facilities, are stored outdoors until they are shipped.*

Response 2: *Girders are stored outside until they are shipped*

Response 3: *All beams are stored outdoors until shipment that I have ever seen in 25 years.*

Response 4: *Outdoors*

Response 5: *Outdoors.*

10. What are the typical w/c material ratios used for girder fabrication? Any comparison of mixes used in the 1980s and 1990s with the current mixes is greatly appreciated.

Response 1: *I don't know*

Response 2: *Most w/c ratios that I have seen are .33 to .36 on average.*

Response 3: *Approximately 0.35. I would not know what the w/c ratios typically were earlier.*

Response 4: *Around 0.32*

Response 5: *Our water cement ratios range from a .32 to .35*

11. Please describe the historical changes that were implemented to mitigate girder cracking at the plants and the observed performance improvements. *If needed, please provide copies of relevant guides/plans/specifications.*

Response 1: *NR*

Response 2: *N/A*

Response 3: *I honestly have not seen many historical changes to address cracking issues. I would think that strand debonding attempts to address cracking. MDOT has changed from the use of split sheath debonding to rigid debonding. Requiring sole plates at the ends of beams has reduced cracking/spalling at the ends of beams when beams are detensioned and they camber on the casting bed.*

Response 4: *NR*

Response 5: *As discussed in the office we had tried many ways to avoid cracking in the beams. From adding additional rebar to changing detensioning sequences. Nothing proved successful.*

12. Please list any additional comments/observations.

Response 1: *NR*

Response 2: *NR*

Response 3: *NR*

Response 4: *NR*

Response 5: *As part of the PCI conventions we had plant tours throughout the United States. One very common denominator was the cracks we observed in several I beams and bulb tees. Apparently, this must be a common issue that has yet to be corrected by changing production practices.*

Appendix C: Causal Evaluation of Concrete Deterioration in the Kalamazoo River Bridge Beams

OVERVIEW

The three-span, PSC I-beam bridge (S.N. 143) that carries US-131 SB over the Kalamazoo River is located in Allegan County, Michigan (Figure C-1a). The bridge width is 59.2 ft and the total length is 400 ft. The bridge was built in 1996. Each span consists of nine I-beams. The latest inspection reported having superficial map cracking and longitudinal cracking along the entire length of the fascia beams. The longitudinal cracks are on the top of the bottom flange along with scattered horizontal cracks on the outside of the bottom flange. Most of the cracks were epoxy injected and repaired (Figure C-1b). Even though the fascias were surface coated in 2013, the paint has cracked and peeled, exposing the cracks in the beams (Figure C-1c and d).



(a) General view of the bridge



(b) Epoxy injected and repaired cracks



(c) Exposed cracks on top of the bottom flange



(d) Surface coating on the interior surface of the fascia

Figure C-1. The Kalamazoo River bridge fascia beam and surface coating condition

INVESTIGATION OF THE CAUSES OF DETERIORATION

A piece of concrete was collected from the south end of the east fascia beam (Figure C-2) and used for petrography, SEM-EDS analysis, along with a uranyl acetate ASR screening test to determine the causes of deterioration.

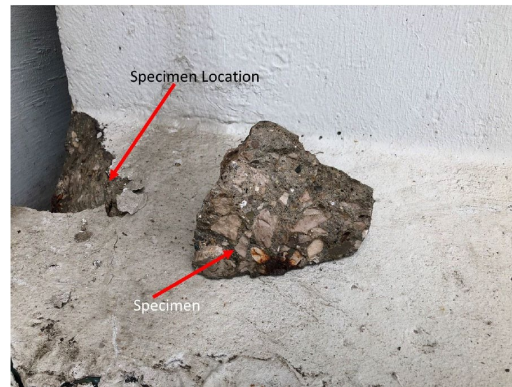


Figure C-2. The piece of concrete removed from the east fascia beam

Petrographic Examination

A slice of the concrete piece shown in Figure C-2 was used for petrographic examination. The condition of the specimen was documented as shown in Figure C-3. One of the sharp edges of the fragment exhibits small dark brown ferruginous deposits believed to be the remnants of corroded steel. Observation of the polished surface indicated no large visible cracks, although close examination found some minor microcracking in the concrete adjacent to the corrosion deposits and shallow microcracks extending inward along the flat, formed, and painted side of the specimen (Figure C-4). The cracks that extend inwards from the surface indicate the presence of deterioration mechanisms other than ASR. Red arrows show a few fine cracks discolored by paste carbonation. The circled edge has brown corrosion products.

The coarse aggregate consists of crushed carbonate rock, mostly limestone and dolomitic limestone. Pieces of the crushed rock are predominantly angular, moderately hard, and apparently sound. Coarse aggregate is uniformly distributed in the concrete specimen. The fine aggregate is natural sand of mixed lithology, with grains composed mainly of quartz, quartzite, and carbonate rocks; with lesser amounts of feldspar, arenaceous rocks (sandstone and greywacke), chert and chalcedonic chert, a variety of siliceous igneous rocks, shale, along with other rocks and minerals. Most grains are rounded to sub-angular, moderately hard to hard (excluding softer grains of shale), and uniformly distributed in the concrete.

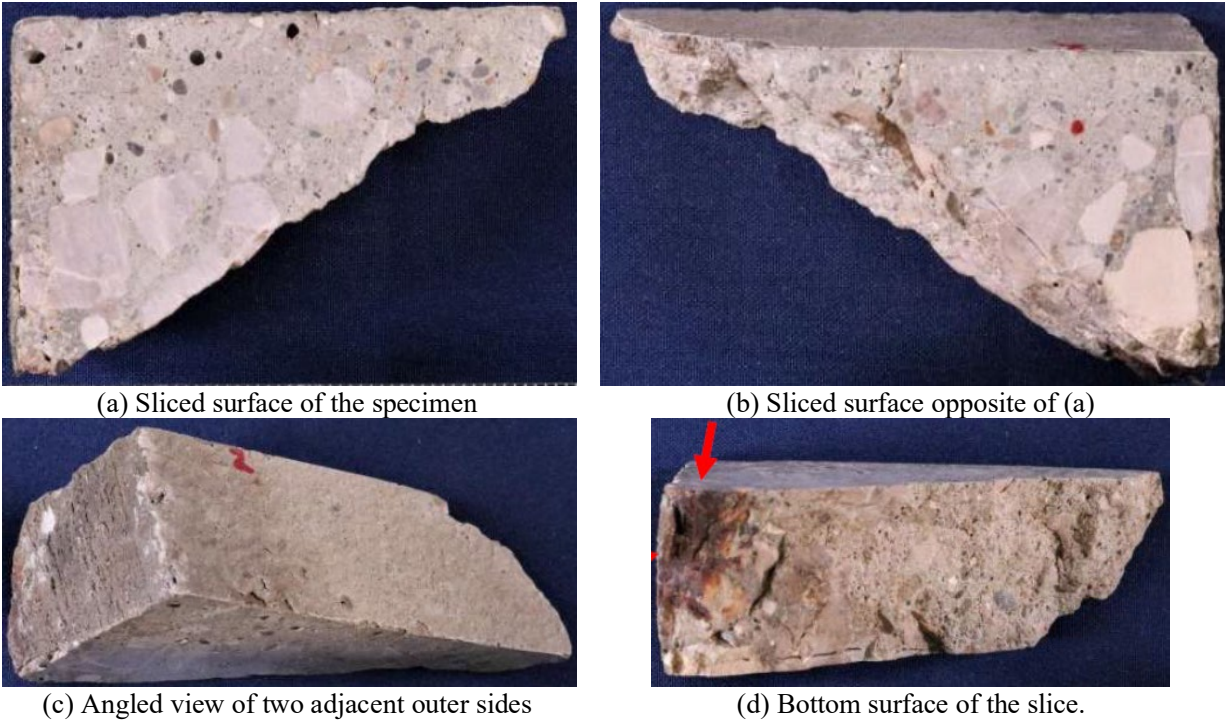


Figure C-3. A sliced section of the specimen used for petrographic examination
 (Red arrow indicates apparent remnants of corrosion product from an embedded steel).

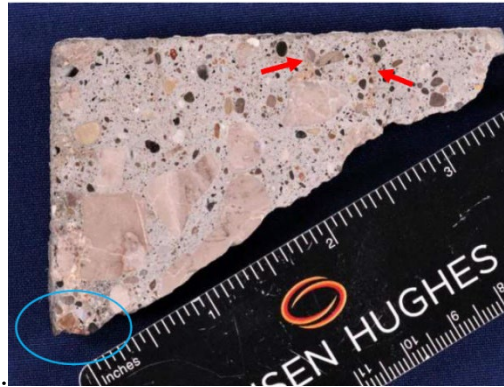
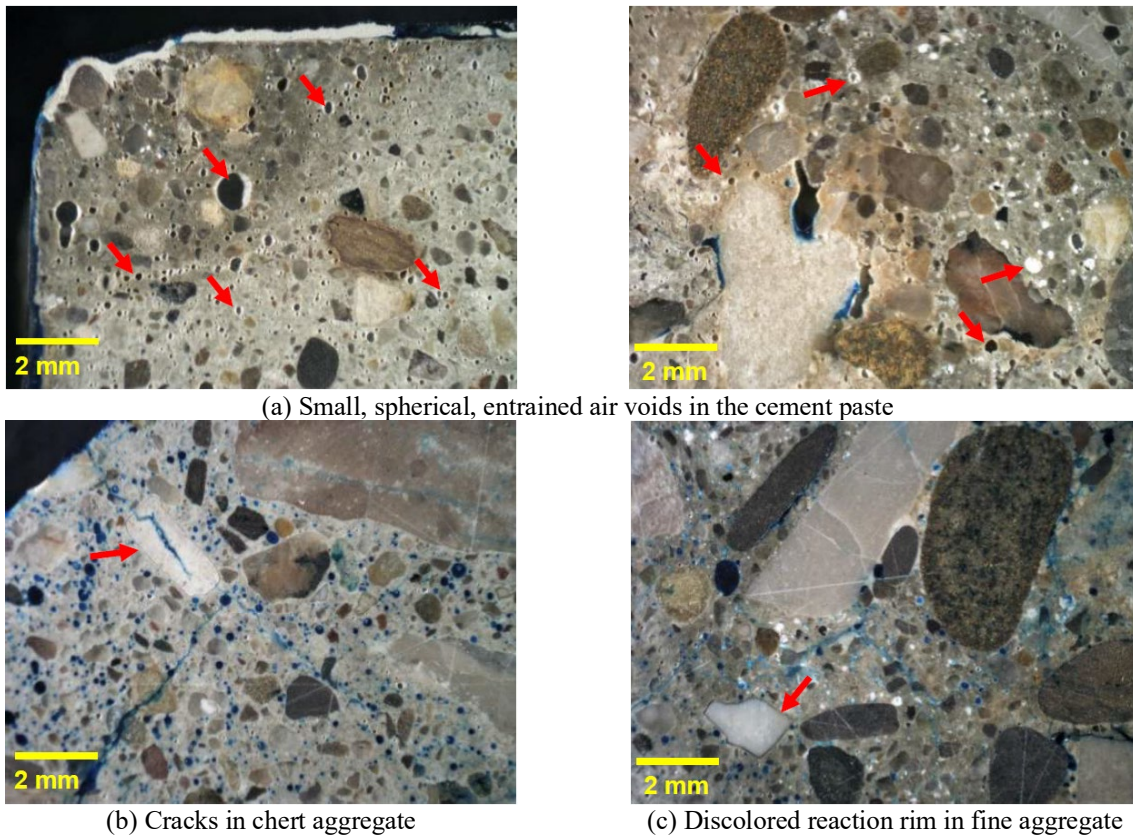


Figure C-4. Polished cross-section of the specimen

The concrete is air-entrained. Figure C-5a shows small, spherical voids in the cement paste. Air content is estimated in the range of 4 to 6% by volume of concrete and is well distributed in the concrete showing an abundance of small, spherical, entrained air voids in the cement paste. Further, the microscopic examination also revealed the presence of white secondary deposits in some of voids and microcracks in the concrete, primarily along the near-surface region and in proximity to the corrosion deposits, as shown in Figure C-5. These deposits include some ettringite, but other compounds are also present that were not identified. The amounts and pattern

of occurrence of these secondary deposits are generally not indicative of a deleterious, expansive reaction and are likely innocuous and void-filling in nature.

Some minor microcracking is also noted in a few fine aggregate grains of chert present in the concrete. Figure C-5 shows the magnified views of two areas of the polished cross-section of the specimen. The red arrow in Figure C-5b indicates a cracked chert aggregate particle while the red arrow in Figure C-5c shows a discolored reaction rim developed around a chert aggregate. The surface was impregnated with blue-dyed epoxy before final polishing to help show fine cracking. Microscopic examination revealed the spotty occurrences of some ASR gel in and around a few of these damaged chert particles; however, the amount was generally meager and not seen in every cracked chert grain.



(a) Small, spherical, entrained air voids in the cement paste

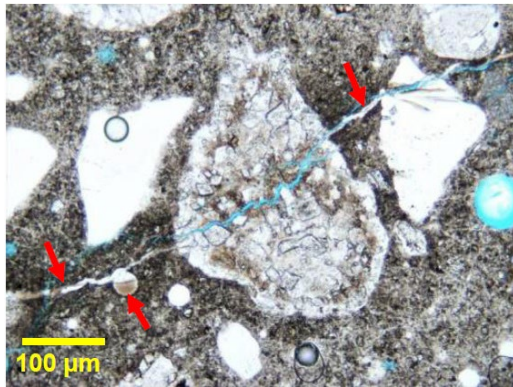
(b) Cracks in chert aggregate

(c) Discolored reaction rim in fine aggregate

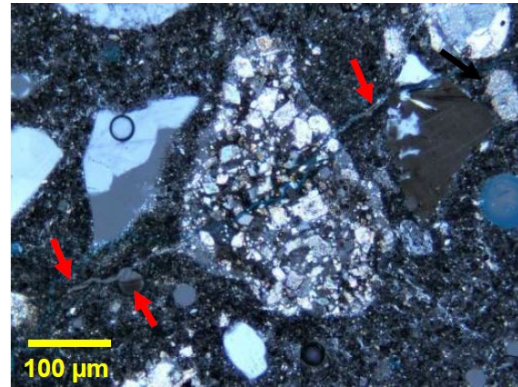
Figure C-5. 10X Magnified views of a polished cross-section of the specimen

As shown in Figure C-6, petrographic examination revealed some ASR-damaged chert grains. Due to the small size of the specimen, only a few ASR-damaged aggregate particles were found, and the severity of ASR could not be fully assessed. The concrete in this portion of the specimen also exhibits more carbonation than seen elsewhere in the specimen. However, no evidence was

observed of ASR affecting or damaging the coarse aggregate used in the concrete or the remaining constituents of the sand.



(a) Image with 200X magnification and plane polarized light.



(b) Image with 200X magnification and partially crossed polarized light.

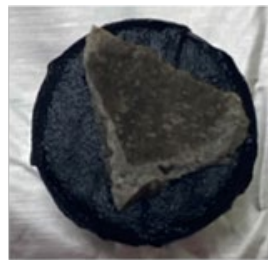
Figure C-6. Thin-section photomicrographs showing microcracks in and extending from a cherty fine aggregate particle.

SEM-EDS Investigation

Two specimens were prepared as shown in FigureC-7.



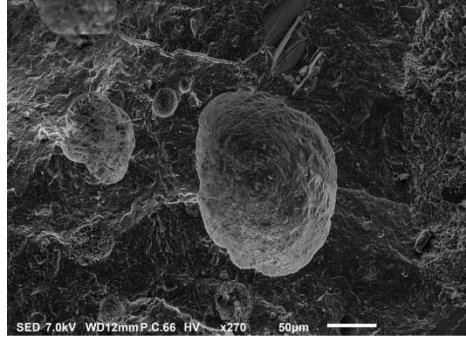
KR-SEM-1



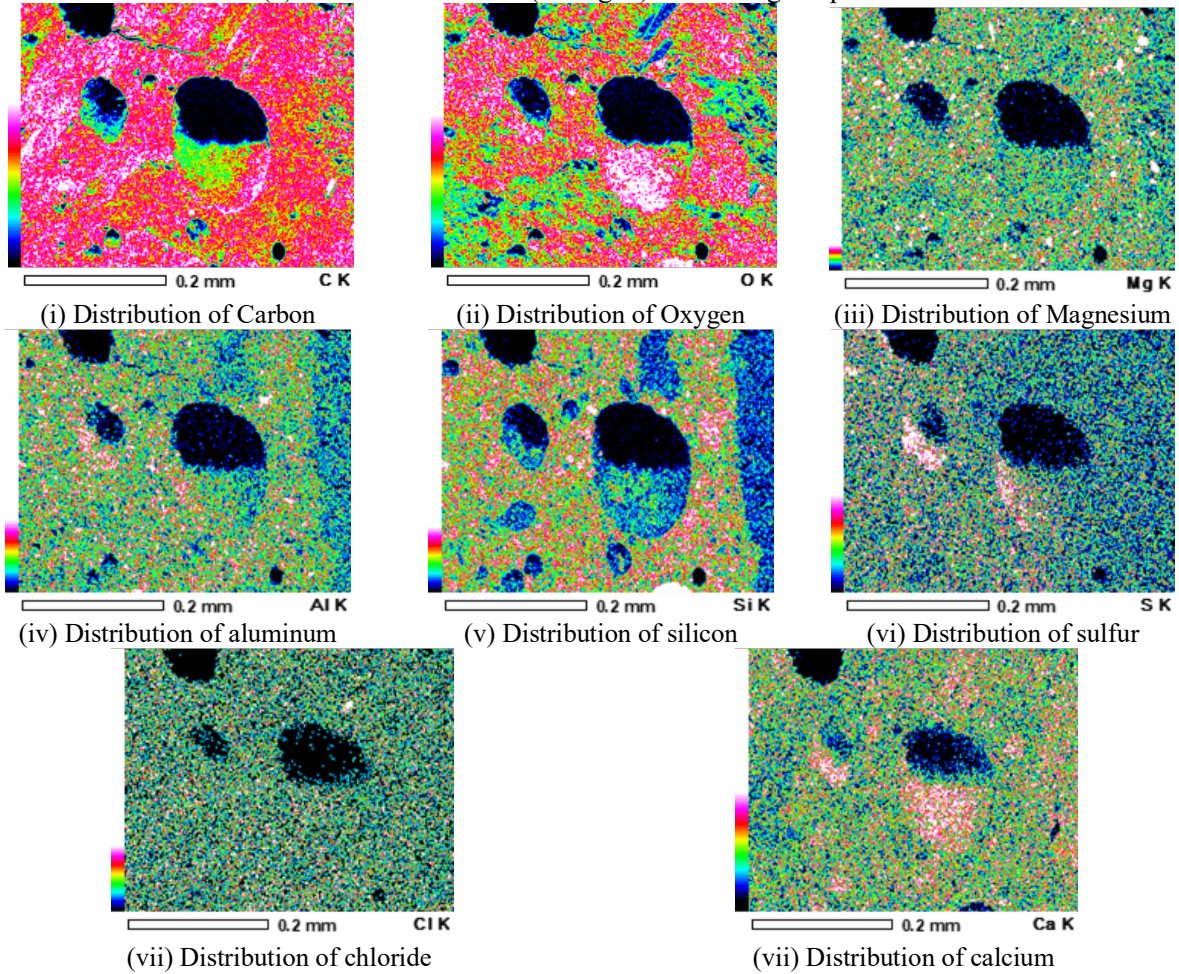
KR-SEM-2

FigureC-7. Specimens for SEM-EDS examination

As shown in Figure C-8a, ettringite is observed in some air voids. This observation supports the findings from thin-section petrography. Aluminum, calcium, oxygen, and sulfur elements are rich in such locations. The distribution of such elements can be mapped using EDS, as shown in Figure C-8b. As an example, the white areas in Figure C-8b represent the distribution of (i) carbon, (ii) oxygen, (iii) magnesium, (iv) aluminum, (v) silicon, (vi) sulfur, (vii) chloride, and (viii) calcium. Fine random cracking is observed; however, no evidence is found regarding ASR-induced cracking or damage in the examined specimen.



(a) The fibrous mineral (ettringite) seen filling the pores.



(b) EDS element mapping

Figure C-8. SEM and EDS analysis of the specimen.

Evaluation of ASR Potential

To verify the presence of ASR, a uranyl acetate screening test was conducted as per the ASTM C856-14 (ASTM 2014) and the results are shown in Figure C-9. The screening test confirms the presence of ASR in fine aggregates.

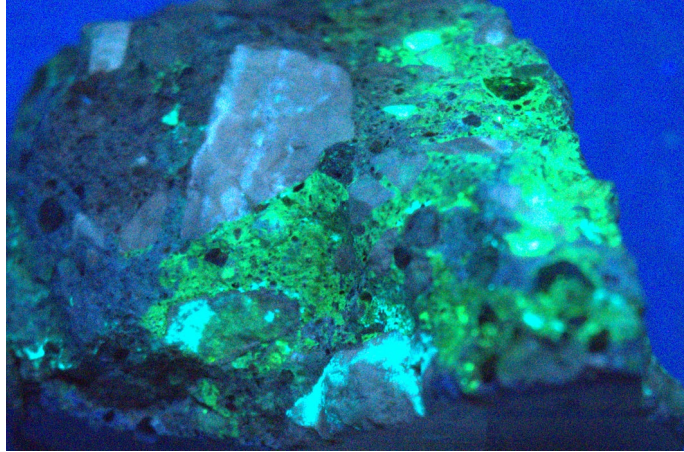


Figure C-9. Screening for ASR using uranyl acetate

SUMMARY

The investigations revealed that the presence of (i) adequate amount of entrained air, (ii) a very small portion of ASR susceptible fine aggregate, (iii) shallow microcracks extending inward along the flat, formed, and painted side of the specimen; and (iv) deterioration mechanisms other than ASR.

Appendix D: Causal Evaluation of Concrete Deterioration in the Brady Street Bridge Beams

OVERVIEW

The bridge (S.N. 12314) that carried Brady Street over the lower branch of the Rouge River was a single span with side-by-side box-beams located in Wayne County, Michigan (Figure D-1a). The bridge width was 57.5 ft with a total length of 100 ft. The bridge was built in 1994. This bridge consisted of a total of 16 single cell, 39 in. deep and 36 in. wide box-beams. Due to significant deteriorations in the beams, this bridge was demolished during the last week of March 2020, after being in service for 26 years. The latest inspection reports indicated typical deteriorations, such as widespread longitudinal cracking at the bottom flange of many beams. These cracks were mostly concentrated towards the north end of the bridge and extended up to 1/4th of the span. In addition to longitudinal cracking, concrete spall, corroded and broken strands, exposed strands, and efflorescence were documented (Figure D-1 b to c).



(a) General view of the bridge



(b) Moist shear keys and longitudinal cracking



(c) A close-up view of a deteriorated beam

Figure D-1 Brady Street bridge location, superstructure cross-section, and typical deteriorations

An inspection of beam soffits at “arm’s length” showed severe deteriorations with significant random cracking towards the north end of the beams. Significant scaling on box beam webs and ends was observed after removing the beams. Such cracking and deterioration, as shown in Figure D-2 and Figure D-3, are atypical to prestressed beams. Therefore, a detailed investigation was

conducted to identify the potential causes of the observed deteriorations, and the findings are summarized.



(a) Severe random cracking at beam soffit at beam end



(b) Close up view random cracking at beam end



(c) Scaling on the web within beam span



(d) Close up view of the scaled area

Figure D-2. Atypical deterioration observed on box beams



Figure D-3. Severely deteriorated beam ends (north end of the bridge)

INVESTIGATION OF THE CAUSES OF DETERIORATION

Specimens collected during bridge demolition were used to prepare concrete prisms and evaluate the potential for having ASR and DEF by exposing them to 1N NaOH at 176° F and lime-saturated water at 73° F, respectively. ASR screening tests were conducted using uranyl acetate as per the ASTM C856-14 (ASTM 2014) procedures. Also, a thin section petrography as well as Scanning Electron Microscopy (SEM) and Energy Dispersive X-ray Spectroscopy (EDS) analyses were conducted. Experimental procedures and findings are described in the subsequent sections.

Evaluation of ASR and DEF Potential using Expansion Testing

According to Thomas et al. (2008), potential residual expansion due to ASR is evaluated by placing concrete prisms in a hot alkaline solution, while the potential expansion due to DEF is evaluated by placing concrete prisms in lime-saturated water at room temperature. Three concrete prisms were prepared from the concrete specimens extracted from the beams during bridge demolition. Due to the challenges during saw cutting, the dimensions of the prisms were slightly different from the standard sizes. Two stainless steel Demec gauge studs were attached to one side of each prism. The distance between the studs was maintained at approximately 8 in. Figure D-4 shows the concrete prisms and the Demec gauges. The specimen labels, dimensions of the prisms, and the exposure conditions are listed in Table D-1. The control specimen (*BS-Control*) was placed under standard laboratory conditions. The *BS-1N NaOH-176* specimen was exposed to 1N NaOH at 176° F after taking the zero reading. The *BS-Lime Saturated-73* specimen was exposed to lime-saturated water at 73° F after taking the zero reading. Both *BS-1N NaOH-176* and *BS-Lime Saturated-73* prisms were initially immersed in lime-saturated water at 73° F for 24 hours before taking the zero readings. The zero reading of the control specimen was recorded at the same time. The subsequent expansion measurements were recorded periodically every 7 days at room temperature by taking three measurements per specimen. Exposure conditions were maintained for 84 days.

Table D-1. Specimen ID, Dimensions, and Exposure Conditions

Specimen ID	Dimensions (in.)	Exposure	
		Medium	Temperature (° F)
BS-1N NaOH-176	9.637 × 2.140 × 2.255	1N NaOH	176
BS-Lime Saturated-73	10.109 × 2.418 × 2.000	Lime saturated water	73
BS-Control	9.438 × 2.123 × 2.210	Standard laboratory conditions	73

Figure D-5 shows the results. The length of the *BS-Control* specimen decreased until 21 days and reached a plateau at -0.008%. The *BS-Lime Saturated-73* specimen shows a slight expansion with a plateau at 0.038%. The *BS-1N NaOH-176* expanded and reached 0.28% in 84 days. Even though the potential for expansion due to DEF is minimum, there is a potential to develop ASR with long-term exposure to necessary conditions. To verify the presence of ASR, a uranyl acetate screening test was conducted as per the ASTM C856-14 (ASTM 2014) and the results are shown in Figure D-6. The screening test confirms the presence of ASR in both specimens due to reactive silica in fine aggregates.

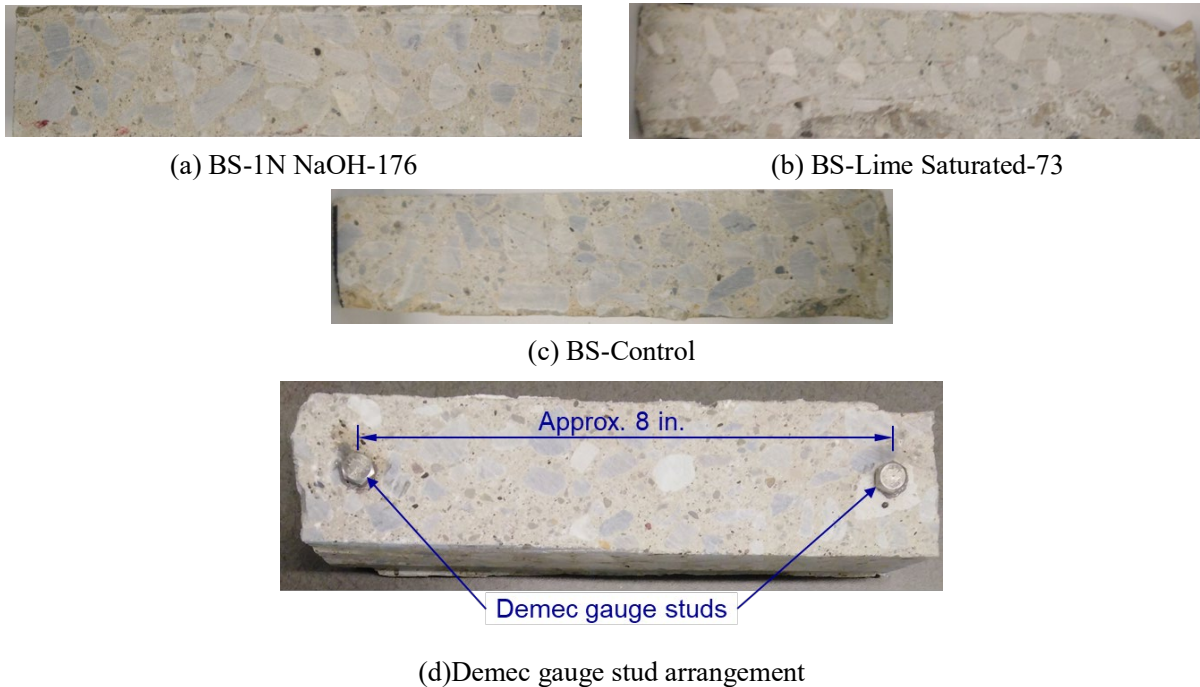


Figure D-4. Concrete prisms and the Demec gauge arrangement

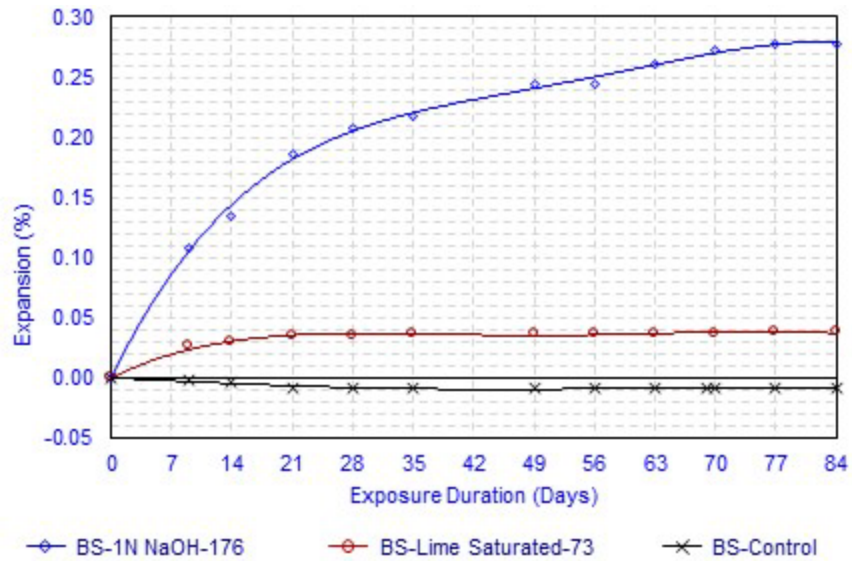
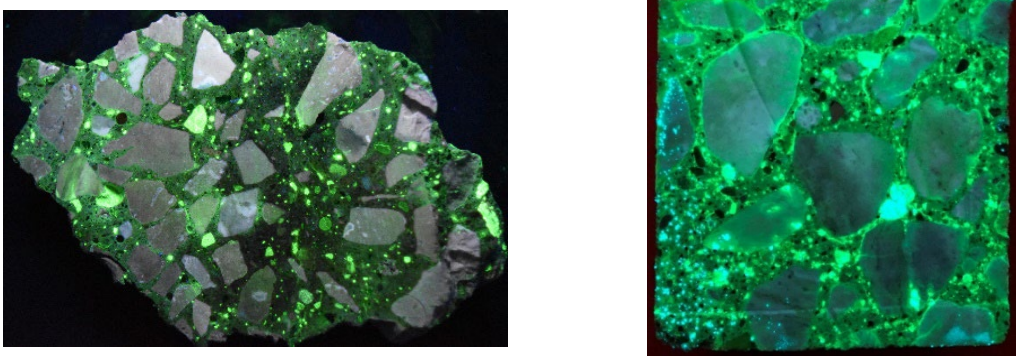


Figure D-5. Expansion of concrete prisms under three different exposure conditions



(a) Specimen extracted from a beam

(b) Specimen extracted from a beam and exposed to 1N NaOH at 176° F for 84 days

Figure D-6. Screening for ASR using uranyl acetate

Petrographic Examination

Figure D-7 shows a large fragment of concrete extracted from a beam to cut into thin sections. The specimen contained a partially embedded segment of 7-wire steel strand and an imprint of a second strand. Two sides of the specimen represent the outside faces of the beam. The remaining sides of the specimen were fractured surfaces that pass mostly through aggregate.

Visual and microscopic examination of saw-cut and polished cross-sections of the specimen revealed finer cracks in the body of the concrete, most oriented rectilinear to the formed outer face (Figure D-8). Yellow arrows show the occurrences and patterns of fine cracking in the concrete. Dashed white lines show the approximate depths of strands.

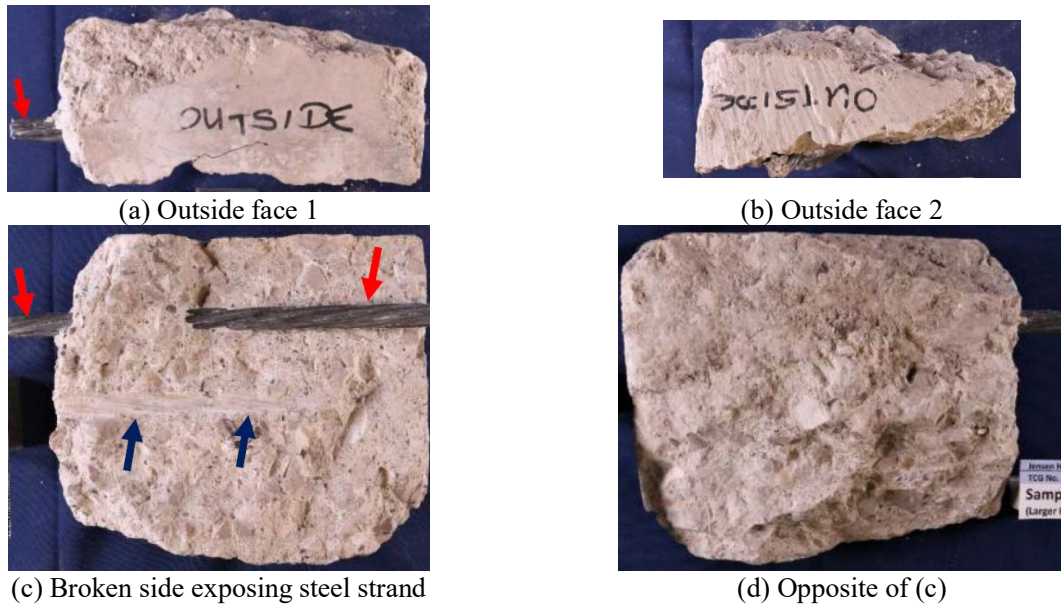


Figure D-7. A specimen extracted from a beam for petrographic examination
 (Red arrows indicate a segment of 7-wire steel strand. Blue arrows indicate an imprint of another strand.)

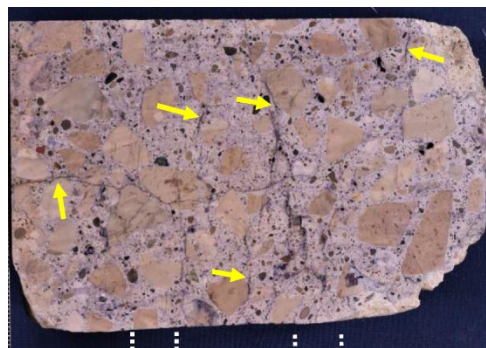


Figure D-8. Polished cross-section of the specimen, with the formed outer side placed to the left

The coarse aggregate used in the concrete consists of crushed carbonate rock, mostly limestone and dolomitic limestone. Pieces of the crushed rock are predominantly angular, moderately hard, and apparently sound. Coarse aggregate is uniformly distributed in the concrete specimen. Fine aggregate used in the concrete is a natural sand of mixed lithology, with grains composed mainly of quartz, quartzite, and carbonate rocks; lesser amounts of feldspar, arenaceous rocks (sandstone and greywacke), chert and chalcedonic chert, a variety of siliceous igneous rocks, shale, and other rocks and minerals are also present. Most grains are rounded to sub-angular, are moderately hard to hard (excluding softer grains of shale), and are uniformly distributed in the concrete.

Figure D-9 shows the magnified views of a polished cross-section of the specimen with a cracked fine (chert) aggregate. ASR gel exuding from one of the microcracks is marked with red arrows. The presence of the gel confirms ASR. Chert is susceptible to both ASR and freeze-thaw damage.

The surface was impregnated with blue-dyed epoxy before the final polishing to highlight fine cracking.

Small, spherical, entrained air voids in the paste are marked with blue arrows. The air content in the concrete is judged below the specified limits and estimated in the range of 2 to 3% by volume of concrete. The observed low air content of the concrete may have been insufficient to provide proper protection of the concrete from freeze-thaw damage in areas that are exposed to moisture saturating conditions during winter months.

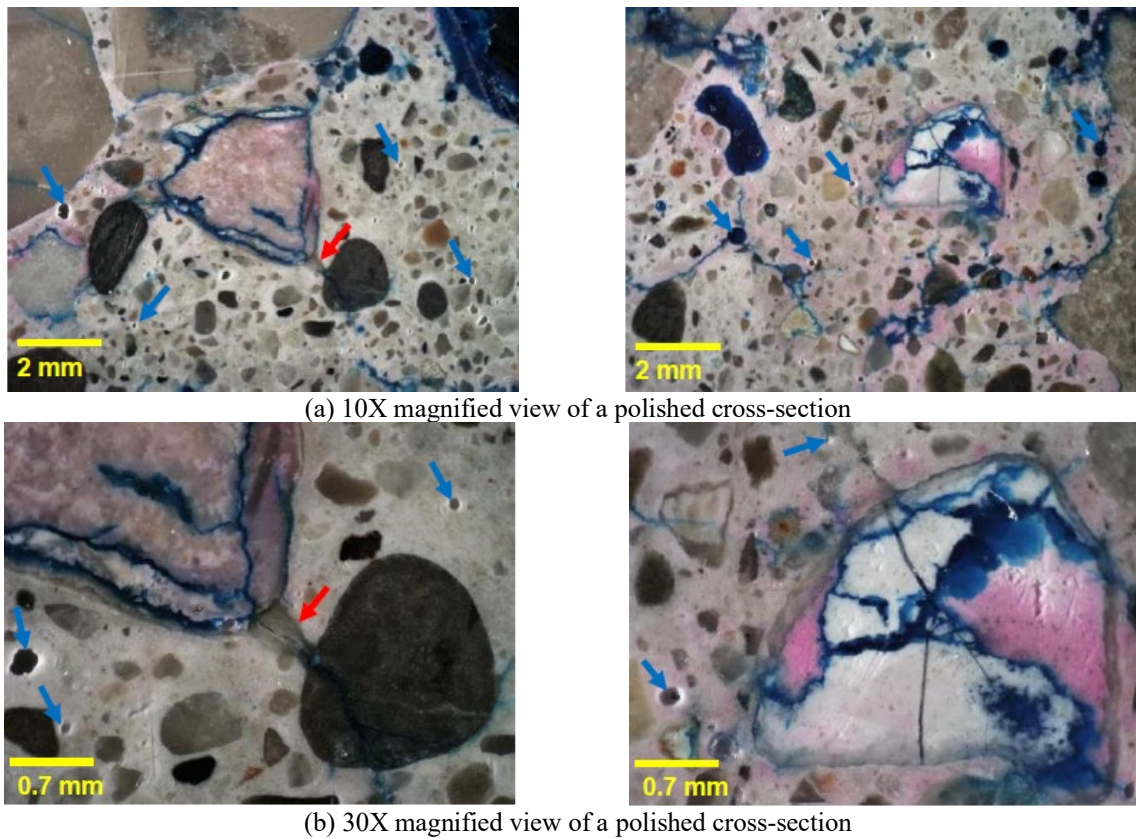


Figure D-9. Magnified views of a polished cross-section of the specimen

Petrographic examination revealed the development of some ASR in the concrete involving a portion of the fine aggregate that appears to have contributed to damage in the concrete. The affected portion of the sand includes mostly chert and chalcedony, with spotty reactions involving shale and quartzite in the concrete sand. Microscopic examination of polished cross-sections and thin sections produced from the concrete revealed the affected grains are internally micro cracked, with many of the microcracks extending into the surrounding concrete. Discolored reaction rims are noted in several of the grains. Isolated occurrences of ASR gel were observed in the concrete,

mainly in the microcracks extending along the periphery of the damaged grains (Figure D-10). No evidence was observed of ASR affecting or damaging the coarse aggregate used in the concrete or the remaining constituents of the sand.

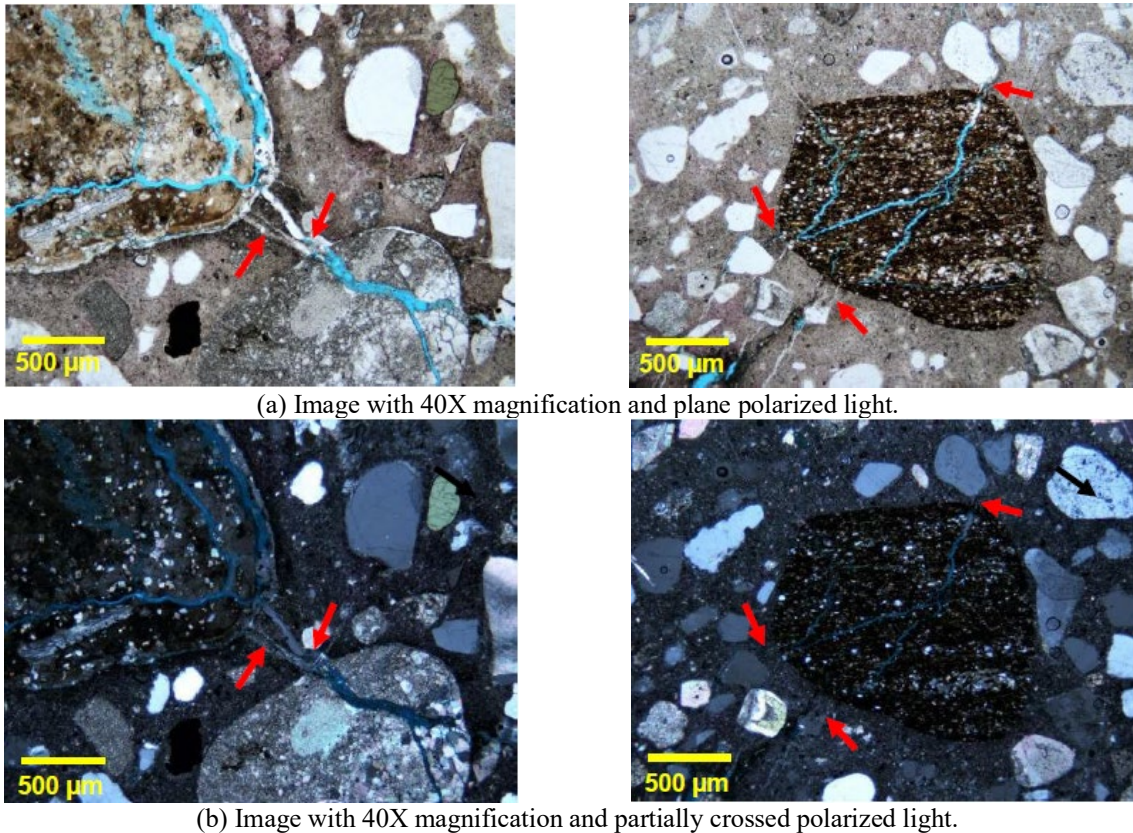
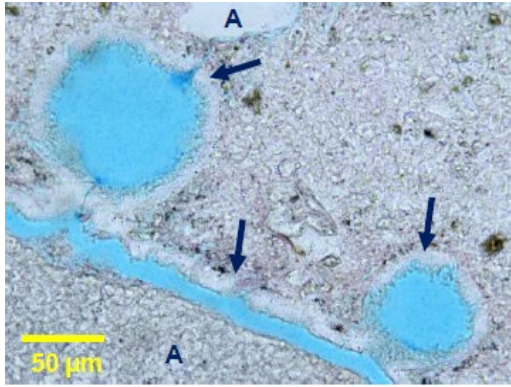
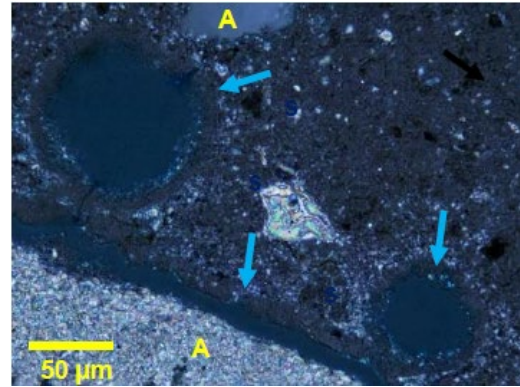


Figure D-10. Thin-section photomicrographs showing microcracks in and extending from a cherty fine aggregate particle.

As shown in Figure D-11, the microscopic examination of the concrete also revealed the presence of secondary deposits of sulfate compounds, primarily ettringite (Calcium sulfoaluminate hydrate), in some of the cracks and voids in the concrete. The amounts of these secondary deposits and patterns of occurrence are generally not indicative of a deleterious, expansive reaction, such as delayed ettringite formation (DEF); therefore, they are likely innocuous and void-filling in nature. The microscopic examination of the hardened paste in this specimen also exhibits evidence of advanced and continued hydration of the cement paste suggesting the concrete was likely exposed to saturating conditions in service. Such conditions could promote the deposits of secondary ettringite and other compounds.



(a) 400X magnification. PPL.



(b) 400X magnification. PXPL.

Figure D-11. Thin-section photomicrographs showing delayed ettringite in voids and a microcrack (Aggregates are marked as “A”).

SEM-EDS Investigation

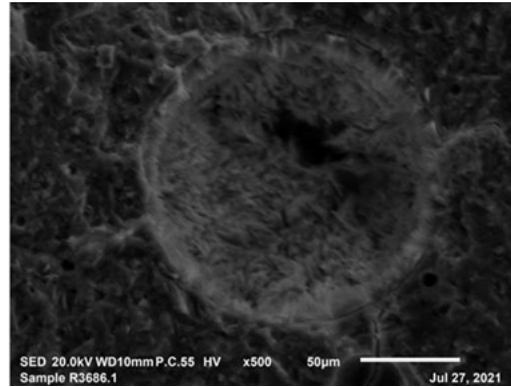
Specimen from Beam Web

As shown in Figure D-12, four specimens were prepared by breaking a large fragment of beam concrete collected from a box beam web area and coated with a thin carbon layer to improve the secondary electron flux.

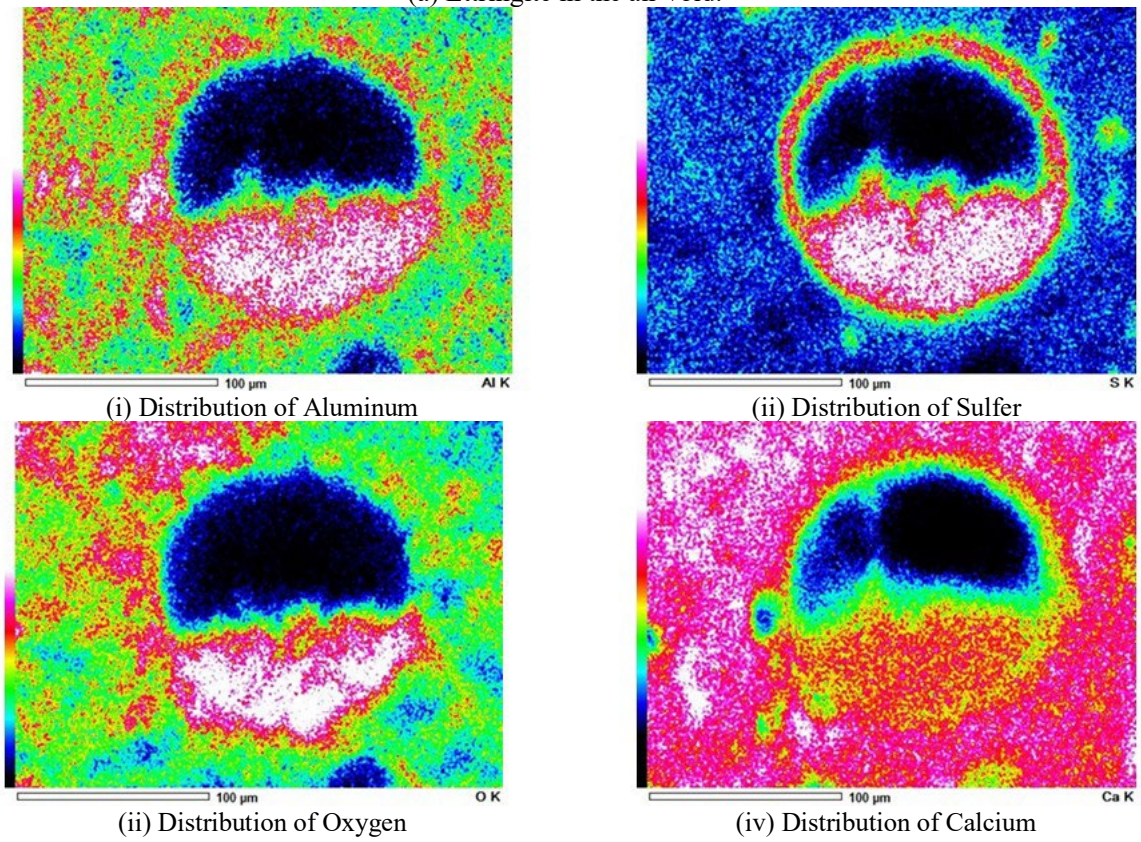


Figure D-12. Specimens for SEM-EDS examination

As shown in Figure D-13a, ettringite is observed in a few air voids. This observation supports the findings from thin section petrography. Aluminum, calcium, oxygen, and sulfur elements are rich in such locations. The distribution of such elements can be mapped using EDS, as shown in Figure D-13b. As an example, the white areas in Figure D-13b(i) represent the distribution of aluminum. Similarly, the distribution of sulfur, oxygen, and calcium is shown in Figure D-13b(ii) to (iv).



(a) Ettringite in the air void.



(b) EDS element mapping

Figure D-13. SEM and EDS analysis of the minerals present in air voids.

Even though the SEM image in Figure D-14 shows a crack in fine aggregate, no evidence is found on ASR.

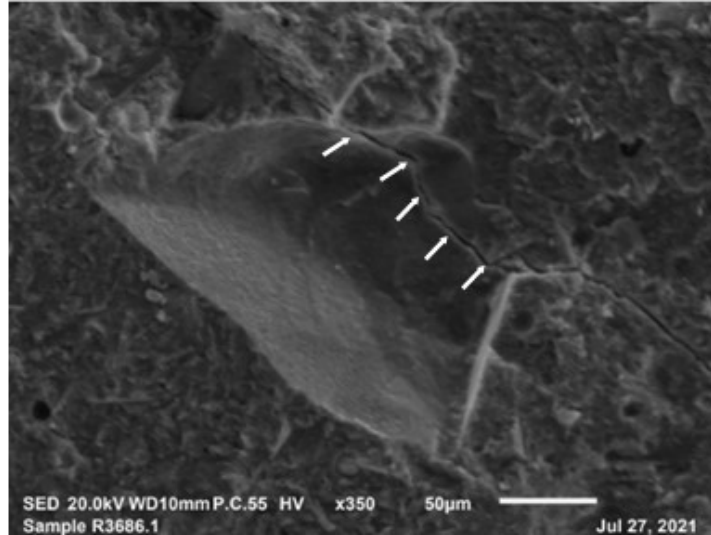


Figure D-14. SEM image of a cracked fine aggregate
(White arrows show the crack in the aggregate.)

Specimen from Beam End

As shown in Figure D-15, a specimen was prepared from the concrete collected from the severely deteriorated area at the north end of the box-beam shown in Figure D-3.

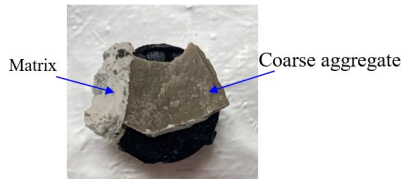
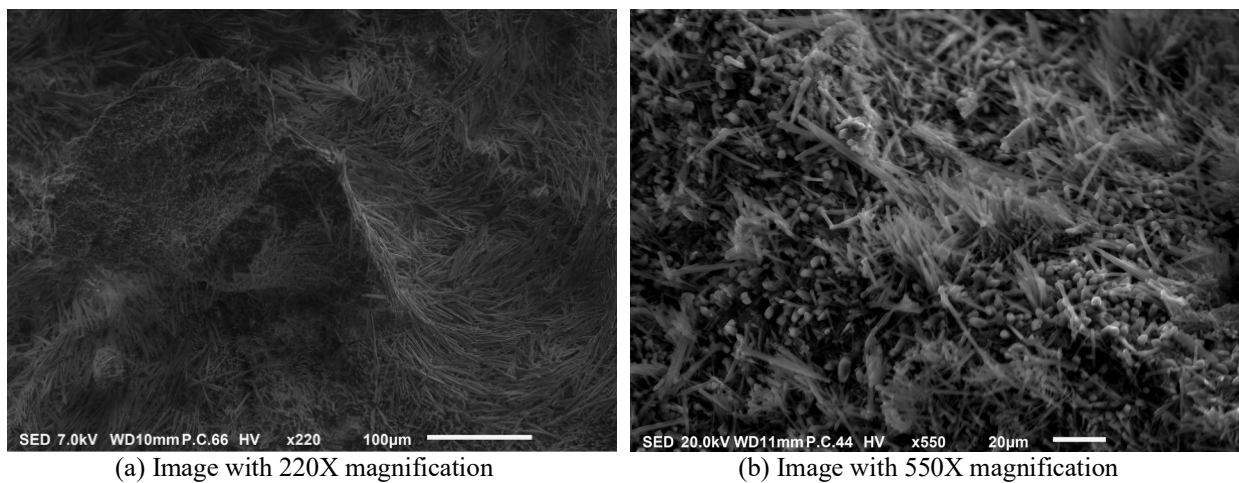


Figure D-15. Specimen for SEM-EDS examination

As shown in Figure D-16, ettringite is abundantly present in the specimen.



(a) Image with 220X magnification

(b) Image with 550X magnification

Figure D-16. SEM image showing the presence of ettringite

Point analysis was conducted to identify the chemical elements. As shown in Figure D-17, point 1 is selected over the fine aggregate. Point 2 is chosen away from the aggregate while point 3 is selected closer to the aggregate. The EDS results presented in Figure D-17b through d show that these three locations are rich in carbon and oxygen, in addition to having small amounts of aluminum and silicon. The detection of aluminum, calcium, and sulfur at locations 2 and 3 indicates the presence of ettringite. The lead (Pb) shown in Figure D-17c might be due to an interference from the surroundings or a mishap, and thus, can be neglected.

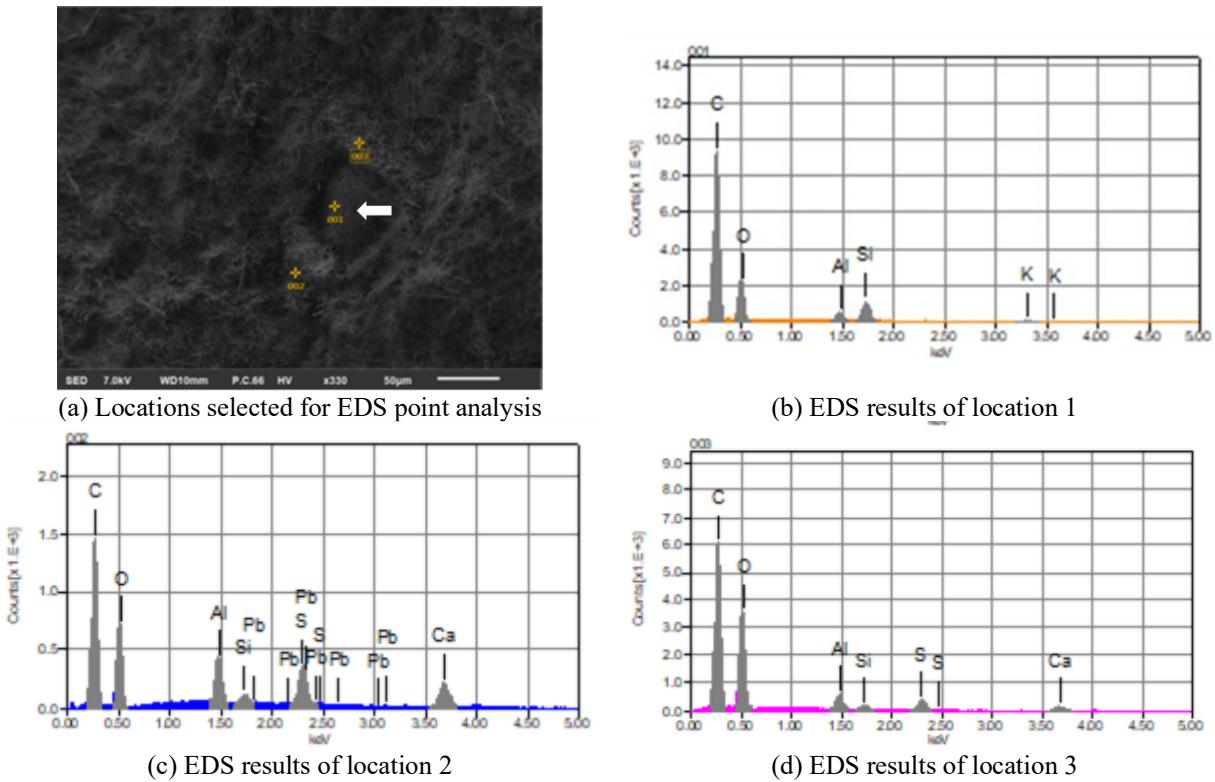


Figure D-17. EDS point analysis results

EDS element mapping was performed closer to the coarse aggregate, and the results are shown in Figure D-18. The presence of aluminum, calcium, and sulfur with the specific microstructure represents ettringite. A small amount of silicon is in both aggregate and the cement matrix. The SEM-EDS element mapping results of the potentially ettringite microstructure are shown in Figure D-19. This aluminum, calcium, and sulfur rich mineral structure confirms the presence of ettringite. Chemical elements identified through point analysis shown in Figure D-20 confirm the findings. Chloride (Cl⁻) was not present in any of the specimens.

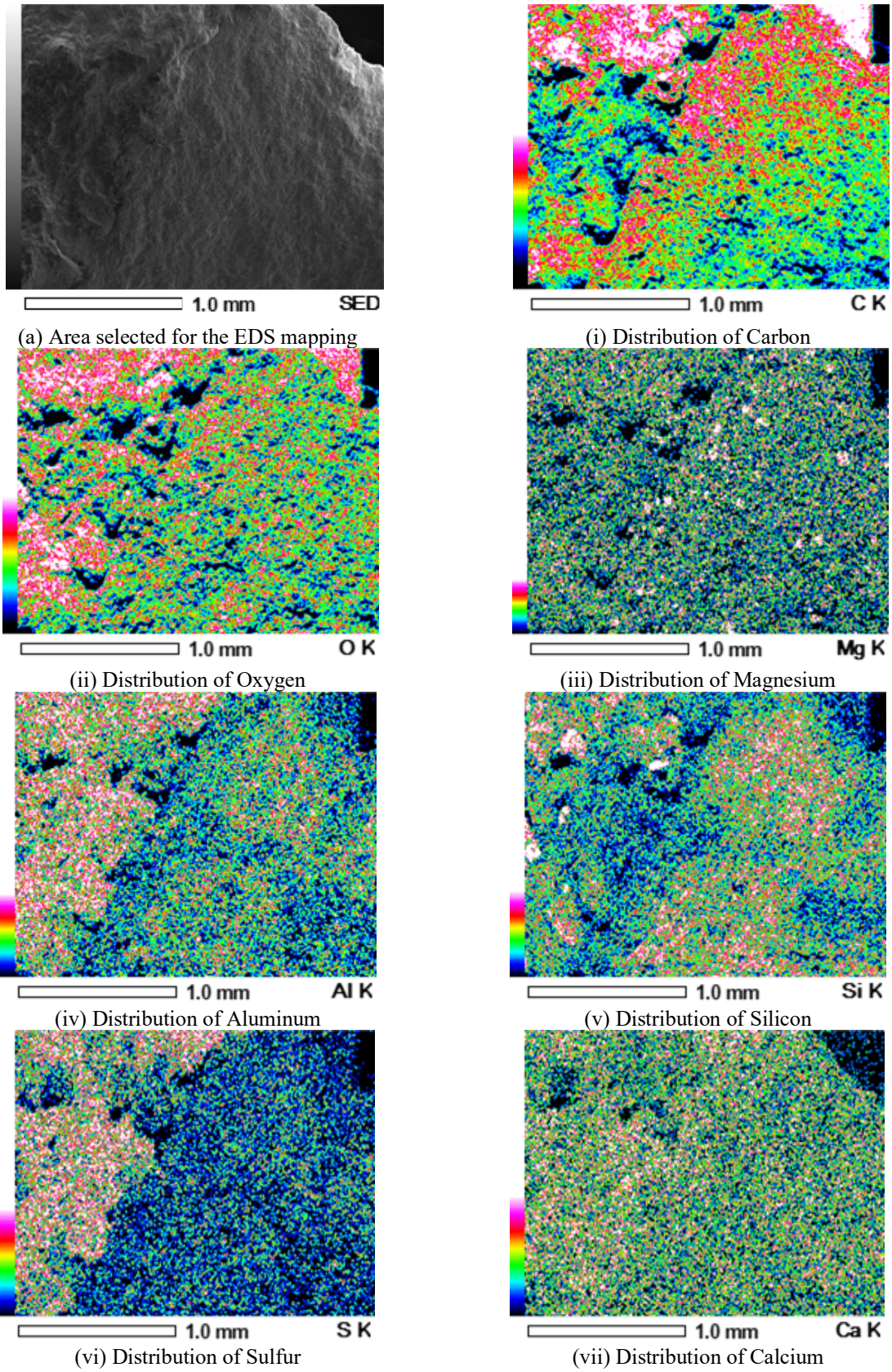
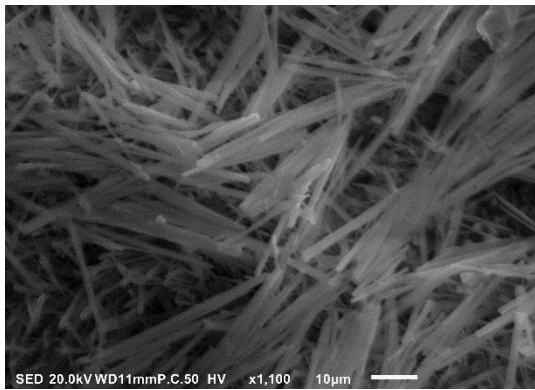
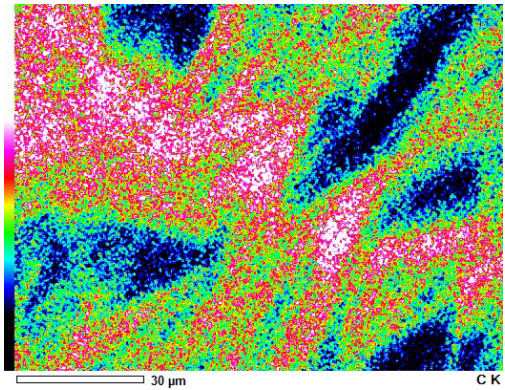


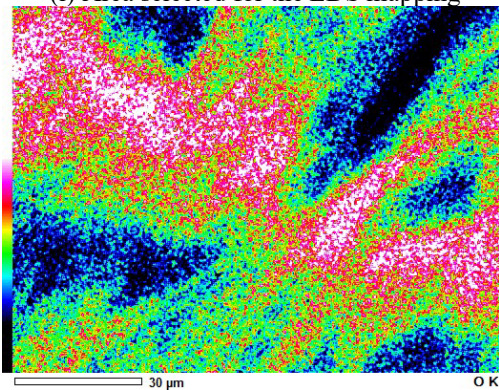
Figure D-18. EDS element mapping closer to coarse aggregate



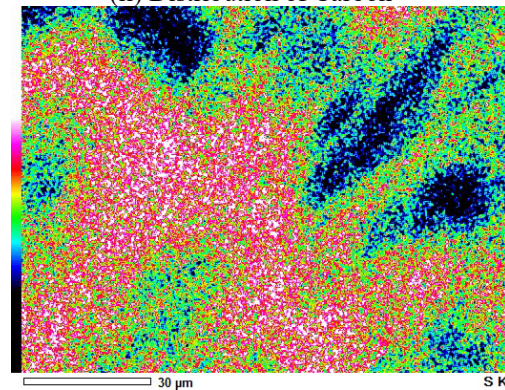
(i) Area selected for the EDS mapping



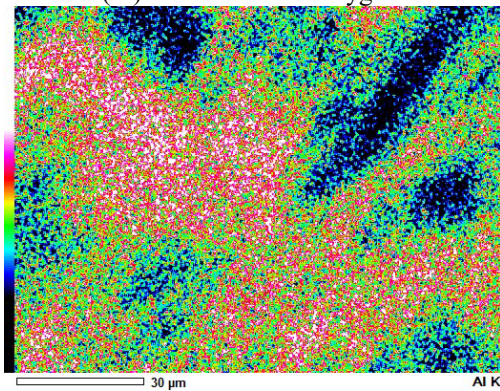
(ii) Distribution of Carbon



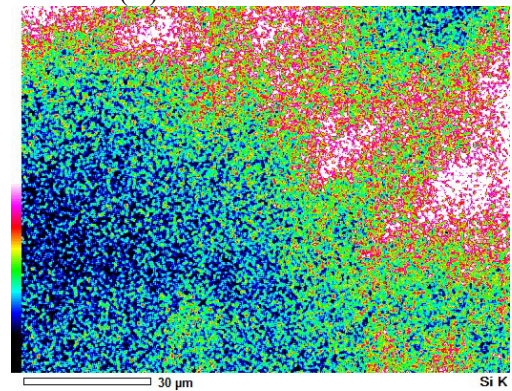
(iii) Distribution of Oxygen



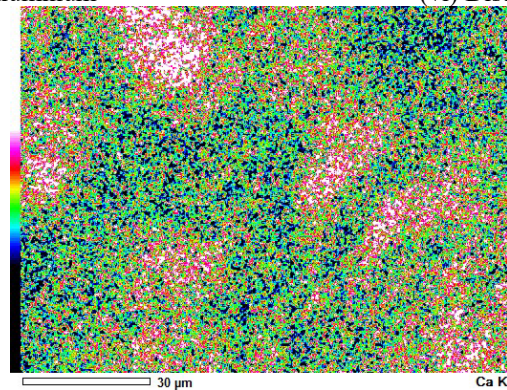
(iv) Distribution of Sulfur



(v) Distribution of Aluminum



(vi) Distribution of Silicon



(vii) Distribution of Calcium

Figure D-19. EDS element mapping results over ettringite

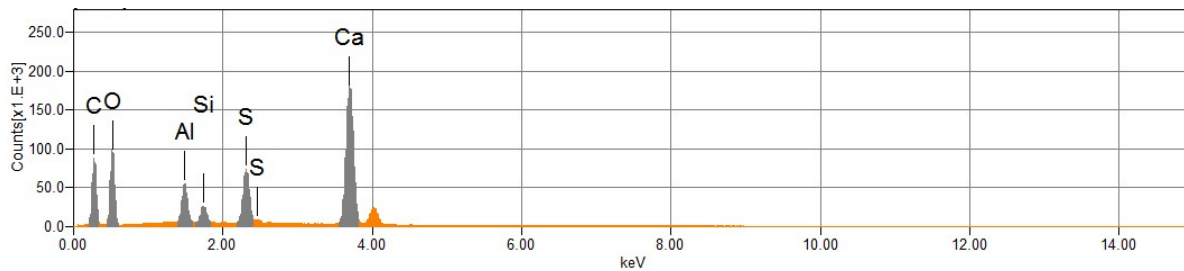


Figure D-20. EDS point analysis results of ettringite

SUMMARY

After being in service for 26 years, the bridge (S.N. 12314) that carried Brady Street over the lower branch of the Rouge River was demolished during the last week of March, 2020. Inspection reports only documented the typical distress and deteriorations observed in side-by-side box beam bridges. A close inspection of beam soffits showed severe deteriorations with significant random cracking towards the north end of the beams. A significant scaling of box beam webs and north ends was observed after removing the beams. Concrete prism expansion testing, petrography, and SEM-EDS analysis were conducted to identify the potential causes of concrete deterioration.

Concrete prisms taken from beam webs eliminated any concerns related to the impacts of DEF. Uranyl acetate testing on specimens extracted from beam ends showed ASR in fine aggregate. The ASR potential of fine aggregate was confirmed by measuring the expansion of concrete prisms taken from beam webs under 1N NaOH exposure at 176° F, and subsequent uranyl acetate testing. The petrography analysis results confirmed the presence of ASR in fine aggregate. Another major contributor to concrete deterioration is the low air content, 2 to 3%, as per the petrography analysis report. Significant scaling was observed at the north ends of the beams and concealed webs, an indication of freeze-thaw damage. North ends of beams were exposed to surface water due to the road profile. However, the concerns regarding salt scaling of beam ends was eliminated since EDS analysis did not find Cl⁻ in the collected specimens. Water seeped through the longitudinal joints, accumulated inside the airpockets in the grouted shear keys, and contributed to the freeze-thaw damage of beam webs. Freeze-thaw is identified as the most probable primary concrete deterioration mechanism. Even though similar damages could be caused by alternative methods, such as salt scaling, verification testing was not conducted using beam web specimens during this investigation. Once the beam end concrete was severely cracked, ettringite filled the cracks. SEM-EDS results confirmed the presence of ettringite at the severely deteriorated beam ends.

The findings highlight the need for enhancing inspection guidelines to identify bridges with similar deteriorations, improving concrete quality control to assure an adequate amount of entrained air in hardened concrete, encouraging the use of fine aggregate with a good record of performance against ASR, and protecting girders from surface runoff.

REFERENCES

1. ASTM International. (2014). "C856-14: Standard Practice for Petrographic Examination of Hardened Concrete." ASTM International, 100 Barr Harbor Drive, P.O. Box C700, West Conshohocken, PA, 19428-2959, USA
2. Thomas, M., Folliard, K., Drimalas, T, and Ramlochan, T. (2008). "Diagnosing Delayed Ettringite Formation in Concrete Structures," *Cement and Concrete Research*, 38, 841-847.

APPENDIX E: LOAD RATING OF PSC BOX-BEAMS – USER MANUAL

This document describes the content of the Mathcad calculation sheet submitted with this report. The user actions required to complete load rating are described using **light blue** text. The main topics in the Mathcad sheet are presented with **gray highlights**.

LEGEND

Presents the format and color coding used in the calculation sheet to identify *commentary*, *input variables*, *references*, and *results and checks*.

REFERENCES

Lists the primary references used to develop the calculation process.

ASSUMPTIONS AND LIMITATIONS

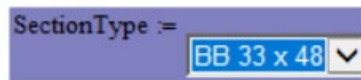
Lists the assumptions and limitations in the calculation process.

INPUT VARIABLES

Beam Geometry

MDOT box-beam sections are defined and included in the calculation sheet.

Select the beam section from the drop-down menu.



Note: The cross-section properties are stored in the Excel file “SectionTable.xlsx.” Always keep this Excel file and the Mathcad sheet in the same folder. The following image appears when the Excel file is properly linked.

SectionData :=



SectionTable.xlsx

Beam Section Properties

Section properties of the selected beam section are extracted from the spreadsheet and assigned to the variables defined in this section.

Deck Section Properties

User defines concrete deck and haunch dimensions.

Input effective flange width (b_{eff}), deck thickness (t_s), and haunch thickness (t_h).

Material Properties

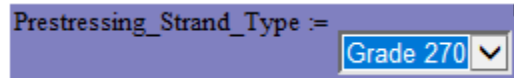
User defines material properties.

Deck Concrete

Input deck concrete compressive strength (f'_{c_deck}).

Prestressing Steel

Select the type of prestressing strands from the drop-down menu:



Input ultimate tensile strength (f_{pu}), specified yield strength (f_{py}), and modulus of elasticity (E_{ps}) of prestressing strands.

Beam Concrete (As-Designed)

Input beam concrete compressive strength (f'_{c_beam}).

Input density modification factor for beam concrete (λ).

Beam Concrete (Damaged)

Input the percentage reduction in the beam concrete tensile strength (Reduction_of_ f_t_beam).

Input the percentage reduction in the beam concrete modulus of rupture (Reduction_of_ f_r_beam).

The impact of concrete deterioration due to alkali-silica reaction (ASR) and freeze-thaw damage on concrete tensile strength and modulus of rupture is not well defined to use in the capacity calculation of prestressed concrete beams. The following table was developed using published data to demonstrate the reduction in concrete tensile strength due to ASR.

Table E - 1. Reduction in Concrete Tensile Strength Due to Alkali-Silica Reaction (ASR)

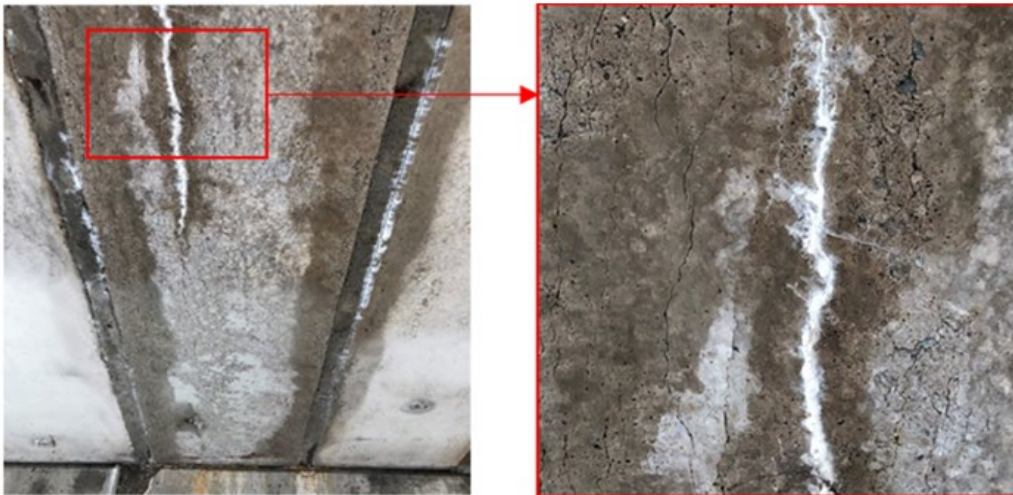
Expansion level (%)	Reduction in tensile strength (%)
$0.00 < \epsilon \leq 0.01$	0 – 6
$0.01 < \epsilon \leq 0.03$	6 – 22
$0.03 < \epsilon \leq 0.04$	22 – 29
$0.04 < \epsilon \leq 0.05$	29 – 38
$0.05 < \epsilon \leq 0.07$	38 – 43
$0.07 < \epsilon \leq 0.10$	43 – 47
$0.10 < \epsilon \leq 0.30$	47 – 61
$0.30 < \epsilon \leq 0.50$	> 61
$0.50 < \epsilon \leq 1.00$	> 61

The implementation of these expansion limits for load rating is challenging since the level of expansion to concrete cracking in prestressed concrete box-beams is not yet correlated. Therefore, the following guidelines are provided:

- 1) No reduction in concrete properties for beams with bottom flange longitudinal cracking, as shown in Figure E - 1(a). The possibility of not having ASR or freeze-thaw damage needs to be confirmed.
- 2) Zero tensile strength and modulus of rupture should be used when severe random cracking due to ASR or freeze-thaw is observed at the bottom flange, as shown in Figure E - 1(b).



(a) Longitudinal cracking



(b) Severe random cracking due to freeze-thaw damage

Figure E - 1. Box-beam bottom flange cracking

Prestressing Strand Layout

User defines the cross-section area of a single strand and prestressing strand layout for the selected beam section.

Input the cross-section area of a single strand (StrandArea).

A default strand layout for a box-beam section is defined as shown in Figure E - 2. The layout includes 4 rows (Row 1 to Row 4) and 23 columns (L11, L10, ..., CL, ..., R10, R11). The center-to-center spacing between strands in each column and row is 2 in.

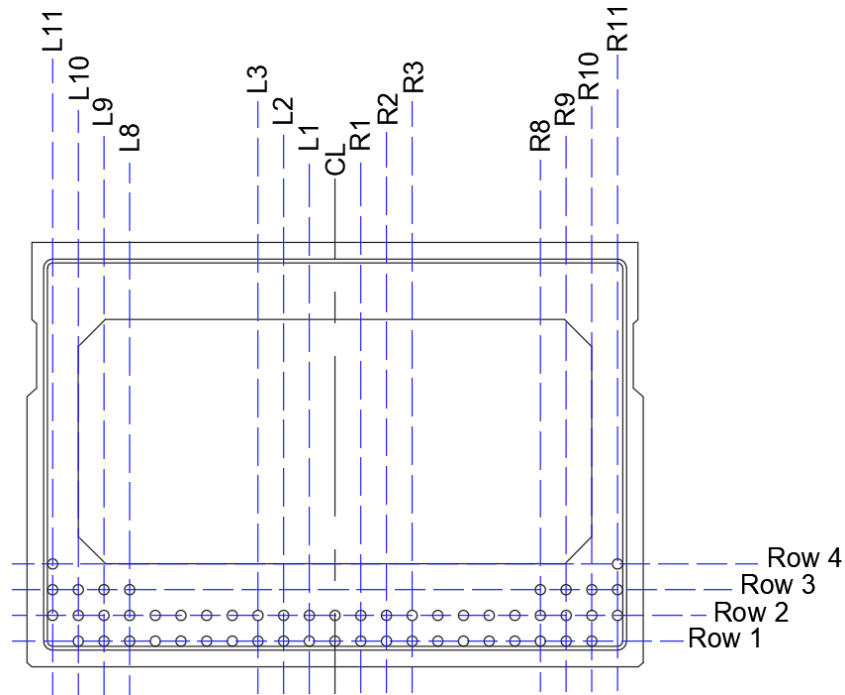


Figure E - 2. Default strand layout

Accordingly, 4 rows are defined in the Mathcad calculation sheet as follows:

StrandLayout_Hor :=

	0	1	2
0	"Row 1"	21	2
1	"Row 2"	23	4
2	"Row 3"	8	6
3	"Row 4"	2	8

Column 0 defines the row number.

Column 1 defines the number of strands in each row.

Column 2 defines the distance to each row from the bottom of the beam.

The columns are defined in the Mathcad calculation sheet as follows:

StrandLayout_Ver :=

	0	1	2
0	"L11"	3	-22
1	"L10"	3	-20
2	"L9"	3	-18
3	"L8"	3	-16
4	"L7"	2	-14
5	"L6"	2	-12
6	"L5"	2	-10
7	"L4"	2	-8
8	"L3"	2	-6
9	"L2"	2	-4
10	"L1"	2	-2
11	"CL"	2	0
12	"R1"	2	2
13	"R2"	2	4
14	"R3"	2	6
15	"R4"	2	8
16	"R5"	2	10
17	"R6"	2	12
18	"R7"	2	14
19	"R8"	3	16
20	"R9"	3	18
21	"R10"	3	20
22	"R11"	3	...

Column 0 defines the column number.

Column 1 defines the number of strands in each column.

Column 2 defines the distance to each column from the beam vertical centerline.

The user is ***NOT*** required to make any changes to the already defined strand layout.

The strand layout is defined to accommodate the strand patterns in all MI box-beam sections listed in the MDOT BDG as of **12/31/2021**. Strand layouts of MDOT standard box-beam sections are shown in Figure E - 3 and Figure E - 4. Table E - 2 summarizes the number of strands in each section and the number of strands selected to develop the default layout.

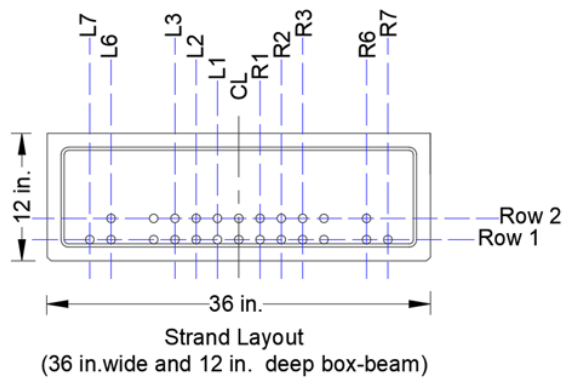
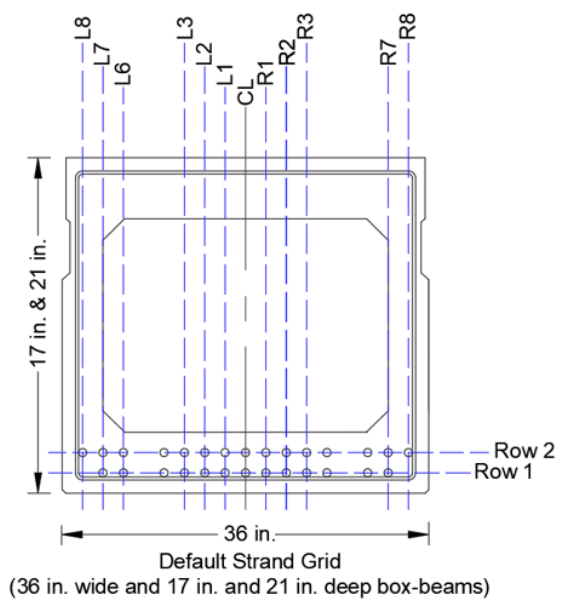
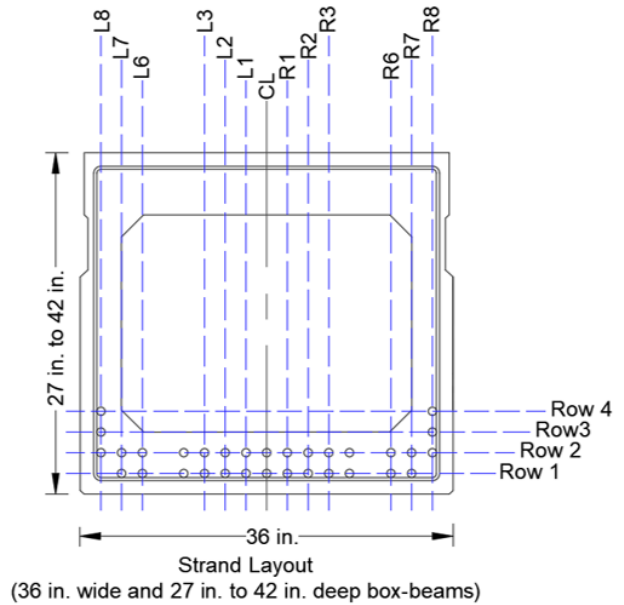


Figure E - 3. Strand layout for 36 in. wide beams

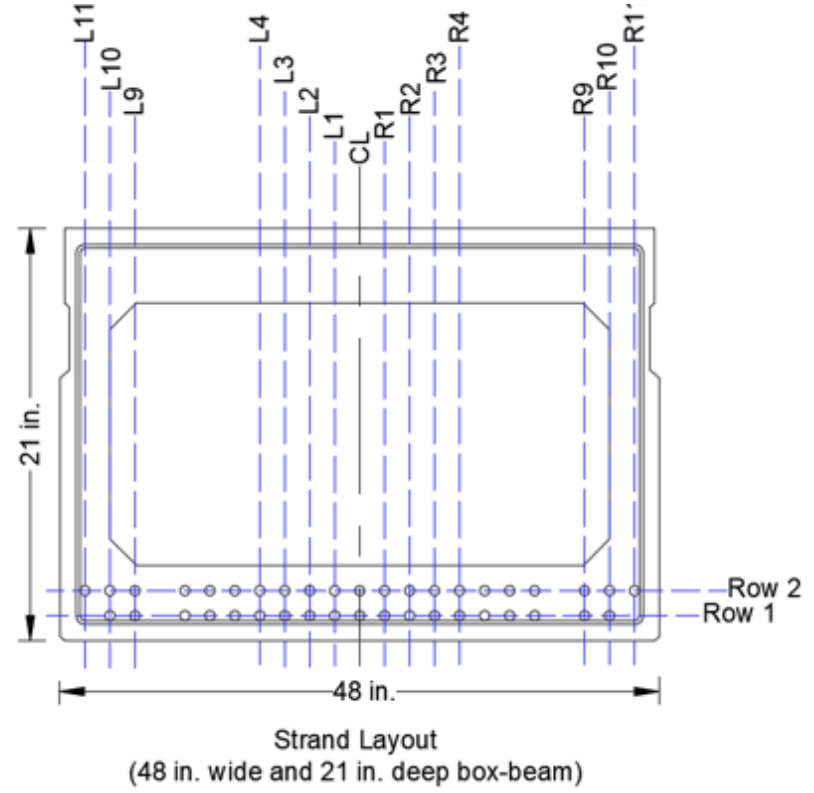
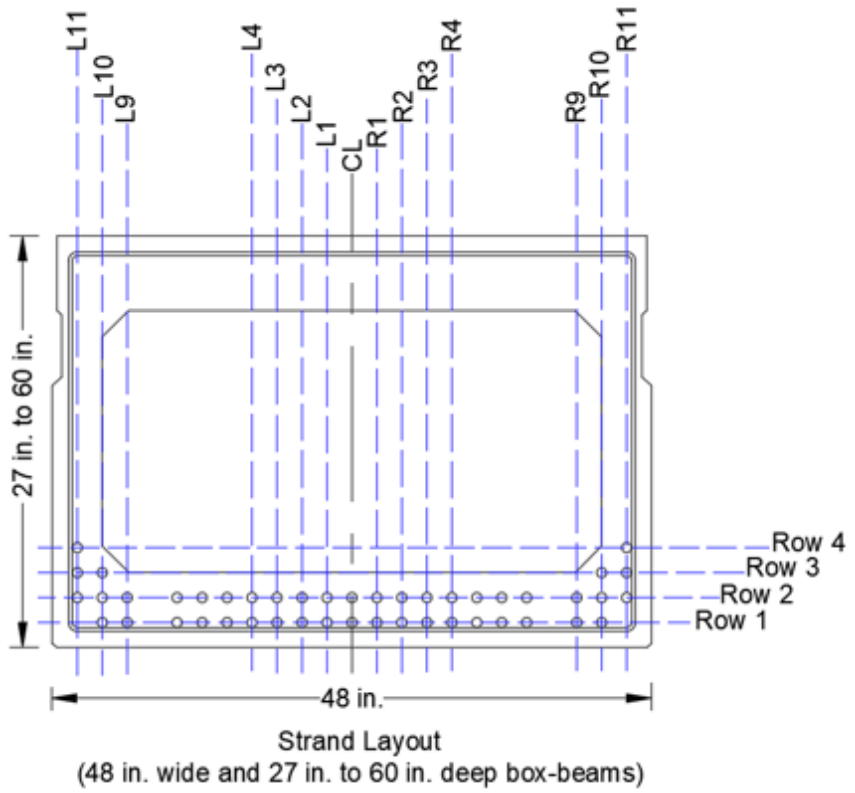


Figure E - 4. Strand layout for 48 in. wide beams

Table E - 2. Number of Strands in MDOT Standard Sections and the Number of Strands Selected to Develop the Default Layout

Column no.	36×12 in. (a)	36×17 and 21 in. (b)	36×27 to 42 in. (c)	48×21 in. (d)	48×27 and 33 in. (e)	48×39 to 60 in. (f)	No. of strands in the default layout (g) = max (a to f)
L11	0	0	0	1	3	3	3
L10	0	0	0	2	3	3	3
L9	0	0	0	2	2	2	3 ¹
L8	0	1	3	0	0	0	3
L7	1	2	2	2	2	2	2
L6	2	2	2	2	2	2	2
L5	0	0	0	2	2	2	2
L4	2	2	2	2	2	2	2
L3	2	2	2	2	2	2	2
L2	2	2	2	2	2	2	2
L1	2	2	2	2	2	2	2
CL	2	2	2	2	2	2	2
R1	2	2	2	2	2	2	2
R2	2	2	2	2	2	2	2
R3	2	2	2	2	2	2	2
R4	2	2	2	2	2	2	2
R5	0	0	0	2	2	2	2
R6	2	2	2	2	2	2	2
R7	1	2	2	2	2	2	2
R8	0	1	3	0	0	0	3
R9	0	0	0	2	2	2	3 ¹
R10	0	0	0	2	3	3	3
R11	0	0	0	1	3	3	3

¹ – No. of strands in the default layout at L9 and R9 is taken as 3 to maintain the same number with the adjacent columns L8, L10, R8, and R10.

Dead and Permanent Loads

User defines the moments due to dead and permanent loads.

Input,

- *total unfactored dead load moment acting on the noncomposite section, M_{dnc} (i.e. beam self-weight, diaphragm weight, slab weight, and haunch weight)*
- *total unfactored dead load moment acting on the composite section, M_{dc} (i.e. barrier weight) and M_{DW} (i.e. unfactored dead load moment due to wearing surface and utilities)*
- *unfactored moment due to permanent loads other than dead loads, M_P .*

Prestress Loads

User defines prestressing steel stress prior to transfer, losses, and the secondary effects of prestressing.

Input,

- *initial prestressing steel stress immediately prior to transfer (f_{ps})*
- *the lump sum percentage loss in prestressing force ($TotalPrestressLoss$)*
- *unfactored moment due to secondary prestress forces, M_s .*

The following references can be used to calculate the lump sum percentage loss in prestressing force:

1. ACI. (2016). ACI 423.10R-16: Guide to Estimating Prestress Losses. American Concrete Institute (ACI), Farmington Hills, Detroit, MI 48331
2. AASHTO LRFD. (2020). AASHTO LRFD Bridge Design Specifications. 9th Edition, American Association of State Highway and Transportation Officials (AASHTO), Washington D.C. 20004.

Live Loads

User defines live load moments due to federal loads, Michigan operating loads, and permit loads.

Input the following information:

- *beam span length ($Span$)*
- *live load distribution factor for LFR method (DF_{L_LFR})*
- *live load distribution factor for LRFR method (DF_{L_LRFR}).*

Federal Loads

Input the following information:

- *moment due to HS 20 truck (M_{LL_HS20})*
- *moment due to HL 93 (M_{LL_HL93}) load.*

Depending on the location of interest along the span, either use MDOT BAG (2009) Table 10.9 or conduct an analysis to determine the moment due to a HS 20 truck load (M_{LL_HS20}). Also, conduct an analysis to determine the moment due to HL 93 load.

Michigan Operating (Legal) Loads

Input moment on the beam due to a one-unit truck (M_{LL_M1}), two-unit truck (M_{LL_M2}), and three-unit truck (M_{LL_M3}).

Determine if normal, designated, or special designated loading applies to the selected bridge. Then, depending on the location of interest along the span, either use MDOT BAG (2009) Table 10.1 to

Table 10.7 or conduct an analysis to determine the moment due to a one-unit, two-unit, and three-unit trucks on the beam.

Permit Loads

Input moment on the beam due to permit loads (M_{LL_permit}).

Depending on the location of interest along the span or the type of truck considered for rating, either use MDOT BAG (2009) Table 10.10 to Table 10.12 or conduct an analysis to determine the moment due to the selected permit truck.

Load & Impact Factors

User defines the load factors for dead and live loads under different limit states and the impact factors as per LFR and LRFR methods.

For Dead Loads

Input LRFD load factor for wearing surface and utilities for strength I and II limit states ($\gamma_{DW_strength}$).

Typically, $\gamma_{DW_strength} = 1.50$, but may be taken as 1.25 where thickness is field measured.

For Live Loads

Input evaluation live load factor for strength I limit state for MI legal loads ($\gamma_{LL_strengthI_Mloper}$).

Refer to MDOT BAG (2009) Table 4a-1, 4a-2, and 4a-3 for $\gamma_{LL_strengthI_Mloper}$ or AASHTO MBE (2019) Table 6A.4.4.2.3a-1 and 6A4.4.2.3b-1.

Input evaluation live load factor for service III limit state for federal inventory loads ($\gamma_{LL_serviceIII_inv}$).

Refer to AASHTO MBE (2019) Table 6A.4.2.2-2 for $\gamma_{LL_serviceIII_inv}$.

Input evaluation live load factor for strength II limit state for permit loads ($\gamma_{LL_strengthII_permit}$).

Refer to MDOT BAG (2009) Table 4a-4, 4a-5, and 4a-6 or AASHTO MBE (2019) Table 6A.4.5.4.2a-1 for $\gamma_{LL_strengthII_permit}$.

Impact Factors

Input the following information:

- *portion of the span loaded to produce the maximum stress in the beam (Loaded_length) (ft)*
- *dynamic load allowance (LRFR) for permit loads (IM_LRFR_permit).*

Refer to AASHTO MBE (2019) Art. 6A.4.5.5 for more information.

Beam Section Damage Details

Typically, box-beam damage is concentrated along the edges. The following figure defines the damage magnitude using L_1 , L_2 , R_1 , and R_2 definitions.

Input the following:

- *vertical length of damage at the left bottom corner (L_1)*
- *horizontal length of damage at the left bottom corner (L_2)*
- *vertical length of damage at the right bottom corner (R_1)*
- *horizontal length of damage at the right bottom corner (R_2).*

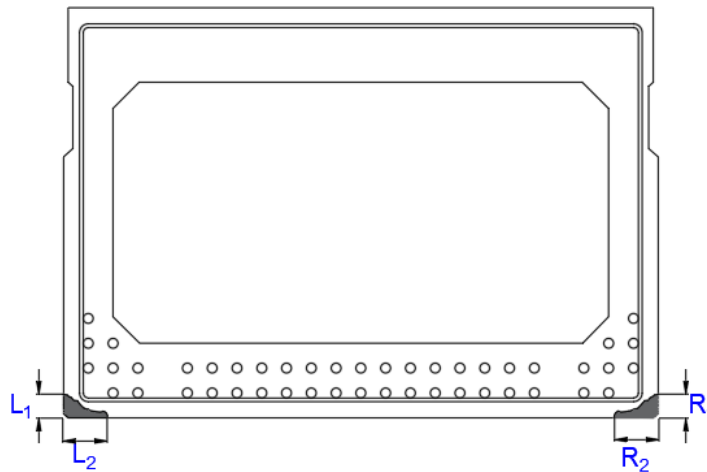


Figure E - 5. Beam corner damage description

Prestressing Strand Elimination from the Default (As-Designed) Layout

The number of prestressing strands in the as-designed box-beam section is defined with respect to the default layout presented in the “Prestressing Strand Layout” section.

Fill Column 1 of the table “AsDesignedStrands_Hor” with the number of strands to be removed from each row (Row 1 to Row 4) representing the number of strands absent from the default layout.

Fill Column 1 of the table “AsDesignedStrands_Ver” with the number of strands to be removed from each column (L11 to R11) representing the number of strands absent from the default layout.

The following two examples demonstrate the procedures for defining prestressing strand layouts for as-designed box-beams.

Example 1: 60 × 48 in. beam section

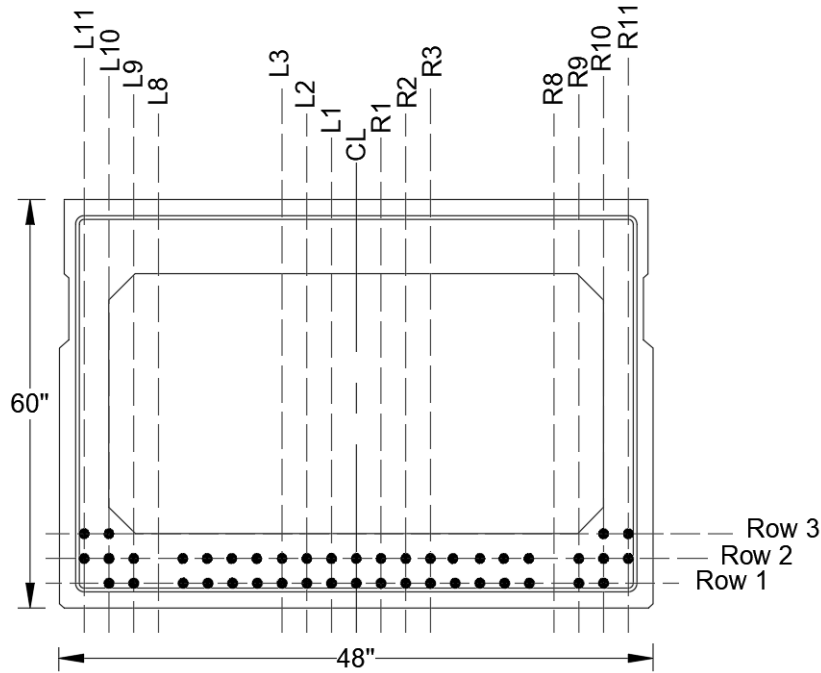


Figure E - 6. As-designed box-beam for Example 1

The following tables present the procedures to identify the number of strands to be removed from the default layout to define the number of strands in rows and columns of this 60 × 48 in. box-beam.

Table E - 3. Number of Strands to be Removed from Each Row to Define As-Designed Details

Row no.	No. of strands in the default layout	No. of strands absent from the default layout	No. of strands to be removed from the default layout	No. of strands in the beam section
(a)	(b)	(c)	(d) = (c)	(e) = (b) - (d)
1	21	2	2	19
2	23	2	2	21
3	8	4	4	4
4	2	2	2	0

Table E - 4. Number of Strands to be Removed from Each Column to Define As-Designed Details

Column no.	No. of strands in the default layout	No. of strands absent from the default layout	No. of strands to be removed from the default layout	No. of strands in the beam section
(a)	(b)	(c)	(d) = (c)	(e) = (b) – (d)
L11	3	1	1	2
L10	3	0	0	3
L9	3	1	1	2
L8	3	3	3	0
L7	2	0	0	2
L6	2	0	0	2
L5	2	0	0	2
L4	2	0	0	2
L3	2	0	0	2
L2	2	0	0	2
L1	2	0	0	2
CL	2	0	0	2
R1	2	0	0	2
R2	2	0	0	2
R3	2	0	0	2
R4	2	0	0	2
R5	2	0	0	2
R6	2	0	0	2
R7	2	0	0	2
R8	3	3	3	0
R9	3	1	1	2
R10	3	0	0	3
R11	3	1	1	2

As shown below, the tables in the Mathcad calculation sheet are completed using the data in the gray highlighted columns of the above two tables.

AsDesignedStrands_Hor :=		
	0	1
0	"Row 1"	2
1	"Row 2"	2
2	"Row 3"	4
3	"Row 4"	2

AsDesignedStrands_Ver :=		
	0	1
0	"L11"	1
1	"L10"	0
2	"L9"	1
3	"L8"	3
4	"L7"	0
5	"L6"	0
6	"L5"	0
7	"L4"	0
8	"L3"	0
9	"L2"	0
10	"L1"	0
11	"CL"	0
12	"R1"	0
13	"R2"	0
14	"R3"	0
15	"R4"	0
16	"R5"	0
17	"R6"	0
18	"R7"	0
19	"R8"	3
20	"R9"	1
21	"R10"	0
22	"R11"	...

Example 2: 21 × 36 in. beam section

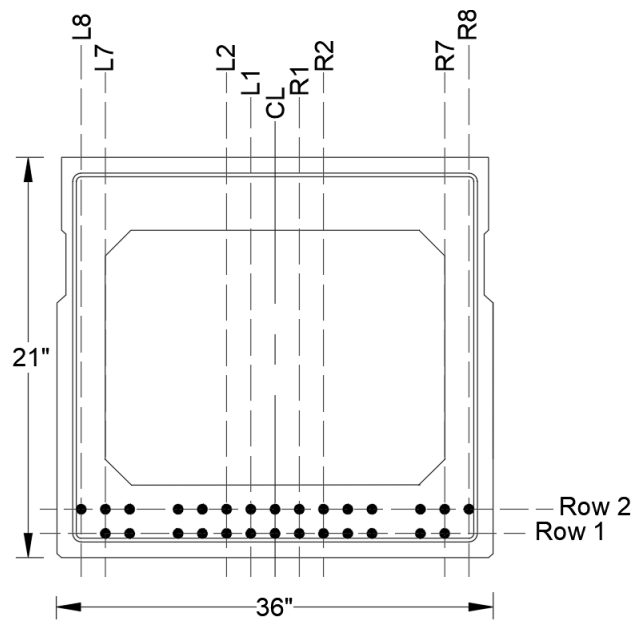


Figure E - 7. As-designed box-beam for Example 2

The following tables present the procedures to identify the number of strands to be removed from the default layout to define the number of strands in rows and columns of this 21 × 36 in. box-beam.

Table E - 5. Number of Strands to be Removed from Each Row to Define As-Designed Details

Row no.	No. of strands in the default layout	No. of strands absent from the default layout ¹	No. of strands to be removed from the default layout	No. of strands in the beam section
(a)	(b)	(c)	(d) = (c)	(e) = (b) – (d)
1	21	8	8	13
2	23	8	8	15
3	8	8	8	0
4	2	2	2	0

Table E - 6. Number of Strands to be Removed from Each Column to Define As-Designed Details

Column no.	No. of strands in default layout	No. of strands absent from the default layout	No. of strands to be removed from the default layout	No. of effective strands in the beam section
(a)	(b)	(c)	(d) = (c)	(e) = (b) – (d)
L11	3	3	3	0
L10	3	3	3	0
L9	3	3	3	0
L8	3	2	2	1
L7	2	0	0	2
L6	2	0	0	2
L5	2	2	2	0
L4	2	0	0	2
L3	2	0	0	2
L2	2	0	0	2
L1	2	0	0	2
CL	2	0	0	2
R1	2	0	0	2
R2	2	0	0	2
R3	2	0	0	2
R4	2	0	0	2
R5	2	2	2	0
R6	2	0	0	2
R7	2	0	0	2
R8	3	2	2	1
R9	3	3	3	0
R10	3	3	3	0
R11	3	3	3	0

As shown below, the tables in the Mathcad calculation sheet are completed using the data in the gray highlighted columns of the above two tables.

AsDesignedStrands_Hor :=		
	0	1
0	"Row 1"	8
1	"Row 2"	8
2	"Row 3"	8
3	"Row 4"	2

AsDesignedStrands_Ver :=		
	0	1
0	"L11"	3
1	"L10"	3
2	"L9"	3
3	"L8"	2
4	"L7"	0
5	"L6"	0
6	"L5"	2
7	"L4"	0
8	"L3"	0
9	"L2"	0
10	"L1"	0
11	"CL"	0
12	"R1"	0
13	"R2"	0
14	"R3"	0
15	"R4"	0
16	"R5"	2
17	"R6"	0
18	"R7"	0
19	"R8"	2
20	"R9"	3
21	"R10"	3
22	"R11"	...

Damaged Beam: Prestressing Strand Elimination from the Default Layout

The strand layout of a damaged beam is defined by eliminating the number of damaged strands and the numbers absent from the default layout presented in the “Prestressing Strand Layout” section.

Fill Column 1 of the table “DamagedStrands_Hor” with the number of strands to be removed from each row (Row 1 to Row 4) representing damaged strands and the number of strands absent from the default layout.

Fill Column 1 of the table “DamagedStrands_Ver” with the number of strands to be removed from each column (L11 to R11) representing damaged strands and the number of strands absent from the default layout.

Please refer to the report Section 6.2.4 on **Effective Number of Prestressing Strands and Strand Development** to identify the number of prestressing strands to be removed based on the type and significance of deterioration.

The following examples demonstrate the process for defining prestressing strand layouts for distressed box-beams.

Example 3: 60 × 48 in. distressed beam section

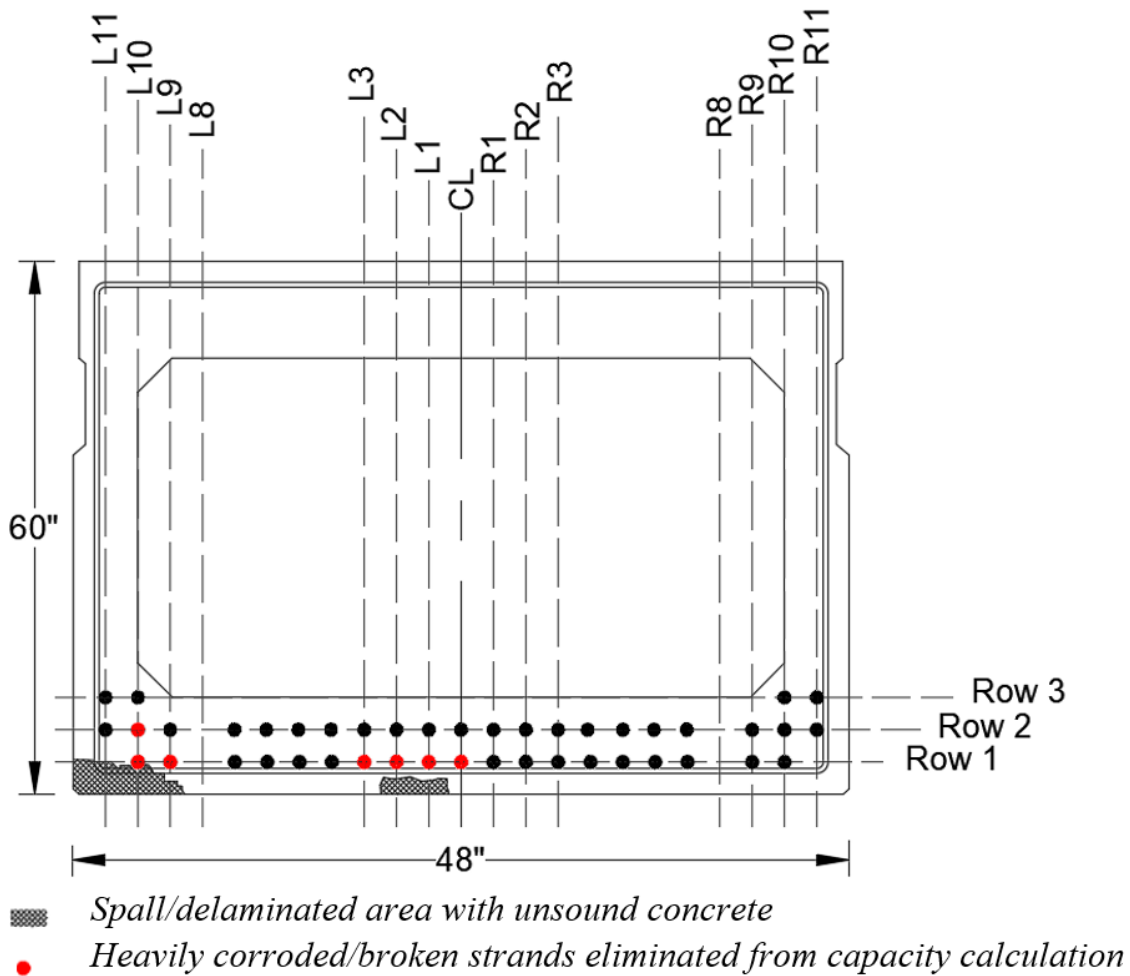


Figure E - 8. Distressed box-beam for Example 3

The following tables present the number of effective strands in this 60 × 48 in. distressed box-beam.

Table E - 7. Number of Strands Removed from Each Row to Define Damaged Section Details

Row no.	No. of strands in the default layout	No. of strands absent from the default layout ¹	No. of damaged strands ²	No. of strands to be removed from the default layout (e) = (d) + (e)	No. of effective strands in the beam section (f) = (b) – (e)
(a)	(b)	(c)	(d)	(e) = (d) + (e)	(f) = (b) – (e)
1	21	2	6	8	13
2	23	2	1	3	20
3	8	4	0	4	4
4	2	2	0	2	0

¹ - The specific section does not include strands at every location in the default layout. These are considered to be the "absent" strands.

² - The strands eliminated from capacity calculation due to heavy corrosion or damages

Table E - 8. Number of Strands Removed from Each Column to Define Damaged Section Details

Column no.	No. of strands in the default layout	No. of strands absent from the default layout	No. of damaged strands	No. of strands to be removed from the default layout	No. of effective strands in the beam section
(a)	(b)	(c)	(d)	(e) = (c) + (d)	(f) = (b) - (e)
L11	3	1	0	1	2
L10	3	0	2	2	1
L9	3	1	1	2	1
L8	3	3	0	3	0
L7	2	0	0	0	2
L6	2	0	0	0	2
L5	2	0	0	0	2
L4	2	0	0	0	2
L3	2	0	1	1	1
L2	2	0	1	1	1
L1	2	0	1	1	1
CL	2	0	1	1	1
R1	2	0	0	0	2
R2	2	0	0	0	2
R3	2	0	0	0	2
R4	2	0	0	0	2
R5	2	0	0	0	2
R6	2	0	0	0	2
R7	2	0	0	0	2
R8	3	3	0	3	0
R9	3	1	0	1	2
R10	3	0	0	0	3
R11	3	1	0	1	2

As shown below, the tables in the Mathcad calculation sheet are completed using the data in the gray highlighted columns of the above two tables.

DamagedStrands_Hor :=

	0	1
0	"Row 1"	8
1	"Row 2"	3
2	"Row 3"	4
3	"Row 4"	2

DamagedStrands_Ver :=

	0	1
0	"L11"	1
1	"L10"	2
2	"L9"	2
3	"L8"	3
4	"L7"	0
5	"L6"	0
6	"L5"	0
7	"L4"	0
8	"L3"	1
9	"L2"	1
10	"L1"	1
11	"CL"	1
12	"R1"	0
13	"R2"	0
14	"R3"	0
15	"R4"	0
16	"R5"	0
17	"R6"	0
18	"R7"	0
19	"R8"	3
20	"R9"	1
21	"R10"	0
22	"R11"	...

Example 4: 33 × 48 in. distressed beam section

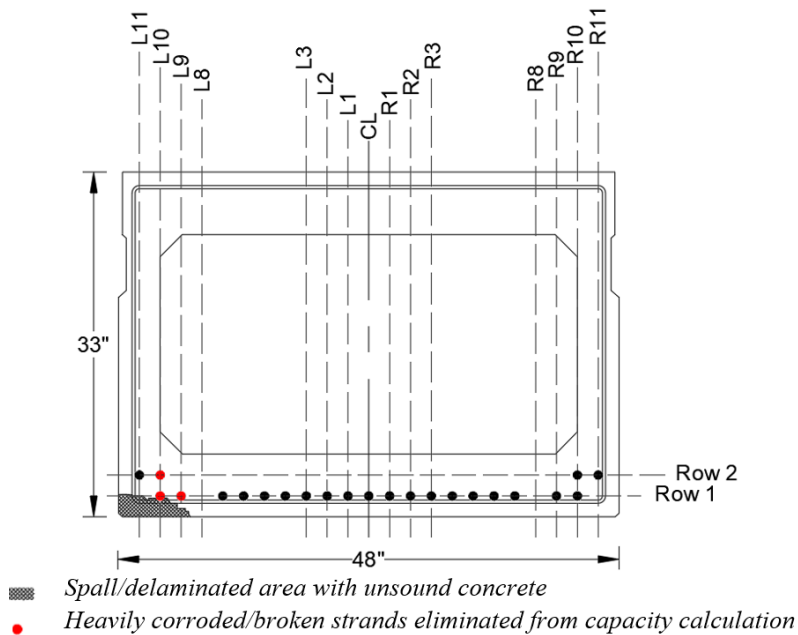


Figure E - 9. Distressed box-beam for Example 4

The following tables present the number of effective strands in this 33 × 48 in. distressed box-beam.

Table E - 9. Number of Strands Removed from Each Row to Define Damaged Section Details

Row no.	No. of strands in the default layout	No. of strands absent from the default layout ¹	No. of damaged strands ²	No. of strands to be removed from the default layout	No. of effective strands in the beam section
(a)	(b)	(c)	(d)	(e) = (c) + (d)	(f) = (b) – (e)
1	21	2	2	4	17
2	23	19	1	20	3
3	8	8	0	8	0
4	2	2	0	2	0

¹ - The specific section does not include strands at every location in the default layout. These are considered to be the "absent" strands.

² - The strands eliminated from capacity calculation due to heavy corrosion or damages.

Table E - 10. Number of Strands Removed from Each Column to Define Damaged Section Details

Column no.	No. of strands in the default layout	No. of strands absent from the default layout	No. of damaged strands	No. of strands to be removed from the default layout	No. of effective strands in the beam section
(a)	(b)	(c)	(d)	(e) = (c) + (d)	(f) = (b) – (e)
L11	3	2	0	2	1
L10	3	1	2	3	0
L9	3	2	1	3	0
L8	3	3	0	3	0
L7	2	1	0	1	1
L6	2	1	0	1	1
L5	2	1	0	1	1
L4	2	1	0	1	1
L3	2	1	0	1	1
L2	2	1	0	1	1
L1	2	1	0	1	1
CL	2	1	0	1	1
R1	2	1	0	1	1
R2	2	1	0	1	1
R3	2	1	0	1	1
R4	2	1	0	1	1
R5	2	1	0	1	1
R6	2	1	0	1	1
R7	2	1	0	1	1
R8	3	3	0	3	0
R9	3	2	0	2	1
R10	3	1	0	1	2
R11	3	2	0	2	1

As shown below, the tables in the Mathcad calculation sheet are completed using the data in the gray highlighted columns of the above two tables.

DamagedStrands_Hor :=		
	0	1
0	"Row 1"	4
1	"Row 2"	20
2	"Row 3"	8
3	"Row 4"	2

DamagedStrands_Ver :=		
	0	1
0	"L11"	2
1	"L10"	3
2	"L9"	3
3	"L8"	3
4	"L7"	1
5	"L6"	1
6	"L5"	1
7	"L4"	1
8	"L3"	1
9	"L2"	1
10	"L1"	1
11	"CL"	1
12	"R1"	1
13	"R2"	1
14	"R3"	1
15	"R4"	1
16	"R5"	1
17	"R6"	1
18	"R7"	1
19	"R8"	3
20	"R9"	2
21	"R10"	1
22	"R11"	...

Example 5: 21 × 36 in. distressed beam section

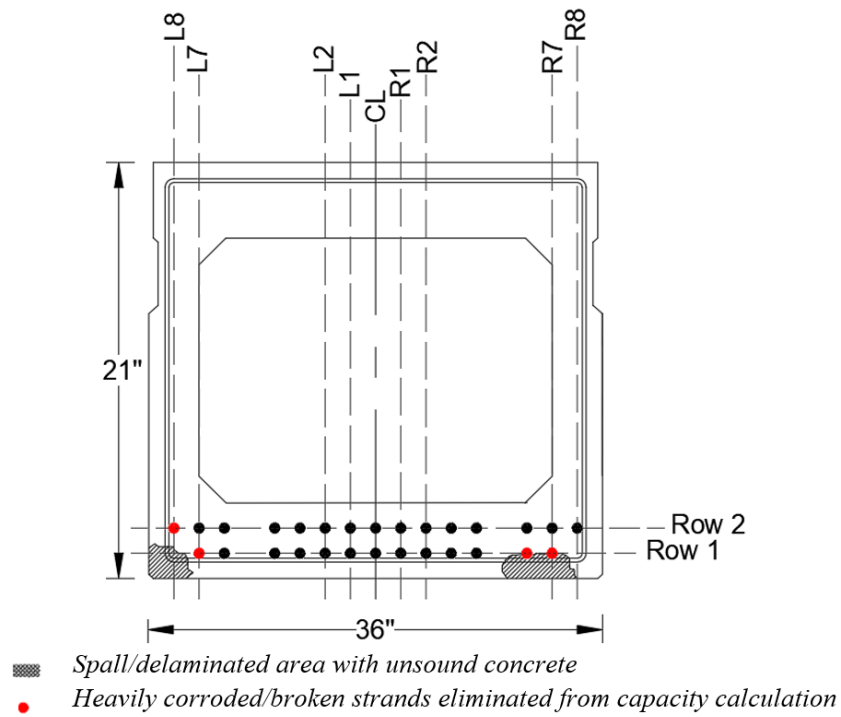


Figure E - 10. Distressed box-beam for Example 5

The following tables present the number of effective strands in this 21 × 36 in. distressed box-beam.

Table E - 11. Number of Strands Removed from Each Row to Define Damaged Section Details

Row no. (a)	No. of strands in the default layout (b)	No. of strands absent from the default layout ¹ (c)	No. of damaged strands ² (d)	No. of strands to be removed from the default layout (e) = (c) + (d)	No. of effective strands in the beam section (f) = (b) – (e)
1	21	8	3	11	10
2	23	8	1	9	14
3	8	8	0	8	0
4	2	2	0	2	0

¹ - The specific section does not include strands at every location in the default layout. These are considered to be the "absent" strands.

² - The strands eliminated from capacity calculation due to heavy corrosion or damages.

Table E - 12. Number of Strands Removed from Each Column to Define Damaged Section Details

Column no. (a)	No. of strands in default layout (b)	No. of strands absent from the default layout (c)	No. of damaged strands (d)	No. of strands to be removed from the default layout (e) = (c) + (d)	No. of effective strands in the beam section (f) = (b) – (e)
L11	3	3	0	3	0
L10	3	3	0	3	0
L9	3	3	0	3	0
L8	3	2	1	3	0
L7	2	0	1	1	1
L6	2	0	0	0	2
L5	2	2	0	2	0
L4	2	0	0	0	2
L3	2	0	0	0	2
L2	2	0	0	0	2
L1	2	0	0	0	2
CL	2	0	0	0	2
R1	2	0	0	0	2
R2	2	0	0	0	2
R3	2	0	0	0	2
R4	2	0	0	0	2
R5	2	2	0	2	0
R6	2	0	1	1	1
R7	2	0	1	1	1
R8	3	2	0	2	1
R9	3	3	0	3	0
R10	3	3	0	3	0
R11	3	3	0	3	0

As shown below, the tables in the Mathcad calculation sheet are completed using the data in the gray highlighted columns of the above two tables.

DamagedStrands_Hor :=

	0	1
0	"Row 1"	11
1	"Row 2"	9
2	"Row 3"	8
3	"Row 4"	2

DamagedStrands_Ver :=

	0	1
0	"L11"	3
1	"L10"	3
2	"L9"	3
3	"L8"	3
4	"L7"	1
5	"L6"	0
6	"L5"	2
7	"L4"	0
8	"L3"	0
9	"L2"	0
10	"L1"	0
11	"CL"	0
12	"R1"	0
13	"R2"	0
14	"R3"	0
15	"R4"	0
16	"R5"	2
17	"R6"	1
18	"R7"	1
19	"R8"	2
20	"R9"	3
21	"R10"	3
22	"R11"	...

Example 6: 12 × 36 in. distressed beam

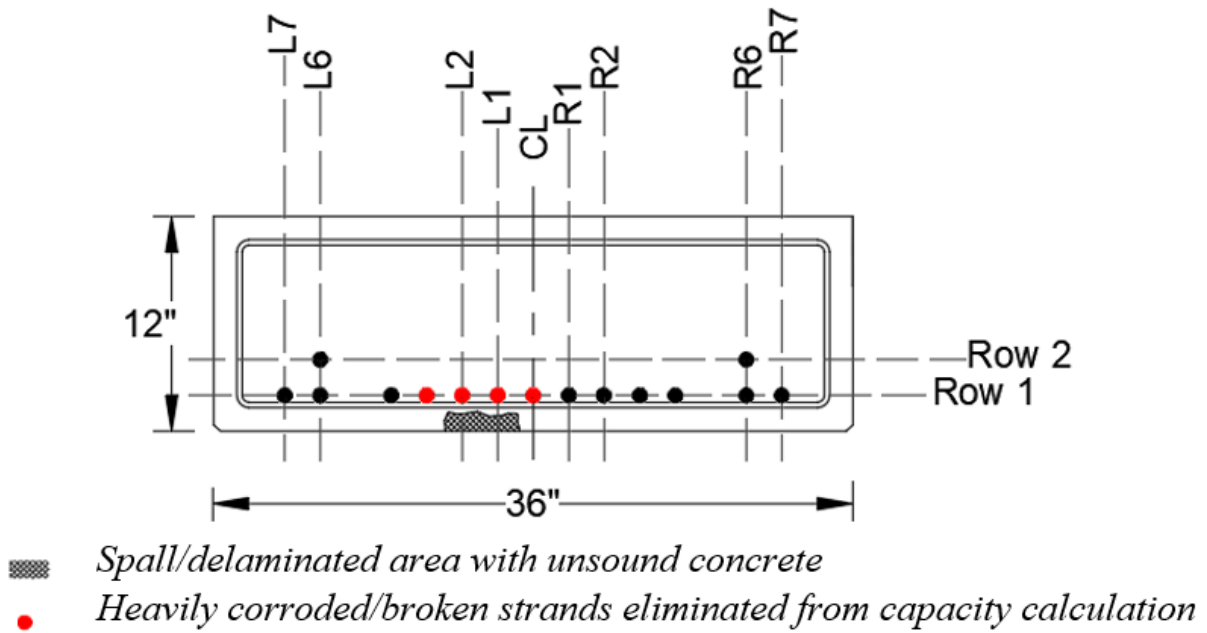


Figure E - 11. Distressed box-beam for Example 6

The following tables present the number of effective strands in this 12 × 36 in. distressed box-beam.

Table E - 13. Number of Strands Removed from Each Row to Define Damaged Section Details

Row no. (a)	No. of strands in the default layout (b)	No. of strands absent from the default layout ¹ (c)	No. of damaged strands ² (d)	No. of strands to be removed from the default layout (e) = (c) + (d)	No. of effective strands in the beam section (f) = (b) – (e)
1	21	8	4	12	9
2	23	21	0	21	2
3	8	8	0	8	0
4	2	2	0	2	0

¹ - The specific section does not include strands at every location in the default layout. These are considered to be the "absent" strands.

² - The strands eliminated from capacity calculation due to heavy corrosion or damages.

Table E - 14. Number of Strands Removed from Each Column to Define Damaged Section Details

Column no. (a)	No. of strands in default layout (b)	No. of strands absent from the default layout (c)	No. of damaged strands (d)	No. of strands to be removed from the default layout (e) = (c) + (d)	No. of effective strands in the beam section (f) = (b) – (e)
L11	3	3	0	3	0
L10	3	3	0	3	0
L9	3	3	0	3	0
L8	3	3	0	3	0
L7	2	1	0	1	1
L6	2	0	0	0	2
L5	2	2	0	2	0
L4	2	1	0	1	1
L3	2	1	1	2	0
L2	2	1	1	2	0
L1	2	1	1	2	0
CL	2	1	1	2	0
R1	2	1	0	1	1
R2	2	1	0	1	1
R3	2	1	0	1	1
R4	2	1	0	1	1
R5	2	2	0	2	0
R6	2	0	0	0	2
R7	2	1	0	1	1
R8	3	3	0	3	0
R9	3	3	0	3	0
R10	3	3	0	3	0
R11	3	3	0	3	0

As shown below, the tables in the Mathcad calculation sheet are completed using the data in the gray highlighted columns of the above two tables.

DamagedStrands_Hor :=

	0	1
0	"Row 1"	12
1	"Row 2"	21
2	"Row 3"	8
3	"Row 4"	2

DamagedStrands_Ver :=

	0	1
0	"L11"	3
1	"L10"	3
2	"L9"	3
3	"L8"	3
4	"L7"	1
5	"L6"	0
6	"L5"	2
7	"L4"	1
8	"L3"	2
9	"L2"	2
10	"L1"	2
11	"CL"	2
12	"R1"	1
13	"R2"	1
14	"R3"	1
15	"R4"	1
16	"R5"	2
17	"R6"	0
18	"R7"	1
19	"R8"	3
20	"R9"	3
21	"R10"	3
22	"R11"	...

STEP 1. BASIC CALCULATIONS

Step 1.1: Noncomposite Beam Section Properties

Noncomposite As-Designed Section Properties

The cross-section properties of the selected box-beam section are automatically populated from the linked Excel spreadsheet.

The user is NOT required to make any changes to the calculations presented in this section.

Noncomposite Damaged Beam Section Properties (Calculations)

The cross-section properties of the damaged section are calculated and presented in this section. The damaged regions are assumed to be rectangular because of possible degradation of material properties closer to the damaged area.

The user is NOT required to make any changes to the calculations presented in this section.

Noncomposite Damaged Beam Section Properties (Summary)

A summary of noncomposite damaged beam section properties is presented.

The user is NOT required to make any changes to the calculations presented in this section.

Step 1.2: Composite Beam Section Properties

Common Parameters

This section lists the modular ratio between deck and beam concretes.

The user is NOT required to make any changes to the calculations presented in this section.

Composite As-Designed Beam Cross-Section Properties (Calculations)

The cross-section properties of the composite as-designed box-beam are calculated and presented.

The user is NOT required to make any changes to the calculations presented in this section.

Composite Damaged Beam Cross-Section Properties (Calculations)

The composite cross-section properties of the distressed box-beam section are calculated and presented.

The user is NOT required to make any changes to the calculations presented in this section.

Composite Damaged Beam Cross-Section Properties (Summary)

A summary of composite cross-section properties of the distressed box-beam is presented.

The user is NOT required to make any changes to the values presented in this section.

Step 1.3: Prestressing Strand Layout

Prestressing Strand Layout: As-Designed Beam Section (Calculations)

The number of prestressing strands in the as-designed beam section is calculated.

The number of prestressing strands in the as-designed beam in *Example 1* is shown below.

The number of strands in each row of the as-designed beam section:

$$\text{StrandLayout_Hor_UD}^{(1)} := (\text{StrandLayout_Hor}^{(1)}) - (\text{AsDesignedStrands_Hor}^{(1)}) = \begin{pmatrix} 19 \\ 21 \\ 4 \\ 0 \end{pmatrix}$$

Total number of strands in the as-designed beam section (considering horizontal strand layout):

$$N_{ps_UD_Hor} := \sum_{i=0}^3 \text{StrandLayout_Hor_UD}_{i,1} = 44$$

Number of strands in each column in the as-designed beam section:

$$\text{StrandLayout_Ver_UD}^{(1)} := (\text{StrandLayout_Ver}^{(1)}) - (\text{AsDesignedStrands_Ver}^{(1)}) =$$

	0
0	2
1	3
2	2
3	0
4	2
5	2
6	2
7	2
8	2
9	2
10	2
11	2
12	2
13	2
14	2
15	...

Total number of strands in the as-designed section (considering vertical strand layout):

$$N_{ps_UD_Ver} := \sum_{i=0}^{22} \text{StrandLayout_Ver_UD}_{i,1} = 44$$

The total number of strands calculated using horizontal and vertical prestressing strand layouts shall be the same. The accuracy of calculation is checked as follows:

$$\text{Check_AsDesigned_Strand_Layout} := \begin{cases} \text{"Okay"} & \text{if } N_{ps_UD_Hor} = N_{ps_UD_Ver} \\ \text{"Not Okay, CHECK"} & \text{otherwise} \end{cases} = \text{"Okay"}$$

The user is NOT required to make any changes to the calculations presented in this section.

However, if the *Check_AsDesigned_Strand_Layout* check results in “Not Okay, CHECK”, please reevaluate the number of strands defined in the *AsDesignedStrands_Hor* and *AsDesignedStrands_Ver* for the selected beam section.

Prestressing Strand Layout: As-Designed Beam Section (Summary)

This section provides the area of prestressing strands, vertical distance to the centroid of prestressing strands from the as-designed beam bottom extreme fiber, horizontal distance to the centroid of prestressing strands from the as-designed beam vertical centerline, and the eccentricity of the centroid of prestressing strands from the centroid of the noncomposite and the composite as-designed beam sections.

The user is NOT required to make any changes to the calculations presented in this section.

Prestressing Strand Layout: Damaged Beam (Calculations)

The effective number of prestressing strands in the distressed beam section is calculated.

The effective number of prestressing strands in the distressed beam used in *Example 3* is shown below.

The number of strands in each row of the damaged beam section:

$$\text{StrandLayout_Hor_D}^{(1)} := \left(\text{StrandLayout_Hor}^{(1)} \right) - \left(\text{DamagedStrands_Hor}^{(1)} \right) = \begin{pmatrix} 13 \\ 20 \\ 4 \\ 0 \end{pmatrix}$$

Total number of strands in the damaged section (considering horizontal strand layout):

$$N_{ps_D_Hor} := \sum_{i=0}^3 \text{StrandLayout_Hor_D}_{i,1} = 37$$

Number of strands in each column in the damaged beam section:

$$\text{StrandLayout_Ver_D}^{(1)} := (\text{StrandLayout_Ver}^{(1)}) - (\text{DamagedStrands_Ver}^{(1)}) =$$

	0
0	2
1	1
2	1
3	0
4	2
5	2
6	2
7	2
8	1
9	1
10	1
11	1
12	2
13	2
14	2
15	...

Total number of strands in the damaged section (considering vertical strand layout):

$$N_{ps_D_Ver} := \sum_{i=0}^{22} \text{StrandLayout_Ver_D}_{i,1} = 37$$

The total number of strands calculated using horizontal and vertical prestressing strand layout shall be the same. The accuracy of calculation is checked as follows:

$$\text{Check_Damaged_Strand_Layout} := \begin{cases} \text{"Okay"} & \text{if } N_{ps_D_Hor} = N_{ps_D_Ver} \\ \text{"Not Okay, CHECK"} & \text{otherwise} \end{cases} = \text{"Okay"}$$

The user is NOT required to make any changes to the calculations presented in this section.

However, if the *Check_Damaged_Strand_Layout* check results in “**Not Okay, CHECK**”, please reevaluate the number of strands defined in the *DamagedStrands_Hor* and *DamagedStrands_Ver* for the selected beam section.

Prestressing Strand Layout: Damaged Beam (Summary)

The effective area of prestressing strands, vertical distance to the centroid of prestressing strands from the damaged beam bottom extreme fiber, horizontal distance to the centroid of prestressing strands from damaged beam vertical centerline, and the eccentricity of the centroid of prestressing

strands from the centroid of the noncomposite and composite damaged beam sections are defined in this section.

The user is NOT required to make any changes to the calculations presented in this section.

Step 1.4: Transformed Section Properties

Transformed Section Properties: As-Designed Noncomposite Section (Calculations)

The transformed section properties of the as-designed noncomposite section are calculated.

The user is NOT required to make any changes to the calculations presented in this section.

Transformed Section Properties: Damaged Composite Section (Calculations)

The transformed section properties of the damaged composite section are calculated.

The user is NOT required to make any changes to the calculations presented in this section.

Step 1.5: Live Loads & Prestress Loads with Losses

Live Loads on the Beam

The federal and Michigan live loads acting on the beam are calculated after applying the respective live load distribution factors.

The user is NOT required to make any changes to the calculations presented in this section.

Effective Prestress at the Section

The effective prestress force at a section with and without damage is calculated after accounting for prestress losses.

The user is NOT required to make any changes to the calculations presented in this section.

Step 1.6: Biaxial Bending

Biaxial bending analysis requirement is checked. This calculation sheet does NOT cover biaxial bending analysis. If the check fails, the user is required to identify alternative methods that are capable of evaluating biaxial bending stresses for load rating.

Common Parameters

This section lists the common parameters needed for the biaxial bending check.

Input the following:

- *total moment acting on the section about y-y axis (M_y)*
- *total moment acting on the section about x-x axis (M_x)*

Calculations

The product of moment of inertia and the tangent of the angle of rotation of the neutral axis of the damaged beam section are calculated.

The user is NOT required to make any changes to the calculations presented in this section.

Check for Biaxial Bending

The requirement for biaxial bending analysis is checked in this section.

Note: A biaxial bending analysis is not required for a box-beam section if the tangent of the angle of rotation of the neutral axis from the horizontal is less than 0.158 (Harries 2006).

The user is NOT required to make any changes to the calculations presented in this section.

Step 1.7: Girder Stresses Due to Dead Loads, Prestress Loads, and Live Loads

Stress at the Top and Bottom Extreme Fibers of the Damaged Beam

The calculation of compressive stresses at the extreme top fiber and tensile stresses at the extreme bottom fiber in a damaged concrete beam section due to dead loads, permanent load (other than dead loads), prestress loads, secondary prestress load, and live loads are demonstrated.

Noncomposite Dead Load Stresses

In a composite prestressed concrete girder-slab system, the dead loads (such as the weight of girder, haunch, and slab) and the prestress loads are resisted by the noncomposite section. Any damage to a composite prestressed girder would redistribute the stresses developed under noncomposite dead loads and prestress into both the girder and the slab. This calculation sheet implemented the procedures in Tabatabai and Nabizadeh (2019) to estimate the change in stress in a damaged girder under noncomposite dead loads.

The stresses at the top and bottom fibers of the damaged section under noncomposite dead loads are calculated. Transformed section properties are used.

Input the change in noncomposite dead load moment on the beam (ΔM_{dnc}).

If there is a reduction in the noncomposite dead load moment, define ΔM_{dnc} as a negative value. Other than the above input, the user is NOT required to make any changes to the calculations presented in this section.

Superimposed Dead Load Stresses

Superimposed dead loads act on the composite section. Since the bottom fiber stresses are greater when the beam composite section without the transformed steel area is used, transformed section properties are NOT used for the top and bottom fiber stress calculation under superimposed dead loads.

The user is NOT required to make any changes to the calculations presented in this section.

Permanent Load (Other Than Dead Load) Stresses (for LRFR)

These loads act on the composite section. Stresses at the top and bottom fibers of the damaged beam are calculated.

The user is NOT required to make any changes to the calculations presented in this section.

Stresses Due to Prestressing

In a composite prestressed concrete girder-slab system, the prestress loads are resisted by the noncomposite section. Any damage to a composite prestressed girder would redistribute the stresses developed under prestress into both the girder and the slab. This calculation sheet implemented the procedures in Tabatabai and Nabizadeh (2019) to estimate the change in stress in a damaged girder section under prestress. Transformed section properties are used.

The user is NOT required to make any changes to the calculations presented in this section.

Secondary Prestress Load Stresses (for LFR)

Even though this calculation step is included in the sheet, the secondary prestress effects are not typical to the simple spans.

The user is NOT required to make any changes to the calculations presented in this section.

Live Load Stresses (for LFR)

Live loads act on the composite section. Since the bottom fiber stresses are greater when the beam composite section without the transformed steel area is used, transformed section properties are NOT used for the top and bottom fiber stress calculation under live loads.

The user is NOT required to make any changes to the calculations presented in this section.

Live Load Stresses (for LRFR)

Live loads act on the composite section. Since the bottom fiber stresses are greater when the beam composite section without the transformed steel area is used, transformed section properties are NOT used for the top and bottom fiber stress calculation under live loads.

The user is NOT required to make any changes to the calculations presented in this section.

Strand Stress in the Damaged Beam

The stress in prestressing steel of the damaged concrete beam section due to dead loads, permanent load (other than dead loads), prestress loads, secondary prestress load, and live loads is calculated in this section. The change in stress at the steel under noncomposite dead loads due to the damage in the composite section is calculated using transformed section properties and the procedures in Tabatabai and Nabizadeh (2019). For all other load cases, transformed section properties are NOT used.

The user is NOT required to make any changes to the calculations presented in this section.

STEP 2. LOAD AND RESISTANCE FACTOR RATING (LRFR)

Step 2.1: Moment Capacity (Calculation)

Common Parameters

Input the following information:

- *system factor (ϕ_s)*
- *LRFD resistance factor for moment (ϕ)*
- *condition factor (ϕ_c).*

Note: Use the following references:

System factor (ϕ_s): AASHTO MBE (2019) Table 6A.4.2.4-1

LRFD resistance factor for moment (ϕ): AASHTO LRFD (2020) Art. 5.5.4.2

Condition factor (ϕ_c): AASHTO MBE (2019) Table 6A.4.2.3-1

Damaged Beam Capacity for LRFR (Calculations)

The capacity of the damaged beam section is calculated following the LRFR method.

The user is NOT required to make any changes to the calculations presented in this section.

Damaged Beam Capacity for LRFR

The capacity of the damaged beam section is provided as a summary in this section.

The user is NOT required to make any changes to the calculations presented in this section.

Step 2.2: Cracking Moment of Inertia Calculation

Common Parameters

This section lists the common parameters needed for cracking moment

Input the following information:

- *flexural cracking variability factor (γ_1)*
- *prestress variability factor (γ_2)*
- *distance from the beam bottom to the nearest (outermost) prestressing strand layer (y_{cover}).*

Note: The flexural cracking variability factor is 1.2 for precast segmental structures and 1.6 for all other concrete structures. The prestress variability factor is 1.1 for bonded strands and 1.0 for unbonded strands.

Cracking Moment of Inertia of the Damaged Beam (Calculations)

The cracking moment of inertia of the damaged beam is calculated.

The user is NOT required to make any changes to the calculations presented in this section.

Cracking Moment of Inertia of the Damaged Beam (Summary)

The cracking moment of inertia of the damaged beam section is presented in this section.

The user is NOT required to make any changes to the calculations presented in this section.

Step 2.3: Flexural Resistance (f_R)

Flexural Resistance of the Damaged Beam (Calculations)

The flexural resistance of the damaged beam section is calculated.

The user is NOT required to make any changes to the calculations presented in this section.

Step 2.4: Federal Inventory Ratings

Strength I Limit State

The federal inventory rating as per Strength I limit state is calculated.

The user is NOT required to make any changes to the calculations presented in this section.

Service III Limit State

The federal inventory rating as per Service III limit state is calculated.

The user is NOT required to make any changes to the calculations presented in this section.

Step 2.5: Federal Operating Rating

Strength I Limit State

The federal operating rating as per Strength I limit state is calculated in this section.

The user is NOT required to make any changes to the calculations presented in this section.

Step 2.6: Michigan Operating Ratings

Strength I Limit State

The Michigan operating rating as per Strength I limit state is calculated for all three truck configurations.

The user is NOT required to make any changes to the calculations presented in this section.

Service III Limit State

The Michigan operating rating as per Service III limit state is calculated for all three truck configurations.

The user is NOT required to make any changes to the calculations presented in this section.

Step 2.7: Permit Load Ratings

Strength II Limit State

The permit load rating as per Strength II limit state is calculated.

The user is NOT required to make any changes to the calculations presented in this section.

Service I Limit State (Calculations)

The stress in the outermost prestressing steel layer is calculated.

The user is NOT required to make any changes to the calculations presented in this section.

Service I Limit State Check (Optional)

The optional strand stress check is performed.

The user is NOT required to make any changes to the calculations presented in this section.

STEP 3. LOAD FACTOR RATING (LFR)

Step 3.1: Capacity (C) Calculation

Common Parameters

This section lists the common parameters needed for LFR calculation.

Input the following:

- *factor for type of prestressing steel (γ)*
- *LFR resistance factor for moment (ϕ_{LFR}).*

Note: The factor for type of prestressing steel (γ) is 0.28 for low-relaxation steel, 0.40 for stress-relieved steel, and 0.55 for bars. Refer to AASHTO SSD (2002) Art. 9.14 for LFR resistance factor for moment.

Damaged Beam Capacity for LFR (Calculations)

The necessary steps for damaged beam capacity calculations are presented.

The user is NOT required to make any changes to the calculations presented in this section.

Damaged Beam Capacity for LFR

The capacity of the damaged beam section is presented.

The user is NOT required to make any changes to the calculations presented in this section.

Step 3.2: Federal Inventory Ratings

Federal Inventory Rating

The federal inventory rating for concrete tension, concrete compression, prestressing steel tension, and flexural strength are calculated.

The user is NOT required to make any changes to the calculations presented in this section.

Step 3.3: Federal Operating Ratings

Federal Operating Rating

The federal operating rating for prestressing steel tension and flexural strength are calculated.

The user is NOT required to make any changes to the calculations presented in this section.

Step 3.4: Michigan Operating Ratings

Michigan Operating Rating

The Michigan operating rating for prestressing steel tension and flexural strength are calculated.

The user is NOT required to make any changes to the calculations presented in this section.

Step 3.5: Permit Load Ratings

Permit Load Rating

The permit load rating for prestressing steel tension and flexural strength are calculated.

The user is NOT required to make any changes to the calculations presented in this section.

.

STEP 4. SUMMARY

The user is NOT required to make any changes to the calculations presented in this section.

Biaxial Bending

The need for considering biaxial bending is evaluated. Please note that this Mathcad sheet does NOT support the evaluation of biaxial bending.

Concrete Cross-Section Properties for AASHTOWARE BrR

Lists concrete cross-section properties needed for AASHTOWARE BrR.

Strand Layout for AASHTOWARE BrR

Lists prestressing steel properties needed for AASHTOWARE BrR.

LRFR Moment Capacity

Provides the moment capacity of the damaged beam section.

LFR Moment Capacity

Provides the moment capacity of the damaged beam section.

Load Rating Results (LRFR Method)

Lists federal inventory, federal operating, MI operating, and permit load rating values calculated as per the LRFR method.

Load Rating Results (LFR Method)

Lists federal inventory, federal operating, MI operating, and permit load rating values calculated as per the LFR method.